



<https://theses.gla.ac.uk/>

Theses Digitisation:

<https://www.gla.ac.uk/myglasgow/research/enlighten/theses/digitisation/>

This is a digitised version of the original print thesis.

Copyright and moral rights for this work are retained by the author

A copy can be downloaded for personal non-commercial research or study,
without prior permission or charge

This work cannot be reproduced or quoted extensively from without first
obtaining permission in writing from the author

The content must not be changed in any way or sold commercially in any
format or medium without the formal permission of the author

When referring to this work, full bibliographic details including the author,
title, awarding institution and date of the thesis must be given

Enlighten: Theses

<https://theses.gla.ac.uk/>
research-enlighten@glasgow.ac.uk

MULTIPLE QUANTUM WELL STRUCTURES

AS OPTICAL WAVEGUIDES

*A Thesis submitted to the Faculty of Engineering
of the University of Glasgow
for the degree of Doctor of Philosophy*

by

Myles D. A. MacBean

October 1986

ProQuest Number: 10991753

All rights reserved

INFORMATION TO ALL USERS

The quality of this reproduction is dependent upon the quality of the copy submitted.

In the unlikely event that the author did not send a complete manuscript and there are missing pages, these will be noted. Also, if material had to be removed, a note will indicate the deletion.



ProQuest 10991753

Published by ProQuest LLC (2018). Copyright of the Dissertation is held by the Author.

All rights reserved.

This work is protected against unauthorized copying under Title 17, United States Code
Microform Edition © ProQuest LLC.

ProQuest LLC.
789 East Eisenhower Parkway
P.O. Box 1346
Ann Arbor, MI 48106 – 1346

A C K N O W L E D G E M E N T S

I wish to express my gratitude to Professor J. Lamb for his support and the use of facilities and materials at the Department of Electronics and Electrical Engineering at the University of Glasgow.

I am very grateful for the guidance, help and encouragement given throughout the duration of the project by my academic supervisor, Professor C. D. W. Wilkinson, and my industrial supervisor, Dr. S. Ritchie.

Some of the work reported in this thesis was carried out with or by colleagues, whose contributions are most gratefully acknowledged. Dr. O. Mikami is thanked for his practical support in the testing of multiple quantum well waveguides; Mr J. Frost, Dr. J. S. Roberts and Dr. N. J. Mason for the growth of waveguide structures; and Mr J. Isaac, Dr. R. A. Taylor, Dr. N. Balkan, Dr. M. Al-Mudares and Mr C. Reeves for their help in various aspects of the analysis and measurement of MQWS.

In addition, I would like to acknowledge the advice and practical assistance given by many members and former members of the department, particularly Mr R. Hutchins, Dr. G. Doughty, Mrs L. Hobbs, Mr J. Cochrane, Mr H. Anderson (and his staff), Mr J. Clarke, Mr V. Law, Mr D.F. Clarke, and all in the Ultra Small Structures Lab..

I would like to thank the many students in the department who helped create a friendly and supportive atmosphere conducive to the free exchange of ideas, especially Mr M. Grant and Mr J. Duffy.

I give my special thanks to my wife, Ruth, whose practical assistance in the typing, correcting and drawing of diagrams helped produce this thesis so swiftly. Her loving support has continually sustained me over the last three years.

* * *

This work was supported by the U.K. Science and Engineering Research Council with a C.A.S.E. studentship in association with British Telecom Research Laboratories, Martlesham Heath.

S U M M A R Y

This thesis is concerned with the design, fabrication and characterisation of semiconductor optical waveguides in which the high index guiding layer is a multiple quantum well structure (MQWS), consisting of alternate layers of high and low band gap semiconductors with the electrons and holes in the MQWS being confined to the low band gap material. This confinement in two dimensions alters greatly the electronic and optical properties of the MQWS in comparison to the bulk properties of the constituent layers.

The basic concepts involved in MQW waveguides are introduced using an elementary quantum mechanical analysis of quantum wells together with a brief description of the properties of dielectric waveguides. A more detailed treatment of the electronic and optical properties of MQWS and a review of published experimental work is used to show that the fundamental absorption edge is much more abrupt than that in the corresponding bulk material with strong excitonic characteristics being evident even at room temperature. In addition, the absorption edge is seen to be anisotropic with the fundamental energy gap being larger for light polarised perpendicular to the MQW layers. This anisotropic absorption edge, together with the layered dielectric nature of MQWS, makes them birefringent with a smaller refractive index for light polarised perpendicular to the MQW layers. The quantum confinement of carriers in MQWS also enhances their electro-absorption and electro-optic properties through the quantum confined Stark effect.

Standard techniques used in the design, fabrication and analysis of bulk semiconductor waveguides are developed for application to MQW waveguides. These include analytical and numerical techniques for the design of dielectric waveguides; dry etching and metallisation processes for the fabrication of devices; and a laser/optics system to analyse the waveguide devices. To verify these techniques they are first applied to the well-understood case of n/n^+ GaAs waveguides and are used to successfully fabricate and analyse single-mode, passive, rib waveguides at $\lambda=1.15\mu\text{m}$. The electro-optic coefficient is also measured in an active, planar n/n^+ waveguide and found to be close to that reported by other workers.

The design techniques are then applied to MQWS waveguides resulting in the design of a MQW double heterostructure (MQW-DH), p-i-n diode which was predicted to produce the required quantum properties (strong, room temperature, excitonic behaviour), waveguide properties (single-mode propagation up to the fundamental absorption edge) and electronic properties (a high reverse bias breakdown voltage and uniform applied electric field). Most of the theoretical work and all the experimental work included is devoted to MQWS in the (Al,Ga)As, III-V semiconductor alloy system. Accordingly, the methods available for growing MQWS in this system are reviewed with Molecular Beam Epitaxy (MBE) being found the most likely method to satisfactorily reproduce the desired structure.

MQW-DH were grown at two establishments and are initially studied by photoluminescence and scanning electron microscopy before their planar optical waveguide characteristics are checked using the laser system. Only one sample is found to satisfy all the design requirements, and then only partially. Detailed analysis of the properties of MQW waveguides is therefore limited to this structure.

Passive MQW-DH waveguides are demonstrated to exhibit an anisotropic absorption edge as predicted, and it is shown that the design and fabrication techniques developed can be successfully used to obtain single, double and multi-mode strip loaded waveguides. Single-mode waveguides are also used to fabricate passive directional couplers with coupling lengths in good agreement with theoretically predicted values.

A semi-empirical model is put forward to describe the band edge electro-absorption of MQWS. Although simple, the model is in qualitative and approximate quantitative agreement with published results. To allow a comparison to be made, the electro-absorption of bulk GaAs is also modelled. A realistic electro-absorption figure of merit is the ratio of the change in absorption for a given applied field to the initial absorption for no applied field. It is found that the maximum figure of merit obtainable in MQWS is 5-6 times larger than that in bulk GaAs. In MQWS this maximum is obtained at an optimum applied field of approximately 30% of the available avalanche breakdown field whereas in bulk GaAs the figure of merit steadily

increases with applied field to reach a maximum at the avalanche breakdown field.

Electro-absorption is experimentally investigated in both planar and stripe MQW-DH waveguides. Although no quantum confined Stark effect is observed there is a strong shift in band edge with applied electric voltage. This is measured to produce a figure of merit of 35 for a voltage of -4 volts compared with a published figure of merit of 4.6 at -24 volts for GaAs-DH.

The very large electro-absorption observed precludes any measurement of the electro-optic effect in MQW-DH close to the band edge. A strong electro-optic effect is observed at $\lambda=1.15\mu\text{m}$ but further work is required before this can be confidently stated to imply an enhanced electro-optic coefficient.

In conclusion recommendations are made concerning the application of the observed properties of MQW-DH p-i-n diodes to integrated optics. These properties, together with the reported low passive waveguide loss of MQW laser diodes, make MQW-DH an ideal medium for the monolithic integration of optical circuits.

C O N T E N T S

	PAGE
ACKNOWLEDGEMENTS	I
SUMMARY	II
CONTENTS	V
 CHAPTER ONE INTRODUCTION	
1.1 GENERAL	1
1.2 INTEGRATED OPTICS	3
1.2.1 Planar Waveguides	3
1.2.2 Stripe Waveguides	6
1.3 MULTIPLE QUANTUM WELL STRUCTURES	8
1.4 SYNOPSIS OF THESIS	13
 References to Chapter One	 14
 CHAPTER TWO THE OPTICAL PROPERTIES OF MULTIPLE QUANTUM WELL STRUCTURES	
2.1 INTRODUCTION	19
2.2 BAND STRUCTURE MODELLING	19
2.2.1 The Finite Single Potential Well Model	21
2.2.2 Multiple Quantum Wells	22
2.2.3 Density of States Function and Fermi Level	27
2.3 ABSORPTION AND REFRACTION	29
2.3.1 Inter-Miniband Effects	29
2.3.2 Inter-Band Effects	31
2.4 THE EFFECT OF APPLIED ELECTRIC FIELD	39
2.4.1 Electro-Absorption	40
2.4.2 Electro-Optic Effect	41
2.5 CONCLUSIONS	43
 References to Chapter Two	 44

**CHAPTER THREE THE DESIGN & FABRICATION TECHNIQUES AND THE ANALYSIS
SYSTEM USED FOR SEMICONDUCTOR WAVEGUIDES**

3.1	INTRODUCTION	49
3.2	WAVEGUIDE MODELLING	49
	3.2.1 The Four Layer Slab Model	49
	3.2.2 The Modified Effective Index Method	51
	3.2.3 The WAVE Variational Method	52
	3.2.4 Comparison of Methods	54
3.3	FABRICATION	54
	3.3.1 Substrate Preparation	55
	3.3.2 Photoresist Patterning	55
	3.3.3 Dry Etching	56
	3.3.4 Metal Contacts	59
	3.3.5 Cleaving	61
3.4	WAVEGUIDE ANALYSIS SYSTEM	62
	3.4.1 End-Fire Coupling System	63
	3.4.2 Dye-Laser System	64
3.5	CONCLUSIONS	67
	References to Chapter Three	68

CHAPTER FOUR GaAs WAVEGUIDES

4.1	INTRODUCTION	70
4.2	DESIGN AND GROWTH	70
	4.2.1 Refractive Index	71
	4.2.2 Single-Mode Condition	71
	4.2.3 Propagation Loss Criterion	72
	4.2.4 Layer Growth	73
	4.2.5 Ridge Waveguide Design	74
4.3	RIDGE WAVEGUIDE FABRICATION	75
	4.3.1 Etch Conditions and Procedure	76
	4.3.2 Ridge Profile	76
	4.3.3 GaAs Etch Rate	77
	4.3.4 Waveguide Etch	77
4.4	MODAL CHARACTERISTICS	78
4.5	PROPAGATION LOSS	79
	4.5.1 Theory	79
	4.5.2 Sequential Cleave Measurements	81
	4.5.3 Fabry-Perot Method	83

4.6	THE ELECTRO-OPTIC EFFECT IN GaAs	84
4.6.1	Theory	84
4.6.2	Crystal Orientation	86
4.6.3	Variational Theorem for Dielectric Waveguides..	86
4.6.4	Experimental Techniques	87
4.6.5	Experimental Results	89
4.6.6	Discussion	92
4.7	CONCLUSIONS	92
	References to Chapter Four	93

CHAPTER FIVE THE DESIGN, GROWTH AND INITIAL TESTING OF MQW-DH

5.1	INTRODUCTION	95
5.2	DESIGN	96
5.2.1	Design Requirements and Assumptions	96
5.2.2	Quantum Properties	97
5.2.3	Waveguide Properties	98
5.2.4	Electronic Properties	100
5.2.5	Miscellaneous.. .. .	103
5.3	GROWTH OF MQWS	103
5.3.1	Metal Organic Vapour Phase Epitaxy (MOVPE) ..	104
5.3.2	Molecular Beam Epitaxy (MBE)	106
5.3.3	Comparison	108
5.4	ANALYSIS	109
5.4.1	History	110
5.4.2	Methods	111
5.4.3	Results	114
5.4.4	Conclusions	118
5.5	CONCLUSIONS	119
	References to Chapter Five	119

CHAPTER SIX PASSIVE MQW-DH WAVEGUIDES

6.1	INTRODUCTION	123
6.2	PLANAR WAVEGUIDES	123
6.2.1	Near Field Pattern	123
6.2.2	Absorption Edge	126
6.3	DESIGN OF PASSIVE STRIPE WAVEGUIDES	129

6.4	FABRICATION OF PASSIVE STRIPE WAVEGUIDES	130
6.4.1	Etch Conditions and Procedure	130
6.4.2	Ridge Profile	131
6.4.3	Waveguide Etch	132
6.5	MODAL CHARACTERISTICS	132
6.6	PROPAGATION LOSS	134
6.7	PASSIVE DIRECTIONAL COUPLER	134
6.7.1	Design and Fabrication	135
6.7.2	Experimental Results	137
6.8	CONCLUSIONS	138
	References to Chapter Six	139

CHAPTER SEVEN THE ELECTRO-ABSORPTION EFFECT IN MQW-DH

7.1	INTRODUCTION	140
7.2	THEORETICAL MODEL	140
7.2.1	Model Description	140
7.2.2	Results of Model	143
7.2.3	Results Compared with Published MQW	144
7.2.4	Comparison Between Electro-Absorption in MQWS and Bulk GaAs	145
7.2.5	Conclusions and Model Limitations	146
7.3	I-V AND C-V TESTS	147
7.3.1	I-V Tests	147
7.3.2	C-V Tests	149
7.4	PHOTOCURRENT SPECTROSCOPY	151
7.4.1	Description of Method	152
7.4.2	Experimental Method and Results	154
7.4.3	Conclusions and Recommendations	155
7.5	PLANAR WAVEGUIDE RESULTS	156
7.5.1	Absorption Edge Shift	157
7.5.2	Modulation Depth	158
7.6	ACTIVE RIB WAVEGUIDE FABRICATION	160
7.6.1	Fabrication Procedure	160
7.6.2	Device Results	162
7.7	CONCLUSIONS	163
	References to Chapter Seven	164

CHAPTER EIGHT THE ELECTRO-OPTIC EFFECT IN MQW-DH

8.1 INTRODUCTION 166
8.2 EXPERIMENTAL METHOD 167
8.3 RESULTS 168
8.4 DISCUSSION AND CONCLUSIONS 168

References to Chapter Eight 171

CHAPTER NINE CONCLUSIONS 172

APPENDIX A 177

APPENDIX B 179

CHAPTER ONE

INTRODUCTION

1.1 GENERAL

The object of this chapter is to give a brief description of the application and theory of integrated optics and multiple quantum well structures as an introduction to the more detailed and specific topics covered in the rest of the thesis.

The rapid progress made in recent years in the development of low-loss, wide-band single-mode optical fibres and reliable semiconductor lasers and detectors has stimulated great interest in the field of integrated optics. The field of integrated optics involves the fabrication and characterisation of optical waveguide devices that only sustain a low number of propagating modes. Integrated optics has the potential of facilitating the direct processing of the optical signals transmitted along optical fibres. The areas of most interest for the application of integrated optical devices are communications systems¹, sensors² and signal processing³.

Much of the early research and development in integrated optics was carried out on materials such as lithium niobate and glass, in which both active devices⁴⁻⁶ (modulators and switches) and passive devices⁷⁻⁹ (couplers, bends etc.) have been successfully fabricated. However, the ultimate goal of integrated optics is the monolithic fabrication of laser sources, detectors and devices, as well as active electronic components. Semiconductor materials such as GaAs, InP and related compounds are the obvious materials for such monolithic integration, and much research is currently being carried out into the fabrication of active devices¹⁰⁻¹³ (eg. phase and amplitude modulators, and switches), passive devices¹⁴⁻¹⁷ (low-loss guides, Y-junctions, directional couplers and bends), laser/modulator integration and detector/amplifier integration^{18, 19}.

Independent from the field of integrated optics, recent advances in semiconductor growth techniques such as vapour phase epitaxy (VPE) and molecular beam epitaxy (MBE) have made it possible to prepare complex

structures involving two or more compounds (for example GaAs and (Al,Ga)As) with good control of the material parameters such as layer thickness, composition, and impurity concentration²⁰. This allows new freedom to engineer the band structure of "synthetic" semiconductor structures with novel optical and electronic properties²¹. In particular, the multiple quantum well structure (MQWS) has been of great interest. Quasi-two-dimensional behaviour can be produced in these structures where a thin layer of a low band gap semiconductor (for example GaAs) has been sandwiched between layers of a compound with a larger band gap (for example (Al,Ga)As) with the electrons and holes generally being confined in the low gap layer ^{22,23}. One such set of alternating layers is called a quantum well since electrons and holes fall into the potential well formed by the low gap material. Several such sets of alternating layers can be grown so that, although the individual wells behave independently of each other, their effects add together. This is the MQWS. If the wells do not behave independently, and electrons have a significant probability of tunnelling from one well to another, the structure is termed a superlattice (SL).

The motivation for the study of the properties of MQW optical waveguides reported in this thesis came from two considerations. Firstly, MQW lasers have become the centre of considerable attention because of their low threshold current density²⁴, the weak temperature dependence of their threshold current²⁵, and the large gain difference between TE and TM modes²⁶. These features make them especially suited for use in integrated optics which will encounter heat problems when the number of components in the optical and electronic devices increases. MQW structures also exhibit lower waveguide propagation loss at their lasing wavelength²⁷, making them ideally suited for use in monolithic integrated optical circuits. If MQW lasers are to be thus used, it will be necessary to have a detailed understanding of MQW optical waveguides.

The second consideration is that MQWS exhibit novel properties due to their quasi-two-dimensional nature, such as a steep fundamental absorption edge that exhibits strong excitonic characteristics at room temperature²⁷⁻³³. These properties have led to the prediction of enhanced electro-absorption and electro-optic effects, as well as enhanced non-linear effects close to the absorption edge of MQWS.

Recently, various opto-electronic devices designed to use these effects for high speed modulation and switching have been proposed and tested, such as bistable optical devices³⁴, quantum confined Stark modulators³⁵ and the "Self Electro-optic Device" (SEED)³⁶. Most of these devices utilise propagation perpendicular to the epitaxial MQW layers. If the optical field is constrained to propagate along the plane of the MQW layers, using an optical waveguide, certain advantages can be obtained:

- (i) enhanced effects due to the optical mode being confined over a guided distance,
- (ii) the possibility of travelling-wave type modulators to enhance high speed operation,
- (iii) suitability for integration of devices into integrated opto-electronic circuits.

Very recently initial studies in leaky mode waveguides^{37,38} and MQW double heterostructure waveguides³⁹ have shown the feasibility of MQW waveguides, and some interesting anisotropic effects^{37,38} have been observed.

It is the aim of this thesis to investigate further the characteristics of active and passive MQW optical waveguides and waveguide devices for use in integrated optic circuits.

1.2 INTEGRATED OPTICS

The following section gives a brief overview of integrated optics theory. Many review papers and text books deal with the analysis of the optical properties of dielectric waveguides for integrated optics⁴⁰, and the reader is directed there for more detail on the subject.

1.2.1 Planar Waveguides

The following brief discussion of the ray optical model of light propagation in a planar waveguide introduces the basic concepts and terminology of dielectric waveguide theory, i.e. the nature of propagation modes, waveguide cut-off, and the propagation constant. The planar waveguide structure will be analysed because of its considerable use in the experimental work contained in this thesis.

This ray-optics approach is very simple and does not give as rigorous a description as that provided by electromagnetic theory. The more rigorous analysis will be outlined in a later chapter.

The simplest form of integrated optical component is the three layer planar waveguide shown in cross-section in Fig 1-1. This consists of a layer of constant refractive index n_2 and thickness t_2 , on top of a semi-infinite substrate of index n_1 , and below a semi-infinite superstrate (often air) of index n_3 .

If a ray is incident on a dielectric interface with an angle θ , then it will be transmitted through the interface if θ is smaller than the critical angle, and reflected if θ is greater than the critical angle. The critical angles for the two interfaces are given by:

$$\theta_{3,2} = \sin^{-1}(n_3/n_2) \quad \text{and} \quad \theta_{1,2} = \sin^{-1}(n_1/n_2) \quad (1.1)$$

Thus, if a ray is incident with $\theta < \theta_{1,2}$ or $\theta < \theta_{3,2}$ it will be radiated, but if $\theta > \theta_{1,2}$ or $\theta > \theta_{3,2}$, total internal reflection will confine it to the high index film. These conditions are shown in Fig 1-2.

At this stage it is worth emphasising that an unusual choice of cartesian axes is used throughout this thesis, with the propagation direction being +y and the epitaxial layers being perpendicular to the z axis. This choice is made so that the coordinate system used in the analysis of MQW waveguides will be consistent with the quantum mechanical convention that quantum confinement take place along the z axis.

In the ray model, the guided ray is represented by a local plane wave propagating through the structure with propagation constant β in the direction of propagation (y) and k_z in the orthogonal direction (z). These are related to θ by:

$$\beta = k_0 n_2 \sin \theta \quad \text{and} \quad k_z = k_0 n_2 \cos \theta \quad (1.2)$$

where k_0 is the free space wave number. Defining the effective index (n_e) of the guided mode as β/k_0 , the cut-off condition $n_e \leq n_1$ can be

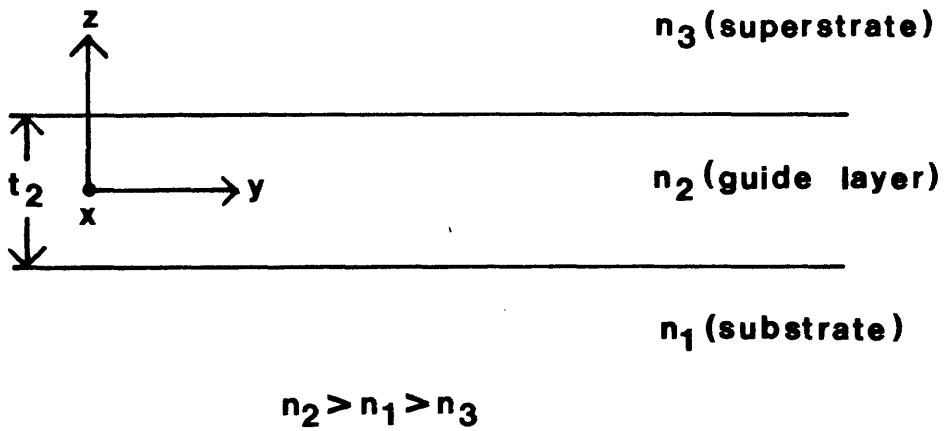


Fig 1-1 The three layer planar waveguide.

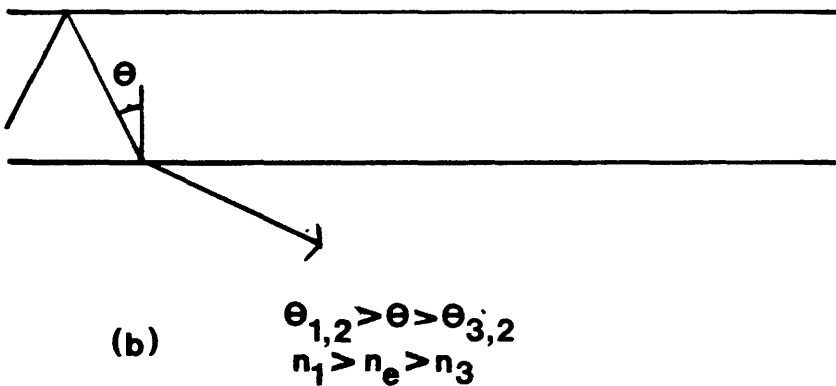
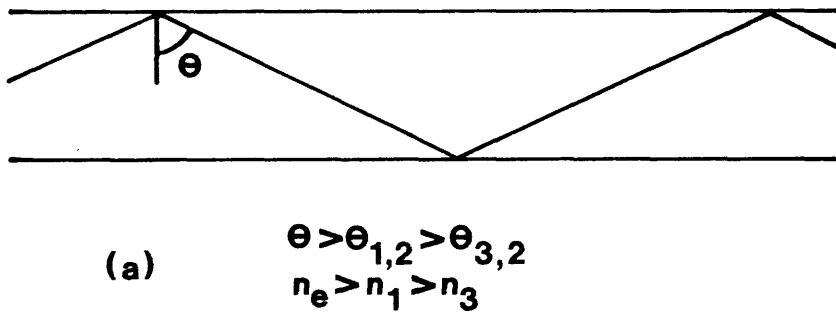


Fig 1-2 The ray model of the planar waveguide.

(a) guided mode,

(b) substrate radiation mode.

obtained from (1.1) and (1.2), within which region no guided mode will propagate.

Not all values of β (ie. angles θ) are allowed; only a discrete set of angles (and sometimes none) lead to a self-consistent model with these discrete values of β corresponding to "guided modes" of propagation. In order for the model to be consistent, the phase change in the orthogonal direction introduced by a ray travelling from one interface to the other and back, including the two interface reflections, must be a multiple of 2π , so that the waves add constructively. This leads to the eigenvalue equation (also known as the "transverse resonance condition"):

$$2k_x t_2 - 2\theta_{1,2} - 2\theta_{3,2} = 2m\pi \quad (1.3)$$

with

$$k_x^2 = (\beta^2 - k_0^2 n_2^2)$$

t_2 = guide layer thickness

θ = interface reflection phase shifts

m = an integer (0,1,2,...)

Two distinct types of guided modes can be sustained in a planar waveguide; those where the transverse electric field is in the x direction (TE modes) and those where the transverse electric field is in the z direction (TM modes). The phase shifts at the guide-substrate and guide-superstrate interfaces ($-2\theta_{1,2}$ and $-2\theta_{3,2}$) depend on whether a TE or TM mode is propagating, and are given for TE modes by:

$$\tan^2 \theta_{3,2} = (n_e^2 - n_s^2) / (n_z^2 - n_e^2)$$

$$\tan^2 \theta_{1,2} = (n_e^2 - n_1^2) / (n_z^2 - n_e^2)$$

By solving (1.3), $n_e(t_2)$, can be determined for any step-index, slab waveguide geometry. For a given set of conditions the solution will consist of a discrete set of values of n_e , each n_e satisfying (1.3) for a different value of m . These different values of n_e correspond to different angles θ and may be considered to be different waveguide modes of order m .

To obtain information on the field distribution for these guided modes, electromagnetic theory must be used and this will be left to the more detailed discussion of later chapters. However, the field distribution within the guide region varies as $\cos(k_x z + h)$, where the

modal order number (m) gives the number of field zeros, and h is a phase constant which depends on m . Outside the guide layer the field is evanescent and decays exponentially as $\exp(-\gamma z)$, where $\gamma = k_0(n_0^2 - n_{1,2}^2)^{1/2}$.

1.2.2 Stripe Waveguides

Slab waveguides confine the light in only one of the directions perpendicular to the direction of propagation. To enable the fabrication of more compact devices, and the directing and switching of light on the surface of a substrate, stripe waveguides which confine light in both directions perpendicular to the propagation direction are needed. There are many different methods of obtaining such two-dimensional (2D) confinement, and Fig 1-3 shows several different step-index, rectangular, waveguide structures. The embedded channel guide laterally confines light through its real lateral refractive index step. In the rib and strip loaded guides, lateral confinement occurs due to the higher effective index under the ridge.

In general, the rectangular 2D optical waveguide is a far more complex structure to analyse than the slab guide, with the propagating modes being hybrid (TEM), pure TE or TM modes being impossible. The full, general solution of the wave equation for the structure has never been calculated. Without this exact solution two different approaches have been used to obtain an approximation to the exact solution. The first approach is to reduce the two-dimensional problem into two one-dimensional problems by using suitable approximations. The second is to use the numerical power of a computer to carry out rigorous numerical calculations.

Marcatili's method⁴¹ is the earliest example of the former approach. He uses the principle of separation of fields, whereby the orthogonal fields in the x and z directions are solved separately assuming them to be uncoupled. This solution is only applicable to step-index rectangular waveguides which are far from cut-off. This is a severe limitation to the method since in designing single-mode structures, the guides are relatively close to cut-off. Knox and Toullos⁴² modified Marcatili's method to deal with modes closer to cut-off by using an Effective Index Method to couple the two orthogonal fields. This method has been applied to a wide range of

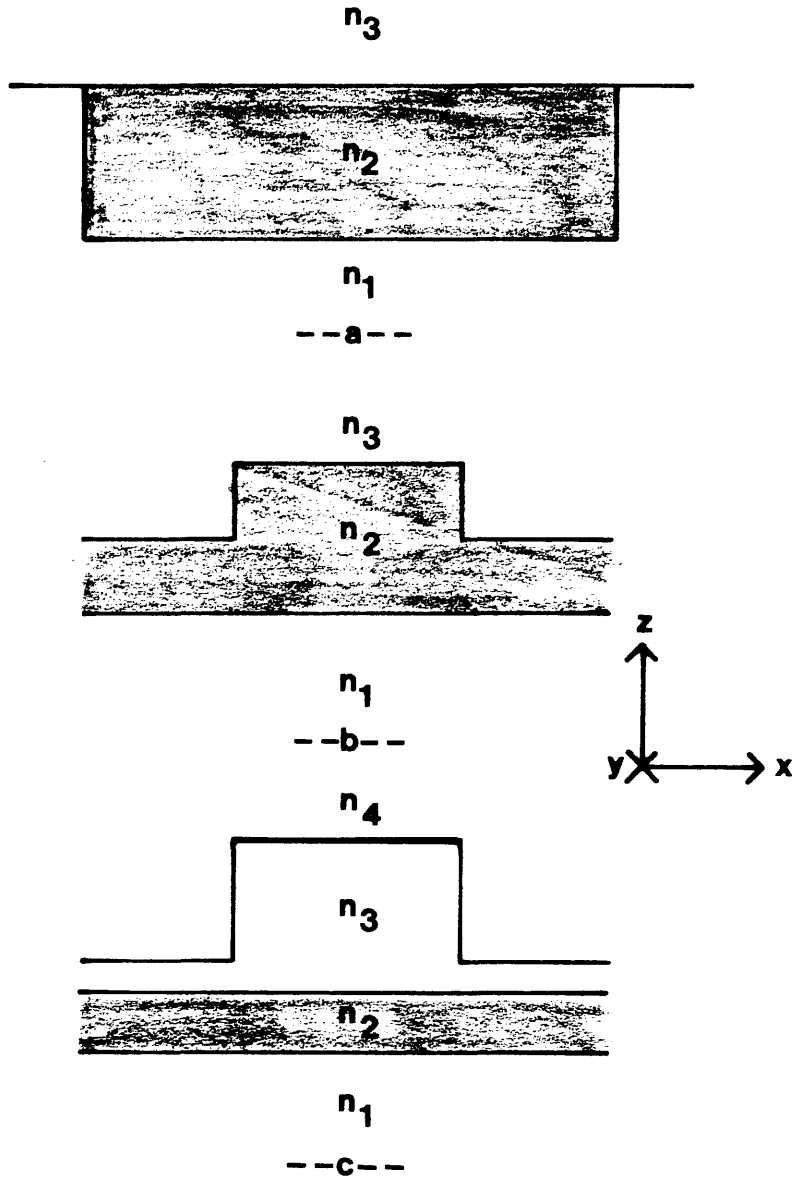


Fig 1-3 Various stripe waveguide structures.

(a) embedded channel guide,

(b) rib guide,

(c) strip loaded guide.

In all cases $n_2 > n_1 > n_3 > n_4$.

problems and is dealt with in depth in the literature ⁴³. It is the simplest method of obtaining a relatively good approximation to the propagation constant and gives clear physical insight into the physics of 2D optical waveguides. A detailed description of this method is given in a later chapter.

Although more accurate than Marcatili's method and applicable closer to cut-off, the Effective Index Method is still far from satisfactory very close to cut-off⁴⁴. To try and improve on the Effective Index Method, Koshiha and Suzuki⁴⁵ applied an equivalent network approach to the problem to obtain the Modified Effective Index Method. This method obtains results which are very close to the results of more expensive and time consuming computer numerical methods. This Modified Effective Index Method has been used throughout this thesis and is also described in more detail in a later chapter.

Of the second approach, which uses the power of a computer to numerically solve the problem, several methods have become generally accepted for use in the analysis of rectangular, step-index waveguides. These include the finite difference method⁴⁶, the finite element method⁴⁷ and the WAVE variational method^{8,48}. All three use the variational expression of the wave equation. Due to its availability, the WAVE variational method was used in this thesis. This method solves the Helmholtz scalar wave equation which describes the propagation of TEM modes through an arbitrary refractive index distribution thus:

$$\nabla^2_{x,z} E_x + k_0^2 (n^2(x,z) - n_m^2) E_x = 0$$

where $E_x = E_x(x,z)$ and $\nabla^2_{x,z} = (\delta^2/\delta x^2) + (\delta^2/\delta z^2)$

In the variational method this wave equation is restated as the variational expression for the propagation constant $\beta = n_m k_0$:

$$F(E_x) = \beta^2 = \left(\int_{-\infty}^{+\infty} \int_{-\infty}^{+\infty} [\nabla^2 E_x + k_0^2 (n^2(x,z) - n_m^2)] \cdot E_x \, dx \, dz \right) / \left(\int_{-\infty}^{+\infty} \int_{-\infty}^{+\infty} E_x \cdot E_x \, dx \, dz \right)$$

If $E_x(x,z)$ is now replaced by a trial function $\theta(x,z) = E_x(x,z)$ then $F(\theta)$ is at a stationary maximum value and is equal to β^2 . In the Rayleigh-Ritz method used by WAVE, the trial function used is a series

of orthogonal basis functions, the Hermite-Gaussian functions. Each term in the series has a coefficient which can be varied to alter $\theta(\mathbf{x}, z)$. In practice, the series is finite in length and θ can therefore never exactly model E_x . However, when $F(\theta)$ is maximised it provides a lower bound to β^2 which can be obtained to any required precision by increasing the number of terms in the series. WAVE converts this maximisation problem to that of finding the eigenvalues of a matrix equation in the basis function coefficients, the eigenvalues being related to the modal propagation constants β .

If the waveguide geometry is rectangular with a long dimension (width) and a short dimension (height), the general characteristics of stripe waveguides can be summarised thus:

(1) A pair of distinct but not independent transverse resonances across the width (x direction) and height (z direction) may be distinguished. Associated with these resonances are what may be termed the "lateral" mode order (n) and the "planar" mode order (m) respectively. n and m give the number of field zeros of the quasi-sinusoidal standing wave pattern across the width and depth respectively.

(2) Associated with each planar mode is a full spectrum of lateral modes. These respond to width and lateral index-difference in the same way as do planar modes to depth and index-difference.

(3) If the guide is excited by means of a TE plane wave with no x direction propagation component, the resulting TEM mode has a large E_x component and is referred to as "quasi-TE" and denoted TE_{nm} . Similarly, TM excitation leads to TM_{nm} , hybrid modes with a large E_z component.

1.3 MULTIPLE QUANTUM WELL STRUCTURES

The physical properties of MQWS are governed by their electron energy band structure. This section introduces the study of multiple quantum well structures by analysing the simplest model of the electron energy band structure in MQWS; the one-dimensional, infinitely deep, quantum well.

In quantum mechanics the wave function of a particle, $\psi(\mathbf{r}, t)$, is defined such that the modulus squared of ψ is proportional to the probability of finding the particle at position $\mathbf{r}=(\mathbf{x}, \mathbf{y}, \mathbf{z})$ at time t .

This complex function ψ is assumed to describe completely the dynamical state of the particle. Schrödinger's wave equation for a particle in three dimensions describes the progress of a particle in space and time as:

$$i\hbar(\delta/\delta t)\psi(r,t) = H\psi(r,t) \quad (1.4)$$

where H is called the Hamiltonian operator and is defined as:

$$H = P^2/2m_0 + V$$

where m_0 = particle free mass, P = momentum operator, where $P^2 = -\hbar^2\nabla^2$, and $\nabla^2 \equiv (\delta^2/\delta x^2) + (\delta^2/\delta y^2) + (\delta^2/\delta z^2)$.

In the problems of interest in this thesis, the potential energy (V) is independent of time and so if $\psi(r,t)$ is considered as the product of a spatial and a temporal function, then separation of variables allows (1.4) to be rewritten as the time independent eigenvalue equation:

$$H\psi(x,y,z) = E\psi(x,y,z) \quad (1.5)$$

where E , the separation constant, is the total energy of the system.

In MQWS the potential V can be considered as consisting of the main crystal lattice potential $V_0(x,y,z)$ and a periodic additional potential $\phi(z)$. In this general form, equation (1.5) would be practically impossible to solve. However, in the structures of interest the period of $\phi(z)$ is much greater than the period of V_0 and its amplitude is much less. The energy bands that exist in the host crystal without any MQWS are thus only distorted at the band edge. Close to the band edge a semiconductor crystal's dispersion law can be considered quadratic, that is:

$$E(\mathbf{k}) \propto \mathbf{k}^2$$

where \mathbf{k} is the particle's momentum.

The effective mass theorem then allows an effective mass m^* to be defined as:

$$m^* = - \hbar^2 (d^2E/dk^2)^{-1}$$

so that the full Hamiltonian:

$$H = P^2/2m_0 + V_0(x, y, z) + \emptyset(z)$$

can be replaced by:

$$H = P^2/2m^* + \emptyset(z)$$

The rapidly varying, atomic scale potential $V_0(x, y, z)$ is therefore transformed away and the heterojunction problem is reduced to a well-defined potential problem for a quasi-free electron. This method is valid unless the layer widths are so small that the period of $\emptyset(z)$ is of the order of $V_0(r)$ when more powerful methods are needed.

At its simplest, the behaviour of a MQWS can be modelled by a potential of the form of a set of infinitely deep, one-dimensional, single potential wells so that $\emptyset(z)$ is defined as:

$$\begin{aligned} \emptyset(z) = 0 & : & -a/2 + md < Z < a/2 + md \\ \emptyset(z) = \infty & : & a/2 + md < Z < a/2 + b + md \end{aligned}$$

where a = well thickness, b = barrier thickness, m = integer (...-1, 0, 1...), $d = a + b$.

For this potential system (1.5) becomes:

$$\begin{aligned} (d^2/dz^2)\psi(z) &= -(2m^*E_x/\hbar^2)\psi(z) \\ &= -k_x^2\psi(z) \end{aligned} \quad (1.6)$$

where k_x is the wave vector of the particles under consideration. This equation has the general solution:

$$\psi = A \cdot \exp(ik_x z) + B \cdot \exp(-ik_x z) \quad (1.7)$$

where A and B are arbitrary constants.

The general boundary conditions on ψ are that ψ and ψ' should be continuous. However, for the infinitely deep well it is clear that the probability of an electron being outside the well is zero. Thus:

$$\psi(a/2) = 0 \quad ; \quad \psi(-a/2) = 0$$

Applying the boundary conditions and (1.6) to the general solution, (1.7), it is found that:

$$(A/B)^2 = 1 \quad \text{i.e.} \quad A = B \quad \text{or} \quad A = -B$$

The continuity of ψ' implies that:

$$\psi'(a/2) = ik_x(A-B)\cos(k_x a/2) = i(B+A)\sin(k_x a/2) = 0$$

so that

$$A=B \Rightarrow \sin(k_x a/2) = 0 \Rightarrow k_x a = n\pi \quad ; \quad n \text{ even}$$

$$A=-B \Rightarrow \cos(k_x a/2) = 0 \Rightarrow k_x a = n\pi \quad ; \quad n \text{ odd}$$

where n is an integer (0,1,2...). Thus the energy eigenvalues of the system are:

$$E_x = E_n = n^2 \pi^2 \hbar^2 / (2m^* a^2) = E_1 n^2 \quad (1.8)$$

where E_1 is the ground state eigenvalue and n the quantum number.

From this model it is seen that the continuous band of states in a bulk semiconductor will be split in the quantum well structure into discrete energy levels with the following properties:

- (1) In the z direction, energy is quantised into discrete energy eigenvalues, the value being proportional to the square of the quantum number, n (See Fig 1-4).
- (2) The ground state energy is inversely proportional to the square of the well width, so the wider the well the closer the ground state is to the bottom of the well.
- (3) The eigenstate wave functions have alternating symmetry with the quantum numbers defining the number of wave function zeros within the well.

Fig 1-5 schematically depicts these conclusions. Both the conduction and the valence bands of the bulk semiconductor will be

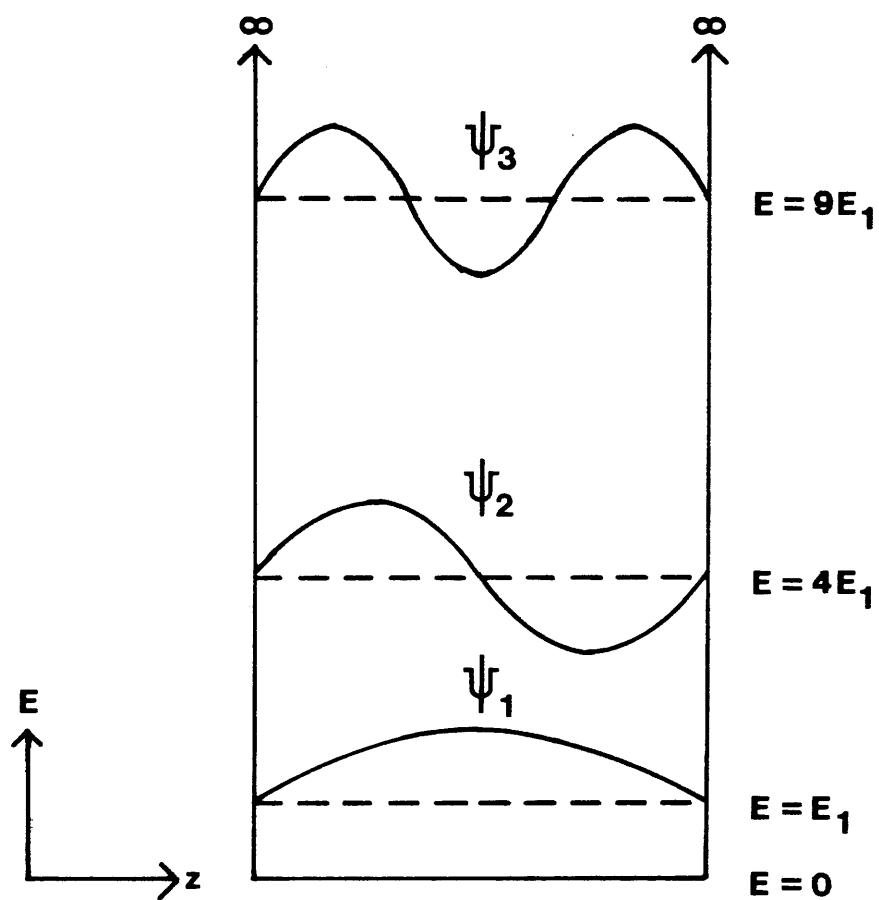


Fig 1-4 A real space, energy diagram of the energy eigenvalues and eigenfunctions of the infinite well model.

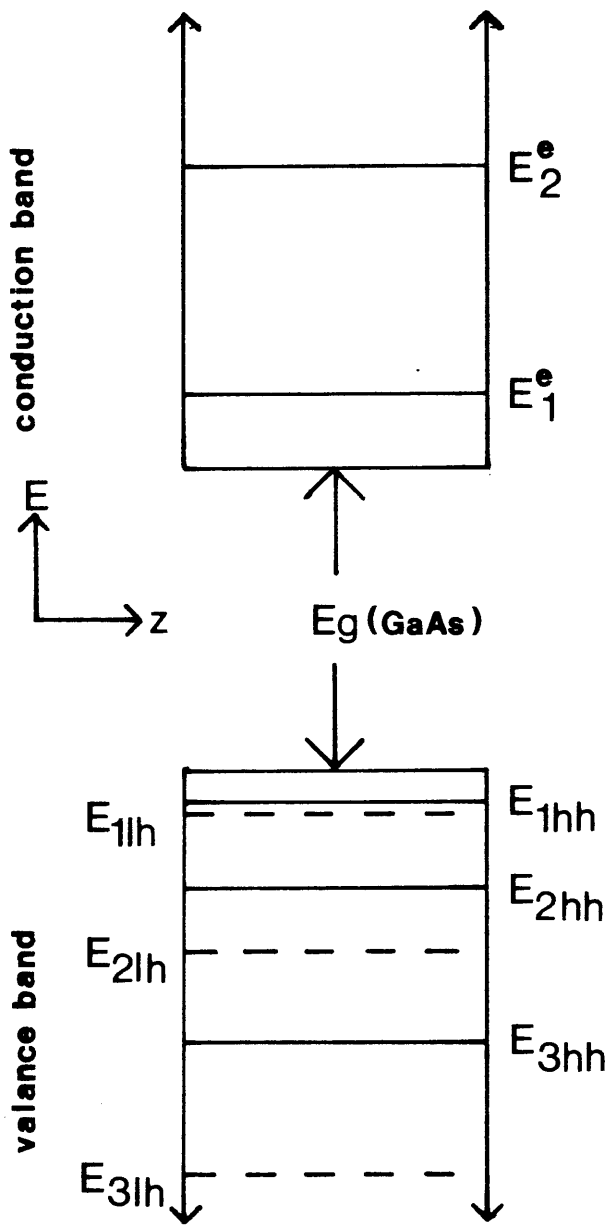


Fig 1-5 A schematic representation of the energy levels of an $(\text{Al,Ga})\text{As}/\text{GaAs}$ MQWS as derived by the infinite well model. The energy levels are denoted:

- E^e = electron state,
- E_{hh} = heavy hole state,
- E_{lh} = light hole state.

split into energy levels, the conduction and valance band energy levels being calculated from (1.8) using the respective Γ valley effective masses in the quantisation direction. Since the effective mass enters into (1.8), the degeneracy of the valance band of GaAs (see section 2.2) will be lifted, and the quantum well in the valance band will have two sets of energy levels corresponding to the heavy hole and light hole valance bands.

The density of states per unit area of this quantum well structure can also be deduced. In a 2D system the free electron density of states per unit area is independent of energy with:

$$g(E) = (m^*/\pi\hbar^2)$$

where $E(k) = (\hbar^2 k^2 / 2m^*)$, $k^2 = k_x^2 + k_y^2$

In this quasi-2D system we have total energy:

$$E = (\hbar^2 k^2 / 2m^*(x, y)) + n^2 E_1$$

so that

$$g(E) = (m^*(x, y) / \pi\hbar^2) n \quad : \quad E_n \leq E < E_{n+1}$$

where $m^*(x, y)$ is the particle effective mass in the plane of the wells. Thus, for a total energy less than E_1 , no states exist and $g(E)=0$. But when $E=E_1$, $m^*(x, y)/\pi\hbar^2$ states become available. Until $E=E_2$ no further states become available, then at $E=E_2$ another $m^*(x, y)/\pi\hbar^2$ states become available, giving $g(E)=2m^*(x, y)/\pi\hbar^2$.

This form of density of states is shown schematically in Fig 1-6. The second curve represents the density of states curve for bulk semiconductors where $g(E) \propto E^{1/2}$. It can be seen that as the energy E increases, the effect of the well becomes less (i.e. $g(E)_{2D} \rightarrow g(E)_{3D}$). It is also apparent that the 2D electron density of states function has an abrupt edge in comparison with the 3D density of states. The analogous hole density of states will be slightly more complex, having steps at both the heavy hole levels (E_{1hh} , E_{2hh} etc) and the light hole levels (E_{1lh} , E_{2lh} etc), but its general properties will be identical.

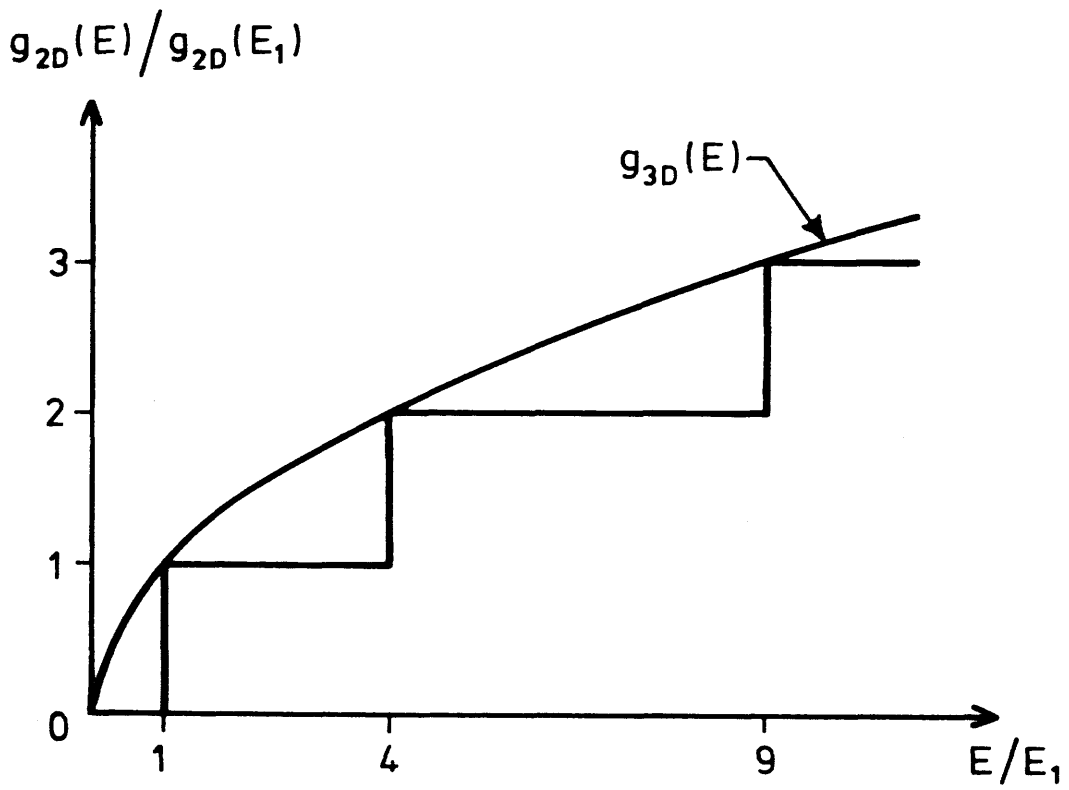


Fig 1-6 A schematic diagram of the quasi-2D density of states function of a MQWS. The 3D function is included for comparison.

1.4 SYNOPSIS OF THESIS

Both the potential monolithic integration of MQW diode lasers with single-mode stripe waveguides, and the predicted enhancement of the interaction of an applied electric field with the guided optical mode in MQW waveguides, lead to a requirement for a greater understanding of the properties of multiple quantum well structure optical waveguides. The aim of the research described in this thesis was to design and fabricate active and passive, planar and rib optical waveguide devices in MQWS waveguides, and investigate their optical and electrical characteristics.

In chapter two the fundamental properties of MQWS are discussed, with several models that describe the quasi-2D nature of the electronic band structure of MQWS being presented from the literature. These models are then used to investigate the effects of this 2D band structure on the optical and electro-optical properties of MQWS.

Chapter three briefly outlines the equipment and methods used to design, fabricate and characterise planar and stripe semiconductor optical waveguides, with chapter four presenting the results of these methods as applied to conventional GaAs waveguides.

The criteria used in the design of MQW-DH waveguides are presented in chapter five along with the final design. A brief description of the epitaxial growth techniques used for their eventual manufacture leads into an outline of the tests used to check the quality and accuracy of this growth. Details of the results of these tests on the MQWS actually used in later experiments are given.

The results of the experimental and theoretical investigation of the optical properties of MQWS are presented in chapters six to eight.

In chapter six the optical properties of passive planar optical waveguides are presented, before the fabrication of single-mode stripe waveguides is described. The design and analysis of a synchronous directional coupler formed from these single-mode rib structures is then reported.

Chapter seven outlines a simple semi-empirical model for the prediction of the electro-absorption properties of MQWS waveguides, and then reports the measured electro-absorption properties of active planar and stripe waveguides at wavelengths close to the absorption edge of the MQWS. These properties are then compared with those predicted from theoretical considerations and with those of GaAs/(Al,Ga)As waveguides.

The electro-optic effects of MQW-DH are studied in chapter eight. Results are presented for $\lambda=1.15\mu\text{m}$, far from the absorption edge. The electro-optic effect proved impossible to measure closer to the absorption edge due to the very large electro-absorption described in chapter seven.

Finally, conclusions and suggestions for further research are presented in chapter nine.

References to Chapter One

- 1 D. Botez and G. J. Herskowitz;
"Components for Optical Communication Systems: A Review", Proc. IEEE **6**, 689 (1980).
- 2 A. J. Arditty, M. Papuchon and C. Peuch;
"Fibre-optic Rotation Sensor: Towards an Integrated Device. A Review", CLEO'81 THE-1 10 (1981).
- 3 G. B. Brandt and M. Gottlieb;
"Performance Limits of Integrated Optical Signal Processors", SPIE Guided Wave Optical Systems and Devices, 159 (1978).
- 4 R. C. Alferness;
"Waveguide Electrooptic Modulators", IEEE Trans. Microwave Theory Tech. **MTT-30**, 1121 (1982).
- 5 R. C. Alferness;
"Guided-Wave Devices for Optical Communications", IEEE J. Q. Electron. **QE-17**, 946 (1981).
- 6 A. Neyer;
"Electro-optic X-switch Using Single-Mode Ti:LiNbO₃ Channel Waveguides", Electron. Lett. **19**, 553 (1983).
- 7 T. J. Cullen and C. D. W. Wilkinson;
"Radiation Losses from Single-Mode Optical Y-junctions Formed by Silver Ion-Exchange in Glass", Opt. Lett. **9**, 134 (1984).

- 8 R.G.Walker, C.D.W.Wilkinson and J.A.H.Wilkinson;
 "Integrated optical waveguiding structures made by silver ion-exchange in glass. 1: The propagation characteristics of stripe ion-exchanged waveguides; a theoretical and experimental investigation", Appl. Opt. **22**, 1923 (1983),
 R.G.Walker and C.D.W.Wilkinson;
 "Integrated optical waveguiding structures made by silver ion-exchange in glass. 2: Directional coupler and bends", Appl. Opt. **22**, 1929 (1983).
- 9 L.M.Johnson and F.J.Leonberger;
 "Design Rules for Low-Loss Coherently-Coupled LiNbO₃ Waveguide Bends", Tech. Digest 5th Topical Meeting on Integrated and Guided Wave Optics WD2-1 (1982).
- 10 V.Evtuhov and A.Yariv;
 "GaAs and GaAlAs Devices for Integrated Optics", IEEE Trans. Microwave Theory Tech. **MTT-23**, 44 (1978).
- 11 P.Buchmann, H.Kaufmann, H.Melchior and G.Guekos;
 "Reactive Ion Etched GaAs Optical Waveguide Modulators with Low Loss and High Speed", Electron. Lett. **20**, 295 (1984).
- 12 F.J.Leonberger, J.P.Donnely and C.O.Bozler;
 "GaAs p⁺n⁻n⁺ directional-coupler switch", Appl. Phys. Lett. **29**, 652 (1976).
- 13 J.C.Shelton, F.K.Reinhart and R.A.Logan;
 "Rib waveguide switches with MOS electrooptic control for monolithic integrated optics in GaAs-Al_xGa_{1-x}As", Appl. Optics **17**, 2548 (1978).
- 14 K.Hiruma, H.Inoue, K.Ishida and H.Matsumara;
 "Low loss GaAs optical waveguides grown by the metalorganic chemical vapor deposition method", Appl. Phys. Lett. **47**, 186 (1985).
- 15 A.J.N.Houghton, D.A.Andrews, G.J.Davies and S.Ritchie;
 "Low-Loss Optical Waveguides in MBE-grown GaAs/GaAlAs Heterostructures", Opt. Comm. **46**, 164 (1983).
- 16 B.Buchmann and A.J.N.Houghton;
 "Optical Y-junctions and S-bends Formed by Preferentially Etched Single-Mode Rib Waveguides in InP", Electron. Lett. **18**, 850 (1982).
- 17 M.W.Austin;
 "GaAs/GaAlAs Curve Rib Waveguides", IEEE J. Q. Electron. **QE-18**, 795 (1982).

- 18 S.Tarucha and H.Okamoto;
 "Monolithic integration of a laser diode and an optical waveguide modulator having a GaAs/GaAlAs quantum well double heterostructure", Appl. Phys. Lett. **48**, 1 (1986).
- 19 O.Wada, T.Sakurai and T.Nakagami;
 "Recent Progress in Optoelectronic Integrated Circuits (OEIC's)", IEEE J. Q. Electron. **QB-22**, 805 (1986).
- 20 A.C.Gossard;
Thin films: Preparation and properties, ed. K.N.Tu and R.Rosenberg (Academic Press, New York, 1983).
- 21 L.Esaki and R.Tsu;
 "Superlattice and Negative Differential Conductivity in Semiconductors", IBM J. Res. Dev. **14**, 61 (1974).
- 22 R.Dingle, W.Wiegmann and C.H.Henry;
 "Quantum States of Confined Carriers in Very Thin $\text{Al}_x\text{Ga}_{1-x}\text{As}$ -GaAs- $\text{Al}_x\text{Ga}_{1-x}\text{As}$ Heterostructures", Phys. Rev. Lett. **33**, 827 (1974).
- 23 L.L.Chang, L.Esaki and R.Tsu;
 "Resonant tunnelling in semiconductor double barriers", Appl. Phys. Lett. **24**, 593 (1974).
- 24 W.T.Tsang;
 "Extremely low threshold (AlGa)As modified multiquantum well heterostructure lasers grown by mol-beam epitaxy", Appl. Phys. Lett. **39**, 786 (1981).
- 25 R.Chin, N.Holonyak Jr., B.A.Vojak, K.Hess, R.D.Dupuis and P.D.Dapkus;
 "Temperature dependence of threshold current for quantum-well $\text{Al}_x\text{Ga}_{1-x}\text{As}$ -GaAs heterostructure laser diodes", Appl. Phys. Lett. **36**, 19 (1980).
- 26 H.Kobayashi, H.Iwamura, T.Saku and K.Otsuka;
 "Polarisation-dependent gain-current relationship in GaAs-AlGaAs MQW laser diodes", Electron. Lett. **19**, 166 (1983).
- 27 D.S.Chemla, T.C.Damen, D.A.B.Miller, A.C.Gossard and W.Wiegmann;
 "Electroabsorption by Stark effect on room-temperature excitons in GaAs/GaAlAs multiple quantum well structures", Appl. Phys. Lett. **42**, 864 (1983).
- 28 D.A.B. Miller, D.S.Chemla, T.C.Damen, A.C.Gossard, W.Wiegmann, T.H.Wood and C.A.Burrus;
 "Band-Edge Electroabsorption in Quantum Well Structures: The Quantum-Confined Stark Effect", Phys. Rev. Lett. **53**, 2173 (1984).

- 29 D. A. B. Miller, D. S. Chemla, T. C. Damen, A. C. Gossard, W. Wiegmann, T. H. Wood and C. A. Burrus;
 "Electric field dependence of optical absorption near the band gap of quantum-well structures", Phys. Rev. B **32**, 1043 (1985).
- 30 H. Yamamoto, M. Asada and Y. Suematsu;
 "Electric-field-induced refractive index variation in quantum-well structure", Electron. Lett. **21**, 579 (1985).
- 31 D. A. B. Miller, D. S. Chemla, D. J. Eilenberger, P. W. Smith, A. C. Gossard and W. T. Tsang;
 "Large room-temperature optical nonlinearity in GaAs/Ga_{1-x}Al_xAs multiple quantum well structures", Appl. Phys. Lett. **41**, 679 (1982).
- 32 D. S. Chemla, D. A. B. Miller, P. W. Smith, A. C. Gossard and W. Wiegmann;
 "Room Temperature Excitonic Nonlinear Absorption and Refraction in GaAs/AlGaAs Multiple Quantum Well Structures", IEEE J. Q. Electron. **QE-20**, 265 (1984).
- 33 D. A. B. Miller, D. S. Chemla, D. J. Eilenberger, P. W. Smith, A. C. Gossard and W. Wiegmann;
 "Degenerate four-wave mixing in room-temperature GaAs/GaAlAs multiple quantum well structures", Appl. Phys. Lett. **42**, 925 (1983).
- 34 H. M. Gibbs, S. S. Tarng, J. L. Jewell, D. A. Weinberger, K. Tai, A. C. Gossard, S. L. McCall, A. Passner and W. Wiegmann;
 "Room-temperature excitonic optical bistability in a GaAs-GaAlAs super-lattice", Appl. Phys. Lett. **41**, 221 (1982).
- 35 T. H. Wood, C. A. Burrus, D. A. B. Miller, D. S. Chemla, T. C. Damen, A. C. Gossard and W. Wiegmann;
 "131 ps Optical Modulation in Semiconductor Multiple Quantum Wells (MQW's)", IEEE J. Q. Electron. **QE-21**, 117 (1984).
- 36 D. A. B. Miller, D. S. Chemla, T. C. Damen, A. C. Gossard, W. Wiegmann, T. H. Wood and C. A. Burrus;
 "Novel hybrid optically bistable switch: The quantum well self-electro-optic effect device", Appl. Phys. Lett. **45**, 13 (1984).
- 37 J. S. Weiner, D. S. Chemla, D. A. B. Miller, H. A. Haus, A. C. Gossard, W. Wiegmann and C. A. Burrus;
 "Highly anisotropic optical properties of single quantum well waveguides", Appl. Phys. Lett. **47**, 664 (1985).

- 38 J.S.Weiner, D.A.B.Miller, D.S.Chemla, T.C.Damen, C.A.Burrus, T.H.Wood, A.C.Gossard and W.Wiegmann;
 "Strong polarization-sensitive electroabsorption in GaAs/AlGaAs quantum well waveguides", Appl. Phys. Lett. **47**, 1148 (1985).
- 39 M.Glick, F.K.Reinhart, G.Weimann and W.Schlapp;
 "Quadratic electro-optic light modulation in a GaAs/AlGaAs multiquantum well heterostructure near the excitonic gap", Appl. Phys. Lett. **48**, 989 (1986).
- 40 for example T.Tamir (ed.);
Topics in Applied Physics Vol. 7: Integrated Optics (Springer-Verlag, New York, 1975),
 or J.Adams;
An Introduction to Optical Waveguides (Wiley, Chichester, 1981).
- 41 E.A.J.Marcatili;
 "Dielectric Rectangular Waveguide and Directional Coupler for Integrated Optics", Bell Syst. Tech. Journal **48**, 2071 (1969).
- 42 R.M.Knox and P.P.Toulios;
Proceedings of MRI Symposium on submillimeter Waves, ed. J.Fox, (Polytechnic Press, Brooklyn, 1970).
- 43 for example M.J.Adams;
An Introduction to Optical Waveguides (Wiley, New York, 1981).
- 44 T.Itoh;
Infrared and Millimeter Waves, Vol. 4, ed. K.J.Button and J.C.Wiltse (Academic Press, New York, 1981).
- 45 M.Koshiha and M.Suzuki;
 "Equivalent network analysis of dielectric thin-film waveguides for optical integrated circuits and its applications", Radio Sci. **17**, 99 (1982).
- 46 M.T.Benson;
 "Integrated Optical Components Produced In GaAs and InP Epitaxial Layers Using the Photo-Elastic Effect", Ph.D. Thesis, University of Sheffield (1982).
- 47 B.M.A.Rahman and J.B.Davies;
 "Finite-element analysis of optical and microwave waveguide problems", IEEE Trans. Microwave Theory Tech. **MTT-32**, 20 (1984).
- 48 R.G.Walker;
 "The Design of Ring-Resonators for Integrated Optics using Silver Ion-Exchanged Waveguides", Ph.D. Thesis, University of Glasgow (1981).

CHAPTER TWO

THE OPTICAL PROPERTIES OF MULTIPLE QUANTUM WELL STRUCTURES

2.1 INTRODUCTION

This chapter briefly outlines the optical properties of MQWS with particular emphasis being placed on those properties which are observable in MQW waveguides and exploitable in integrated optical devices at wavelengths in the near infrared (approximately 1.5-0.85 μm).

As discussed in chapter one, when a periodic series of alternating layers of high and low band gap semiconductor is grown to form a MQWS, the band structure of the host materials is radically altered because of the quasi-two-dimensional nature of the MQWS. In this chapter, various methods of modelling this new band structure are described before the effect of the new band structure on the absorption and refraction of light in MQWS is assessed.

The modification of the optical properties of materials by the altering of some externally controllable parameter is of major interest in integrated optics for use in active devices. In particular, the effects on the optical properties of a material of applying an electric field is used in many integrated optical devices. The effect of an externally applied electric field on the absorption and refraction of light in a MQWS is thus discussed.

In recent years the non-linear properties of certain materials have been used to fabricate all optical integrated switching devices. However, it was decided not to pursue the use of this effect in MQWS waveguides because of the large effort going on in several centres throughout the world in this area. The optical power dependence of the optical properties of MQWS is thus not dealt with.

2.2 BAND STRUCTURE MODELLING

The modelling of the band structure of MQWS can follow two distinct paths. The first path uses the numerical power of a computer

to solve the one-dimensional quantum mechanical problem using a self-consistent method. This can take into account band-bending due to the free carriers in the structure by successively solving Poisson's equation, and Schrödinger's equation. This method is potentially very precise. The second path is to assume sharp, rectangular band discontinuities in the MQWS and attempt to solve the problem analytically by suitable approximations. The aim of this section is to outline these various models as applied to a MQWS consisting of periodically repeated semiconductor layers of different energy gaps, forming what is termed a contravariant or type I potential of the form shown in Fig 2-1, where the conduction and valance band wells occur in the same material.

It will be assumed that the semiconductor layers forming the MQWS consist of direct band gap III-V semiconductor compounds. The band structure of such materials is complex. Fig 2-2 shows a highly simplified energy band diagram of GaAs which displays characteristics typical of III-V semiconductors; a degenerate Γ valley in the valance band and a conduction band which has an isotropic minima at the Γ point (the "light electron" valley) and anisotropic minima at the L and X points (the "heavy electron" valleys).

In general it is difficult to incorporate this detailed band structure into any model. However, it can be shown¹ that in an ideal periodic lattice (that is, in the absence of impurities and surface states at layer interfaces) electrons passing from one layer to another and belonging originally to a specific valley in the first layer remain in the valley whose position in k space is close to the position of the original valley. The electrons or holes in a given valley can thus be treated as an independent system of energy levels (of the form described in section 1.3) with the characteristics of the different systems depending - within the effective mass approximation - on the effective mass of each valley in the direction of quantisation, the z direction.

In chapter one the fundamental characteristics of the systems of energy levels in a MQWS were introduced by modelling the periodic potential ($\Phi(z)$) that is superimposed on the crystal potential as a series of infinitely deep wells. It will now be shown that this model can be further refined, firstly by taking the finite depth of the

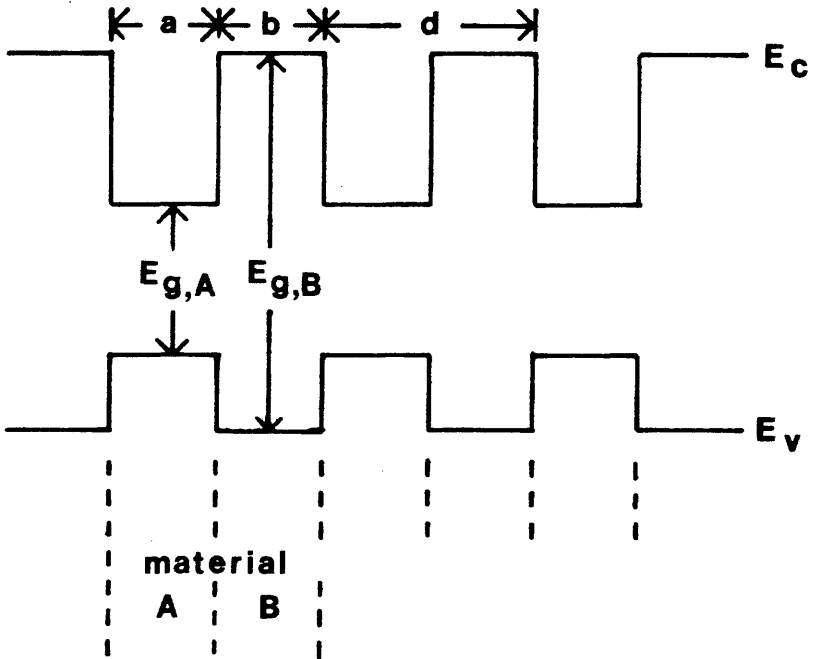


Fig 2-1 An energy, real space diagram of the periodic potential introduced by growing MQWS.

E_c = bulk semiconductor conduction band,

E_v = bulk semiconductor valance band,

$E_{g,A}$ = energy gap of well material,

$E_{g,B}$ = energy gap of barrier material.

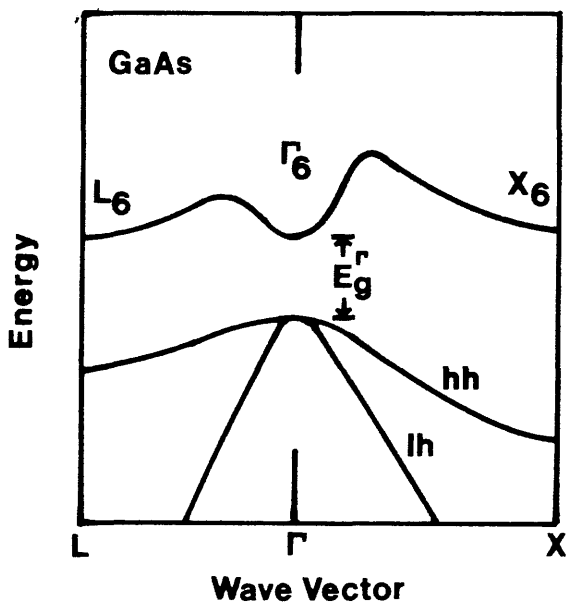


Fig 2-2 A simplified energy band diagram of GaAs showing the Γ , X and L conduction band valleys; the heavy (hh) and light (lh) valance bands; and the direct energy gap (E_g^{Γ}).

wells into account, and then by taking the interaction between wells into account. Finally the numerical methods which take into account band-bending due to free carriers will be described.

2.2.1 The Finite Single Potential Well Model

The finite single potential well model of MQWS is similar to the infinitely deep potential well model described in the introductory chapter in that it assumes that the MQWS to be modelled is such that the wells do not interact to any significant extent. The model does, however, take into account the finite depth (ϕ_0) of the wells. $\phi(z)$ now takes the form:

$$\begin{aligned} \phi(z) &= \phi_0 & |z| \geq a/2 \\ \phi(z) &= 0 & |z| < a/2 \end{aligned}$$

where a is the well width.

Solving Schrödinger's equation for this potential follows in a very similar way to the infinite well problem of chapter one. Now, however, the wave functions penetrate the well walls. This will change the values for the energy eigenvalues, E_n , and produce a finite number of bound states. Proceeding in a way similar to the infinite deep well model, the wave function can be defined thus:

$$\begin{aligned} \psi &= A \cdot \exp(K_2 z) & \text{for } z < -a/2 \\ \psi &= C \cdot \exp(ik_1 z) + D \cdot \exp(-ik_1 z) & \text{for } |z| < a/2 \\ \psi &= F \cdot \exp(-K_2 z) & \text{for } z > a/2 \end{aligned}$$

where A, C, D and F are arbitrary constants, $K_2 = (2m^*(\phi_0 - E))^{1/2}$, $k_1 = (2m^*E)^{1/2}$, and energy (E) is measured from the bottom of the potential well.

Now applying the general boundary condition that the wave functions and their derivatives should be continuous it is found that symmetrical wave functions will satisfy the expression:

$$\alpha \tan(\alpha/2) = \beta \quad (2.1)$$

and the anti-symmetrical wave functions will satisfy the expression:

$$\alpha \cot(\alpha/2) = -\beta \quad (2.2)$$

where $\alpha = k_1 a$, $\beta = K_2 a$. In addition it can be shown that:

$$\alpha^2 + \beta^2 = (2m^* \mathcal{U}_0 a^2 / \hbar^2) = \gamma^2 \quad (2.3)$$

Thus the symmetrical solution is obtained by solving (2.1) and (2.3) simultaneously and the anti-symmetrical by solving (2.2) and (2.3). These solutions can be conveniently shown in a diagrammatic form (see Fig 2-3). The number of solutions (and hence bound states) depends on the radius of the circle. The factor $\gamma = (2m^* \mathcal{U}_0 a^2 / \hbar^2)^{1/2}$ is thus a useful "strength parameter" for any well. The wider or deeper the well the greater the number of states. In particular, the total number of bound states exceeds by one the largest integer contained in γ . It is also worth noting that there is always at least one bound symmetric state, regardless of how weak the well is.

In the limit, as $\mathcal{U}_0 \rightarrow \infty$, the radius of the circle will be ∞ , and the solutions will be reached at the asymptotic limits. These limits are identical to the result of the derivation in chapter one.

This new model only slightly alters the predicted nature of the MQWS band structure. It still gives rise to discrete energy levels (see Fig 2-4) but with slightly different eigenvalues. In addition, the wave functions now penetrate into the walls with the exponential decay factor $\hbar K_2 = (2m^* (\mathcal{U}_0 - E))^{1/2}$. Thus the more energetic the state, the further it penetrates.

2.2.2 Multiple Quantum Wells

Until this point the MQWS has been examined by considering the individual wells in isolation. Before proceeding to quantitatively describe the effects of neighbouring wells in a MQWS, the effects can be qualitatively described by considering an imaginary simple system of two identical wells of finite depth, with each well having a single bound state, the ground state. It is clear that if the two wells are brought close together, the wave functions of the ground states of each individual well will overlap and interact. However, if

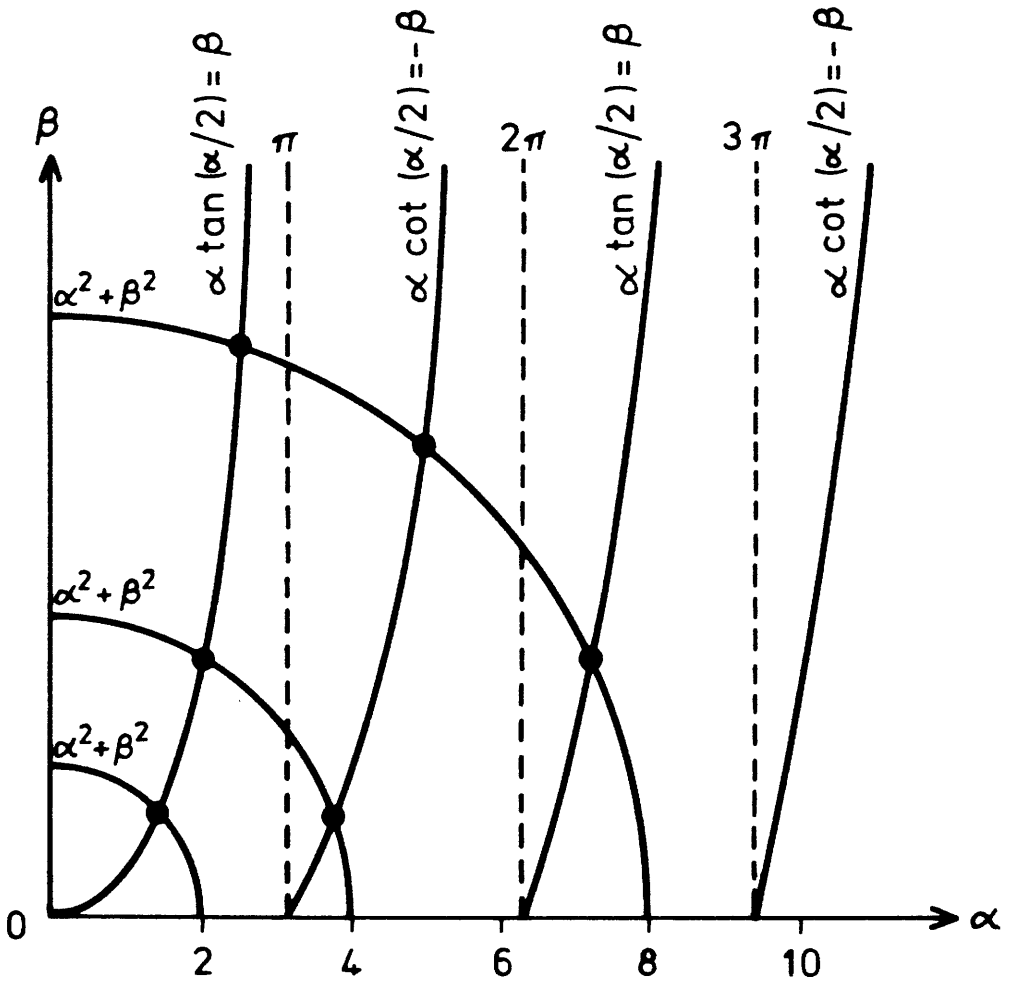


Fig 2-3 The graphical solution of the single, finite square well model.

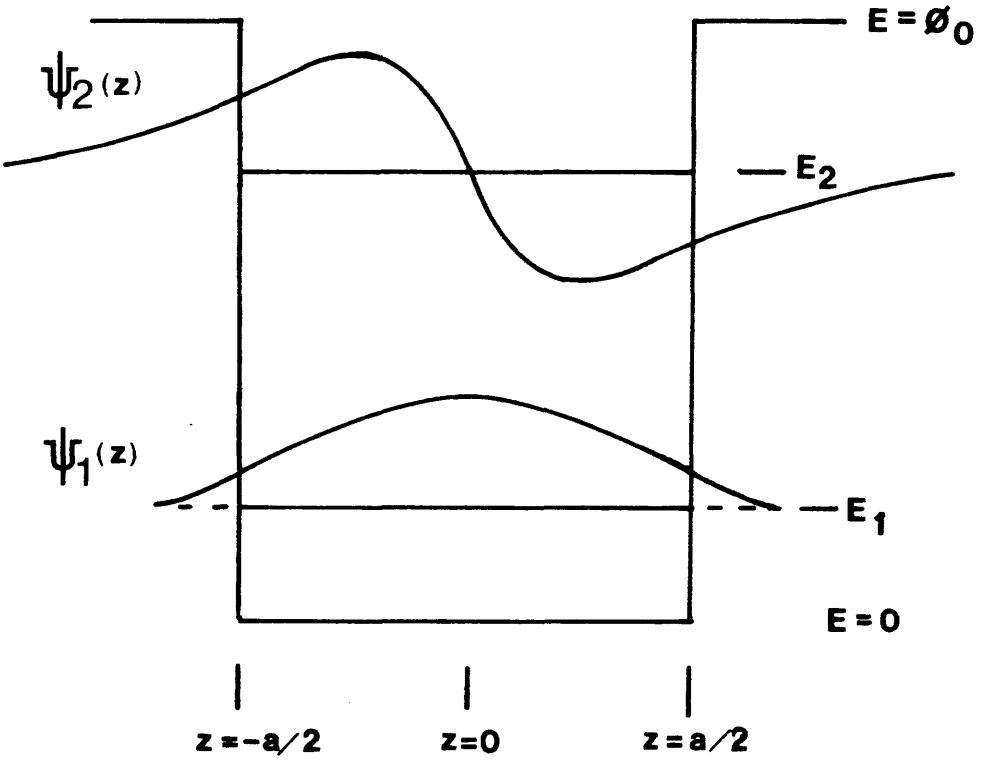


Fig 2-4 A schematic diagram of the energy levels and eigenvalues of the single, finite square well model.

the separation of the two wells is very large then the two wells will not "see" each other and the energy of the total system will be simply the sum of the two individual ground state energies. Analysing this system in more detail, it can be seen that if the wells are very close - separated by only a very narrow barrier - then the total wave function of the system is a linear combination of the two original ground state wave functions, allowing a symmetrical or asymmetrical combination. The energy of these two states is not the same, the difference increasing as the barrier decreases in thickness. In the limit as the barrier disappears, the symmetrical mode becomes equivalent to the ground state of a well double the width of the original, the anti-symmetrical equivalent to the first excited state of this double width well.

So the two wells, having the same energy levels at large separation, interact more strongly as they are brought closer together, the interaction splitting each level into two separate levels. As more wells are brought in, these two levels will further split until, in the limit where the number of wells is very large, the effect is best described as a broadening of the original level of the single well into a miniband in the MQWS. If the overlap between the single well states is small - because the barrier is wide or the state is deep in the well - then the broadening will be small. If the barriers are thin, or the state close to the top of the well, then the broadening will be large.

This allows a distinction to be made between superlattices (SL) and MQWS. In a MQWS the overlap between adjacent wells is small (at least for the lower confined states), the bands are therefore so narrow as to still be effectively levels, and the electrons or holes are well confined and localised. In SL the overlap between adjacent wells is large, broadening the single quantum well level into a wide miniband. The electrons and holes are not well confined to the wells and a significant tunnelling transmission of particles is thus possible perpendicular to the SL layers.

2.2.2.1 Krönig-Penney Model

Krönig and Penney, in analysing the energy of electrons in solids, developed a model which has been widely applied to the MQWS. This

model allows the interaction between wells to be taken into account. $\emptyset(z)$ is defined as having a period d such that:

$$\emptyset(z) = \emptyset(z+d)$$

where $d = a + b$, $a =$ well width, $b =$ barrier width. In order to obtain a simple solution, the MQWS is assumed to repeat itself so that:

$$\emptyset(z) = \emptyset(z + Md)$$

where M is the number of periods in the MQWS. Floquet's theorem shows that the most general solution of the above periodic potential has the form known as a Bloch wave:

$$\psi(z) = \exp(ikz)u(z)$$

where $u(z+d) = u(z)$, $k = 2\pi n/Md$ and $n =$ integer $= (\dots, -2, -1, 0, 1, 2, \dots)$

Defining k_1 and K_2 as in section 2.2.1, and using the boundary condition that ψ and ψ' must be continuous at the layer boundaries with $\psi(z) = \psi(z + d)$, the solution of Schrödinger's equation for $E < E_0$ reduces to²:

$$\cos k_1 a \cdot \cosh K_2 b - 1/2((1/X) - X) \sin k_1 a \cdot \sinh K_2 b = \cos kd \quad (2.4)$$

where $X \equiv K_2/k_1$

For $E > E_0$ Schrödinger's equation reduces to:

$$\cos k_1 a \cdot \cos k_2 b - 1/2((1/X) + X) \sin k_1 a \cdot \sinh k_2 b = \cos kd \quad (2.5)$$

where $X \equiv k_2/k_1$, $k_2 = -iK_2$.

An improvement on this model is to use a Kane-type envelope function approximation³ which can be viewed as a modified Krönig-Penney model. The first stage of modification⁴ takes into account the different effective masses in the GaAs wells and (Al,Ga)As barriers to produce expressions identical to (2.4) and (2.5) except that k_1 , K_2 and X are redefined as:

$$\begin{aligned} \hbar k_1 &= (2m^*(A)E)^{1/2} \\ \hbar K_2 &= (2m^*(B)(\mathcal{E}_0 - E))^{1/2} = i\hbar k_2 \\ X &= m^*(A)K_2 / m^*(B)k_1, \quad \text{for } E < \mathcal{E}_0 \\ X &= m^*(A)k_2 / m^*(B)k_1, \quad \text{for } E > \mathcal{E}_0 \end{aligned}$$

where $m^*(A)$ = effective mass in well, and $m^*(B)$ = effective mass in barrier.

Further improvements to the Krönig-Penney model include taking into account the energy dependence of the effective mass of GaAs⁵ and carrying out a full, many band, Kane envelope function analysis⁶.

These models become progressively more difficult to implement, and a look at the literature shows that they give no clear improvement in the prediction of experimental results⁷. It was thus decided to use the simple, uncorrected Krönig-Penney model.

The solution of the Krönig-Penney model for various periodic potentials is shown in Fig 2-5 and Fig 2-6, where β , d , a and γ are as defined in section 2.2.1. Fig 2-5 shows how, as the well strength parameter γ increases, the number of subbarrier minibands increases, as predicted by the single well model of section 2.2.1. However, the minibands in the Krönig-Penney model have a finite width and it is evident that the deeper the miniband is in the well, the narrower the miniband is. The Krönig-Penney model also shows how suprabarrier bands exist where the continuum of bulk states is split into wide bands separated by narrow gaps. As the well strengthens these gaps broaden and exist at higher and higher energies. The general trend is that as γ increases, suprabarrier bands move down to lower energies and eventually become bound subbarrier minibands.

Fig 2-6 shows that for a given well strength γ , as the ratio of the period of the potential to the well width varies, the width of the subbarrier minibands alter. For $d/a = 1$, the solution is that for a bulk semiconductor, but as d/a increases the wells become less and less coupled, and the minibands become more and more like the energy levels of the single well solution.

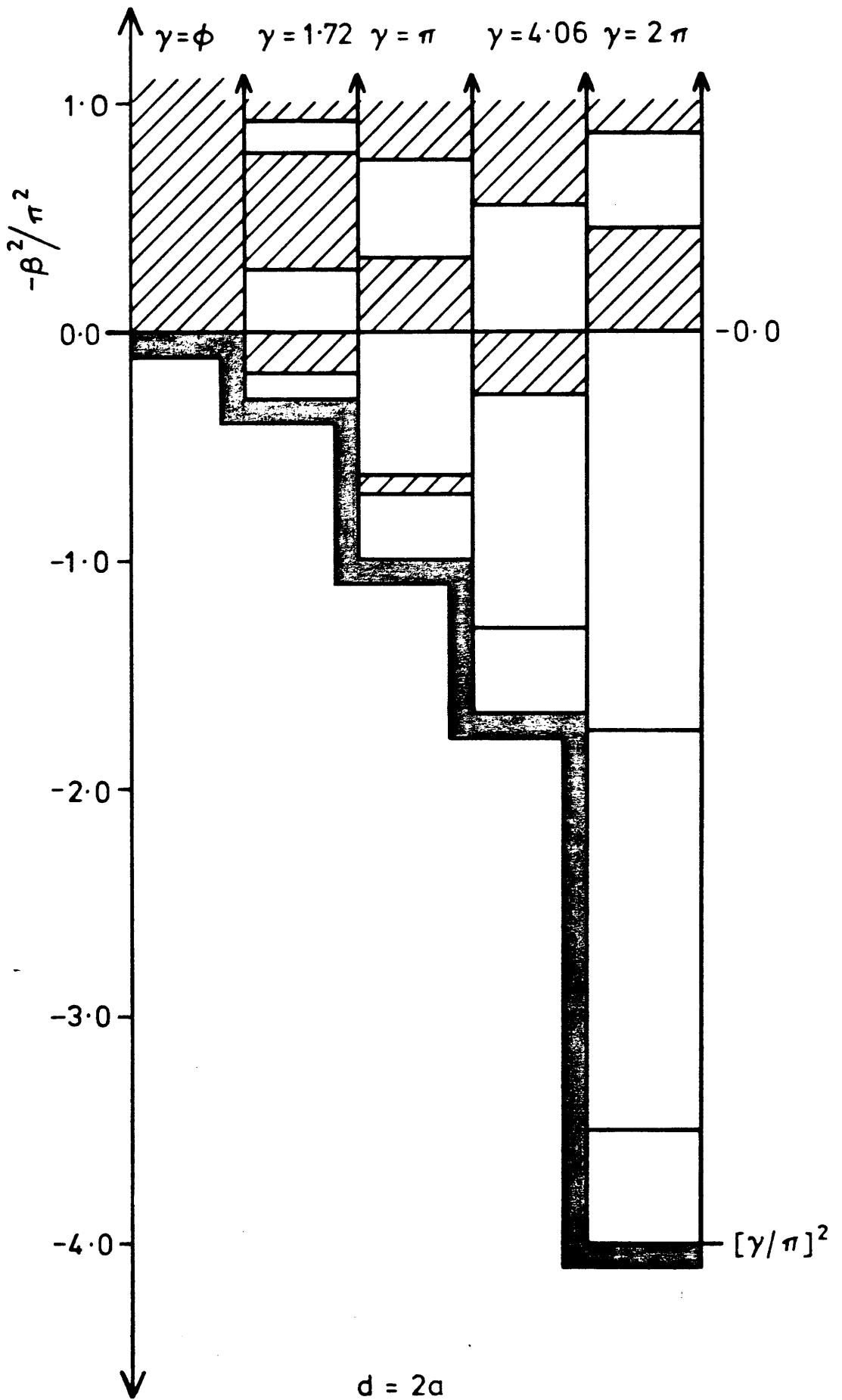


Fig 2-5 The MQWS energy band structure for various well strengths as derived from the Krönig-Penney model assuming equal well and barrier widths.

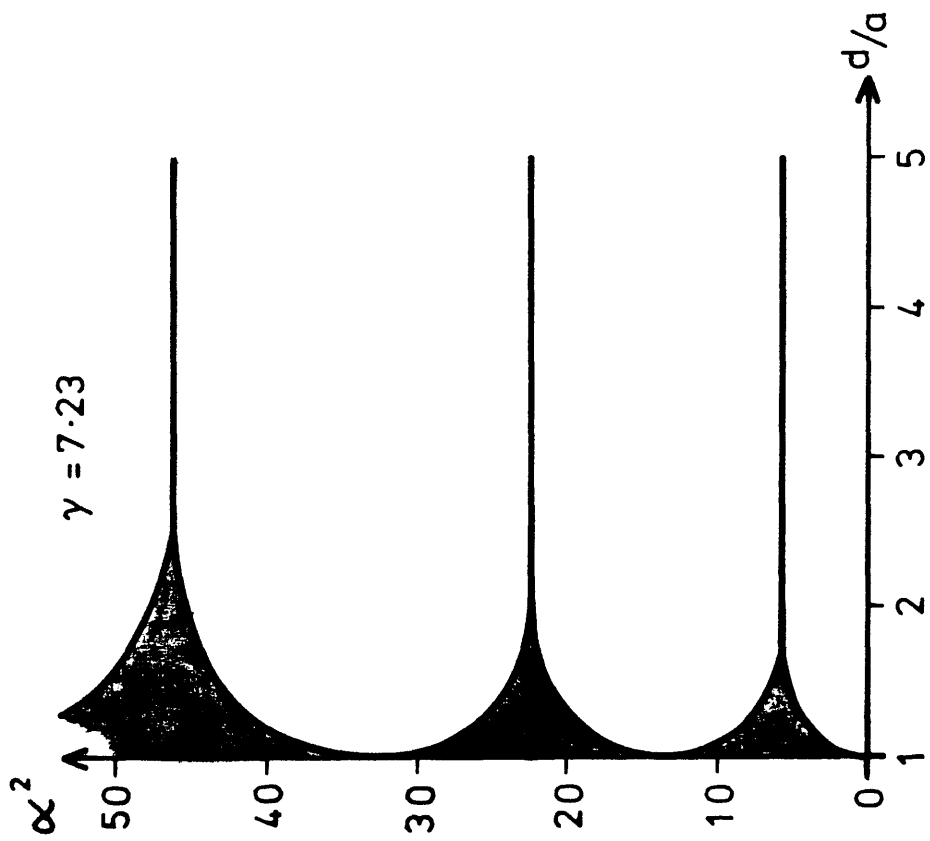
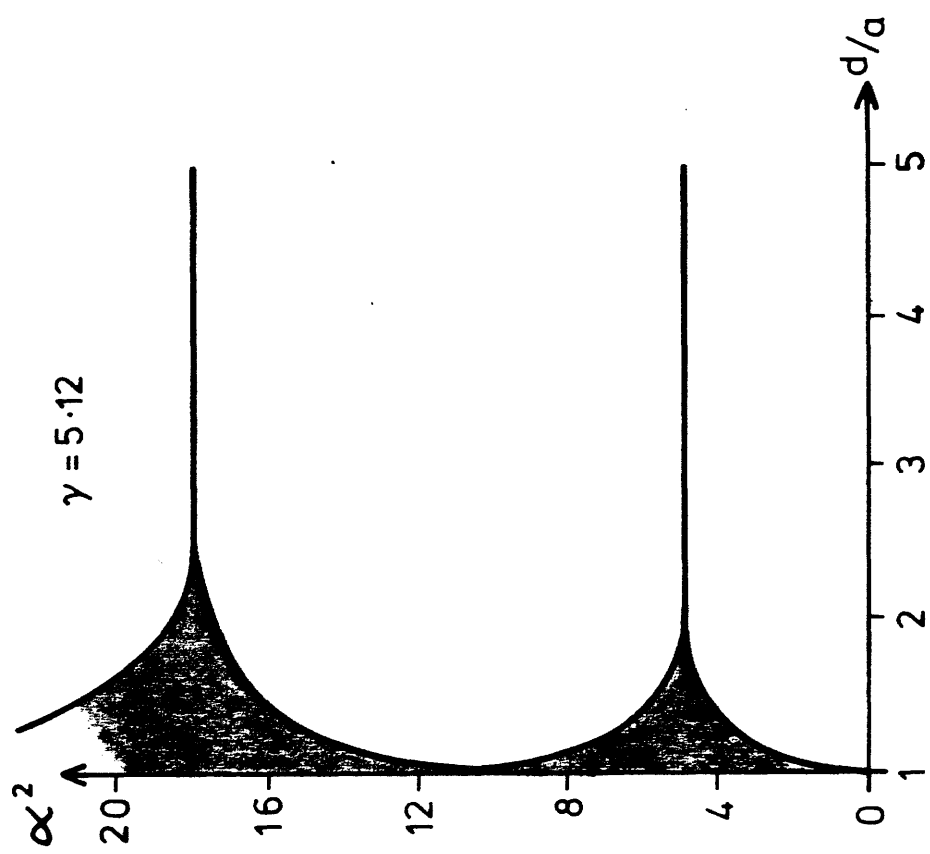


Fig 2-6 The variation of MQWS energy band structure as the period is varied for two well strengths.

2.2.2.2 Self-Consistent Model

So far the models dealt with have treated the MQWS as a rectangular, periodic potential in order to make simplifications that allow analytic expressions to be found for the band structure. However, another approach is available where Schrödinger's wave equation is solved in a self-consistent manner. This approach, although very complicated, takes into account the band-bending⁹ that can distort a MQWS potential away from a rectangular form⁹⁻¹¹. Other improvements such as the inclusion of band non-parabolicity can easily be introduced¹².

The starting point of these models is to assume a rectangular Krönig-Penney potential with the electron density at each point being set equal to the donor density at that point. Poisson's equation is then solved to obtain a new form of the potential, and then Schrödinger's equation is solved to give the wave functions and subband energies. These new states are then populated and Poisson's equation is again solved. If the potential has changed, then Schrödinger's equation is solved again. This process is repeated until a self-consistent solution to the electrostatic problem is obtained.

This procedure is heavy on computing time, and it can be shown that for many situations (i.e. low uniformly doped MQWS) band-bending is negligible, thus negating the main advantage of this procedure. Shik¹³ states that the band-bending at the top of the well (ΔV) is given by:

$$\Delta V = (\pi/2) \cdot (e^2/\epsilon) \cdot N b^2$$

where N is the electron density per unit volume. Although this is strictly valid only at the top of the barrier it gives a qualitative estimate (if b is replaced by a) of the distortion at the bottom of the well. In MQWS waveguides, low doping will be required to minimise optical attenuation. For typical (Al,Ga)As, low uniformly doped MQWS, band-bending (ΔV) is of the order of 1 meV, while the well depth is some 300 meV.

Where this self-consistent method shows a clear advantage is in the modelling of devices where an external field is applied to the MQWS. By including a Monte Carlo simulation¹² to take account of the drift of electrons due to this field, a new electron distribution is found. This can then be fed back into Poisson's and Schrödinger's equations. This produces an inner and outer iterative loop. When both are self-consistent, then information such as the band structure and current flow for a given applied field can be obtained. This is a very powerful technique and it will be shown later how it was used to calculate the I-V curves of MQW p-n diodes.

2.2.3 Density of States Function and Fermi Level

Leaving aside the self-consistent model, the Krönig-Penney model will now be used to derive expressions for the density of states in a MQWS.

The Krönig-Penney model gives rise to a rather complicated expression for the calculation of the position and width of minibands. To allow the calculation of simple expressions for such quantities as the density of states function, it is usual to assume that the minibands are deep in the potential well. In this situation the minibands can be described within the tight binding approximation¹³ which leads to the following dispersion equation:

$$\begin{aligned}
 E &= E_{xy} + E_z, \\
 E_{xy} &= \hbar^2 \cdot (k_x^2 + k_y^2) / 2m^*(x, y), \\
 E_z &= E_n + \Delta_n \cos k_z d
 \end{aligned}$$

where E_n is the eigenvalue of the n^{th} miniband of the finite well problem, and Δ_n is the miniband half-width. Expressions for Δ_n are given by Smith².

Using this approximation it can be shown¹³ that the density of states function $g(E)$ becomes:

$$\begin{aligned}
 g(E) &= (m^*(x, y) / \pi \hbar^2) \cdot n & , & E_n + |\Delta_n| \leq E \leq E_{n+1} - |\Delta_{n+1}| \\
 &= (m^*(x, y) / \pi \hbar^2) \cdot [n - \frac{1}{2} + (1/\pi) \sin^{-1}((E - E_n) / |\Delta_n|)], & E_n - |\Delta_n| \leq E \leq E_n + |\Delta_n|
 \end{aligned}$$

This is plotted in Fig 2-7 together with the bulk density of states function. It can be seen that since the minibands now have a finite width, the density of states function no longer consists of sharp steps. For photon energies within a miniband, the density of states changes continuously until it reaches a plateau value at the miniband edge. The step will be sharper the thinner the miniband.

The carrier density (N) in a MQWS is given by the standard expression¹³:

$$N = \int g(E) dE / (1 + \exp((E - E_F) / k_B T)) \quad (2.6)$$

where E_F is the fermi energy and k_B is Boltzmann's constant.

It is not possible to calculate (2.6) in its general form. However, if the minibands are narrow compared to the characteristic energies of the system (i.e. $|\Delta_n| \ll \max(k_B T, \hbar / \tau)$ where τ is the dominant scattering relaxation time) then the approximation $\Delta_n = 0$ can be used¹ to simplify calculations. Due to the narrowness of minibands deep in wells, this approximation is often valid.

Within this approximation the condition for carriers to fill just one miniband can be seen to be:

$$k_B T \ll (E_2 - E_1), \quad N \ll m^*(x, y) (E_2 - E_1) / \pi \hbar^2 d$$

and for a single filled miniband we have:

$$N = (m^*(x, y) k_B T / \pi \hbar^2 d) \log_e [1 + \exp((E_F - E_1) / k_B T)]$$

From this expression for N , the criterion for non-degeneracy can be found to be:

$$(\pi \hbar^2 d N / m^*(x, y) k_B T) \ll 1$$

To arrive at a better description of the carrier statistics, the contribution of the heavy electron valleys will have to be taken into account. These heavy electrons are assumed to be classical particles¹³. If the electron densities in the wells (material A) and barriers (material B) are determined by the completely ionised donors

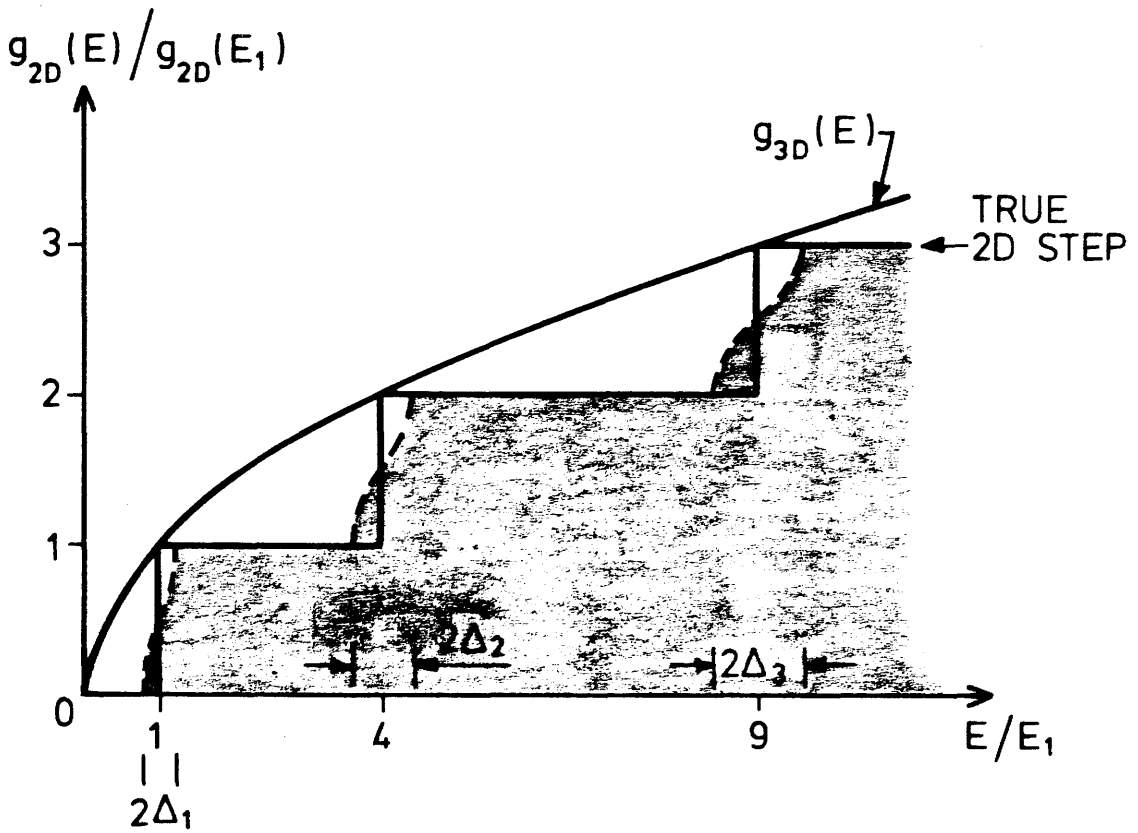


Fig 2-7 The quasi-2D density of states function, $g_{\geq 2D}(E)$, within the tight binding approximation. The 2D and 3D density of states functions are included for comparison.

located near the Γ minimum and these are equal to N_A and N_B , then the fermi energy (E_F) can be found using¹³:

$$N = (N_A a + N_B b) / d = (m_\Gamma k_B T / \pi \hbar^2 d) \sum_n \ln(1 + \exp[(E_F - E_n) / k_B T]) \\ + (2a/d) \cdot (m_\Gamma k_B T / 2\pi \hbar^2)^{3/2} \exp[(E_F - \Delta_\Gamma) / k_B T] \\ + (2a/d) \cdot (m_x k_B T / 2\pi \hbar^2)^{3/2} \exp[(E_F - \Delta_x) / k_B T]$$

where m_Γ, m_x, m_L are the appropriate (x,y) plane effective masses of the Γ, X and L valleys in material A, and Δ_Γ, Δ_x are the energy elevations between the light and heavy electron valleys.

Calculations at room temperature for (Al,Ga)As MQWS show that the ratio of heavy valley electrons to gamma valley electrons is very low (Fig 2-8 and Fig 2-9) and that only the first miniband is occupied for all moderately doped ($N_D < 10^{18} \text{cm}^{-3}$) cases.

2.3 ABSORPTION AND REFRACTION

Now that the nature of the band structure of MQWS has been reviewed, the corresponding optical properties can be determined. The discussion falls neatly into two sections. The first is the less important section and discusses the theory describing absorption and refraction due to electronic transitions between minibands. These effects, although of fundamental interest, are predicted to occur at such low photon energies that they are not of practical interest for communication systems wavelengths (i.e. 0.85-1.5 μm).

The second section deals with absorption and refraction due to electronic transitions between bands, and is of far more practical interest since it describes new optical phenomenon at useful photon energies close to the band gap of MQWS.

2.3.1 Inter-Miniband Effects

The optical properties of MQWS for photon energies well below the band gap are very different from those of bulk semiconductors. They are fundamentally anisotropic. If the electric field of the light is polarised parallel to the MQW layers (in the x,y plane), the carriers are accelerated just as in bulk material, and the usual free carrier absorption should be observed. However, light polarised along the z

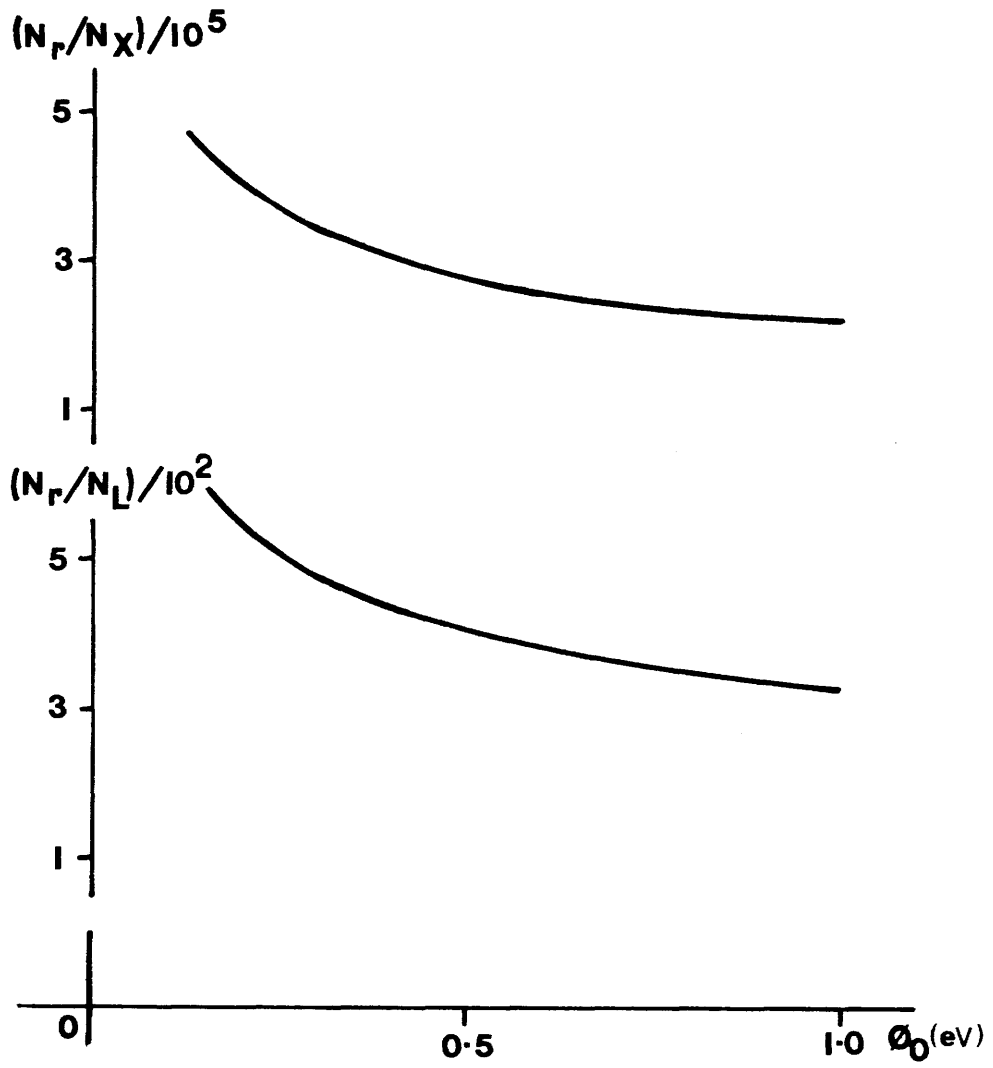


Fig 2-8 The variation of light to heavy electron ratio as well depth (ϕ_0) is varied. N_r , N_x , N_L are the number of Γ , X and L valley electrons respectively. The MQWS is $N_D=7 \times 10^{17} \text{cm}^{-3}$, $T=300\text{K}$, $a=100\text{\AA}$, $d=2a$.

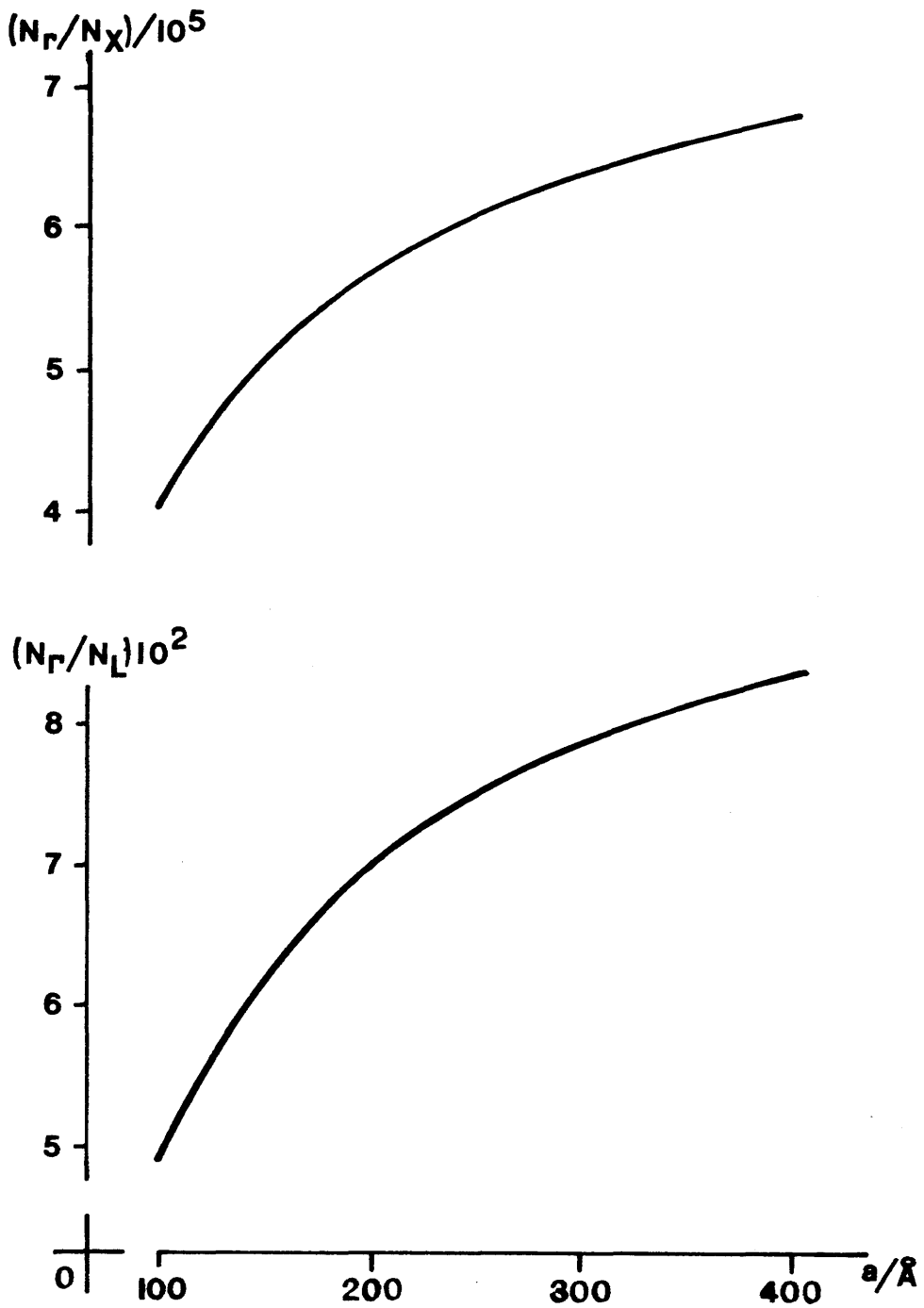


Fig 2-9 The variation of light to heavy electron ratio as well width (a) is varied. The MQWS is $N_D=7 \times 10^{17} \text{cm}^{-3}$, $T=300\text{K}$, $\phi_0=0.3\text{eV}$, $d=2a$.

axis, perpendicular to the layers, will give rise to transitions between minibands. Shik¹³ uses the tight binding approximation of section 2.2.3 to show that the MQW absorption will be large at photon energies corresponding to inter-miniband energy gaps. In these regions, absorption is predicted to be far stronger than the free carrier absorption. Only transitions between states of different parities are allowed. Fig 2-10 shows a schematic diagram of $\alpha(\hbar\omega)$. The asymptotic dependence of the absorption is $\omega^{-3/2}$ according to Shik and the wider absorption bands for higher photon energies are due to subbarrier to suprabarrier inter-miniband transitions which are subject to less stringent selection rules. In the simplest model, singularities occur at the absorption band edges, but these are smoothed out by electron scattering. A more detailed numerical calculation by Ando and Mori⁹ using a self-consistent model predicts that the asymptotic dependence of $\alpha(\hbar\omega)$ would be much faster, $\alpha(\hbar\omega)$ being virtually zero after the first two or three absorption bands.

The polarisability, and hence refractive index, of a MQWS must have a corresponding anisotropy and period since $\alpha(\hbar\omega)$ and $n(\hbar\omega)$ are related via the Kramers-Krönig relationship¹⁴. Indeed Kazarinov and Shmartsev¹⁵ show just this with the transverse (x,y) polarisation being given by the usual free electron formula:

$$\chi_{x,y} = -N \cdot e^2 / m^*(x,y) \omega^2$$

(where N = free electron density, $m^*(x,y)$ = carrier effective mass in (x,y) plane, ω = optical frequency) and the perpendicular refractive index (n_z) being given by an expression that is schematically plotted in Fig 2-11. Refractive index n_0 in Fig 2-11 is taken by Kazarinov and Shmartsev to be the mean refractive index:

$$n_0 = (an_A + bn_B) / d$$

where n_A and n_B are the bulk refractive indices of the well and barrier materials, and a, b and d are as defined in Fig 2-1. For photon energies well below the band edge, n_z can be seen to be n_0 for all photon energies except those close to the edge of an allowed inter-miniband transition. In this region the refractive index tends asymptotically to $\pm\infty$. As with absorption, this extreme behaviour is smoothed out to a finite amplitude due to electron scattering. It is

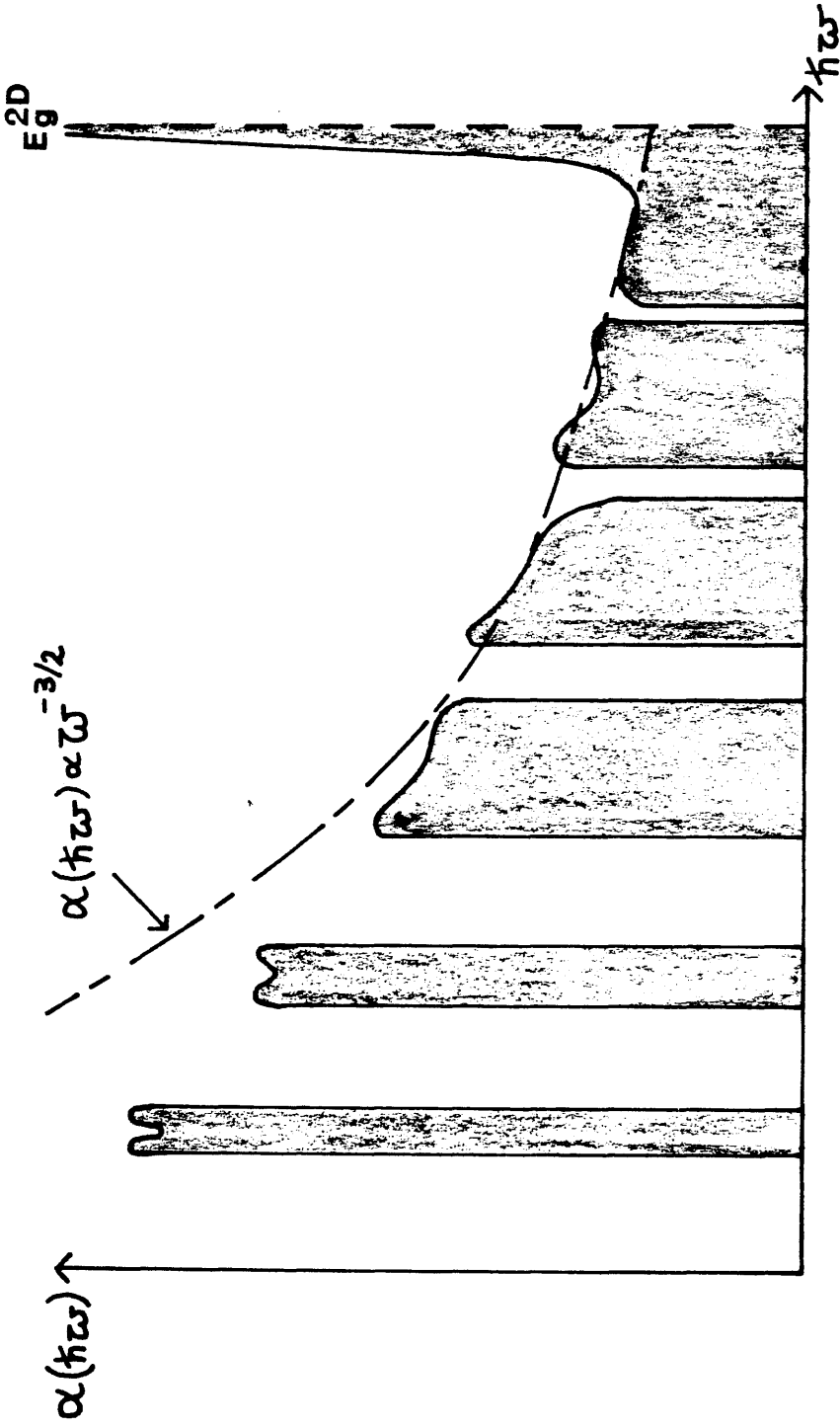


Fig 2-10 A schematic representation of the inter-miniband absorption, $\alpha(\hbar\omega)$, for light polarised along the quantisation direction (z).

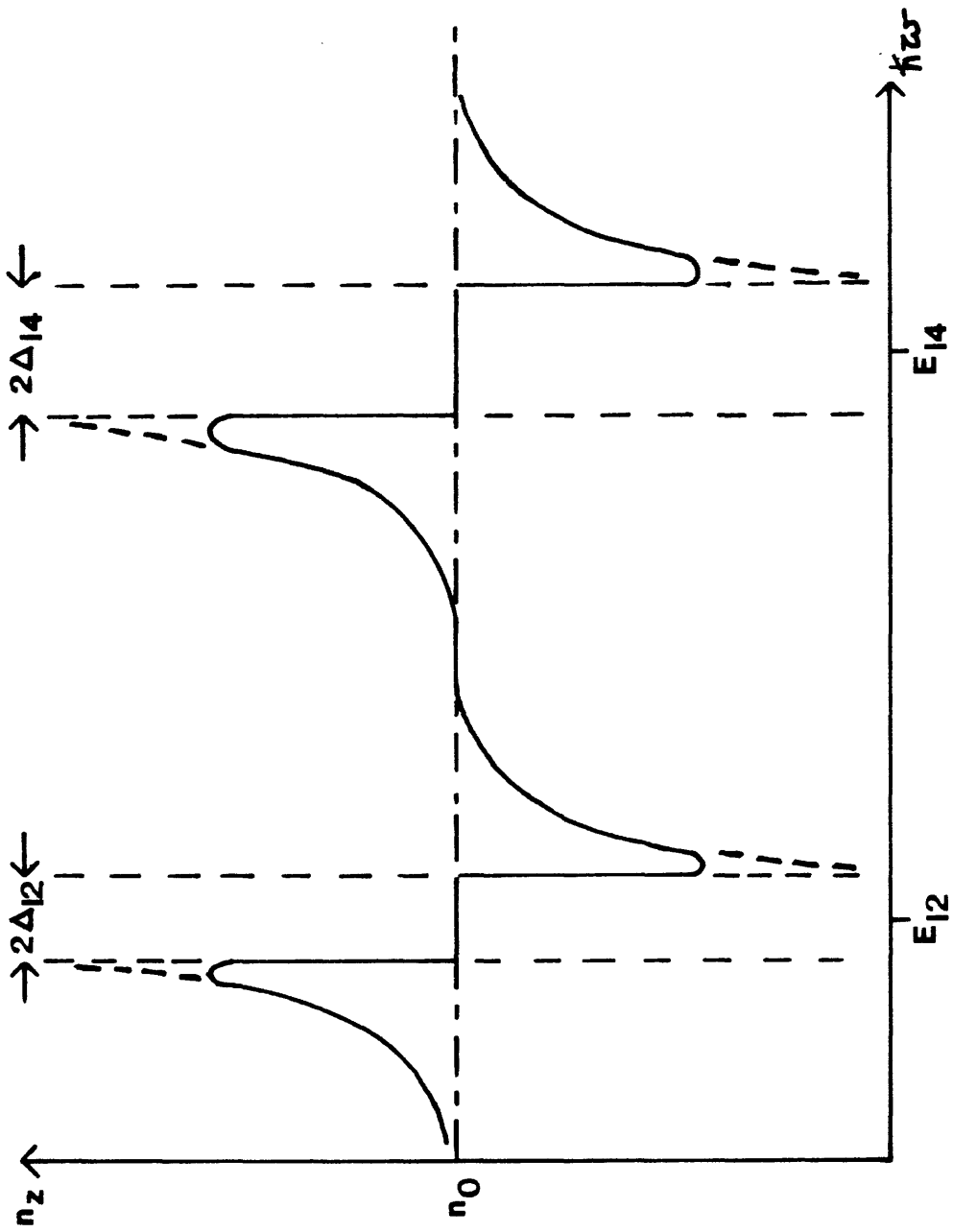


Fig 2-11 A schematic representation of the refractive index of light polarised along the quantisation direction

also predicted that there will be photon energies within the minibands where $n_x = n_0$. This result is only valid in the case of electron transitions between lower minibands.

In summary then, absorption and refraction in MQWS for photon energies well below the band gap are strongly anisotropic in certain well-defined photon energy bands. These photon energy bands are dependent on the miniband structure of the MQWS and could therefore be tuned by careful design of the MQW. The effects are limited in their usefulness for application to optical devices since they occur at very low photon energies.

2.3.2 Inter-Band Effects

2.3.2.1 Absorption Close to the Band Edge

In contrast to the inter-miniband processes that have just been discussed, inter-band absorption, on an initial investigation, turns out to be practically isotropic as in bulk semiconductors. The special feature of inter-band absorption in MQWS is the step-like absorption edge due to the step-like density of states. This step-like nature will be especially evident for the absorption due to the first few minibands, since these minibands are very narrow. Shik' again using the tight binding model, ignores the very small miniband widths, and derives the following expression for $\alpha(\hbar\omega)$:

$$\alpha(\hbar\omega) \propto (1/\omega) \sum_{n,n'} \langle n, e | n', h \rangle^2 \theta(\hbar\omega - E_g - E_{n'} - E_n) \quad (2.7)$$

where E_g = energy gap of material A, the well

$E_{n'}$ = electron energy level from bottom of well

E_n = hole energy level from bottom of well

$\theta(X) = 1$, $X > 0$

0 , $X < 0$

n' = initial hole quantum number

n = final electron quantum number

From this expression it can be seen that the absorption will have a steep edge at the quantum band gap ($E_{g,2D}$) where:

$$E_{g,2D} = E_{g,A} + E_{1'} + E_1$$

Above the quantum band edge the absorption will rise in abrupt steps. The quantum band gap is thus an important parameter with its value being strongly dependent on the well thickness. Fig 2-12 plots the results of calculating $E_{g,2D}$ using the finite single well model and assuming $Al_{0.3}Ga_{0.7}As$ barriers.

As in the inter-miniband case not all transitions are "allowed". For an arbitrary periodic potential that is symmetrical about the origin it can be shown by symmetry arguments that transitions will be limited to those where $n=n' \pm$ even number. However, expression (2.7) shows that the transition probability is proportional to the square of the overlap integral between initial and final states. This overlap will be very low for transitions other than $n=n'$, and indeed most QW absorption data^{16,17} shows only these transitions. In good photoluminescence data, however, the parity allowed transitions $n=n' \pm$ even number are seen¹⁸, and with strong photopumping even parity forbidden transitions ($n=n' \pm$ odd number) have been observed¹⁹ and are attributed to three-particle processes that conserve overall parity.

There is added detail to the absorption of MQWS in the (Al,Ga)As system due to the fact that the quantum confinement of the carriers lifts the degeneracy of the heavy and light hole valance bands about the Γ centre. For each strong $n=n'$ transition there are thus two "allowed" transitions, normally labelled 1h and 1l; 2h and 2l etc. corresponding to a heavy and light hole transition. Thus steps in $\alpha(\omega)$ will occur at $\hbar\omega = E_{g,A} + E_n^e + E_n^{hh}$ and $\hbar\omega = E_{g,A} + E_n^e + E_n^{lh}$, $n=1,2$ etc.. However, the prediction of a step-like $\alpha(\omega)$ is only correct for a single perfect well. In reality the finite width of the minibands, thermal broadening and carrier scattering broaden the step so that the hh and lh steps are indistinguishable at the fundamental absorption edge.

Excitonic effects

In considering the optical absorption of MQWS thus far, the presence of excitons has been ignored. In bulk semiconductors at low temperature the absorption near the band edge is dominated by excitonic effects²⁰. Excitons are bound electron-hole pairs similar to hydrogen atoms, which produce sharp absorption peaks at energies

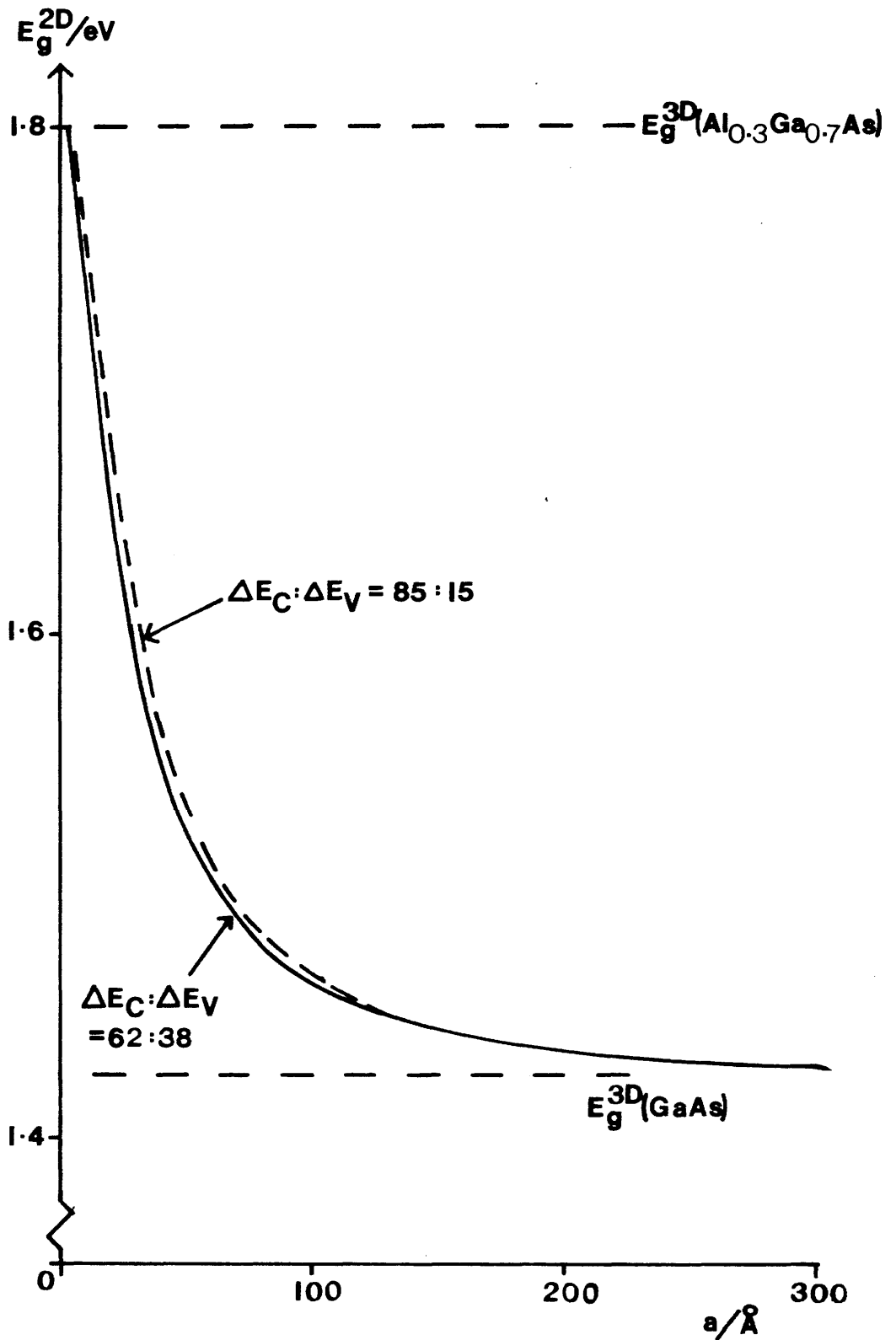


Fig 2-12 A graph of the 2D energy gap against well width using the single well model and assuming $\text{Al}_{0.3}\text{Ga}_{0.7}\text{As}$ barriers. Graphs are shown assuming two conduction band to valence band ratios.

just below the band edge. The excitonic characteristics of bulk semiconductors have been extensively studied but their usefulness for practical devices is limited by the fact that they are only observed at low temperature. This is because at room temperature phonons can easily ionise the very weakly bound excitons.

In quantum well structures, where both electrons and holes are confined, enhanced excitonic behaviour has been observed and fully investigated right up to room temperature^{18,21-25}. The enhanced effects are accounted for by the fact that the carrier confinement in the z direction reduces the average distance between an electron and a hole, thus increasing the exciton binding energy^{21,26,27}. If the infinitely deep well model is used for both electrons and holes, and both electrons and holes are confined in the same layer, then it can be shown that the exciton binding energy increases steadily with decreasing layer thickness, tending towards four times the 3D value as the well width tends to zero. Thus the 2D exciton binding energy is :

$$B_{2D} = -4R_y = -2e^2\mu/\epsilon^2\hbar^2 = 4B_{3D}$$

(where ϵ is the dielectric constant, and μ the reduced mass of the exciton) and the exciton wave function can be pictured as having been squashed from a 3D sphere to a 2D disc. MQWS are quasi-2D systems and thus the exciton binding energy lies between the 2D and 3D values. Greene and Bajaj²⁷ show that B_{MQW} first increases with reduced well width, and then decreases for very narrow quantum wells when there is non-negligible penetration of the carrier wave functions into the barriers. The binding energy of an exciton in a MQWS is thus found to be a maximum for well widths typically in the range $0.5r_{3D} < a < r_{3D}$ where r_{3D} is the 3D exciton Bohr radius (approximately 150Å in GaAs). Chemla et al²⁴ predict a maximum excitonic binding energy in (Al,Ga)As MQWS in this well thickness range of between $-2R_y$ and $-3R_y$.

For the excitonic absorption peak to be distinct from the band edge, its half-width (Γ) must be less than its binding energy (B). In pure crystals, exciton peaks are broadened due to thermal phonon interactions, predominately LO-phonon broadening in polar crystals²⁵. In MQWS this interaction is independent of well size if the wells are

not too small, and so the LO-phonon contribution to the broadening is expected to remain similar to that of the relevant bulk material.

From this argument one would expect the $B>\Gamma$ condition to be easily met. However, in MQWS there are substantial inhomogeneities in well thickness, barrier height etc. that locally vary the confinement energy of the quantum wells and thus broaden the exciton resonances. Even in the very best material, unavoidable fluctuations of one monolayer occur^{23,28} with well thickness fluctuations obviously being more important for narrower wells since:

$$\delta E_n/E_n \propto \delta L_z/L_z$$

Even larger exciton broadening can occur in poorer structures. It is thought likely that these are caused by coulombic impurities trapped at the interfaces during growth²⁹.

In conclusion then, to maximise the "visibility" of the excitonic peaks at room temperature one should:

- (a) grow material as pure as possible,
- (b) minimise inhomogeneity,
- (c) grow larger wells to minimise inhomogeneous broadening,
- (d) grow wells in region $0.5\Gamma_{3D} < a < \Gamma_{3D}$.

Thus Chemla et al²⁴ conclude that a MQWS with $a \approx 100\text{\AA}$ and $X \approx 0.3$ gives the best chance of satisfying (a)-(d) and thus obtaining $B>\Gamma$ at room temperature. With this condition one would expect strong excitonic characteristics in the absorption edge of MQWS. However, to predict the absorption edge shape, we must again take into account the fact that the degeneracy of the valance band of GaAs has been lifted. Thus, instead of one exciton resonance being observed at the 2D band edge, two will occur, one due to the heavy hole and one the light hole transition.

Experimental evidence

These characteristics have been observed experimentally^{24,25,30}, perhaps the best example being the work of Chemla et al²⁴, who present results showing two clearly visible peaks due to the 1e-1hh and 1e-1lh transition which are superimposed on a background step-

like edge due to the density of states absorption edge. They also empirically obtain a very neat functional form for the absorption edge of the MQWS comprising of two Gaussian line shapes for the exciton peaks, and a smoothed out step for the density of states edge. The fit is very good and allows Chemla et al to predict various four wave mixing phenomena²⁴. Fig 2-13 plots the form of this empirical expression.

However, not all experimental measurements of $\alpha(k,\omega)$ show such well distinguished peaks, and some results³⁰ would suggest that crystal imperfection and temperature broadening cause the exciton peaks to become unresolvable, and the tail of the absorption edge to spread out into the band gap.

Polarisation dependence

Up until this point all the work reviewed has supported this section's opening statement that inter-band effects are practically isotropic. However, in certain very important respects the inter-band effects are anisotropic.

It has been noted that the uniaxial perturbation on the crystal band structure that is introduced by a MQW structure splits the heavy and light valance bands at the zone centre. The same symmetry considerations that predict this behaviour predict that at $k=0$ the lh and hh bands have pure $|3/2, \pm 1/2\rangle$ and $|3/2, \pm 3/2\rangle$ character³¹. The oscillator strengths of the lh and hh band to band transitions (and hence the exciton peak heights) are predicted to be 1/4 and 3/4 respectively for light polarised in the x,y plane (TE), and 1 and 0 for light polarised in the z direction (TM).

Recently Weiner et al³¹ have experimentally obtained optical propagation parallel to quantum well layers in a superlattice waveguide structure with two embedded quantum wells. They observe oscillator strengths qualitatively similar to those predicted above but with the lh_{TE} transition being significantly higher than that quantitatively predicted and a very small hh_{TM} peak being observed. These quantitative differences can be accounted for by the fact that the model used to calculate the oscillator strengths does not take into account valance band mixing. In addition, some error could be

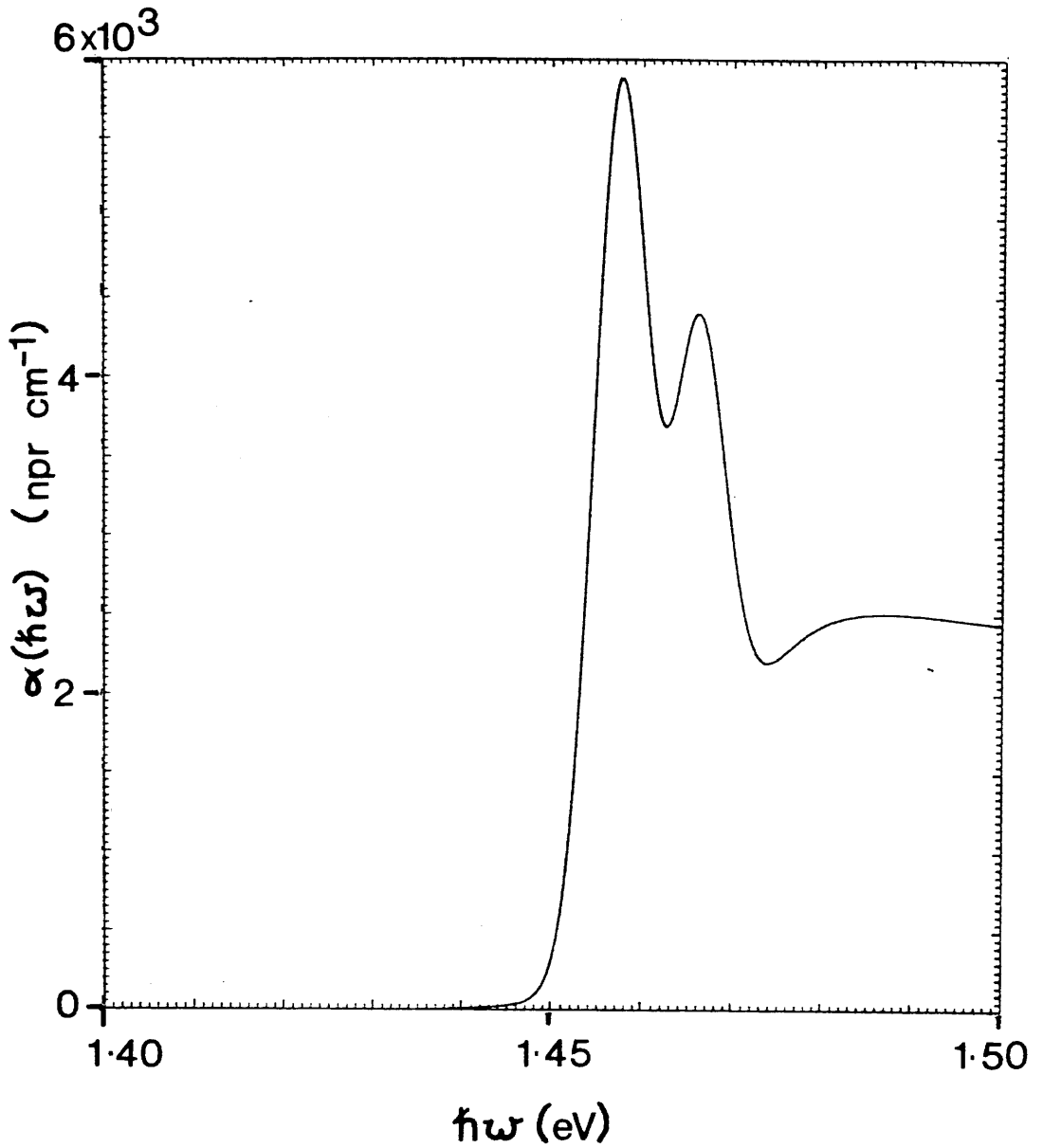


Fig 2-13 A plot of inter-band absorption, $\alpha(\hbar\omega)$, for light polarised parallel to the MQW layers using the empirical expression of Chemla et al²⁴.

introduced since the exact line shape of the light hole exciton transition is not well understood, and the experimental oscillator strengths were calculated using the double Gaussian, semi-empirical fit of Chemla et al²⁴.

2.3.2.2 Refractive Index Close to the Band Edge

Although the band edge absorption of MQWS has been investigated in the literature in some depth, the refractive index of MQWS has not received the same attention.

The refractive index of a MQWS close to the fundamental absorption edge is dominated by two effects: (a) an excitonic effect due to the presence of strong excitonic resonances at the absorption edge, and (b) a background effect due to the composite dielectric nature of the MQWS. Both of these components are fundamentally birefringent giving a refractive index for light polarised parallel to the MQW layers (n_{xy}) greater than that polarised perpendicular to the layers (n_z).

Effect (b) can be considered to be due to two properties of the MQWS: (i) its multilayer nature, and (ii) its 2D density of states. If a multilayer structure has layers of thickness a and b and real components of dielectric constant ϵ_A and ϵ_B then the dielectric constant of the layered medium in the thin film approximation are³²:

$$\epsilon_{xy} = (\epsilon_A a + \epsilon_B b) / (a + b) \quad (2.8)$$

$$\epsilon_z = (a + b) / ((a/\epsilon_A) + (b/\epsilon_B)) \quad (2.9)$$

In multilayer structures with $a, b > 0.1 \mu\text{m}$, ϵ_A and ϵ_B can be assigned the values of the bulk dielectric constant of the relevant material. However, in MQWS size quantisation alters the position and nature of the electron states in material A and B so that bulk dielectric constants cannot be used. It is interesting to note that Ohke et al³³ recently published a paper rederiving expression (2.8) and, using bulk dielectric constants, claimed it modelled ϵ_{xy} for MQWS.

The real part of the dielectric constant is the Kramers-Krönig transform of the imaginary part which contains the density of states information¹⁴. Hence, reasonably far from the band edge the difference in density of states between a quasi-2D system and a 3D

system will tend to average out. In this approximation the position of the band edge becomes the important parameter. Van der Ziel and Gossard³² were thus able to assign a modified value of ϵ_A to (2.8) and (2.9) for MQWS, to take account of property (ii) above. Due to the polarisation dependence of the band to band transitions in a MQWS (see the previous section) the following expressions for ϵ_A are obtained:

$$\begin{aligned}\epsilon_{Axy} &= 0.75\epsilon_{hh} + 0.25\epsilon_{lh} \\ \epsilon_{Az} &= \epsilon_{lh}\end{aligned}$$

where ϵ_{lh} , ϵ_{hh} are the dielectric constants of the (Al,Ga)As alloy with an exciton peak position equal to that of the lh and hh exciton positions respectively. Since the hh transition occurs at the lower energy, $\epsilon_{hh} > \epsilon_{lh}$, and so $\epsilon_{Axy} > \epsilon_{Az}$. Hence, in addition to (2.8) and (2.9) introducing birefringence, ϵ_A will itself be birefringent.

The cladding layers should experience a similar lh and hh splitting in van der Ziel's model but this splitting is not experimentally determinable. Therefore van der Ziel and Gossard used it as an adjustable parameter.

Using a MQW-DH waveguide, van der Ziel and Gossard³² showed that the above model satisfactorily predicted MQW birefringence for $\hbar\omega$ further than approximately 100 meV from the excitonic resonances, with the majority of the birefringence being due to the multi-layer nature of the MQWS (i.e. expressions (2.8) and (2.9)). Closer to the band edge the detailed nature of the quasi-2D density of states becomes important, and so van der Ziel's model underestimates the measured birefringence in this region.

Recently Sonek et al³⁴ used grating coupling to measure the refractive index of MQWS close to the band edge. Once again a strong birefringence was observed. Sonek et al showed that the excitonic term in the refractive index of MQWS can be modelled using a Lorentzian oscillator model. Experimental data on the hh and lh exciton position and width was used to fit the excitonic term to the measured data. The resulting background refractive index was found to vary linearly with $\hbar\omega$ for both xy and z polarised light with a constant birefringence of 0.005 (compared with 0.011 when the

excitonic terms are included) of which 80% was calculated to be due to the multi-layer nature of MQWS.

The above models of the refractive index of MQWS are not entirely suitable for use in the design of MQW-DH since they involve sample specific fittable parameters. However, Sonek et al's data shows that the excitonic component of the refractive index becomes small for photon energies greater than approximately 100 meV away from the exciton peak. In addition, for well widths $a \gg 100 \text{ \AA}$ the hh exciton peak is close to the exciton position of bulk GaAs. It is therefore possible to assign bulk dielectric values to ϵ_A and ϵ_B in (2.8) and still expect a reasonable approximation to n_{xy} for $\lambda \gg 880 \text{ nm}$. This simplification of van der Ziel's model is called the rms model since the refractive index assigned to n_{xy} is the weighted rms average of the bulk indices of the layers. The rms model was used throughout this project to facilitate the design and analysis of MQWS and although simple it still qualitatively models the experimentally observed birefringence of MQWS and the fact that n_{xy} is greater than the refractive index of an (Al,Ga)As alloy with an aluminium concentration equal to the average aluminium content of the MQWS (i.e. $n_{xy} > n_x$)³⁵⁻³⁹.

Kahen et al^{40,41} have modelled the refractive index of MQWS, taking into account the detailed electronic band structure, and obtained dispersion curves qualitatively similar to those obtained experimentally by Suzuki and Okamoto⁴². However, the rms model also fits the experimental data reasonably well except close to the excitonic resonances as shown in Fig 2-14. In this photon energy region the effect of the excitonic peaks and quasi-2D density of states edge can be very simply introduced by modelling the exciton peaks as delta functions and the density of states edge as a step function. If, for simplicity, the exciton binding energy is ignored, this leads to the following expression:

$$\alpha(k\omega) = \{A\theta(k\omega - E_{g,2D}) + B\delta(k\omega - E_{g,2D})\} \quad (2.10)$$

where A and B are arbitrary constants, $E_{g,2D}$ is the 2D energy gap, θ is a step function and δ a delta function. Applying the Kramers-Krönig relation to (2.10) one obtains:

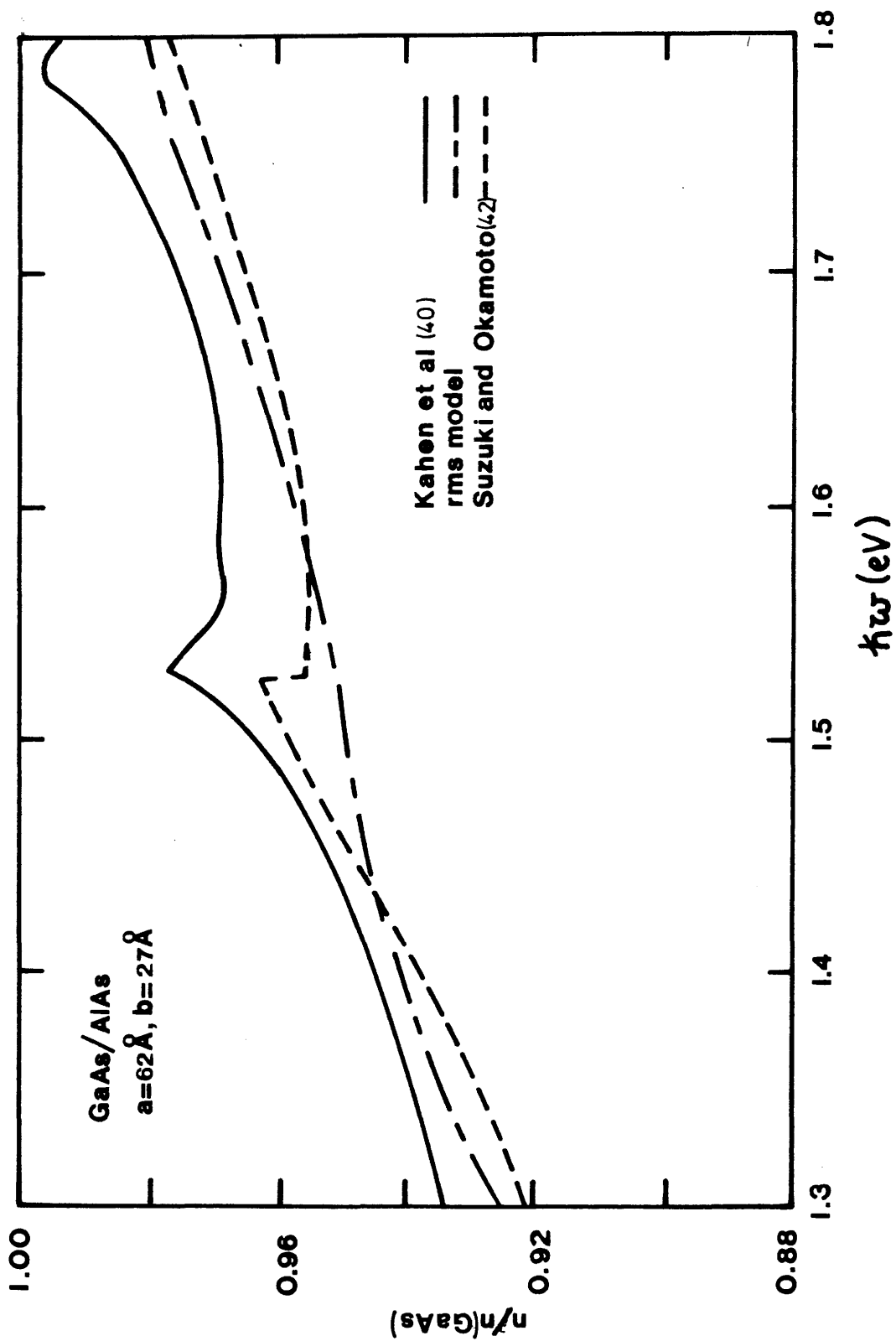


Fig 2-14 The refractive index of a MQWS as a function of photon energy.

$$n(\hbar\omega)-1 = A' \ln[(E_{g,2D}+\hbar\omega)/(E_{g,2D}-\hbar\omega)] + B'/(E_{g,2D}^2-(\hbar\omega)^2)$$

where A' and B' are constants involving A and B respectively.

This expression has been sketched in Fig 2-15 to show that when this 2D contribution is added to the background refractive index given by the rms model, all the structure observed in the experimental results^{34,42} is reproduced. In particular, Fig 2-15 shows that the anomalous dispersion observed in MQWS at photon energies just above the exciton position will be very abrupt.

In summary, MQWS are fundamentally birefringent due to their multi-layer dielectric nature and the valance band splitting introduced by carrier confinement. In addition, the anisotropic excitonic oscillator strengths enhance this birefringence. Both the quantum mechanical model of Kahen et al and the simple rms model fail to accurately predict the available experimental refractive index data. However, the measured birefringence at photon energies far from the exciton peaks can be modelled using the work of van der Ziel, although fitting parameters are needed. Similarly, close to the absorption edge Gaussian²⁴, Lorentzian³⁴ or delta functions can be fitted to the excitonic line shapes and transformed by the Kramers-Krönig relation to model the excitonic refractive index term. Far from the band edge n_x is adequately described by the simple rms model which involves no adjustable parameters. It was decided to proceed with the design of MQW-DH using this model.

2.4 THE EFFECT OF APPLIED ELECTRIC FIELD

In bulk semiconductors at low temperature an applied electric field induces a Stark effect on the excitons analogous to that seen on atoms. This effect induces a small shift in the exciton position but this is very quickly masked by the broadening of the exciton peak due to ionisation of the bound electron-hole pairs into free carriers. At room temperature all excitonic behaviour has disappeared and the effect of an applied electric field on the absorption edge is dominated by the Franz-Keldysh effect. This effect results in a general broadening of the absorption edge. These changes in absorption are reflected in a corresponding change in the refractive index dispersion relation.

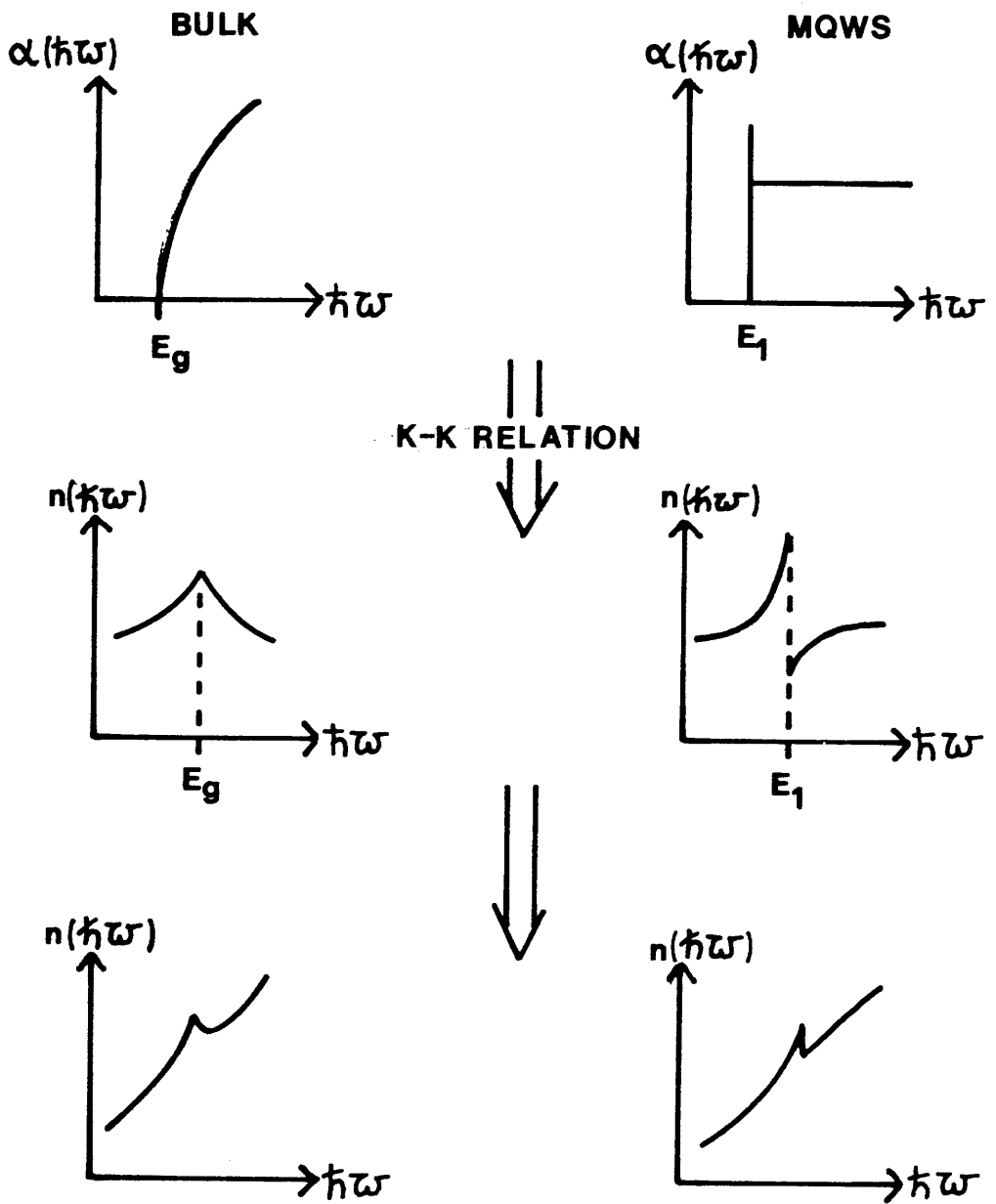


Fig 2-15 A schematic representation of the derivation of the absorption edge component of the refractive index of MQWS.

In MQWS an applied electric field has been predicted and observed to exhibit very different effects. In this section these effects are briefly described.

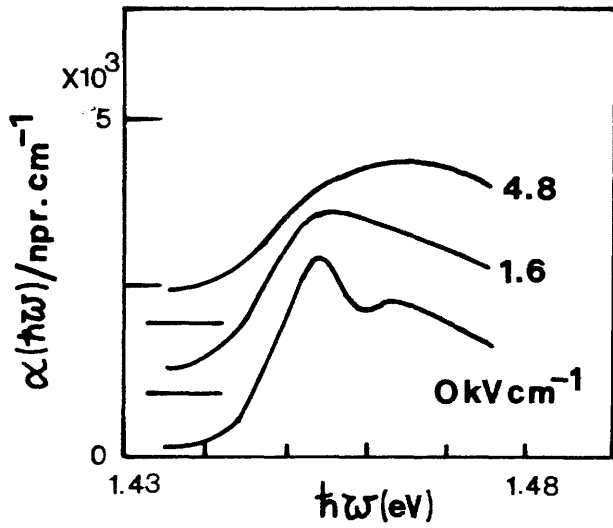
2.4.1 Electro-Absorption

If an electric field is applied in the (x,y) plane the observed effect on the absorption edge is very similar to that in bulk materials with the strong exciton peaks gradually becoming broadened as the electric field is increased⁴³ (as shown in Fig 2-16(a)).

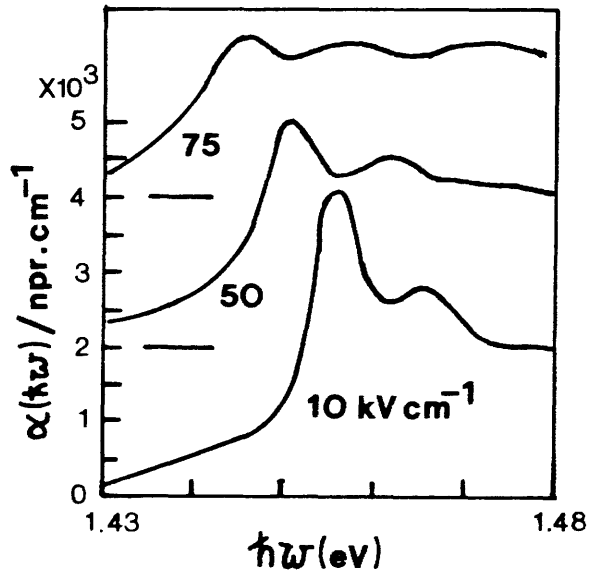
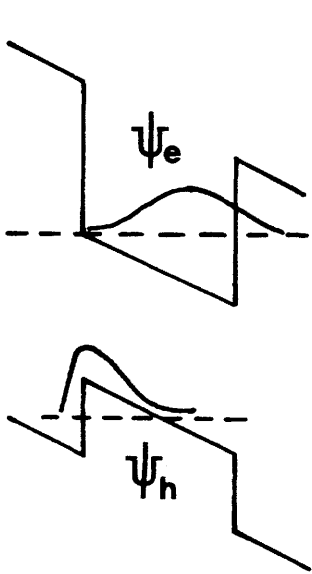
With a perpendicular field an absolutely new process occurs⁴³. The field tends to push the electron and hole forming the exciton apart, but the walls of the wells prevent ionisation by constraining the particles. Ionisation, and hence exciton peak broadening, can only occur when the particles tunnel out of the perturbed wells (Fig 2-16(b)). It is therefore possible to apply up to 50 times the classical ionisation field, thus shifting the absorption peak by 2.5 times the exciton binding energy, and still observe distinct exciton resonances⁴⁴ (see Fig 2-16). This is called the quantum confined Stark effect and it can be adequately modelled by the field induced variations in the energy of the single-particle quantum states and by pair attraction^{43,44}. The abrupt and highly absorbing MQW absorption edge can therefore be shifted into a previously transparent spectral region with the potential of enabling the design of more efficient optical modulators⁴⁵⁻⁴⁸.

These effects have been extensively studied in systems where the light is propagated perpendicular to the MQW layers^{43,48}. An identical effect has also been observed in leaky mode waveguides⁴⁴ where the propagation direction is parallel to the layers and the light can therefore be polarised parallel and perpendicular to the quantum well layers.

The experimental evidence indicates that the shift in exciton absorption peak is the dominant effect at the absorption edge. Miller et al⁴³ model the quantum confined Stark effect by calculating the overall shift of the exciton resonances, the binding energy of the exciton, and resonance broadening due to tunnelling. To do this they consider the usual complete Hamiltonian for the envelope function of



(a)



(b)

Fig 2-16 The effect of an applied electric field on the absorption edge of MQWS for light polarised in the (x,y) plane with the electric field applied in (a) the (x,y) plane, and (b) the z direction. The energy band diagram schematically represents the perturbation introduced to the MQWS due to (b). Diagram after Miller et al⁴³.

electrons and holes within the effective mass approximation. Choosing a simple separable form for the wave function they calculate exciton peak shifts that are close to those observed experimentally⁴⁴ even though no fitted parameters are included in the model. Their conclusions and the experimental verification of them are:

(1) Peak shift

The dominant contribution to the peak shift is the shift of the single-particle energies with the hole shift being dominant due to the holes being less confined. Simple perturbation theory would suggest that this peak shift will be quadratic with applied field and indeed this is the dominant trend in the experimental data⁴⁴. At lower fields, reductions in the binding energy may reduce the dependence of shift on applied field.

(2) Peak width

Significant broadening is not predicted to occur until relatively high fields (10^5 V/cm) and even then remains less than the exciton's binding energy. This agrees with the experimental observations⁴³ even though greater broadening may be observed experimentally due to inhomogeneity in the applied electric field.

Later in this thesis it will be shown how a simpler semi-empirical model was used to model the experimental data of Miller et al and predict the behaviour of MQW waveguides when used as electro-absorption modulators.

2.4.2 Electro-Optic Effect

The electro-optic effect in MQWS is a subject that has received very little attention, even when so much interest has been shown in the electro-absorption properties of MQWS. This is surprising since one of the main drawbacks of bulk III-V semiconductors when compared with other electro-optic materials such as LiNbO_3 is their low electro-optic coefficient, and MQWS may be a way of increasing the electro-optic coefficient obtainable from III-V semiconductors.

2.4.2.1 Theoretical Model in the Literature

The only published theoretical study of the electro-optic effect in MQWS is for GaInAsP MQWS⁴⁹. This analysis relates the electro-absorption due to the quantum confined Stark shift to a change in refractive index by the Kramers-Krönig relationship. In their analysis they do not include excitonic effects, and look at effects up to high applied fields (up to $3 \times 10^5 \text{V/cm}$). Their study may be indicative of the general trend in MQWS. They analyse the TE electro-optic effect only and conclude that the linear component of the change in refractive index (Δn) for photon energies close to the absorption edge is:

$$(\Delta n/n) = (n^2 r_{TE}/2) = 3.0 \times 10^{-8} \text{cm/V}$$

where r is the linear electro-optic coefficient. This value is far larger than the reported bulk value for InP of $\Delta n/n = 7.8 \times 10^{-10} \text{cm/V}$ and is comparable with the value for LiNbO₃ of $\Delta n/n = 7.7 \times 10^{-8} \text{cm/V}$.

Unfortunately this study compares a theoretical result with an experimental value, and may therefore overestimate the advantages of MQWS over other materials. In addition, a more realistic figure of merit for an electro-optic material is not $\Delta n/n$, but the ratio of the refractive index change to propagation loss through the material ($\Delta n/\alpha$). It remains to be seen if MQWS fair as well theoretically using this measure.

2.4.2.2 Experimental Work in the Literature

As far as experiment is concerned, only two reports have appeared of the experimental measurement of the magnitude of the electro-optic effect. Glick et al^{50,51} obtained planar guiding in a MQW double heterostructure that contained a p-i-n diode. They measure the phase difference induced between TE and TM modes in a planar waveguide phase modulator at $1.15 \mu\text{m}$ (far from the absorption edge) and $0.888 \mu\text{m}$ (close to the absorption edge). At $1.15 \mu\text{m}$ the phase change was found to be linear with electric field with a linear electro-optic coefficient:

$$r_{41}(1.15 \mu\text{m}) = -1.47 \times 10^{-10} \text{cm/V}$$

which is approximately equal to that of bulk GaAs with:

$$r_{41}(1.15\mu\text{m}) = -1.50 \times 10^{-10} \text{cm/V}$$

This result is perhaps to be expected since far from the absorption edge the effect of the MQWS will be small.

At $0.888\mu\text{m}$, however, the phase change is drastically altered in character to show a strong quadratic component:

$$(R_{11}-R_{12}) = 6 \times 10^{-16} \text{cm}^2/\text{V}^2$$

and a linear component:

$$r_{41}(0.888\mu\text{m}) = -1.6 \times 10^{-10} \text{cm/V}$$

This strong quadratic term is important for device design since it means that the magnitude of any phase change will depend on propagation direction. It is important to note, however, that the electro-optic coefficients measured in MQWS so far show no sign of being orders of magnitude larger than the bulk material's corresponding coefficient, as the work of Yamamoto et al⁴⁹ would predict.

2.5 CONCLUSIONS

MQWS show novel quasi-two-dimensional characteristics in their electronic band structure, which are reflected in both their optical and electro-optical properties. Relatively simple models can adequately explain the fundamental characteristics of the MQW band structure but even the most detailed models have difficulty in quantitatively explaining experimental results. Several of the models commonly used have been described and will be used later in the design and analysis of MQW waveguides.

The quasi-two-dimensional characteristics of the absorption edge of MQWS have been extensively studied by several workers. The effect on the absorption edge of a MQWS of applying an external electric field across the wells is radically different from that observed in bulk material and has been explained successfully by the quantum

confined Stark effect. This new effect has led to the design and implementation of new devices.

The refractive index of MQWS has not been so extensively studied experimentally or theoretically. However, the work that has been carried out shows that a MQWS will be birefringent, with the refractive index of light polarised parallel to the MQW layers being above that of the (Al,Ga)As alloy with a similar aluminium concentration. The change in refractive index with applied electric field has not been widely investigated. The theoretical investigations that have been carried out predict a large increase in the electro-optic effect, but such an increase has not been observed experimentally.

References to Chapter Two

- 1 A. Ya. Shik;
"Superlattices - periodic semiconductor structures (review)", *Sov. Phys. Semicond.* **8**, 1195 (1975).
- 2 R. A. Smith;
Wave Mechanics of Crystalline Solids (Chapman and Hall, London, 1961) Ch. 4.
- 3 E. O. Kane;
J. Phys. Chem. Solids **1**, 249 (1957).
- 4 G. Bastard;
"Superlattice band structure in the envelope-function approximation", *Phys. Rev. B* **24**, 5693 (1981).
- 5 M. F. H. Schuurmans and G. W. 't Hooft;
"Simple calculations of confinement states in a quantum well", *Phys. Rev. B* **31**, 8041 (1985).
- 6 G. Bastard;
"Theoretical investigations of super-lattice band-structure in the envelope-function approximation", *Phys. Rev. B* **25**, 7584 (1982).
- 7 A. Chomette, B. Deveaud, M. Baudet, P. Auvray and A. Regreny;
"Band discontinuities and calculations of GaAs-AlGaAs superlattice structures", *J. Appl. Phys.* **59**, 3835 (1986).

- 8 K.Hess;
"Impurity and phonon scattering in layered structures", Appl. Phys. Lett. **35**, 484 (1979).
- 9 T.Ando and S.Mori;
"Electronic Properties of a Semiconductor Superlattice. I. Self-Consistent Calculation of Subband Structure and Optical Spectra", J. Phys. Soc. Jpn. **47**, 1518 (1979).
- 10 S.Mori and T.Ando;
"Electronic Properties of a Semiconductor Superlattice. II. Low Temperature Mobility Perpendicular to the Superlattice", J. Phys. Soc. Jpn. **48**, 865 (1980).
- 11 T.Ando;
"Electronic Properties of a Semiconductor Superlattice. III. Energy Levels and Transport in Magnetic Fields", J. Phys. Soc. Jpn. **50**, 2978 (1981).
- 12 M.A.R.Al-Mudares and B.K.Ridley;
"Monte Carlo simulation of scattering-induced negative differential resistance in AlGaAs/GaAs quantum wells", J. Phys. C **19**, 3179 (1986).
- 13 A.Ya.Shik;
"Optical properties of semiconductor superlattices with complex band structures", Sov. Phys. Semicond. **6**, 1110 (1973).
- 14 J.I.Pankove;
Optical Processes in Semiconductors (Dover Publications, Inc., New York, 1971).
- 15 R.F.Kazarinov and Yu.V.Shmartsev;
"Optical phenomena due to the carriers in a semiconductor with a superlattice", Sov. Phys. Semicond. **5**, 710 (1971).
- 16 A.C.Gossard, P.M.Petroff, W.Wiegmann, R.Dingle and A.Savage;
"Epitaxial structures with alternate-atomic-layer composition modulation", Appl. Phys. Lett. **29**, 323 (1976).
- 17 R.Dingle, W.Wiegmann and C.H.Henry;
"Quantum States of Confined Carriers in Very Thin $\text{Al}_x\text{Ga}_{1-x}\text{As}$ -GaAs- $\text{Al}_x\text{Ga}_{1-x}\text{As}$ Heterostructures", Phys. Rev. Lett. **33**, 827 (1974).
- 18 R.C.Miller, D.A.Kleinmann, W.A.Nordland and A.C.Gossard;
"Luminescence studies of optically pumped quantum wells in GaAs- $\text{Al}_x\text{Ga}_{1-x}\text{As}$ multilayer structures", Phys. Rev. B. **22**, 863 (1980).
- 19 R.C.Miller, D.A.Kleinmann, O.Munteanu and W.T.Tsang;
"New transitions in the photoluminescence of GaAs quantum wells", Appl. Phys. Lett. **39**, 1 (1981).

- 20 J.S.Blakemore;
 "Semiconducting and other major properties of gallium arsenide",
 J. Appl. Phys. **53**, R123 (1982).
- 21 R.C.Miller, D.A.Kleinmann, W.T.Tsang and A.C.Gossard;
 "Observation of the excited level of excitons in GaAs quantum
 wells", Phys. Rev. B **24**, 1134 (1981).
- 22 C.Weisbuch, R.C.Miller, R.Dingle, A.C.Gossard and W.Wiegmann;
 "Intrinsic radiative recombination from quantum states in GaAs-
 Al_xGa_{1-x}As multi-quantum well structures", Sol. St. Comm. **37**, 219
 (1981).
- 23 C.Weisbuch, R.Dingle, A.C.Gossard and W.Wiegmann;
 "Optical characterization of interface disorder in GaAs-Ga_{1-x}Al_xAs
 multi-quantum well structures Sol. St. Comm. **38**, 709 (1981).
- 24 D.S.Chemla, D.A.B.Miller, P.W.Smith, A.C.Gossard and W.Wiegmann;
 "Room Temperature Excitonic Nonlinear Absorption and Refraction in
 GaAs/AlGaAs Multiple Quantum Well Structures", IEEE J. Q.
 Electron. **QE-20**, 265 (1984).
- 25 D.S.Chemla, D.A.B.Miller and P.W.Smith;
 "Nonlinear optical properties of GaAs/GaAlAs multiple quantum well
 material: phenomena and applications", Opt. Eng. **24**, 556 (1985).
- 26 G.Bastard, E.E.Mendez, L.L.Chang and L.Esaki;
 "Exciton binding energy in quantum wells", Phys. Rev. B **26**, 1974
 (1982).
- 27 R.L.Greene and K.K.Bajaj;
 "Binding energies of Wannier excitons in GaAs-Ga_{1-x}Al_xAs quantum
 well structures", Sol. St. Comm. **45**, 831 (1983).
- 28 C.Weisbuch, R.Dingle, A.C.Gossard and W.Wiegmann;
 "Summary Abstract: Optical characterization of interface disorder
 in multiquantum well GaAs-Al_xGa_{1-x}As superlattice structures", J.
 Vac. Sci. Tech. **17**, 1128 (1980).
- 29 G.Bastard in *Two Dimensional Systems, Heterostructures, and
 Superlattices*, (Springer Series in Solid State Sciences Vol. 53)
 ed. G.Bauer, F.Kuchar and H.Heinrich (Springer-Verlag, New York,
 1984).
- 30 S.Ovadia, H.M.Gibbs, J.L.Jewell, D.Sarid and N.Peyghambarian;
 "Evidence that room temperature optical bistability is excitonic
 in both bulk and multiple-quantum-well gallium arsenide", Opt.
 Eng. **24**, 565 (1985).

- 31 J.S.Weiner, D.S.Chemla, D.A.B.Miller, H.A.Haus, A.C.Gossard, W.Wiegmann and C.A.Burrus;
 "Highly anisotropic optical properties of single quantum well waveguides", Appl. Phys. Lett. **47**, 664 (1985).
- 32 J.P.van der Ziel and A.C.Gossard;
 "Optical birefringence of ultrathin $\text{Al}_x\text{Ga}_{1-x}\text{As}$ -GaAs multilayer heterostructures", J. Appl. Phys. **49**, 2919 (1978).
- 33 S.Ohke, T.Umeda and Y.Cho;
 "Optical waveguides using GaAs- $\text{Al}_x\text{Ga}_{1-x}\text{As}$ multiple quantum well", Opt. Comm. **56**, 235 (1985).
- 34 G.J.Sonek, J.M.Ballantyne, Y.J.Chen, G.M.Carter, S.W.Brown, E.S.Koteles and J.P.Salerno;
 "Dielectric Properties of GaAs/AlGaAs Multiple Quantum Well Waveguides", IEEE J. Q. Electron. **QE-22**, 1015 (1986).
- 35 N.Holonyak, W.D.Laidig, M.D.Camras, J.J.Coleman and P.D.Dapkus;
 "IR-red GaAs-AlAs superlattice laser monolithically integrated in a yellow-gap cavity", Appl. Phys. Lett. **39**, 102 (1981).
- 36 W.D.Laidig, N.Holonyak, M.D.Camras, K.Hess, J.J.Coleman, P.D.Dapkus and J.Bardeen;
 "Disorder of an AlAs-GaAs superlattice by impurity diffusion", Appl. Phys. Lett. **38**, 776 (1981).
- 37 J.P.Leburton, K.Hess, N.Holonyak, J.J.Coleman and M.D.Camras;
 "Index of refraction of AlAs-GaAs superlattices", J. Appl. Phys. **54**, 4230 (1983).
- 38 T.Fukuzowa, S.Semura, H.Saito, T.Ohta, Y.Uchida and H.Nakashima;
 "GaAlAs buried multiquantum well lasers fabricated by diffusion-induced disordering", App. Phys. Lett. **45**, 1 (1984).
- 39 H.Nakashima, S.Semura, T.Ohta, Y.Uchida, T.Fukuzawa, T.Kuroda and K.L.I.Kobayashi;
 "Device Characteristics of GaAlAs Buried-Multiquantum-Well Lasers Fabricated by Zn-Diffusion-Induced Disordering", IEEE J. Q. Electron. **QE-21**, 629 (1985).
- 40 K.B.Kahen and J.P.Leburton;
 "Structure variation of the index of refraction of GaAs-AlAs superlattices and multiple quantum wells", Appl. Phys. Lett. **47**, 508 (1985).
- 41 K.B.Kahen, J.P.Leburton and K.Hess;
 "General model of the transverse dielectric constant of GaAs-AlAs superlattices", Superlatt. Microstruct. **1**, 289 (1985).

- 42 Y. Suzuki and H. Okamoto;
"Refractive index of GaAs-AlAs superlattice grown by MBE", J. Electron. Mat. **12**, 397 (1983).
- 43 D. A. B. Miller, D. S. Chemla, T. C. Damen, A. C. Gossard, W. Wiegmann, T. H. Wood and C. A. Burrus;
"Electric field dependence of optical absorption near the band gap of quantum-well structures", Phys. Rev. B **32**, 1043 (1985).
- 44 D. A. B. Miller, D. S. Chemla, D. C. Damen, A. C. Gossard, W. Wiegmann, T. H. Wood and C. A. Burrus;
"Band-Edge Electroabsorption in Quantum Well Structures: The Quantum-Confined Stark Effect", Phys. Rev. Lett. **53**, 2173 (1984).
- 45 D. S. Chemla, T. C. Damen, D. A. B. Miller, A. C. Gossard and W. Wiegmann;
"Electro-absorption by Stark-effect on room-temperature excitons in GaAs/GaAlAs multiple quantum well structures", Appl. Phys. Lett. **42**, 864 (1983).
- 46 J. S. Weiner;
"Physics and applications of quantum wells in waveguides", SPIE Vol. 578 Integrated Optical Circuit Engineering II, 116 (1985).
- 47 T. H. Wood, C. A. Burrus, D. A. B. Miller, D. S. Chemla, T. C. Damen, A. C. Gossard and W. Wiegmann;
"131 ps Optical Modulation in Semiconductor Multiple quantum wells (MQW's)", IEEE J. Q. Electron. **QE-21**, 117 (1985).
- 48 D. A. B. Miller, D. S. Chemla, T. C. Damen, T. H. Wood, C. A. Burrus, A. C. Gossard and W. Wiegmann;
"Optical-level shifter and self-linearized optical modulator using a quantum-well self-electro-optic effect device", Opt. Lett. **9**, 567 (1984).
- 49 H. Yamamoto, M. Asada and Y. Suematsu;
"Electric-field-induced refractive index variation in quantum-well structure", Electron. Lett. **21**, 579 (1985).
- 50 M. Glick and F. K. Reinhart;
"Optical waveguide properties of multiquantum wells", Proc. 3rd Euro. Conf. Integrated Opt. 99 (1985).
- 51 M. Glick, F. K. Reinhart, G. Weimann and W. Schlapp;
"Quadratic electro-optic light modulation in a GaAs/AlGaAs multiquantum well heterostructure near the excitonic gap", Appl. Phys. Lett. **48**, 989 (1986).

CHAPTER THREE
THE DESIGN AND FABRICATION TECHNIQUES AND THE ANALYSIS
SYSTEM USED FOR SEMICONDUCTOR WAVEGUIDES

3.1 INTRODUCTION

In this chapter the theoretical and experimental techniques used to design and fabricate planar and stripe waveguides are presented. The experimental equipment used to couple light of the required wavelength into semiconductor waveguides is also outlined. The techniques described were used for the fabrication and analysis of both n/n^+ GaAs and (Al,Ga)As MQW-DH waveguides.

The waveguide properties of semiconductor waveguides are critically dependent on the quality of photolithography and etching used in their fabrication. The outlined fabrication procedures were developed to maximise repeatability and yield.

3.2 WAVEGUIDE MODELLING

In the introductory chapter the ray-optics model was used to introduce the properties of dielectric waveguides. The electromagnetic approach will now be used to analyse three and four layer planar waveguides. The Modified Effective Index Method is then outlined. It is described in later chapters how this method was used to design strip loaded MQW waveguides. The WAVE variational method is also outlined since it was used extensively at an early stage in the project and provided a reference with which to compare the Modified Effective Index Method.

3.2.1 The Four Layer Slab Model

In planar waveguides light is confined in one direction only, along the z axis. The refractive index of the guide structure is thus a function of z only (see Fig 1-1). Maxwell's equations applied to the simplest, three layer planar structure' reduce to a set of equations analogous to those encountered in the finite well model of a MQWS dealt with in section 2.2.1. Maxwell's equations can be solved exactly

for the planar structure and show that two types of modes can be sustained. In the first, the transverse electric (TE) modes, the only non-zero electric field component is in the transverse direction and parallel with the dielectric layers (i.e. $E_x \neq 0$). In the second type, the transverse magnetic (TM) modes, the only non-zero magnetic field is H_x .

Within each of these types of modes two types of solutions can be obtained, guided modes and radiation modes (corresponding to bound and unbound solutions in the quantum well problem). The modal field profiles for these different solutions are shown in Fig 3-1. By applying suitable boundary conditions to Maxwell's equations, dispersion relations can be obtained for the TE and TM modes, the TE relation being identical to that derived by the ray model in section 1.2.1. To ease the design process these dispersion relations can be put in a normalised form² where the number of independent parameters for the TE mode is reduced to two. The TE dispersion relation in its normalised form is:

$$V(1-b)^{1/2} = m\pi + \tan^{-1}[b/(1-b)]^{1/2} + \tan^{-1}[(b+a)/(1-b)]^{1/2}$$

where $b = \text{normalised effective index} = (n_e^2 - n_1^2)/(n_2^2 - n_1^2)$
 $a = \text{asymmetry factor} = (n_1^2 - n_3^2)/(n_2^2 - n_1^2)$
 $V = \text{normalised film thickness} = (2\pi t_2/\lambda) \cdot (n_2^2 - n_1^2)^{1/2}$
 $m = \text{modal order } (0, 1, 2, \dots)$
 and n_1, n_2, n_3, t_2 are as defined in Fig 3-1.

The normalised cut-off frequency for TE modes is therefore:

$$V = \tan^{-1}(a) + m\pi$$

To model double heterostructure planar waveguides the four layer problem of Fig 3-2 must be solved. Maxwell's equations can be exactly solved for this structure³ to obtain a normalised dispersion relation for TE modes of the form:

$$V(1-b)^{1/2} = m\pi + \tan^{-1}[b/(1-b)] + \tan^{-1}[\chi \cdot \{(b+a)/(1-b)\}^{1/2}]$$

where:

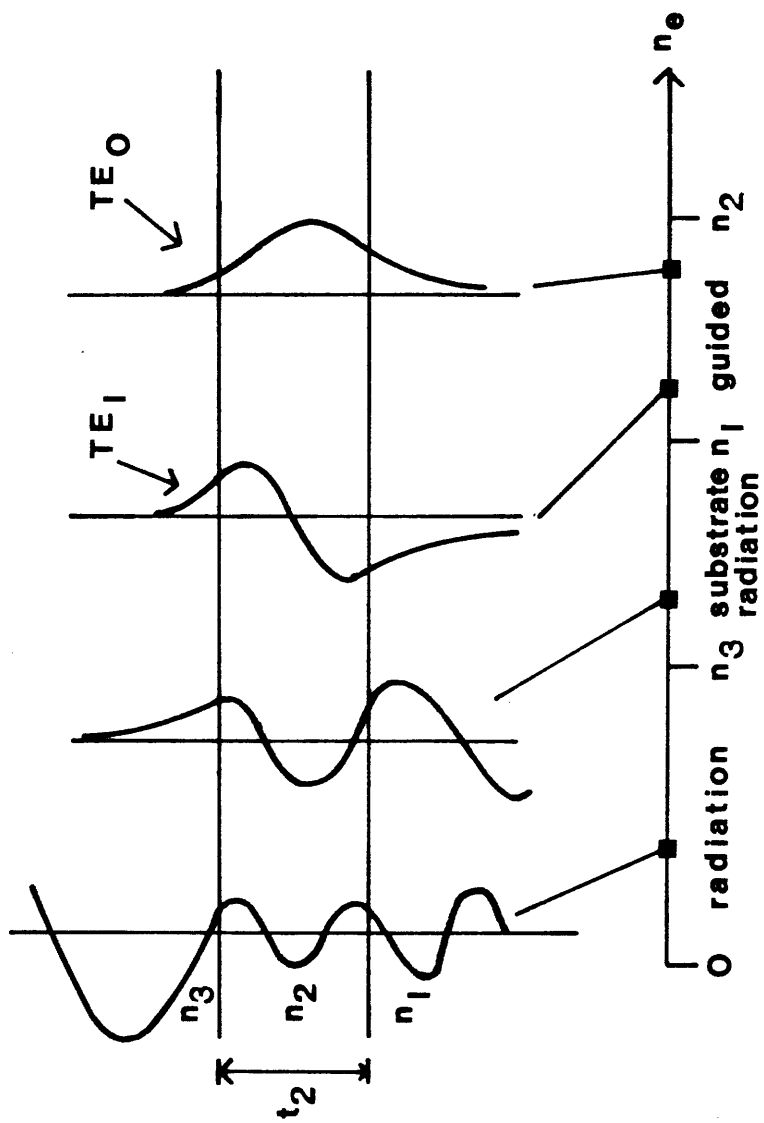


Fig 3-1 The modal field profiles of a general, asymmetrical three layer planar waveguide.

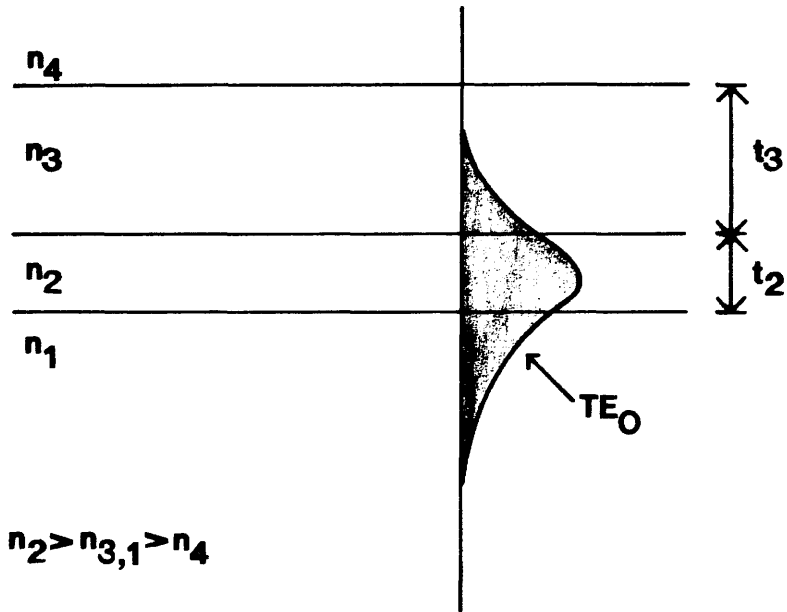


Fig 3-2 The four layer planar waveguide.

$$\begin{aligned} \chi &= \sigma_3 / \sigma_4 \cdot ((1+T) / (1-T)); & T &= (\sigma_4 - \sigma_3) / (\sigma_4 + \sigma_3) \cdot \exp(-2\sigma_3 t_3) \\ \sigma_3 &= (V/t_2) \cdot (a^* + b)^{1/2}; & \sigma_4 &= (V/t_2) \cdot (a + b)^{1/2} \\ a &= (n_1^2 - n_4^2) / (n_2^2 - n_1^2); & a^* &= (n_1^2 - n_3^2) / (n_1^2 - n_4^2) \end{aligned}$$

with V and b defined as before, and $n_1, n_2, n_3, n_4, t_1, t_2$ as defined in Fig 3-2.

Slightly more complicated than the three layer dispersion relation, this expression is easily reduced to the three layer relation if n_4 is set equal to n_3 . The above expression assumes propagation in layer n_2 . For a more general solution the transverse resonance method can be used¹.

3.2.2 The Modified Effective Index Method

The Effective Index Method (EIM) is a well-known simple analytical method of analysing step-index rectangular waveguide structures. The modes supported by such structures are not truly TE or TM but can be classified as quasi-TE or quasi-TM. Splitting the waveguide up into two regions (Fig 3-3), two planar waveguides are obtained. Using a suitable three or four layer planar slab model, the effective index of these planar guides can be obtained and used as the layer indices of an imaginary symmetrical planar waveguide with film index n_f , cover and substrate indices n_{f1} , and thickness W . The EIM uses the guiding characteristics of this equivalent planar guide to predict the guiding characteristics of the ridge guide in the x direction¹. Since the EIM treats region I and II independently, the boundary conditions on the field at the rib edges are not satisfied, and therefore the accuracy of the EIM is reduced as rib height increases or rib width decreases.

The EIM is a low order approximation of a more general solution of the waveguide problem known as the Transverse Resonance Method⁴ which looks at the transverse properties of the waveguide in terms of an electrical circuit (Fig 3-3), the mathematics being identical. A higher order approximation includes an impedance matching transformer between load and line⁵ which is the equivalent of including a term to account for the field mismatch at the edge of the rib (Fig 3-3). Mathematically, a single term is introduced to the planar waveguide dispersion relation where this term is related to the overlap of the planar modal field patterns in regions I and II⁵.

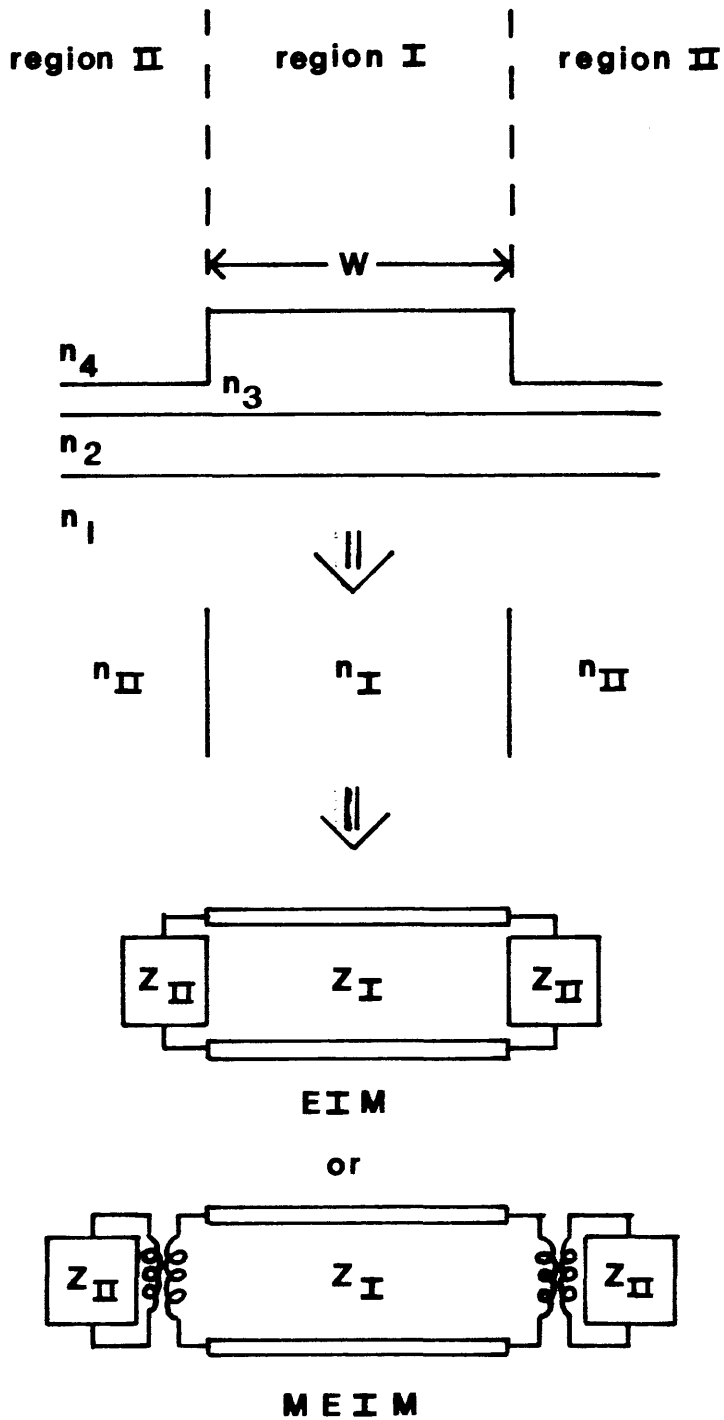


Fig 3-3

The Transverse Resonance Method applied to a strip loaded waveguide. Z_I and Z_{II} are the impedances of the equivalent electrical circuit.

The difference this makes to the calculated effective index (n_e) is small, but is largest for thin high ridges. The calculations of Koshiha and Suzuki⁵ were repeated (see Fig 3-4) to show that this change was enough to bring the MEIM calculations into line with numerical methods. A comparison with the WAVE variational method will be made in the next section.

The Modified Effective Index Method can be simply extended to model directional couplers⁵ (Fig 3-5), with the same improvement in calculated modal effective index as for waveguides. By calculating n_e for the even (n_{e0}) and odd (n_{e1}) modes of the coupler structure, the coupling length (L_c) at which light is completely coupled from one guide to the other can be calculated since⁶:

$$L_c = \lambda/[2(n_{e0} - n_{e1})]$$

3.2.3 The WAVE Variational Method

The WAVE variational method is essentially the same method as that used by Matsuhara⁷ and Taylor⁸ to solve various types of dielectric waveguide problems. The programs used in this project were first developed by Prof. C.D.W. and Dr. J.A.H. Wilkinson to model propagation in ion exchange waveguides. Dr. R.G. Walker, Plessey Research (Caswell) Ltd., later extensively modified these programs for use with step-index stripe waveguides.

An outline of the theoretical basis of the WAVE variational method has been given in the introductory chapter. WAVE uses the Rayleigh-Ritz method to solve the variational version of the scalar wave equation, obtaining an estimate of both the modal propagation constant ($F(\theta)^{1/2}$) and the modal field profile ($\theta(x, z)$). The trial function $\theta(x, z)$ is a series of Hermite-Gaussian functions. Each of the terms in the series must be scaled and normalised. The guide is assumed to be symmetrical around the z-axis but not around the x-axis, so a zero shift parameter (z_0) is introduced. The scaling parameters and z_0 are obtained by maximising $F(\theta(x, z))$ using only one basis function in each direction - in essence giving the Gaussian best fit to the fundamental mode.

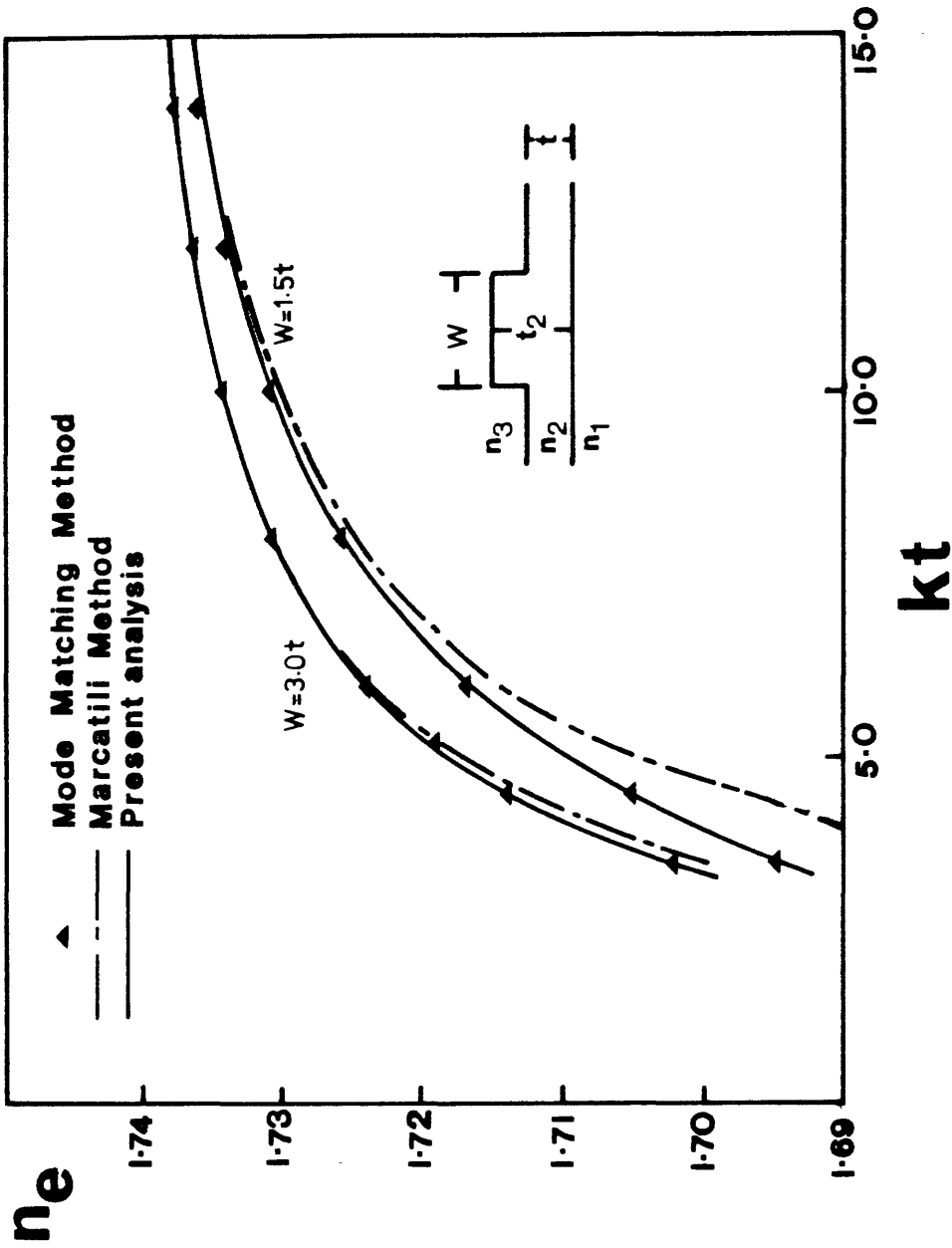


Fig 3-4 The calculated effective index of a rib waveguide as the outer slab thickness (t) is varied. $n_1=1.69$, $n_2=1.742$, $n_3=1.0$, $t_2=t_1$. After Koshiha and Suzuki's.

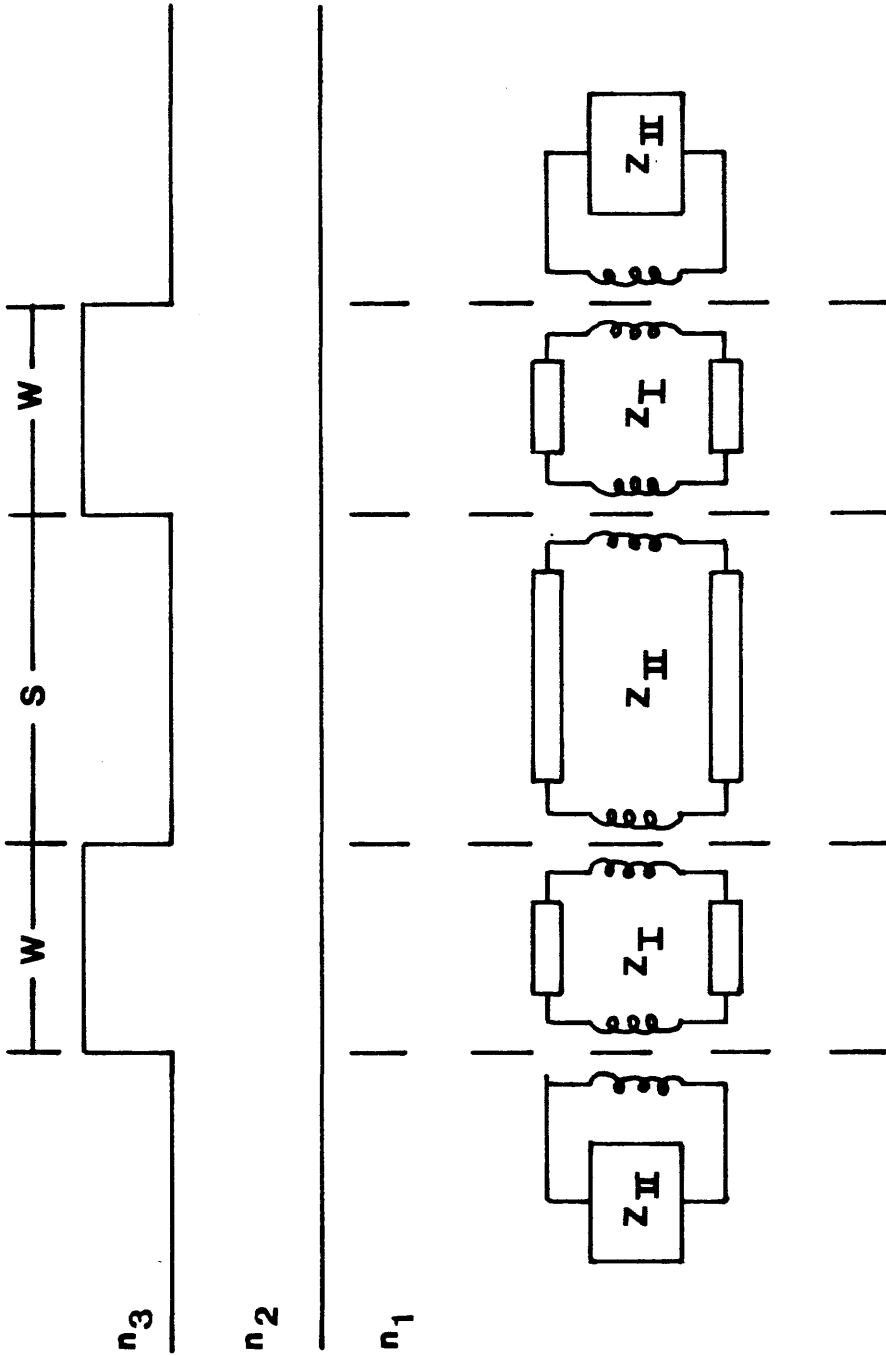


Fig 3-5 The Modified Effective Index Method applied to a directional coupler structure.

The number of terms in the trial function must be chosen so that $F(\theta)$ converges with sufficient accuracy on the true solution. Looking first at the number of basis functions in the z direction (N_z) it is found (see Fig 3-6) that convergence occurs faster for symmetrical waveguide structures, and that there is an absolute error in the WAVE result for the asymmetrical guide. Both these observations are due to the basis functions being themselves symmetrical. Fig 3-6 shows that in excess of thirteen basis functions in the z direction are required for accuracy.

This trend is repeated in Fig 3-7 for the z basis functions used to model an (Al,Ga)As ridge waveguide structure although here convergence occurs for ten basis functions. Convergence tests on the x direction basis functions where N_x is varied with $N_z=10$ (Fig 3-8) shows that a single basis function is able to model the fundamental mode with considerable accuracy. In general, the x direction field, being either symmetric or anti-symmetric like the basis functions, is more easily modelled, and $5 \leq N_x \leq 7$ is commonly used.

The absolute error observed in the planar waveguide calculation will be present in the ridge calculations. However, to an approximation, the vertical field error will be common to all the lateral modes and, if assumed invariant with width, can be subtracted out using the exact analytical planar solutions. Other errors are introduced to the WAVE variational solution when the ridge height becomes large. The correct boundary conditions at the vertical ridge walls are that H_x should be continuous. This implies a discontinuity in E_x which cannot be matched by the finite number of continuous basis functions used by WAVE.

The WAVE variational method can be easily extended to directional couplers. In an identical fashion to the MEIM the coupling length (L_c) can be calculated from the calculated effective indices of the even and odd modes of the coupler structure. However, Fig 3-9 shows that for a realistic asymmetrical coupler structure, convergence is not good even with $N_x=14$, $N_y=7$.

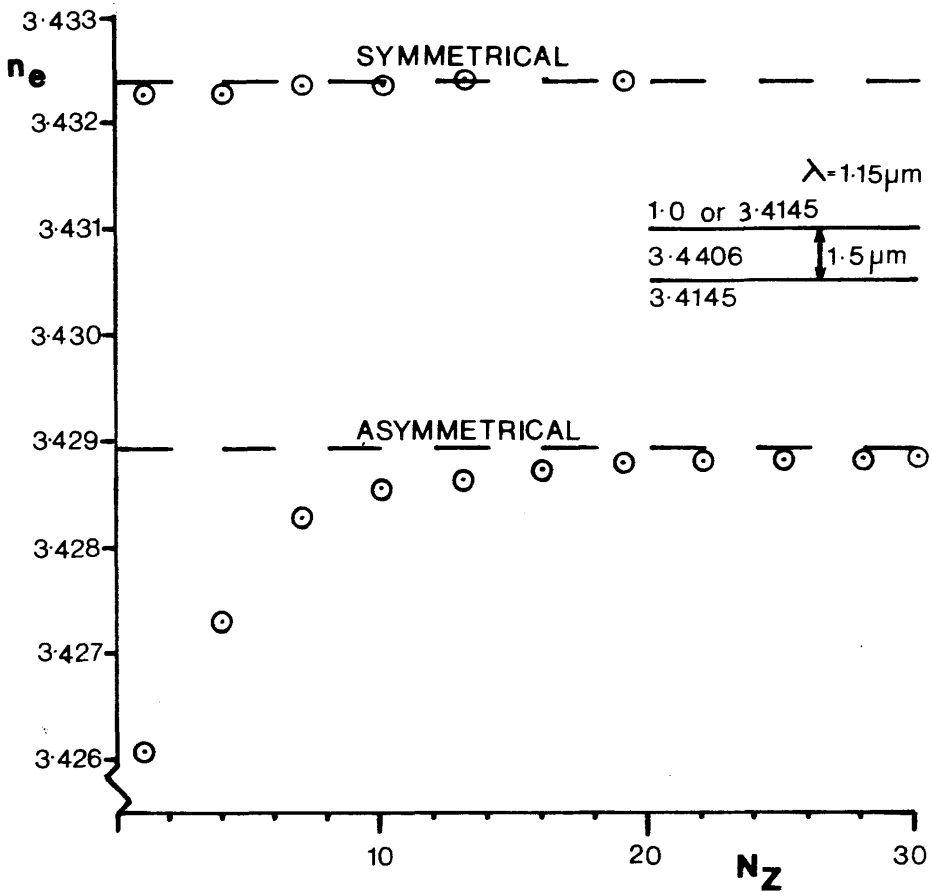


Fig 3-6 The effective index calculated by WAVE versus the number of z direction basis functions for a symmetrical and asymmetrical planar waveguide.

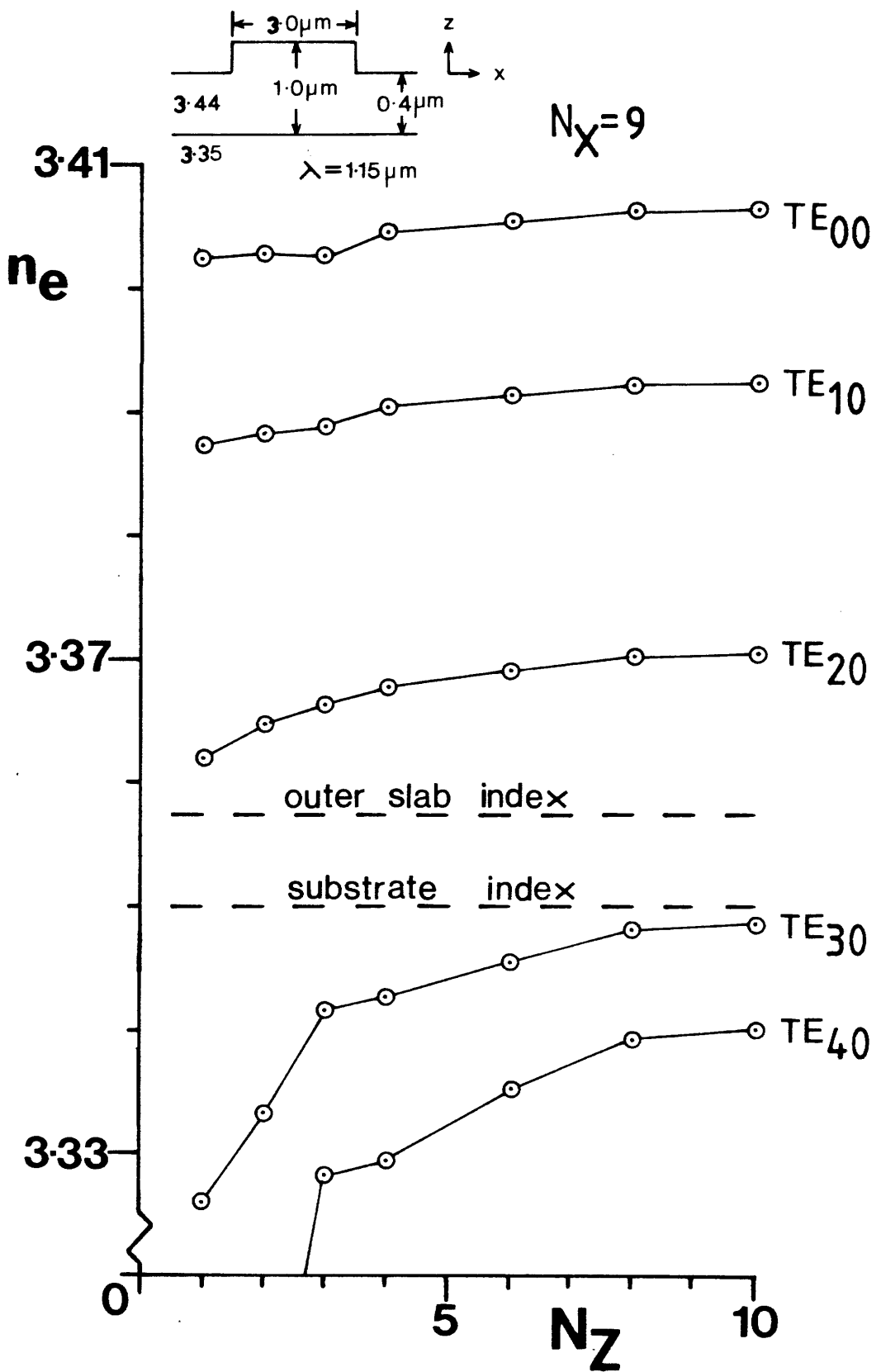


Fig 3-7 The effective index calculated by WAVE versus the number of z direction basis functions for a rib waveguide.

$N_z = 10$

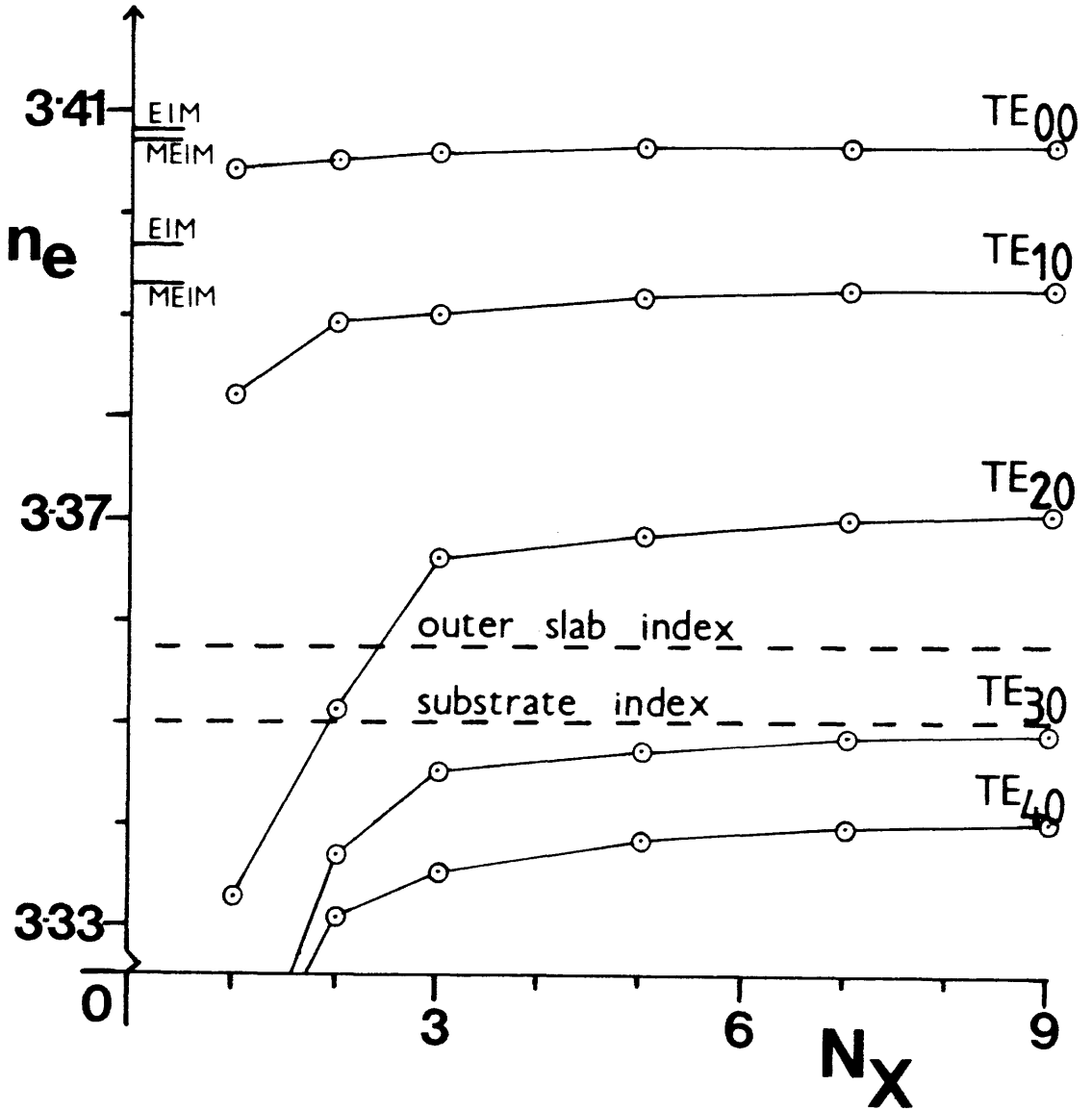
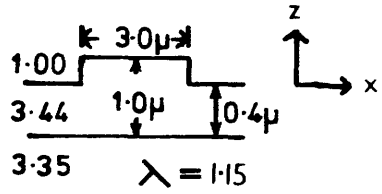


Fig 3-8 The effective index calculated by WAVE versus the number of x direction basis functions for a rib waveguide.

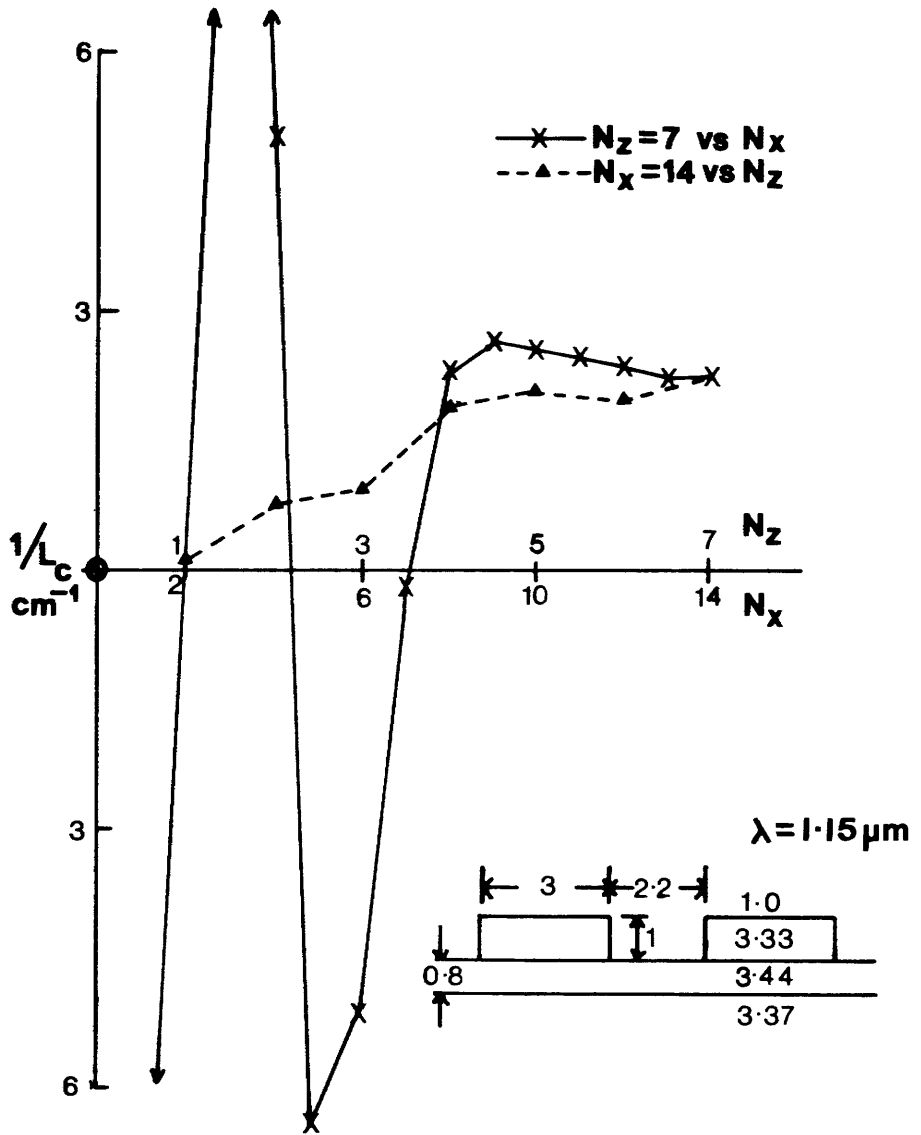


Fig 3-9 The convergence of the WAVE solution for coupling length, L_c , for a typical strip loaded directional coupler structure.

3.2.4 Comparison of Methods

It has already been noted in section 3.2.2 that the MEIM compares very favourably with the numerical results quoted by Koshiba and Suzuki⁵. A comparison with WAVE (Fig 3-8) for a structure with a relatively large ridge height shows that the MEIM makes a large correction to the EIM, with the MEIM result lying very close to that of WAVE (uncorrected for the vertical field error). The EIM is generally considered to overestimate n_e , so the MEIM can be considered to give a result closer to the true value. When the WAVE result is corrected, it rises to lie even closer to the MEIM.

Fig 3-10 compares all three methods using a structure with a relatively small ridge height. It shows that for this structure the correction that the MEIM makes to the EIM is smaller, the MEIM result lying between that of the EIM and the corrected WAVE result. The MEIM is quick, relatively simple to use and capable of being run on a microcomputer. It was therefore used extensively for the initial design of waveguides, WAVE being used for detailed calculations or situations where a knowledge of the modal field pattern was needed.

Fig 3-11 compares the estimated coupling lengths returned by the MEIM and WAVE for a representative coupler structure. There is no significant difference between the results produced by the EIM and MEIM for this structure. It can be seen that WAVE and the MEIM return significantly different results at large etch depths. However, close to the minimum coupling length point, the difference in the results is not practically significant. Since most designs are made in the region of this minimum coupling length point and WAVE requires a large number of basis functions (and hence a large computation time) to model directional couplers accurately, the MEIM was used for coupler design and analysis.

3.3 FABRICATION

The main steps used in the fabrication of semiconductor waveguides in the (Al,Ga)As system are outlined in this section. The waveguide properties of semiconductor waveguides are critically dependent on the quality of photolithography and etching used in their fabrication. The

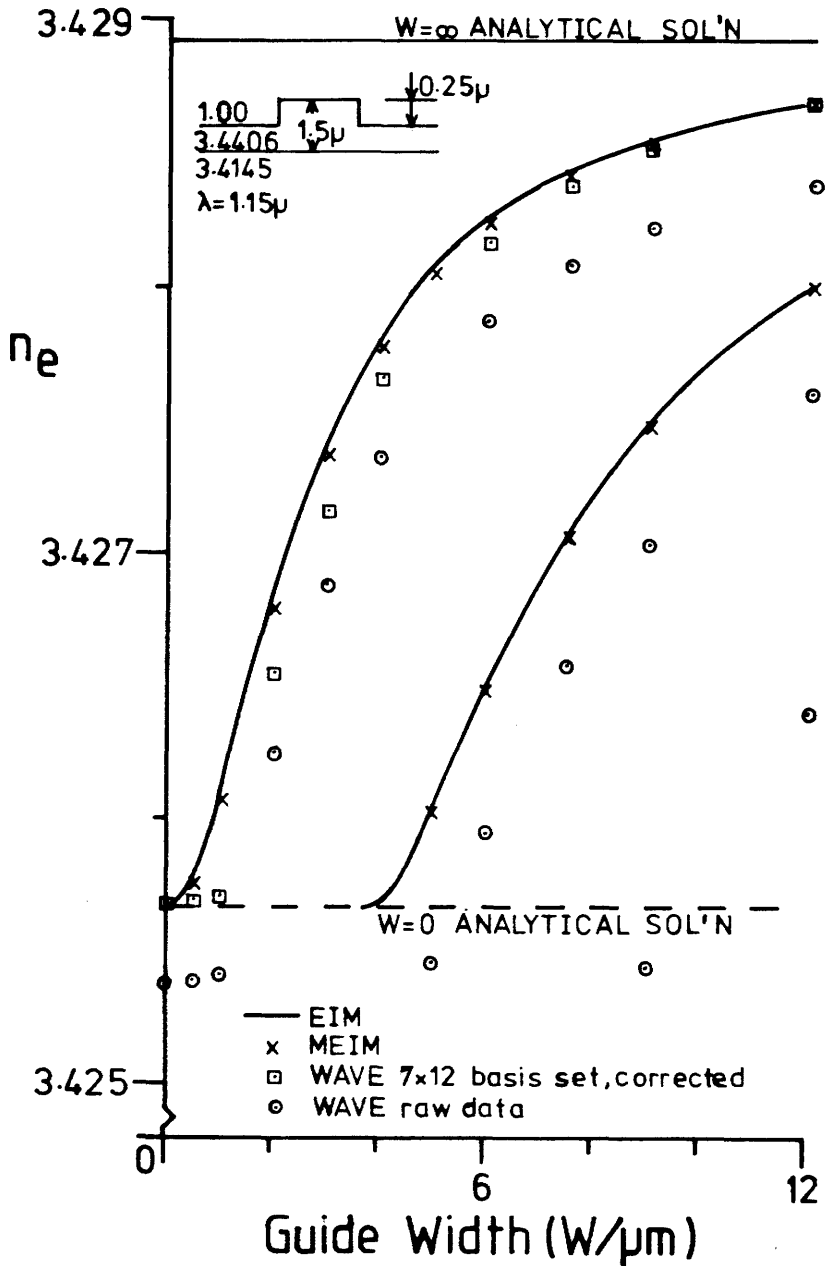


Fig 3-10 Effective index (n_e) against guide width for a rib waveguide as calculated by the Effective Index Method, Modified Effective Index Method and WAVE.

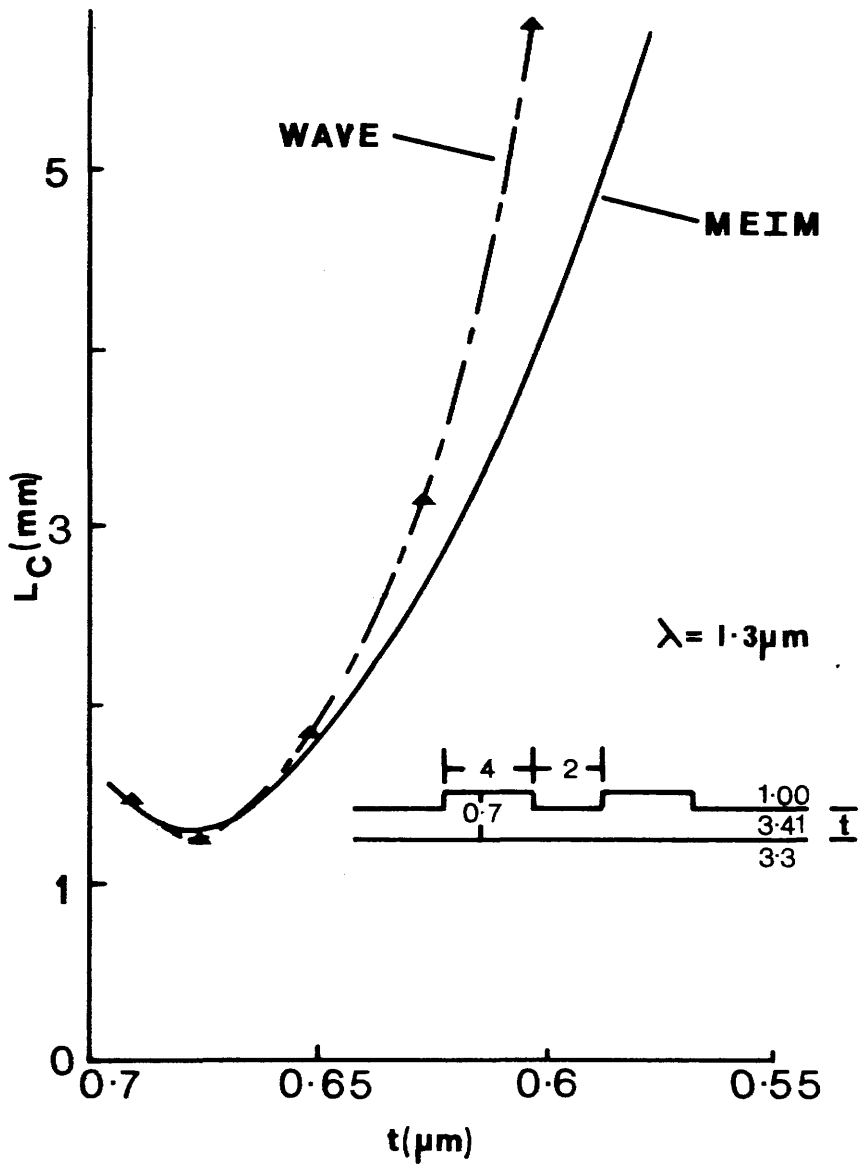


Fig 3-11 Coupling length (L_c) against outer slab thickness (t) as calculated by WAVE and the Modified Effective Index Method for a typical directional coupler structure (WAVE results supplied by Dr. R. G. Walker).

outlined fabrication steps were developed to maximise repeatability and yield.

Waveguide fabrication used conventional photolithographic techniques which were carried out in class 0-100 clean cabinets in a class 10,000 clean-room. The clean-room was equipped with filtered deionised water, analar grade solvents, ultrasonic baths and filtered nitrogen for the cleaning and blow drying of devices together with a resist spinner and contact printer for the deposition and exposure of photoresist.

The steps used to fabricate semiconductor rib waveguides from epitaxial semiconductors are shown schematically in Fig 3-12, and are as follows:

- | | |
|---------------------------|----------------------------|
| (1) Substrate preparation | (2) Photoresist patterning |
| (3) Etching | (4) Facet cleaving |

3.3.1 Substrate Preparation

It was essential to remove all contaminants from the semiconductor samples to ensure good photoresist adhesion, and minimise the disruption of the lithographic pattern due to dust. The samples were therefore cleaned by ultrasonic agitation in several solvents, following the order:

- (1) soapy water (10 min.)
- (2) deionised water (10 min., 3 - 4 changes)
- (3) methanol (5 min.)
- (4) trichloroethylene (to dissolve grease, 5 min.)
- (5) methanol (5 min.)
- (6) acetone (5 min.)
- (7) methanol (10 min., 2 - 3 changes)

Methanol is hygroscopic, so the last stage followed by blow drying leaves the surface free of any water, the lack of which is necessary for good adhesion of the photoresist.

3.3.2 Photoresist Patterning

All processes involving photoresist were carried out in "safe" yellow light. The samples were taken from the substrate preparation

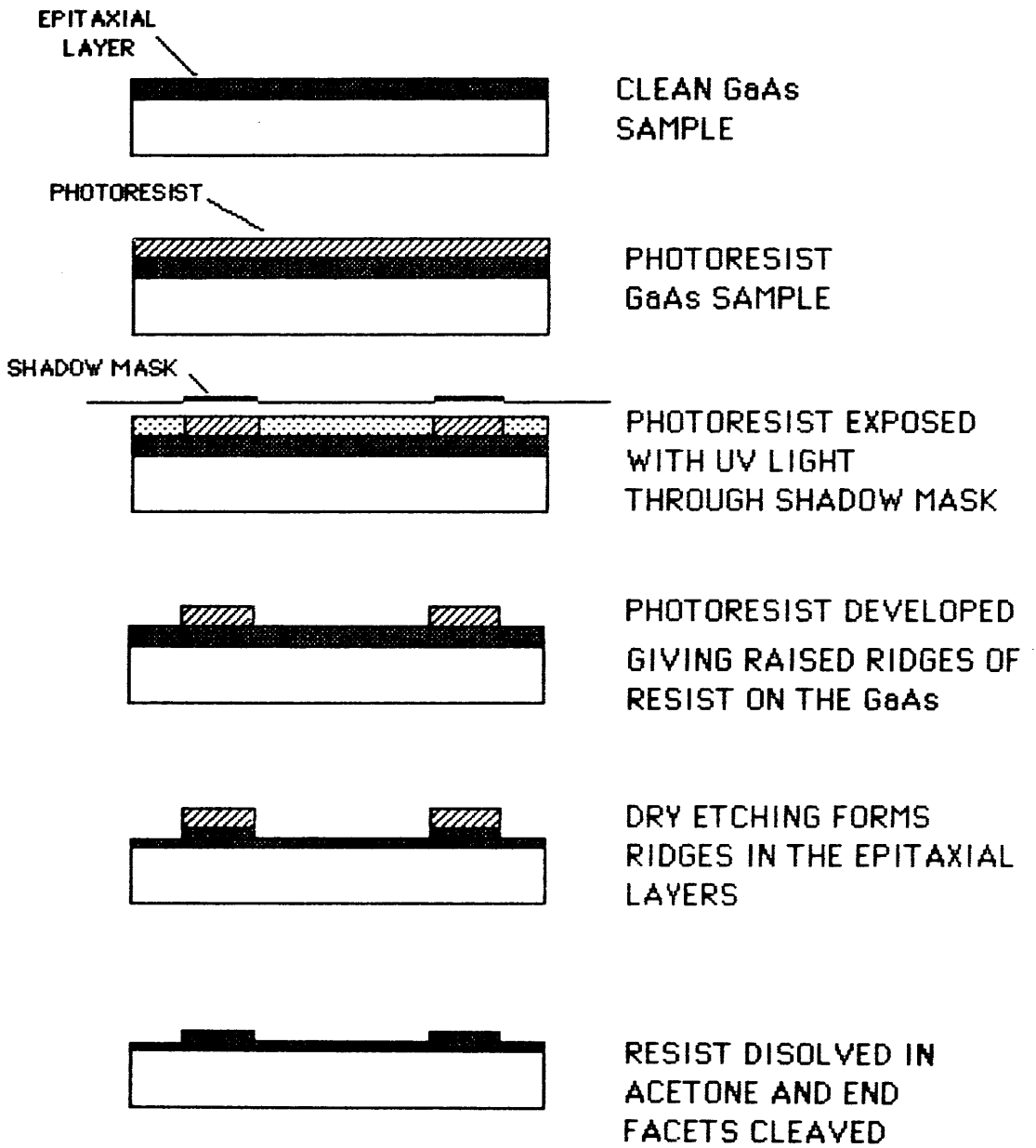


Fig 3-12 The fabrication steps used to produce rib waveguides.

stage and immediately spun with resist. The positive photoresist, Shipley AZ 1350J, dispensed through a 0.2 μ m filter and spun at 8000rpm for 20 seconds, produced an even resist film approximately 1.3 μ m thick. Spinning was carried out in a controlled humidity of less than 50% and greater than 35%, to ensure good resist adhesion. After a check for dust contamination, the samples were placed in an oven at 80-90°C for 30 minutes to drive off solvent from the resist.

The resist was exposed by UV light through chrome shadow masks which were manufactured in-house by photoreduction from ruby-lith master patterns. A mercury lamp contact printer was used to expose the resist for 13-15 seconds. The exposed resist was then developed in a 1:1 (V/V) solution of AZ developer and deionised water. After immersion in the solution for 75 seconds the patterns were fully developed and were rinsed in running deionised water.

At this stage raised ridges of unexposed photoresist are left on the surface of the sample. Each sample was inspected using an optical microscope, for defects in the pattern - the most common being dust particles on the resist ridges, uncleared sections of resist, and poor adhesion of the resist to the semiconductor surface. The uncleared resist is due to pieces of resist and dust on the shadow mask, the poor adhesion due to moisture on the semiconductor surface.

3.3.3 Dry Etching

The resist pattern now had to be translated into ridges on the surface of the semiconductor to form rib or strip loaded guides. Waveguide devices are highly sensitive to etch depth and ridge profile, and so it was decided to use dry etching techniques since the etch rates and ridge profiles obtained from wet etches are very difficult to control. Dry etching itself, however, can produce roughness on ridge walls which is not produced by wet etching. This roughness contributes to propagation loss in the waveguides, and so dry etching conditions must be found to minimise this roughness.

The dry etching systems used were contained in a laboratory separate from the clean room facilities. To minimise surface contamination prior to etching, resist patterned samples were stored in sealed boxes in the clean room and only moved to the dry etching

laboratory immediately prior to etching. Before being placed in the dry etching systems, they were blown with filtered nitrogen to remove any loose dust.

Dry etching techniques can be categorised according to the mechanisms involved in the etching process. At one extreme Ion Beam Etching (IBE)⁹ is a purely physical process, while Plasma Etching (PE)¹⁰ is primarily a chemical process. Between these two extremes are such techniques as Reactive Ion Beam Etching (RIBE) and Reactive Ion Etching (RIE)¹¹. In general, if the ions are more strongly directed in a process, then the etch is more directional, and the more chemical the process the more material selective the etch rate.

Both IBE and RIE were used in this project since both IBE^{12,13} and RIE¹⁴ have been reported as resulting in low-loss GaAs stripe waveguides. The general principles of these two techniques will now be outlined.

Ion Beam Etching

Fig 3-13 schematically depicts a simple IBE system. A beam of inert gas ions (specifically Argon) neutralised by a hot tungsten wire, is directed from an external ion source onto the sample in a high vacuum chamber. Kinetic energy is transferred from the ions to the sample so that surface material is physically dislodged. This physical process results in a directional but generally non-selective etch which tends to disrupt the crystal lattice down to approximately 100nm below the surface. This disruption is due to the high kinetic energies involved. The etch rate of GaAs in the argon ion beam is dependent on many parameters and is found to be proportional to the beam current density and tends to rise with beam energy¹⁵. Although the etch rate is generally non-selective, a ratio of approximately 3:1 is obtained between the etch rate of GaAs and the resist material Shipley AZ 1350J photoresist, the photoresist thus making an adequate etch mask.

IBE produces guide structures with relatively smooth wall edges¹⁵. However, trenching and mask erosion (Fig 3-14)¹⁰ means that the profile is not perfectly rectangular. At normal incidence trenching occurs along the bottom of ridges due to a localised enhanced ion flux. By etching at some angle off from normal the competing effect of

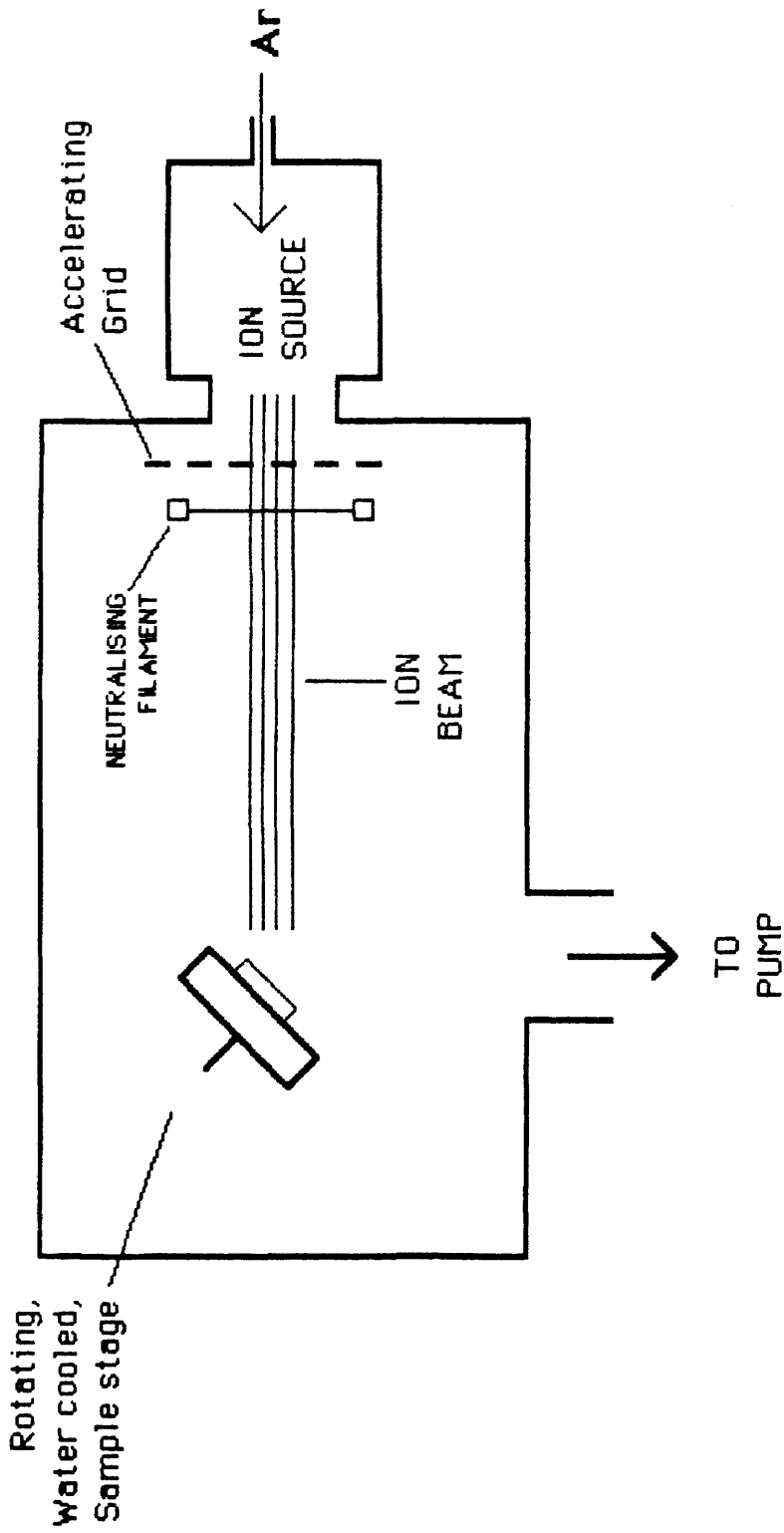


Fig 3-13 A schematic diagram of a simple Ion Beam Etching system.

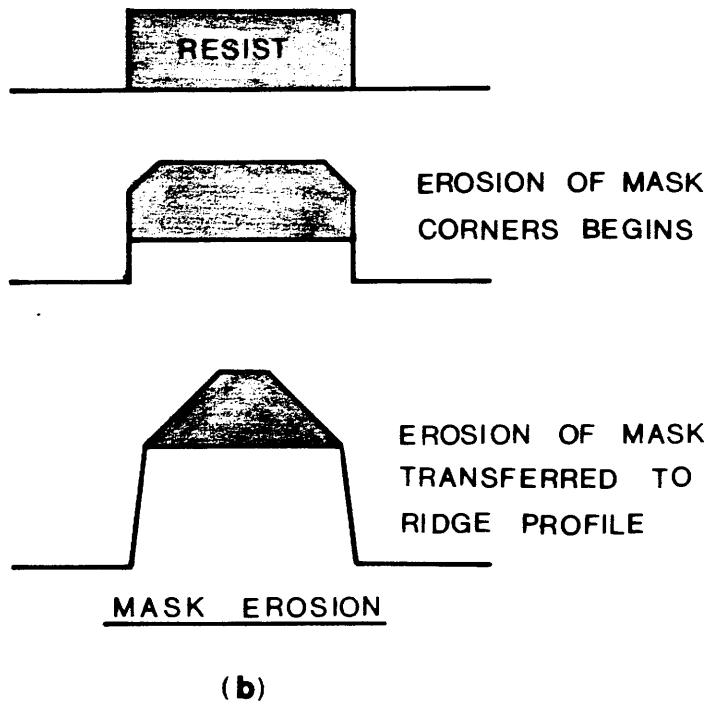
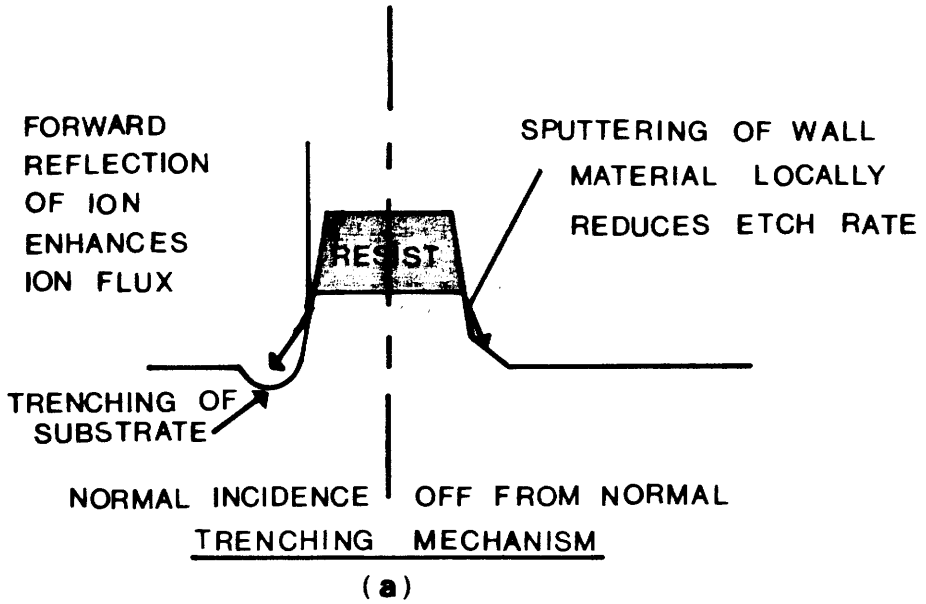


Fig 3-14 A schematic diagram of the mechanisms effecting ridge profile in IBE: (a) trenching, (b) mask erosion.

sputter deposition (Fig 3-14) can be made to cancel the trenching effect producing rectangular ridge profiles. If the mask itself is etched, then the final dimensions of the mask will be less than the initial dimensions, leading to a tapered profile.

An Oxford Applied Research model 2255 machine was used for Ion Beam Etching. The chamber is pumped out by a rotary pump and a cryo-pump. Samples may be rotated on a cooled mount and tilted in the path of a 25mm diameter beam from an Ion Tech Kauffmann-type gun. A shutter in front of the sample mount contains a beam current density meter so that a stabilised beam can be established and monitored before the target is exposed to the beam.

Reactive Ion Etching

Fig 3-15 schematically depicts a simple RIE system. RIE systems developed from sputtering systems. RF power is applied across electrodes within a vacuum chamber producing a chemically active ionic plasma from a suitable single gas or mixture of gases. The sample to be etched is generally mounted on the smaller, non-grounded electrode of a pair of parallel-plate electrodes. The rectifying properties of the plasma produce a DC self-bias which can be varied indirectly by varying gas pressure and used to direct ions across the plasma dark space onto the sample¹⁰. Due to chemically active gases being used, etching is partly chemical, producing a material dependent etch rate. However, the ions arrive at the sample after being accelerated across the dark space, so etching is directional.

A Plasma Technology RIE80 system was used for RIE dry etching. The vacuum chamber is evacuated by rotary and turbo pump, and then kept at working pressure by a Roots-blower pump when introducing the reactive gas. Up to three gases may be used, each with mass-flow control. The upper plate has a diameter of 280mm, with the samples mounted 50mm below on a parallel plate of 170mm diameter. The system is fed by a 375W, 13.56MHz generator.

The etch characteristics of RIE depend on a large number of parameters such as RF power, gas pressure and bias voltage. In general, the slower the etch rate the greater the anisotropy and the better the surface morphology. For a fixed power density, etch rates

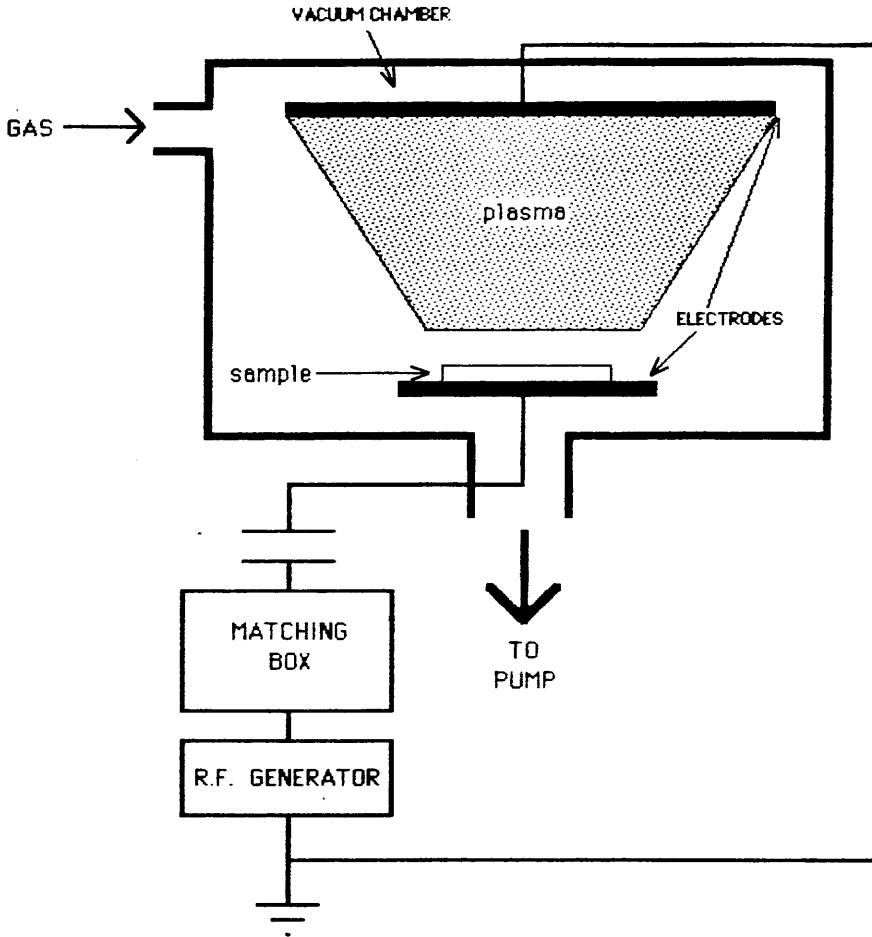


Fig 3-15 A schematic diagram of a simple Reactive Ion Etching system.

increase with pressure, reach a maximum between 5 and 20mm, and then decrease with further increases in pressure. At constant bias voltage, rates increase linearly with pressure. Rates increase with increasing RF power due to the resulting increase in self-bias voltage. With increasing gas flow, etch rates first increase and then plateau. Anisotropy is improved by increasing the directionality of the ions, i.e. by increasing bias voltage or RF power and decreasing pressure.

Several papers report the use of SiCl_4 to etch GaAs¹⁶⁻¹⁸. Chlorine, chlorine mixtures and chlorinated halocarbons have all been demonstrated to be viable etchants of GaAs but SiCl_4 has the advantages that it does not produce chlorinated polymeric films (which can contaminate the sample, etch chamber and pump fluids) and it shows high selectivity over many common mask materials¹⁸. The exact nature of the chemical processes involved in the plasma etch are unknown, but the work carried out by Dr. G. Doughty on the etching of III-V semiconductors using the RIE80 system with silicon tetrachloride as the reactive gas, has resulted in a set of etch conditions that provide a practical etch rate in GaAs, and produce very smooth vertical ridge walls. In addition, Shipley AZ 1350J appears to have an extremely low etch rate using these conditions, and it thus provides a good etch mask.

3.3.4 Metal Contacts

To enable the fabrication of active waveguide structures, metal-semiconductor contacts must be made to facilitate the application of electrical power to the device.

When a metal is in contact with a semiconductor, a potential barrier occurs at the interface due to the difference in work functions between the materials (see Fig 3-16). This barrier produces the well-known rectifying characteristics of Schottky contacts¹⁹. Semiconductor devices also require ohmic contacts across which the voltage drop is negligible compared with the voltage drop across the actual device. In principle, such contacts could be made using a metal with a work function less than that of an n-type semiconductor, or greater than that of a p-type semiconductor. Few metal-semiconductor combinations satisfy this condition, so the vast majority of ohmic contacts involve a thin layer of very highly doped semiconductor

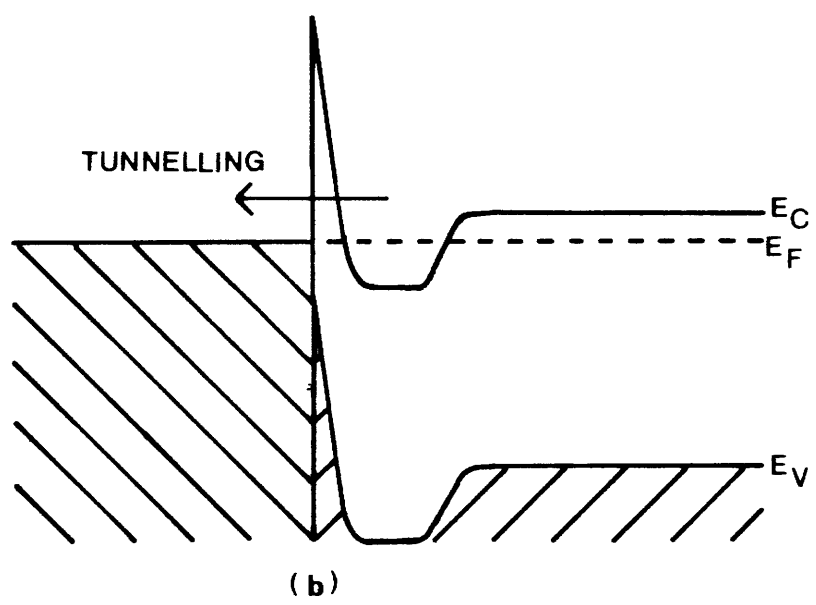
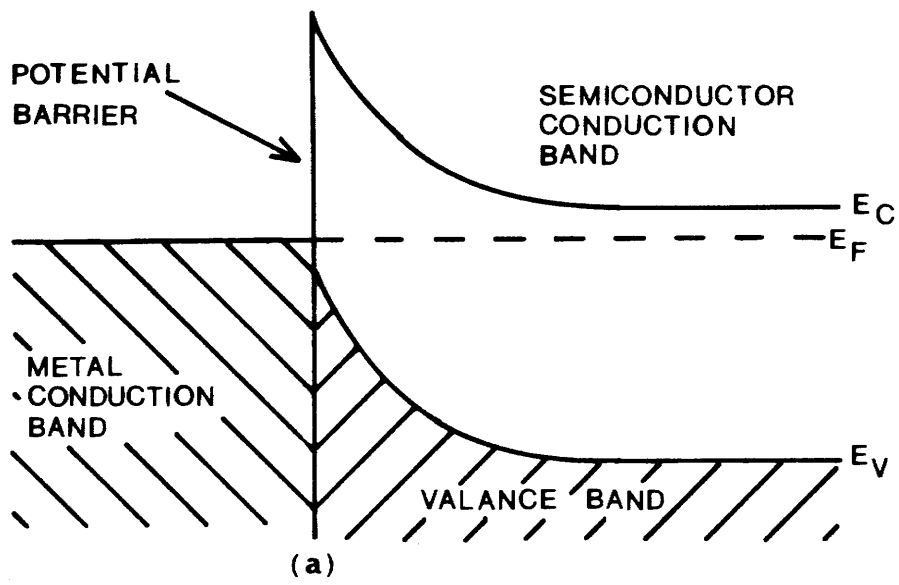


Fig 3-16 Schematic representations of metal-semiconductor contacts: (a) the Schottky contact, (b) the ohmic contact.

immediately next to the metal, so that the potential barrier is so thin that carriers can readily tunnel through it (Fig 3-16). The highly doped layer can either be placed in the semiconductor structure during growth, or formed from the deposition and annealing of an alloy contact containing an element which acts as a donor or acceptor.

Schottky contacts to n-type GaAs

Schottky contacts to n-type GaAs were required to fabricate active waveguide structures in n-n⁺ GaAs waveguides (see section 4.4) where the n doping level is approximately $2 \times 10^{15} \text{cm}^{-3}$. Since any insulating layers between the metal and semiconductor can produce poor Schottky characteristics¹⁹, the GaAs surface was deoxidised immediately prior to evaporation by being placed in a bath of 7:3, H₂O:HCl (V/V) for 30 seconds. This had the effect of removing any GaAs oxide while not attacking the GaAs.

An aluminium film, 0.36 μm thick, was evaporated in a standard evaporator at a base pressure of 1.3×10^{-5} mbar. The resultant diode characteristics were measured using a Hewlett-Packard parameter analyser (P.A.) (Fig 3-17) and found to be poor, with reverse breakdown occurring at approximately -7V. This low breakdown voltage was due to difficulties in evaporating the aluminium without producing an aluminium oxide layer.

It was thus decided to move to a multi-layer titanium-gold structure that had been successfully used by several researchers in the Department of Electronics and Electrical Engineering, University of Glasgow, to fabricate metal gates for FETs. Ti easily oxidises on evaporation, so it was necessary to use a shutter during evaporation. Only after several seconds of Ti evaporation (during which any oxygen remaining in the vacuum chamber would be absorbed by the evaporating Ti) was the shutter opened to allow coating of the sample. Tests showed that a Ti layer > 300 \AA provided excellent Schottky diode characteristics. A layer of gold 1000-1500 \AA thick was evaporated on top of the Ti to protect it from oxidisation and help the probing of the contact. Fig 3-18 shows the resulting I-V characteristics as measured by the P.A.. The results are very good, with negligible reverse leakage current, reverse breakdown at -60 to -70V, and an ideality factor of 1.026 .

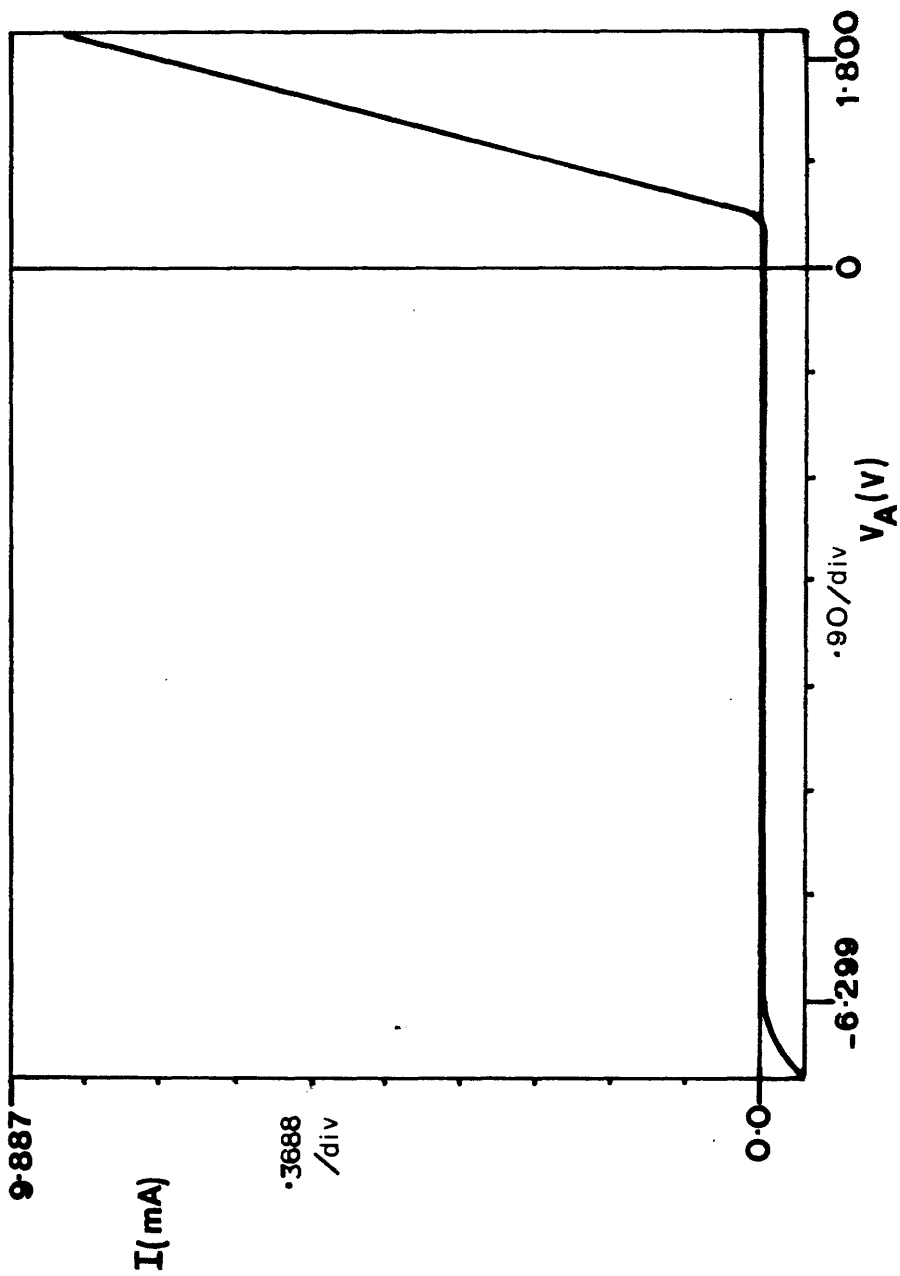


Fig 3-17 A typical I-V plot of an aluminium Schottky contact on n-type GaAs.

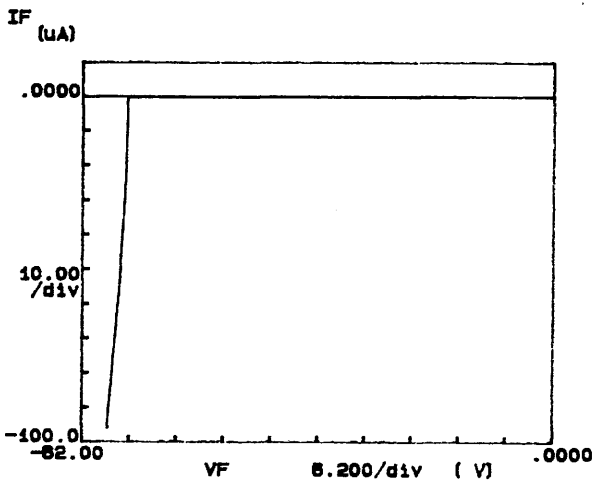
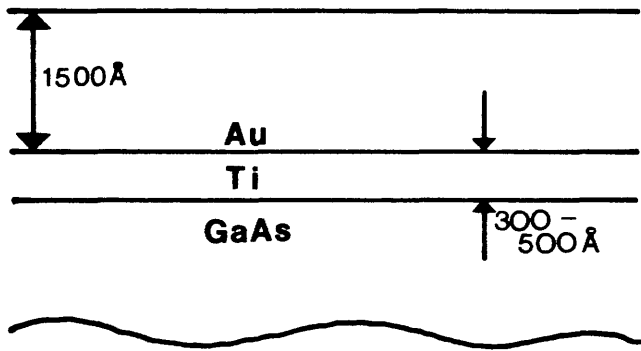


Fig 3-18 The metal layer structure and typical I-V plot of a Ti-Au Schottky contact on n-type GaAs.

Ohmic contacts

Ohmic contacts to n⁺-type GaAs (i.e. doping $\geq 10^{18}\text{cm}^{-3}$) were required to fabricate all the active waveguide structures described in later sections. After deoxidisation of the GaAs surface and evacuation of the evaporation chamber to approximately $5 \times 10^{-5}\text{mbar}$, 1000Å of a Au:Ge alloy was evaporated²⁰, followed by 150Å of Ni. A final 200Å cap of Au was evaporated to reduce the sheet resistance of the contact metal. The alloy consisted of Au:Ge, 88:12 (W/W). After evaporation the sample was annealed for one minute on a strip heater in a reducing atmosphere of 5% H₂ in Argon. This contact structure has been shown²¹ to give a specific contact resistance of approximately $2 \times 10^{-5}\Omega\text{cm}^2$. The ohmic contact is formed by the Ge (a n-type dopant) being driven into lattice sites vacated by Ga, which out-diffuses into the contact metallic layer, thus producing a highly doped region that allows carrier tunnelling. The Ni plays an active role in the formation of the contact as well as providing a barrier which ensures a smooth Au surface for contacting. A typical I-V curve (Fig 3-19) for this contact structure is highly linear.

Ohmic contacts to p-type GaAs (i.e. doping $\geq 6 \times 10^{17}\text{cm}^{-3}$) were needed to fabricate active device structures in MQW-DH p-n diodes (see chapter five). Several reported alloy mixes²⁰ were tested but only an In:Au, 80:20 (W/W) alloy was found to give approximately linear I-V characteristics (Fig 3-20(a)). However, a source of pellets of Au:Zn:Ni, 75:10:5 (W/W) alloy became available. This alloy is used by NTT in Japan for ohmic contacts to p-type III-V semiconductors. Preparing the GaAs sample in the usual way and evacuating the chamber to approximately $5 \times 10^{-6}\text{mbar}$, a 1000Å layer of Au:Zn:Ni alloy was evaporated followed by a 1000Å layer of Au. Annealing for five minutes at 400°C in Argon produced the highly linear characteristics of Fig 3-20(b). The Au:Zn:Ni alloy contact was used for all p-type ohmic contacts on actual devices.

3.3.5 Cleaving

After completion of waveguide fabrication it was necessary to cleave the ends of the waveguides to produce high quality input and output facets. This was done with the use of a Precima scribing machine. Assuming that the rectangular sample (Fig 3-21) had already

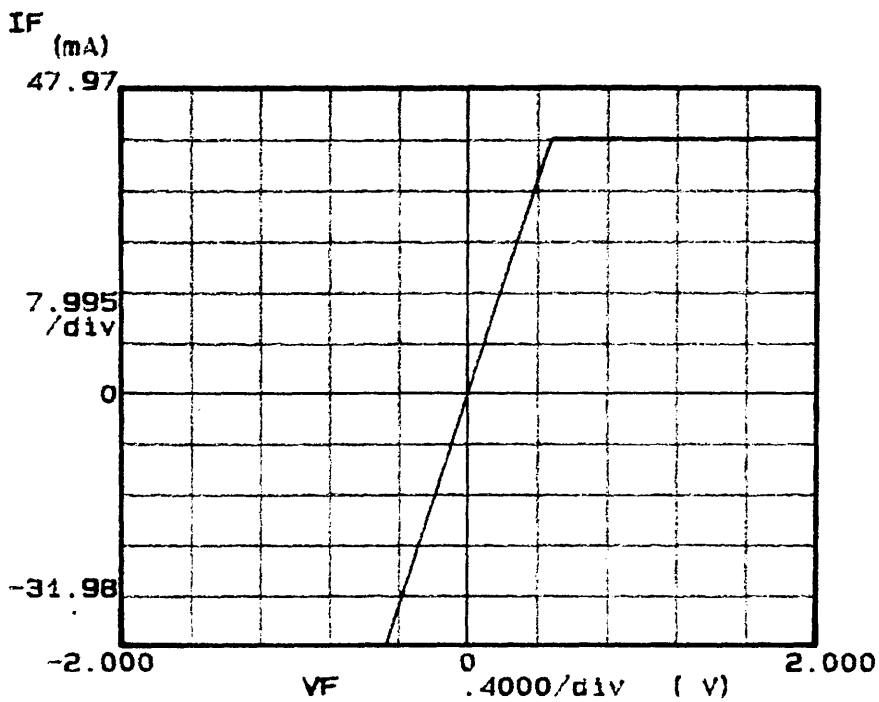
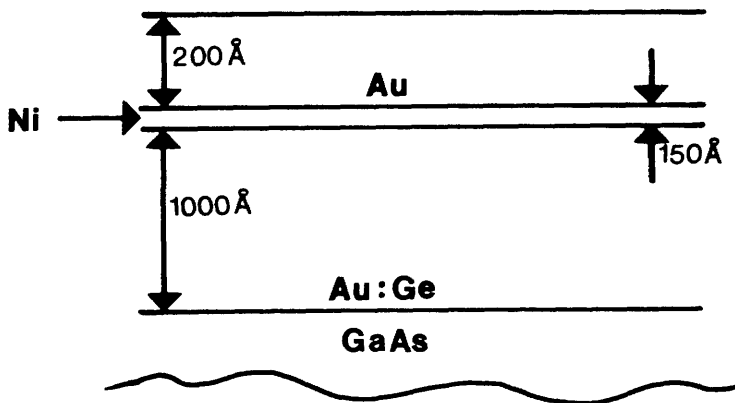
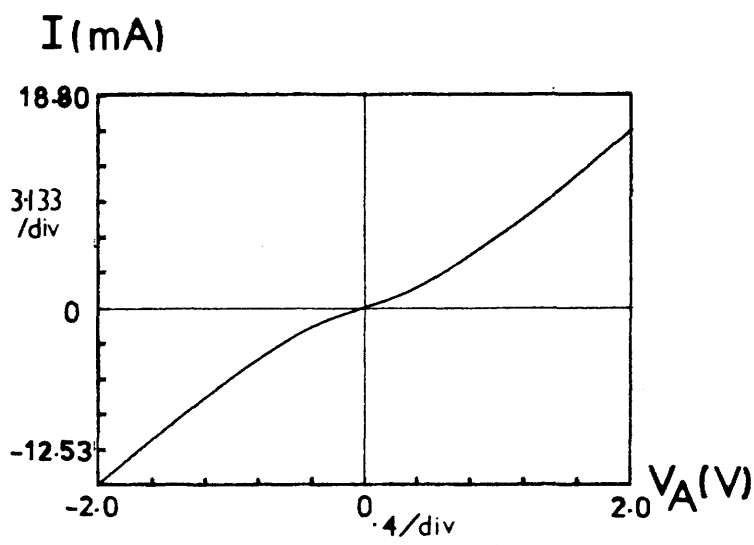
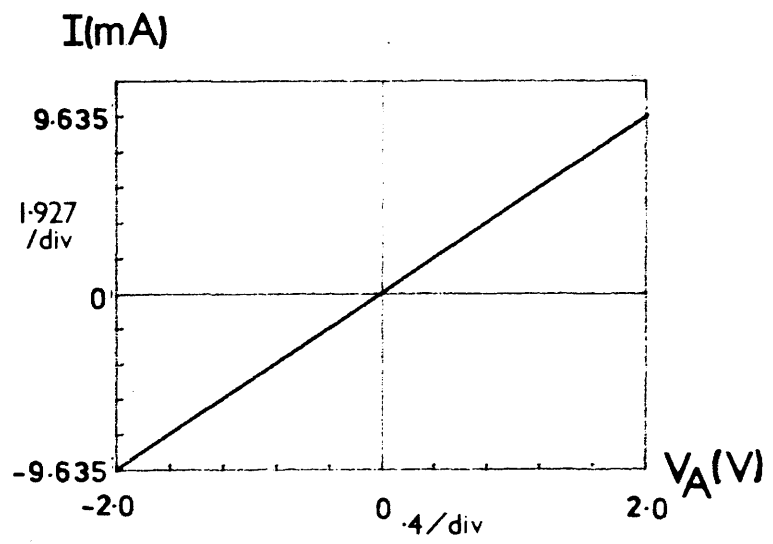


Fig 3-19 The metal layer structure and typical post-anneal I-V plot of a Au:Ge ohmic contact on n^+ GaAs.



(a)



(b)

Fig 3-20 Typical post-anneal I - V plots for ohmic contacts to p-type GaAs: (a) In:Au alloy, (b) Au:Zn:Ni alloy.

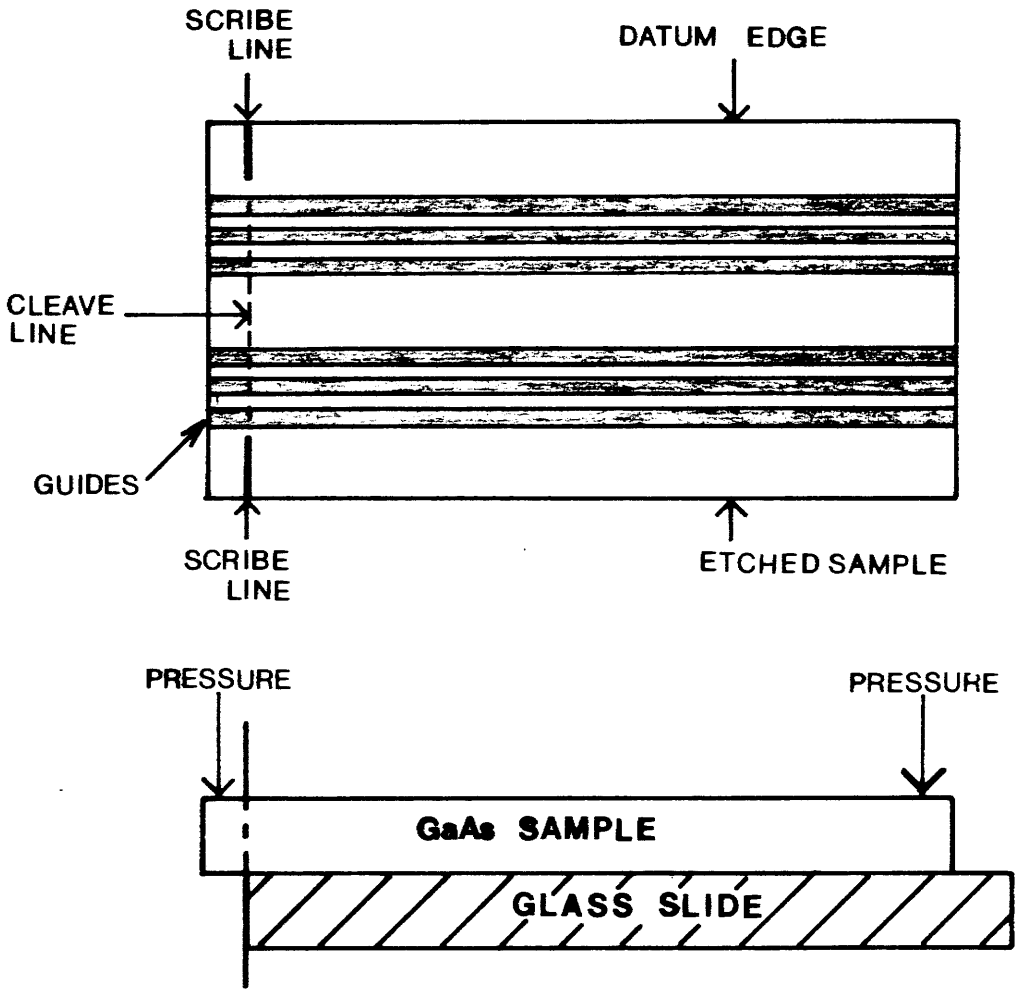


Fig 3-21 A schematic diagram of the technique used to cleave good end facets on GaAs waveguide samples.

been cleaved along crystallographic cleavage planes, it was placed on the scribing machine using an edge of the sample as reference, and with guides uppermost. Two scribe lines were then made, running up to the guide pattern but not touching it. Placing the sample - still guides uppermost - on a glass microscope slide, the scribe lines could be used to align the sample with the edge of the slide. Gentle application of pressure to the side overhanging the slide, while holding the sample steady at the other end, resulted in a cleave line running from one scribe line to the other. This process was reproducible, and could produce good smooth facets on samples down to 0.5mm long.

3.4 WAVEGUIDE ANALYSIS SYSTEM

The optical properties of the fabricated waveguides had to be analysed. This involved the coupling of light of the desired wavelength into and out of the waveguides, and the detection of the transmitted power. For the analysis of active waveguides, some method of applying an electrical signal to the waveguides had to be available.

There are several methods of coupling light into dielectric waveguides. Light can be coupled in by the prism-coupling method'. However, this requires prisms of higher refractive index than the guide, and in the case of GaAs waveguides there are no materials that are transparent over the desired wavelength region and have a higher index than GaAs. Grating couplers could be used for planar guide structures', but the facilities to fabricate such gratings for the 0.85 μ m-1 μ m region were not available. Cleaving and end-fire coupling remain the simplest and easiest techniques for studying the waveguiding properties of GaAs and related crystals. It was this method that was used throughout the work reported in this thesis, and the equipment used to achieve coupling will be described below.

Obtaining near infrared light of the required wavelength was found to be no trivial task. GaAs waveguides are normally studied at $\lambda=1.15\mu$ m and $\lambda=1.5\mu$ m, wavelengths where suitable gas lasers exist. However, to probe the novel optical and electro-optical properties of (Al,Ga)As MQWS, an optical source - ideally a tunable source - had to be found in the $\lambda=0.85-0.9\mu$ m region. Fortunately within the last few

years Styryl-9 (a dye that lases in just this region) has become available²². Obtaining satisfactory performance from a Styryl-9 dye-laser system took up a disproportionate part of the time allocated to this project. The dye-laser system and the dye itself are described below.

3.4.1 End-Fire Coupling System

In end-fire coupling the conversion of the energy in a laser beam into a waveguide mode is achieved by matching the beam's field profile to that of the guided mode. The fundamental mode of a planar or stripe waveguide has a modal field profile very similar to the Gaussian shape of a laser beam. The required field matching can therefore be affected by suitably reducing the input beam so as to conform as closely as possible to the guide mode field profile.

In theory then, the coupling efficiency of this method is only limited by the amount of incident power reflected from the perfect air/dielectric interface. However, in practice any mismatch in profiles will lose energy into radiation modes, and facet damage will increase losses. Also, because the waveguide cross-section has dimensions of the order of $1\mu\text{m}$, input beam position is critical and requires sensitive micromanipulation.

Two trinocular metallurgical microscopes were coaxially mounted on an optical bench, and a red alignment laser was aligned centrally through them (Fig 3-22). The objective turrets, containing 10X, 20X, 50X and 80X objectives, allowed the size of the beam incident on a given guide to be varied to maximise coupling. The eyepieces of the microscopes could be used to ensure that the alignment laser was incident on the desired waveguide. Beams from a $1.15\mu\text{m}$, 1.5mW HeNe laser and a Styryl-9 dye-laser were aligned with the red alignment beam.

Samples were placed on an arm attached to a rotation and translation stage assembly which was positioned between the microscopes (Fig 3-23). This allowed precise positioning of waveguides relative to the laser beams. A long working distance, zoom, stereo microscope allowed the top of the sample to be observed as a probe was lowered onto any active devices.

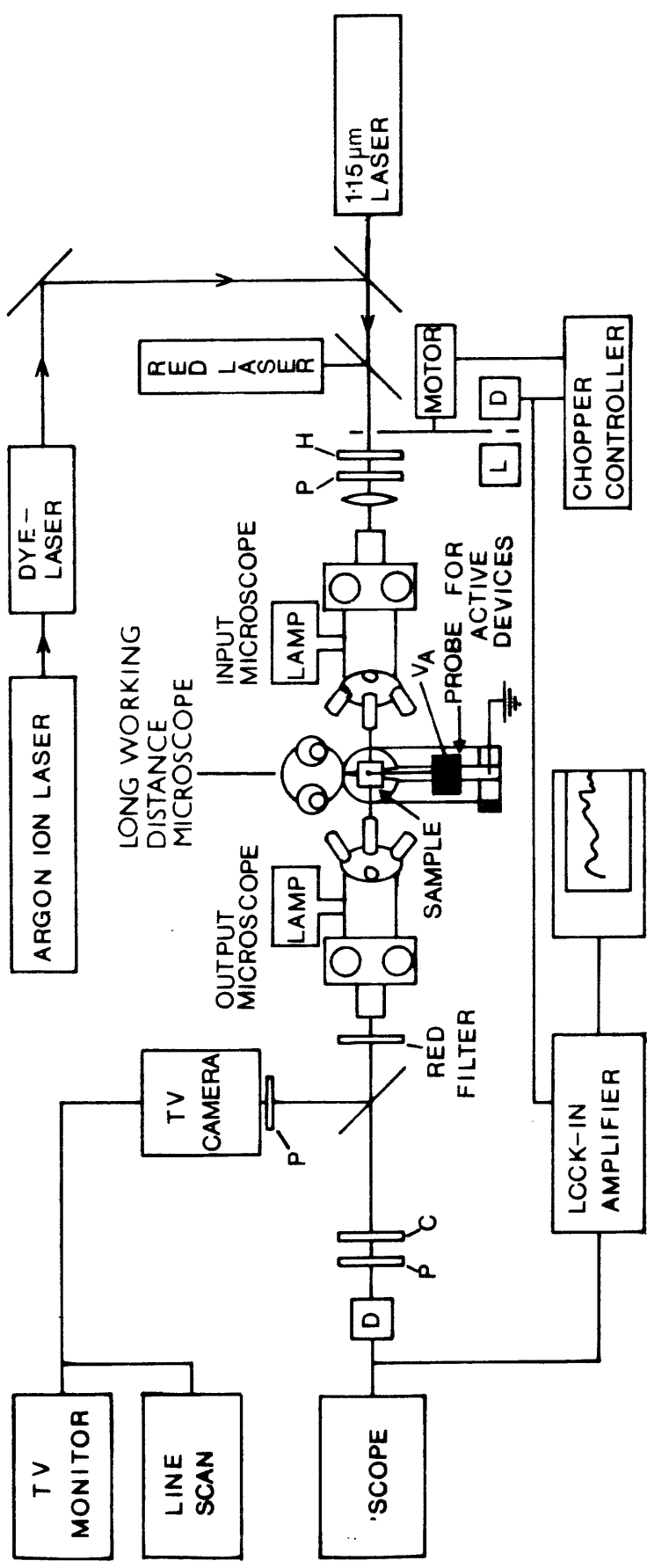


Fig 3-22 The end-fire coupling system

D : photodiode

L : LED

P,C,H : various positions for polarisers, compensators and half-wave plates.

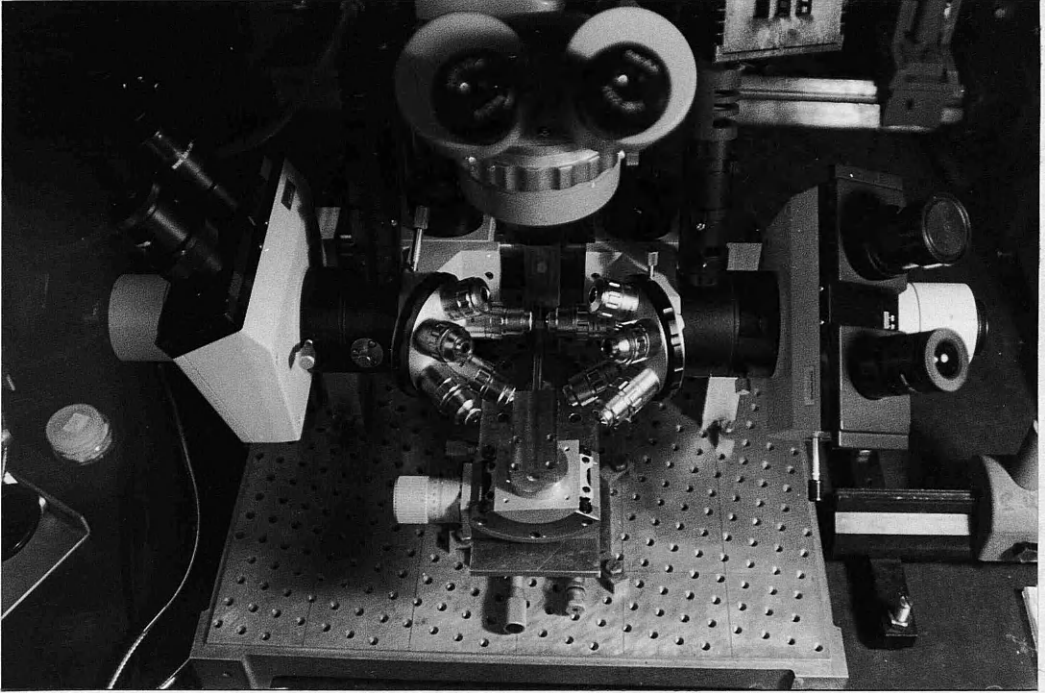


Fig 3-23 A close-up view of the stage assembly, input-output microscopes and zoom, observation microscope in the end-fire coupling system.

The near field pattern of the guided modes could be observed using an infrared camera with a line scan allowing intensity profiles to be taken. Transmitted power was detected by a germanium or silicon photodetector depending on the source wavelength - the linearity of the detectors having been checked.

To increase the signal to noise ratio the laser beam could be mechanically chopped and the detected signal sent to either a narrow-pass-band amplifier or a lock-in amplifier, both of which could drive a chart recorder.

This system thus provided a flexible, general usage, GaAs waveguide analysis system, the three microscopes providing precise visual alignment of waveguides with lasers of a range of wavelengths suitable for analysing (Al,Ga)As waveguides.

3.4.2 Dye-Laser System

The dye-laser system used to obtain a tunable near-infrared laser source will now be described. Although it was realised at an early stage in this project that a Styryl-9 dye-laser would be necessary, it was not until the middle of the project's second year that a dye-laser became available. This had been running at visible wavelengths using Rhodamine 6G dye (R6G). The change over from Rhodamine to Styryl-9 (S9) took far longer than anticipated, and the whole system was found to be unreliable and unstable. Many set backs, such as the plasma tube of the pump laser breaking (twice), meant that the system was not running as initially envisaged until as late as April 1986.

Laser

The dye-laser system consisted of an Argon ion gas laser (Spectra Physics model 165) lasing on all lines and pumping a linear dye-laser (Spectra Physics model 375). The output power of the laser system was stabilised using a Spectra Physics model 373 Dye Laser Amplitude Stabiliser. This monitors the output of the dye-laser and feeds back a control signal to adjust the pump power such that the output power is constant. It can thus maintain a constant output power as the dye-laser is scanned.

Argon lasers emit in the blue-green region of the spectrum with two dominant lines at 488nm and 514nm.

The dye-laser is based on a three mirror, folded, standing wave, cavity design (Fig 3-24). A fourth mirror focuses the incoming pump laser beam into a high velocity horizontal dye jet. This jet is placed at Brewster's angle with respect to the dye-laser beam to minimise intracavity reflection losses. Upon excitation with the intense pump beam, a population inversion between the ground and first excited state of the complex, organic dye molecules is achieved. The dye solution can then act as a gain medium for amplification of the spontaneous emission (fluorescence) of dye molecules returning to the ground state. Since this relaxation takes place into a quasi-continuum of ground state vibrational levels, the fluorescence has a continuous nature, and laser action can be obtained over a broad wavelength range. By inserting a wavelength selective element in the large intracavity space near the output coupler (Fig 3-24), the dye-laser can be tuned over this wavelength range. The high velocity jet restricts the flight time of dye molecules through the pump beam to less than a microsecond, which is long compared to the fluorescence process, but short compared to other processes like phosphorescence that would reduce the dye-laser efficiency.

The first stage in changing the dye-laser from R6G to S9 was to change the mirrors that form the cavity to ones designed for S9 lasing wavelengths. A tunable wedge was used to tune the dye-laser with a band width of 240GHz. Tuning was accomplished by translating this thin film interference wedge across the intracavity beam. Although specified to 900nm, it was found that the physical limit of tunability using this element was 880nm. Dye output power was also found to be very low, peaking at 150mW with new dye and 5W pump power. The low output power was partly a result of the low pump pressure (40psi) being produced by the old dye pump. S9 is reported to increase its output power with pump pressure for pump pressures up to 120psi²³. Therefore a new dye pump capable of these pressures, and a new birefringent filter tuning element, were obtained. The birefringent filter is an uncoated, Brewster's angle tuning element. As a result, it is low-loss and can be used up to $\lambda=1000\text{nm}$. Wavelength tuning is achieved by rotating the plates around an axis normal to the plates. With 120psi pump pressure and a two-plate birefringent filter (60GHz

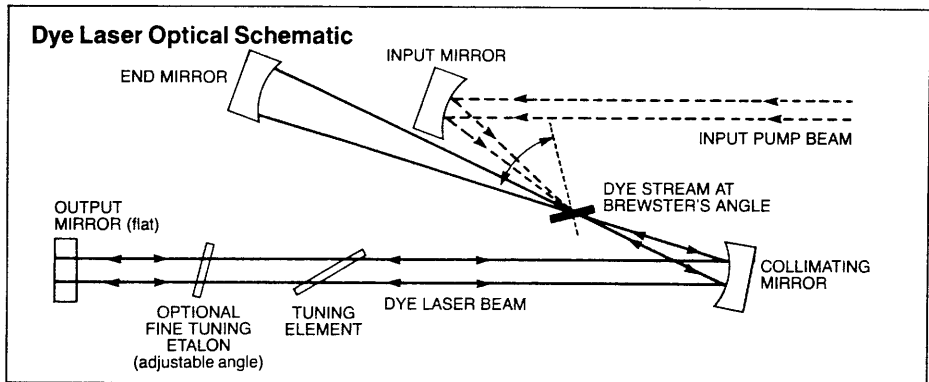


Fig 3-24 A schematic diagram of the three mirror, folded, standing wave, cavity of the dye-laser.

line width) the peak power with new dye was found to be 600mW with 5W pump power with an upper tuning limit of 910nm due to the dye. It was in this final state that the laser was used for the final experiments on MQW waveguides described in chapters six to eight.

The system was found to be mechanically unstable with sudden drops in dye output power taking place from day to day. These drops in power resulted in a restricted dye tuning curve. Eventually the dye-laser and pump laser were securely mounted on a separate, rigid bench placed on top of the main table to ensure that no relative movement between the two took place. However, sporadic slight fluctuations in the dye jet shape still occurred, causing sudden alterations in the alignment conditions of the dye-laser, and reducing output power.

Dye

Laser dyes are organic compounds consisting of an extended system of carbon atoms with alternating single and double bonds (a conjugate system). In a conjugate system the π bonds formed in a double bond can easily switch between adjacent C-C bonds. A well-known example of a conjugate system is benzene.

The free moving π electrons effect the spectroscopic properties of conjugate compounds. Organic laser dye molecules have an energy level structure of the form shown in Fig 3-25(a). G and S_1 are the ground state and first excited singlet state. T_1 and T_2 are triplet states. Because they are spin-forbidden, transitions between a singlet and triplet state are much less likely to occur than a singlet-singlet or triplet-triplet transition.

Each singlet or triplet state is split into vibrational substates which are further split into rotational sublevels, all of which are broadened, producing the practically continuous emission and absorption spectra of the dye molecule.

Upon absorbing a photon from a pump laser beam, a dye molecule is excited to a sublevel in the first excited singlet state, S_1 . A radiationless decay quickly occurs to the lowest S_1 sublevel through collisions with solvent molecules. Within nanoseconds, the majority of dye molecules will have decayed spontaneously to a sublevel in the

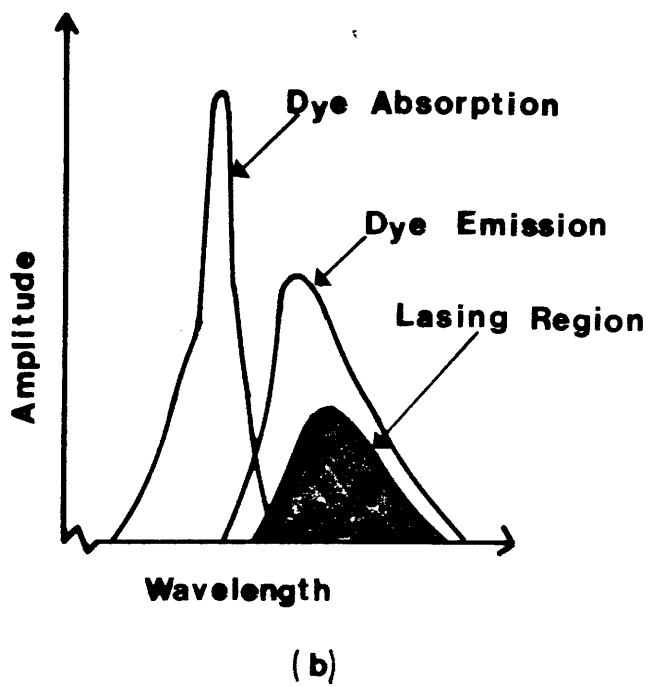
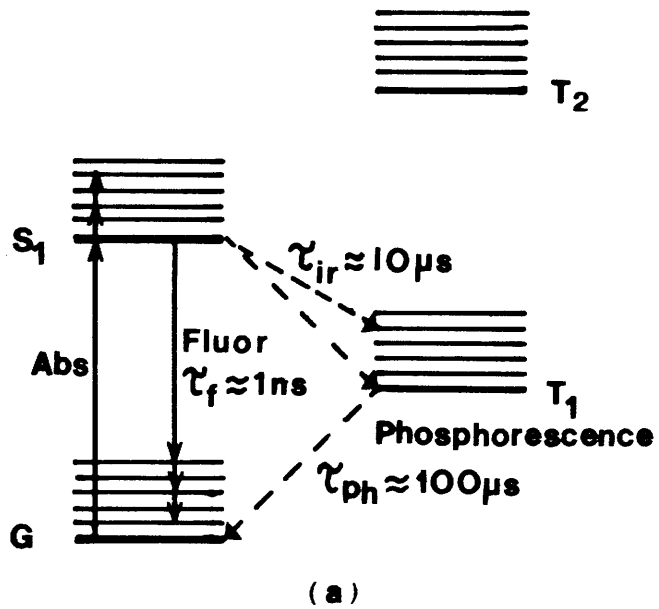


Fig 3-25 The energy levels of an organic laser dye (a) and the corresponding absorption and emission spectra (b).

ground state, emitting a photon. This radiative transition is called fluorescence, and takes place at a photon energy less than the pump laser's photon energy. Fig 3-25(b) shows the absorption and emission spectra, with a Stoke's shift being evident between them.

Other forbidden transitions (such as $S_1 \rightarrow T_1$) can occur and these will tend to reduce the dye's optical efficiency. These transitions take longer than the desired transition, and are therefore minimised by keeping the pump pressure high so that the dye is in the pump beam for as short a time possible.

Styryl-9 is a dye capable of operating with an Argon or Krypton gas pump laser. With a molecular weight of 460 it has a peak laser power at 843nm and is tunable from 790-910nm. The dye itself was dissolved in a solution of Propylene Carbonate (PC) and Ethylene Glycol (EG) in the ratio 85:15, EG:PC (V/V). Peak output power was experimentally found to vary linearly with the dye concentration from the 0.6g/l recommended by Lambda Physik to the 0.92g/l of Spectra Physics. Since dye lifetime could be shortened by excessive pump beam absorption, concentrations above 0.9g/l were not attempted. An experimentally obtained dye tuning curve is plotted in Fig 3-26.

Dye output power was found to decrease steadily over the first 10-14 days of use, and then level out at approximately 60% of the fresh dye power. This is rather more than the 15% drop quoted by Spectra Physics²⁴.

3.5 CONCLUSIONS

The Modified Effective Index Method and the WAVE variational method are two complimentary techniques for the design of ridge and strip loaded waveguides in semiconductors. These designs can then be implemented using standard photolithographic techniques and dry etching. Coupling of light into stripe waveguides is easiest by end-fire coupling which allows the analysis of optical properties of active and passive, planar and stripe waveguides over a range of wavelengths. To allow the waveguide properties of (Al,Ga)As waveguides to be examined at a variety of wavelengths close to their band gap, a Styryl-9 dye-laser system was developed.

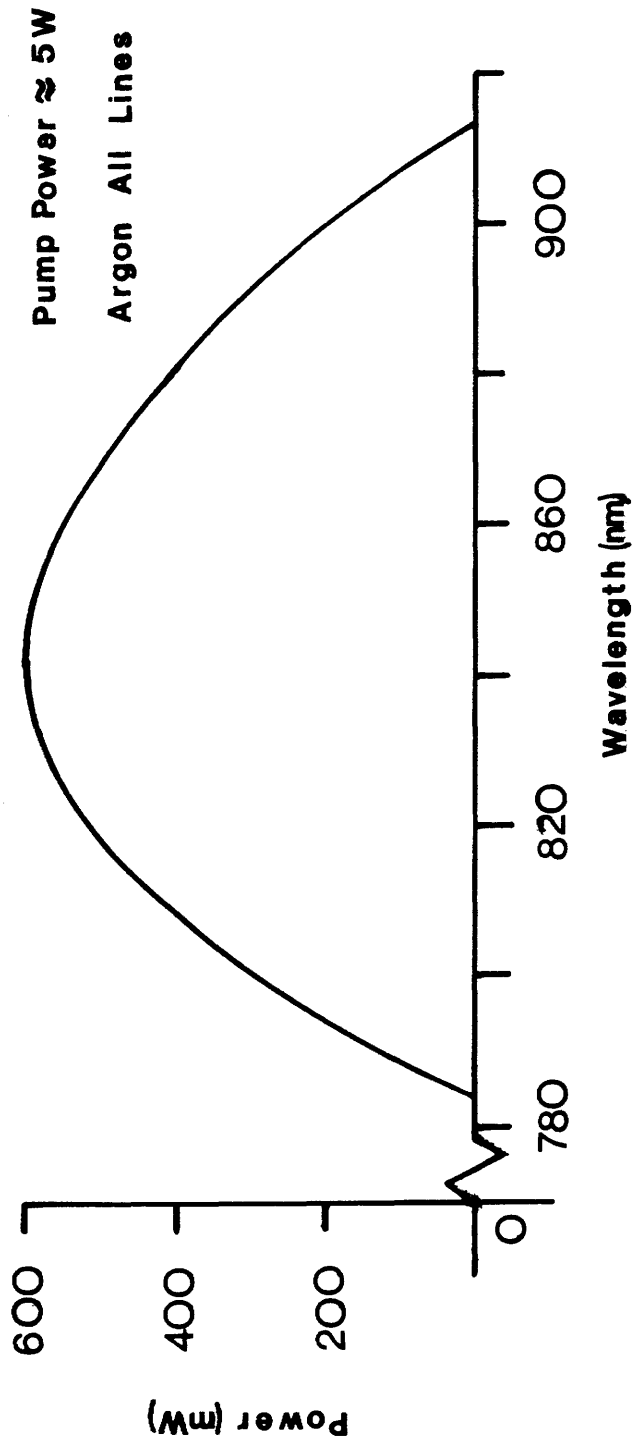


Fig 3-26 The output power obtainable from the Styryl-9 dye-laser as a function of wavelength.

References to Chapter Three

- 1 T. Tamir (ed.);
Topics in Applied Physics Vol. 7: Integrated Optics (Springer-Verlag, New York, 1975).
- 2 H. Kogelnick and V. Ramaswamy;
"Scaling Rules for Thin-Film Optical Waveguides", *Appl. Optics* **13**, 1857 (1974).
- 3 N. Uchida, O. Mikami, S. Uehara and J. Noda;
"Optical field distribution in a waveguide loaded with high refractive index film; modulation efficiency improvement in a planar-type modulator", *Appl. Optics* **15**, 455 (1976).
- 4 S. T. Peng and A. A. Oliner;
"Guidance and Leakage Properties of a Class of Open Dielectric Waveguides: Part I - Mathematical Formulations", *IEEE Trans. Microwave Theory Tech.* **MTT-29**, 843 (1981).
- 5 M. Koshihara and M. Suzuki;
"Equivalent network analysis of dielectric thin-film waveguides for optical integrated circuits and its application", *Radio Sci.* **17**, 99 (1982).
- 6 R. G. Walker;
"The design of ring-resonators for integrated optics using silver ion-exchanged waveguides", Ph.D. Thesis, University of Glasgow (1981).
- 7 M. Matsuhara;
"Analysis of T.E.M. Modes in Dielectric Waveguides by a Variational Method", *J. Opt. Soc. Am.* **63**, 1514 (1973).
- 8 H. F. Taylor;
"Dispersion Characteristics of Diffused Channel Waveguides", *IEEE J. Q. Electron.* **QE-12**, 748 (1976).
- 9 O. Auchiello and R. Kelly (ed.);
Beam modifications of materials, Vol.1: Ion bombardment modification of surfaces (Elsevier, Oxford, 1984).
- 10 B. Chapman;
Glow Discharge Processes, Sputtering and Plasma Etching (John Wiley & Sons, New York, 1980).
- 11 W. Kern and C. A. Deckert;
Thin Film Processes (Academic Press, Inc., 1978).

- 12 A.J.N.Houghton, D.A.Andrews, G.J.Davies and S.Ritchie;
 "Low-loss optical waveguides in MBE-grown GaAs/GaAlAs heterostructures", Opt. Comm. **46**, 164 (1983).
- 13 K.Hiruma, H.Inoue, K.Ishida and H.Matsumura;
 "Low loss GaAs optical waveguides grown by the metalorganic chemical vapor deposition method", Appl. Phys. Lett. **47**, 186 (1985).
- 14 P.Buchmann, H.Kaufmann, H.Melchior and G.Guekos;
 "Reactive ion etched GaAs optical waveguide modulators with low loss and high speed", Electron. Lett. **20**, 295 (1984).
- 15 A.P.Webb and C.D.W.Wilkinson;
 "Ion beam etching GaAs for integrated optical applications", Vacuum **34**, 159 (1984).
- 16 M.B.Stern and P.F.Liao;
 "Reactive ion etching of GaAs and InP using SiCl₄", J. Vac. Sci. Tech. B **1**, 1053 (1983).
- 17 J.Z.Li, I.Adesida and E.D.Wolf;
 "Orientation dependent reactive ion etching of GaAs in SiCl₄", Appl. Phys. Lett. **45**, 897 (1984).
- 18 J.Z.Li, I.Adesida and E.D.Wolf;
 "Evidence of crystallographic etching in (100)GaAs using SiCl₄ reactive ion etching", J. Vac. Sci. Tech. B **3**, 406 (1985).
- 19 E.H.Rhoderick;
Monographs in electrical and electronic engineering: Metal-Semiconductor Contacts (Clarendon Press, Oxford, 1980).
- 20 V.L.Rideout;
 "A review of the theory and technology for ohmic contacts to group III-V compound semiconductors", Sol. St. Electron. **18**, 541 (1975).
- 21 W.Patrick, W.S.Mackie, S.P.Beaumont and C.D.W.Wilkinson;
 "Low-temperature annealed contacts to very thin GaAs epilayers", Appl. Phys. Lett. **48**, 986 (1986).
- 22 J.Hoffnagle, L.Ph.Roesch, N.Schlumpf and A.Weis;
 "CW operation of laser dyes Styryl-9 and Styryl-11", Opt. Comm. **42**, 267 (1982).
- 23 Spectra Physics commercial data.
- 24 *Continuous-Wave Dye Lasers Properties and Performance Reports*, Laser Products Division, Spectra Physics.

CHAPTER FOUR
GaAs WAVEGUIDES

4.1 INTRODUCTION

The design and fabrication techniques and the waveguide analysis system described in chapter three were developed over an extended period. As a practical project to aid their development, it was decided to apply the techniques to the design, fabrication and testing of one of the simplest forms of waveguide in the (Al,Ga)As system - the n/n⁺ GaAs waveguide. This project allowed the waveguide models to be used in a practical context, it allowed the practical skills of photolithography and dry etching to be evaluated against actual waveguide characteristics, and it tested the adequacy of the end-fire system.

One of the fundamental properties of a waveguide is its propagation loss. By measuring the propagation loss of a well-understood waveguide structure such as n/n⁺ GaAs waveguides it was possible to compare the experimental results with results in the literature and hence check the validity of loss measurement methods that would later be used with MQW waveguides.

Another important property of semiconductor waveguides is the presence of an electro-optic effect. It was planned to measure this effect in MQWS waveguides. Measuring the same effect in GaAs allowed the measurement methods to be tested and a result to be obtained with which the MQWS results could be directly compared.

4.2 DESIGN AND GROWTH

A very simple form of semiconductor waveguide is that produced from a low n-doped (n) layer of GaAs on a high n-doped (n⁺) substrate. Waveguiding occurs due to the contribution made by free electrons to the refractive index of a semiconductor. The higher the free carrier concentration in a semiconductor the lower its refractive index.

4.2.1 Refractive Index

In a semiconductor with N free carriers per unit volume, the change in refractive index due to free carriers is¹:

$$\Delta n = -N\lambda^2 e^2 / (\epsilon_0 n^3 \pi^2 m^* c^2) \quad (4.1)$$

where n is the refractive index of the carrier-free semiconductor at free space wavelength λ , e is the charge on the carrier and m^* is the carrier's effective mass.

The small effective mass of electrons in GaAs ($m^*=0.067m_0$) makes this free carrier contribution large². In other semiconductors, and p-doped GaAs, the effect is much smaller. At $\lambda=1.15\mu\text{m}$ undoped GaAs has refractive index³ $n=3.4406$. Substituting these values in (4.1) one obtains:

$$\Delta n = -2.5819 \times 10^{-21} \cdot N \quad (4.2)$$

where N is in units of cm^{-3} .

There are several ways of producing a n/n^+ waveguide in GaAs, including diffused and ion-implanted waveguides¹. However, the waveguide layers that were made available for this project were obtained by growing epitaxial n-type GaAs on a n^+ -type GaAs substrate. These structures are readily available commercially since they are the same as those used for Gunn oscillators and FETs.

As has been mentioned, these waveguides are well-understood with waveguiding having been observed and cut-off measured at $1.15\mu\text{m}$ in such epitaxial structures as long ago as 1970⁴. In these experiments, Δn was shown to be consistent with that expected from (4.1), and epitaxial layers of several microns thick showed propagation loss of less than 4dBcm^{-1} in the near infrared.

4.2.2 Single-Mode Condition

If the carrier concentration of the film (N_F) is less than approximately 10^{16}cm^{-3} (see equation 4.2) then its refractive index can be considered as that of undoped GaAs. This reduces the design

parameters to the substrate carrier concentration and the film thickness. However, the n⁺ substrates commercially available have a donor concentration (N_s) that is limited to the region 1-5x10¹⁸cm⁻³. Fig 4-1 plots the TE modal effective index (n_e) against film thickness (t₂) for the three layer structure at λ=1.15μm for two values of substrate carrier concentration within this range. Fig 4-2 plots the cut-off thicknesses (τ₀ and τ₁) of modes TE₀ and TE₁ as a function of doping concentration. As the doping level of the substrate increases, waveguide confinement becomes stronger, n_e increases, and τ₀ and τ₁ decrease, becoming closer. For a given doping level the waveguide confinement gets stronger as the layer thickness (t₂) increases. In most integrated optical applications single-mode waveguiding is required, and so substrate doping and epitaxial layer thicknesses must be chosen to lie between curves τ₁ and τ₀ of Fig 4-2.

4.2.3 Propagation Loss Criterion

Another requirement of an optical waveguide is that it should have a low propagation loss. At λ=1.15μm, far from the band gap of GaAs, the primary contribution to loss is free carrier absorption². If the guided light is well confined in the n-type epitaxial layer, free carrier loss will be negligible. However, as waveguide confinement becomes poorer, losses due to the substrate's free carriers can become substantial. The free carrier loss of GaAs at room temperature for 1μm < λ < 3μm varies approximately as²:

$$\alpha = 3 \times 10^{-18} \cdot N \text{ npr cm}^{-1}$$

where N, the free carrier concentration, is in units of cm⁻³. The propagation loss of a n/n⁺ waveguide can thus be approximated by calculating the proportion of the modal power present in the substrate layer, and weighting this with the free carrier loss in the substrate¹.

The three layer waveguide model defines the modal field profile for TE modes (see Fig 4-3) as:

$$\begin{aligned}
 E_x(z) &= C \cdot \exp(-qz) & z > 0 \\
 &C \cdot [\cos(hz) - (q/h) \sin(hz)] & -t_2 < z < 0 \\
 &C \cdot [\cos(ht_2) + (q/h) \sin(ht_2)] \cdot \exp(p(z+t_2)) & z < -t_2
 \end{aligned}$$

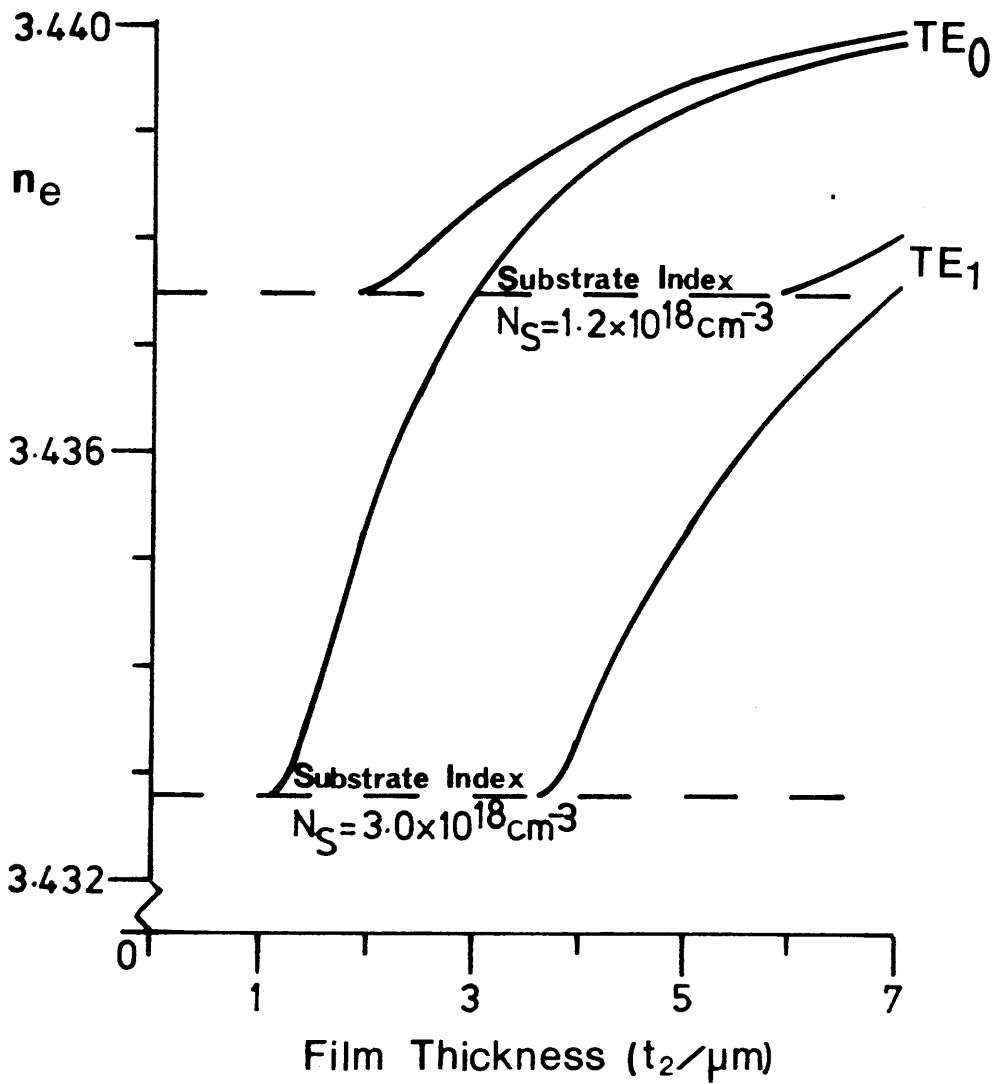


Fig 4-1 TE modal effective index (n_e) versus film thickness for two substrate donor concentrations (N_S).

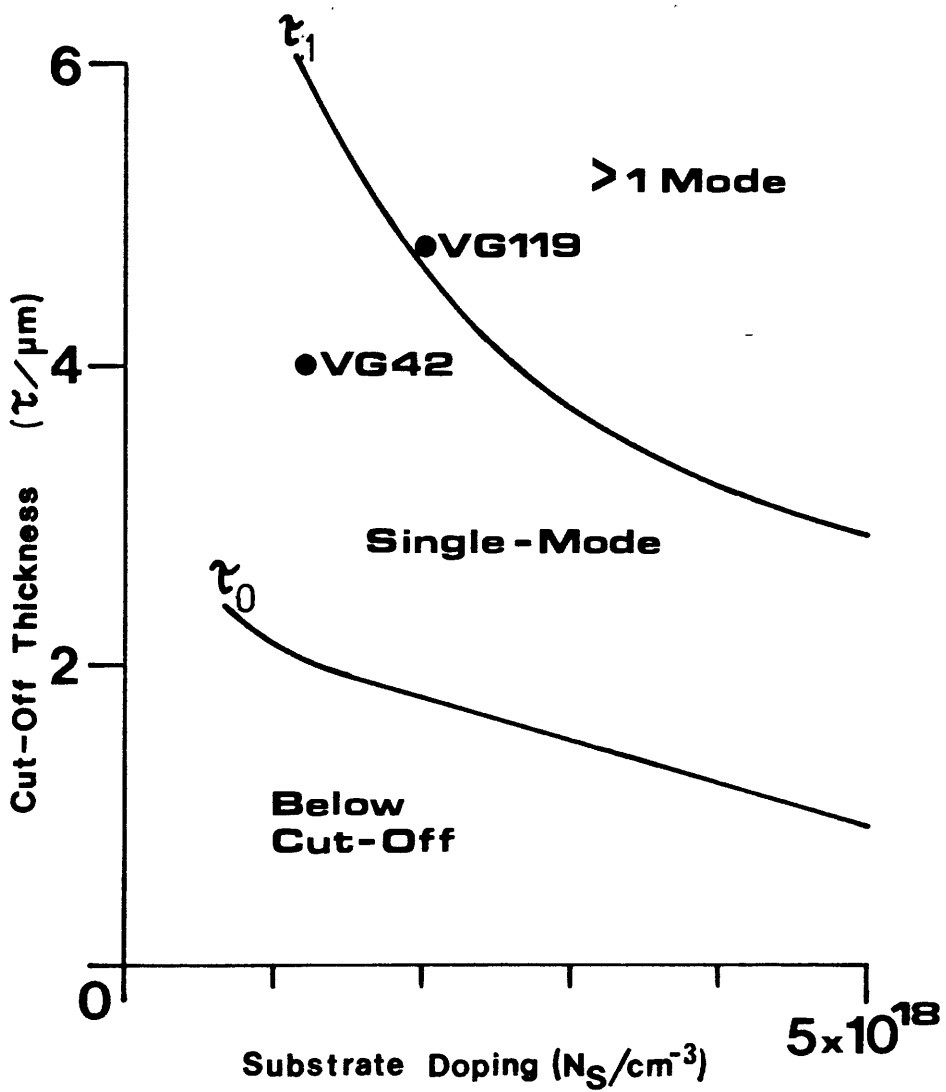


Fig 4-2 The cut-off thickness of the TE_0 (τ_0) and TE_1 (τ_1) modes versus substrate donor concentration (N_S).

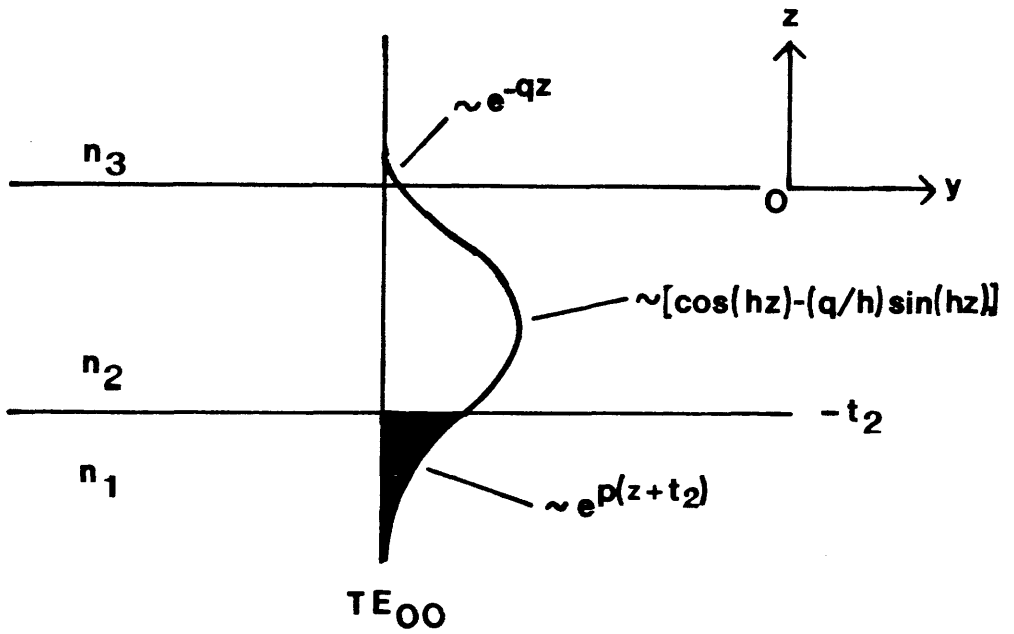


Fig 4-3 The functional form of the modal field profile of the three layer planar structure.

where C is defined such that $\int_{-\infty}^{+\infty} E_x^2 dz = 1$. This results in the expression:

$$C = 2^{1/2} h \cdot [(t + (1/q) + (1/p)) \cdot (h^2 + q^2)]^{-1/2}$$

The proportion of the power in the substrate is thus:

$$\int_{-\infty}^{-t_2} E_x^2(z) dz = c^2 [\cos(ht_2) + (q/h) \sin(ht_2)]^2 / 2p$$

where $h = k_0 (n_2^2 - n_e^2)^{1/2}$, $q = k_0 (n_e^2 - n_3^2)^{1/2}$,
 $p = k_0 (n_e^2 - n_1^2)^{1/2}$, $k_0 = 2\pi/\lambda$

Using this model to calculate the estimated propagation loss of the TE₀ mode as a function of doping concentration and guide thickness, one obtains the results shown in Fig 4-4. From this it is clear that the dominant factor in determining the propagation loss of a n/n⁺ waveguide is its thickness. For a given substrate carrier concentration, the estimated propagation loss drops quickly as t₂ varies from 2 to 6 μm. By the point t₂=6 μm, the fundamental mode is well confined and the propagation loss has settled at approximately 2dBcm⁻¹ or less. The change in propagation loss with substrate doping is less dramatic, with an increased substrate doping slightly reducing the propagation loss through an increase in the confinement of the guided mode.

To model the propagation loss more accurately, the n/n⁺ waveguide structure was analysed using a complex dielectric constant to model the substrate. A computer program developed by Mr. D. F. Clarke, following the work of Suematsu et al⁵ gave results identical to those given in Fig 4-4, indicating the value of the simple "weighted loss" calculation.

Combining the results of Fig 4-4 with the requirement for a single mode structure would suggest the growth of a thick epitaxial layer on a relatively low doped substrate to minimise propagation loss.

4.2.4 Layer Growth

Epitaxial layer VG42 was grown on the department's Molecular Beam Epitaxy (MBE) system (see chapter five for a description of MBE). A

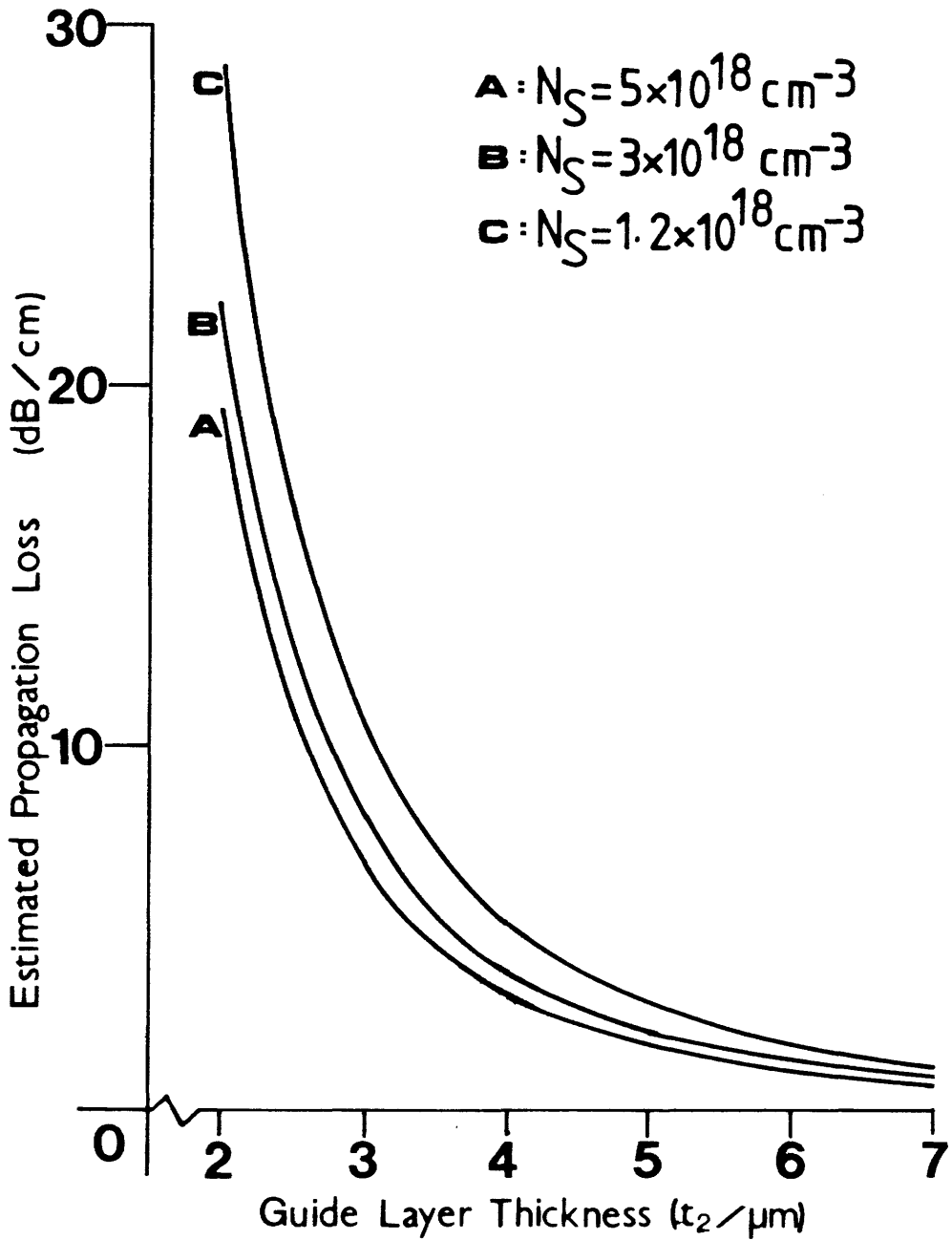


Fig 4-4 The estimated propagation loss of the TE_0 mode in an n/n^+ planar waveguide as the guide layer thickness is varied. Results from the "weighted loss" model.

4 μ m thick epitaxial layer of low doped GaAs was grown on top of a GaAs substrate with a donor concentration $N_D=1.2 \times 10^{18} \text{cm}^{-3}$. The doping profile of the epitaxial layer was measured by a polaron plotter (Fig 4-5) and found to have a free electron concentration of $8 \times 10^{15} \text{cm}^{-3}$. This placed the layer in the single-mode region of Fig 4-2 with a predicted propagation loss for the TE_0 mode of 5.0dBcm^{-1} .

The quality of epitaxial growth was checked by photoluminescence (PL). The system used to analyse semiconductors by PL is described in chapter five. Briefly, in PL the specimen semiconductor is optically pumped and the intensity of re-emitted light is then plotted as a function of wavelength. For a given semiconductor, peaks occur at characteristic photon energies, corresponding to excitonic transitions across the fundamental energy gap, between donor states etc, etc. In general the brighter and sharper the peaks in the PL data the better the quality of the material. Fig 4-6 shows the results of a low temperature PL run on VG42. Two bright, well distinguished peaks are observed at 8211Å and 8326Å, the former being assigned to a GaAs neutral donor bound exciton transition, and the latter to a free-to-bound carbon impurity transition⁶. Despite the presence of the carbon - common in MBE grown material - the material is shown to be of good quality with no deep level traps to cause optical absorption in the near infrared.

4.2.5 Ridge Waveguide Design

Most integrated optical devices require the fabrication of single-mode stripe waveguides. It was therefore necessary to obtain a design for single-mode ridge waveguides in epitaxial structure VG42. The design parameters were the guide width (W) and outer slab thickness (t) of Fig 4-7.

As an initial design aid, the Effective Index Method was used to calculate the widths at which a ridge waveguide would change from having a single transverse mode to having two or three transverse modes. Fig 4-7 plots the results of these calculations using refractive index data for VG42. Ridge structures lying below curve 1 were predicted to sustain only one lateral mode (i.e. only mode TE_{00} would be sustained) while ridge structures above curve 1 but below

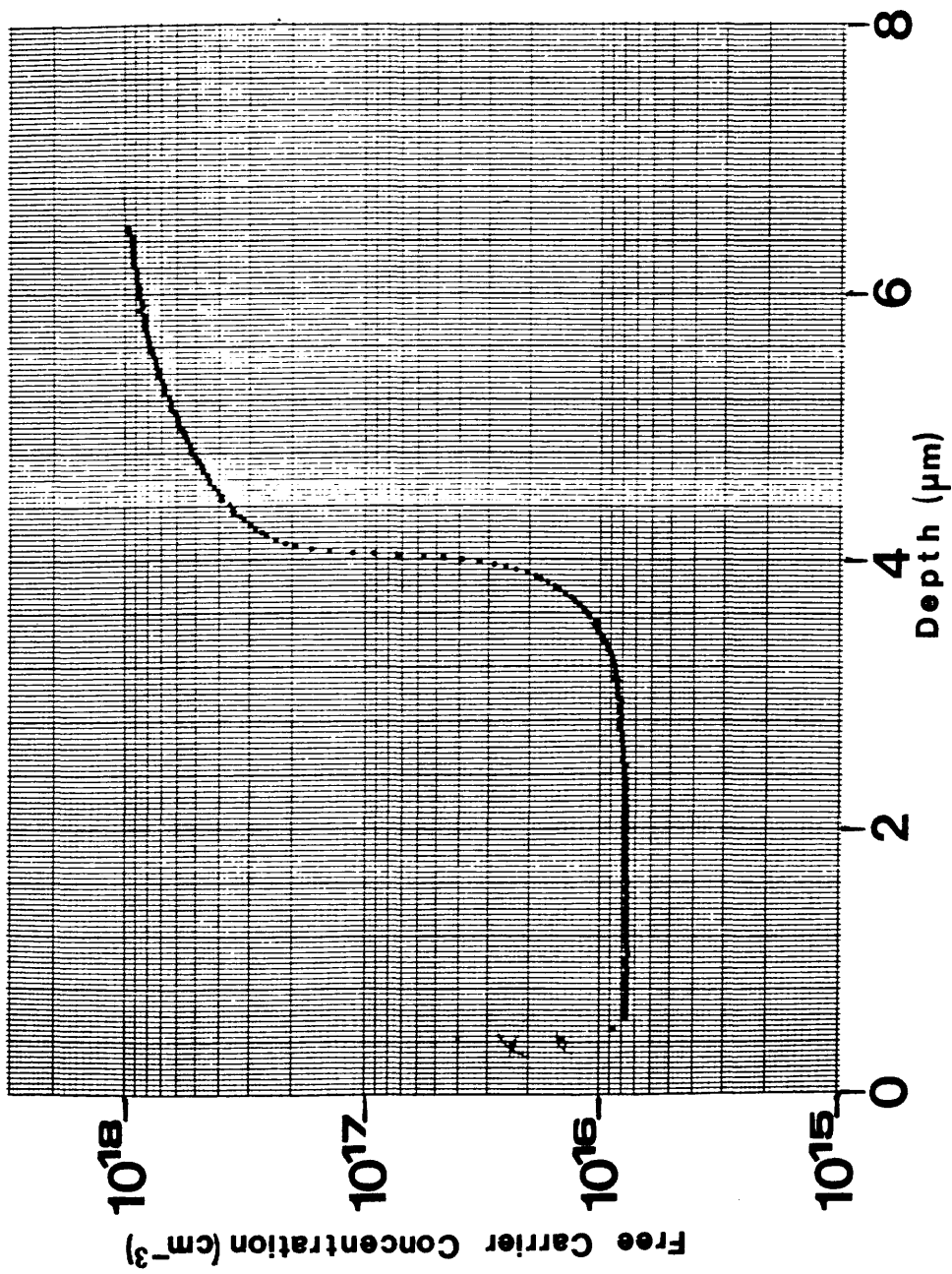


Fig 4-5 The doping profile of VG42 as determined by a polaron plotter.

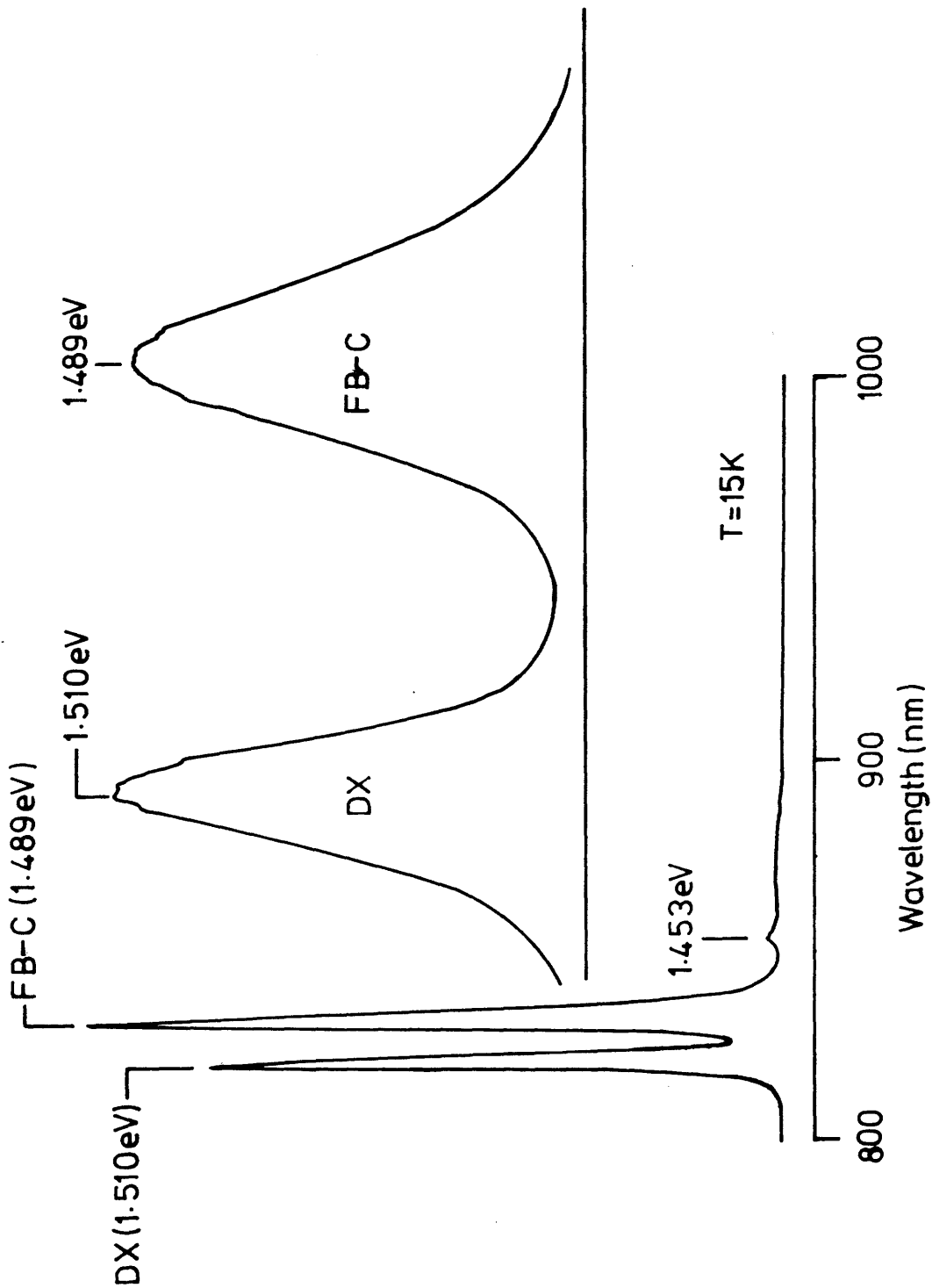


Fig 4-6 Photoluminescence data from VG42.

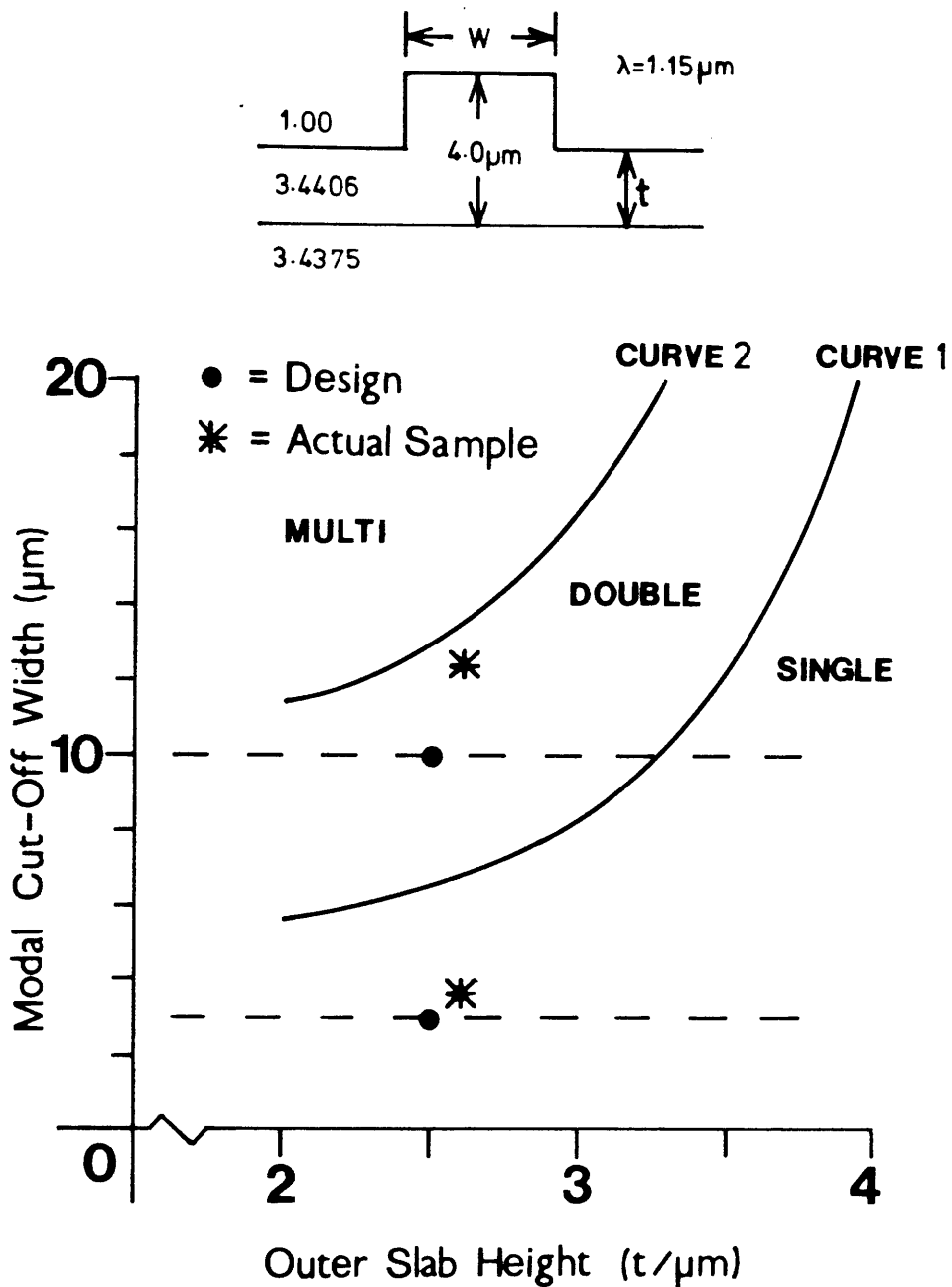


Fig 4-7

The cut-off width of the TE₁₀ (curve 1) and TE₂₀ (curve 2) modes in a n/n^* rib waveguide as the outer slab height (t) is varied.

curve 2 were predicted to sustain two lateral modes (i.e. TE_{00} and TE_{10}).

The line widths around which to design single-mode waveguides were determined by the practical consideration that a suitable light-field chrome shadow mask with nominal line widths of 3, 10 and $50\mu\text{m}$ was already available. Fig 4-7 shows that the number of modes sustainable by ridges of these widths is largely independent of etch depth, with 3, 10 and $50\mu\text{m}$ guides predicted to sustain one, two and many modes respectively until $t \geq 3.25\mu\text{m}$.

As well as straight waveguides, passive directional couplers were present on the mask, consisting of $3\mu\text{m}$ lines, $3\mu\text{m}$ apart. Applying the Modified Effective Index Method to this coupler structure, the coupling length (L_c) was calculated as a function of outer slab thickness (t). Fig 4-8 shows that for $2.3 < t < 2.5$ the coupling length's dependency on t is very low, and has reached a minimum of $L_c = 1.74\text{mm}$. It was thus decided to etch ribs with heights in this region and attempt to fabricate passive directional couplers in addition to straight waveguides.

At this stage, as a final design check, the WAVE variational method was applied to the proposed ridge structures. The number of modes predicted for the 3 and $10\mu\text{m}$ straight waveguides was found to be the same as those predicted by the Effective and Modified Effective Index Methods. The modal intensity profiles predicted by WAVE are plotted in Fig 4-9 and Fig 4-10 for the 3 and $10\mu\text{m}$ guides for $t = 2.5\mu\text{m}$. It can be seen that the $3\mu\text{m}$ guide is rather weakly guided with the mode spreading some distance on either side of the ridge. The fundamental mode of the $10\mu\text{m}$ guide is far better confined but the second mode is weakly guided.

4.3 RIDGE WAVEGUIDE FABRICATION

The substrate preparation and photoresist patterning were carried out in the standard way described in chapter three. Several samples were patterned to allow the fabrication process to be characterised before the final devices were made.

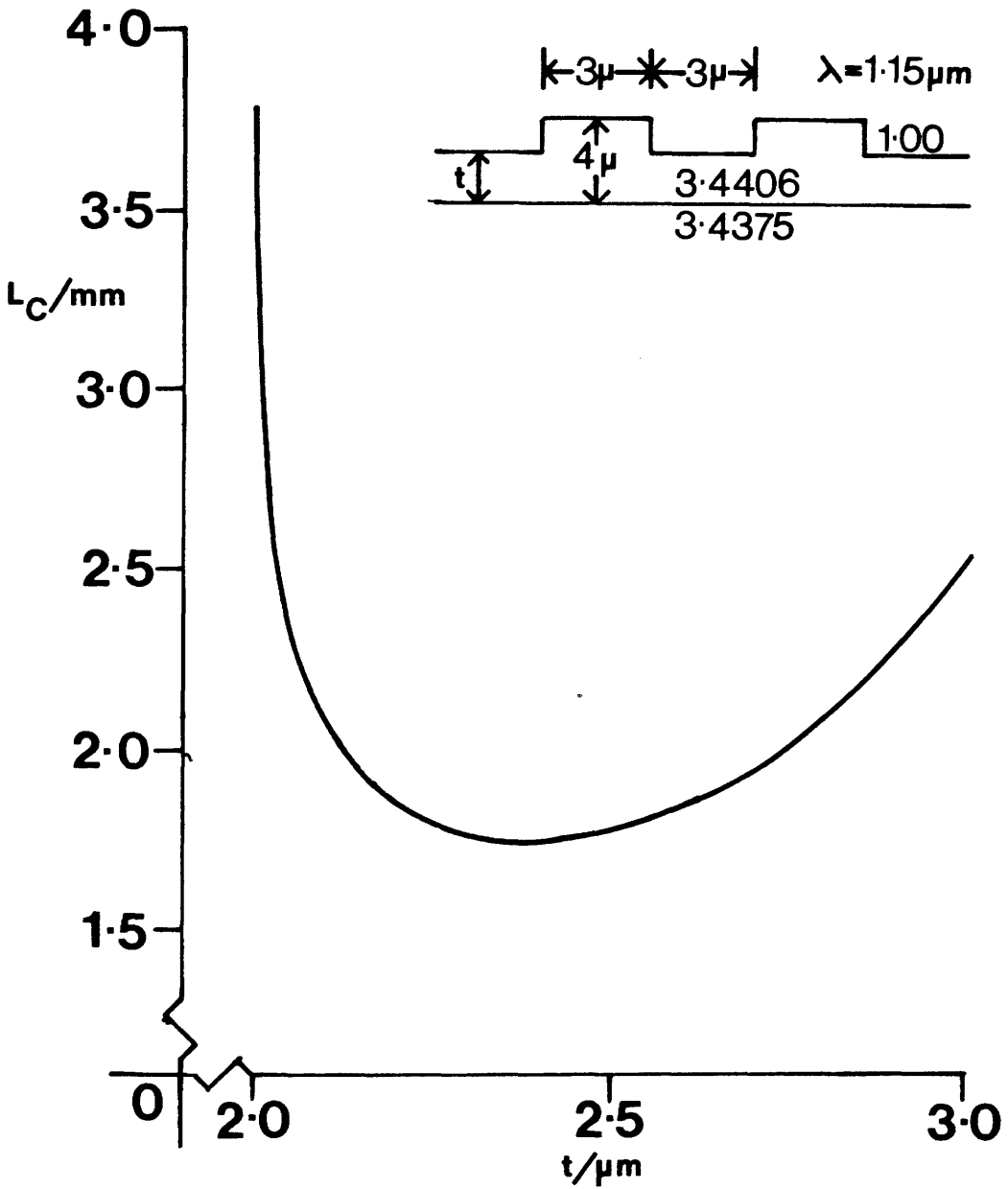


Fig 4-8 Coupling length (L_c) versus outer slab thickness (t) for a n/n^+ rib waveguide, directional coupler using the MBIM.

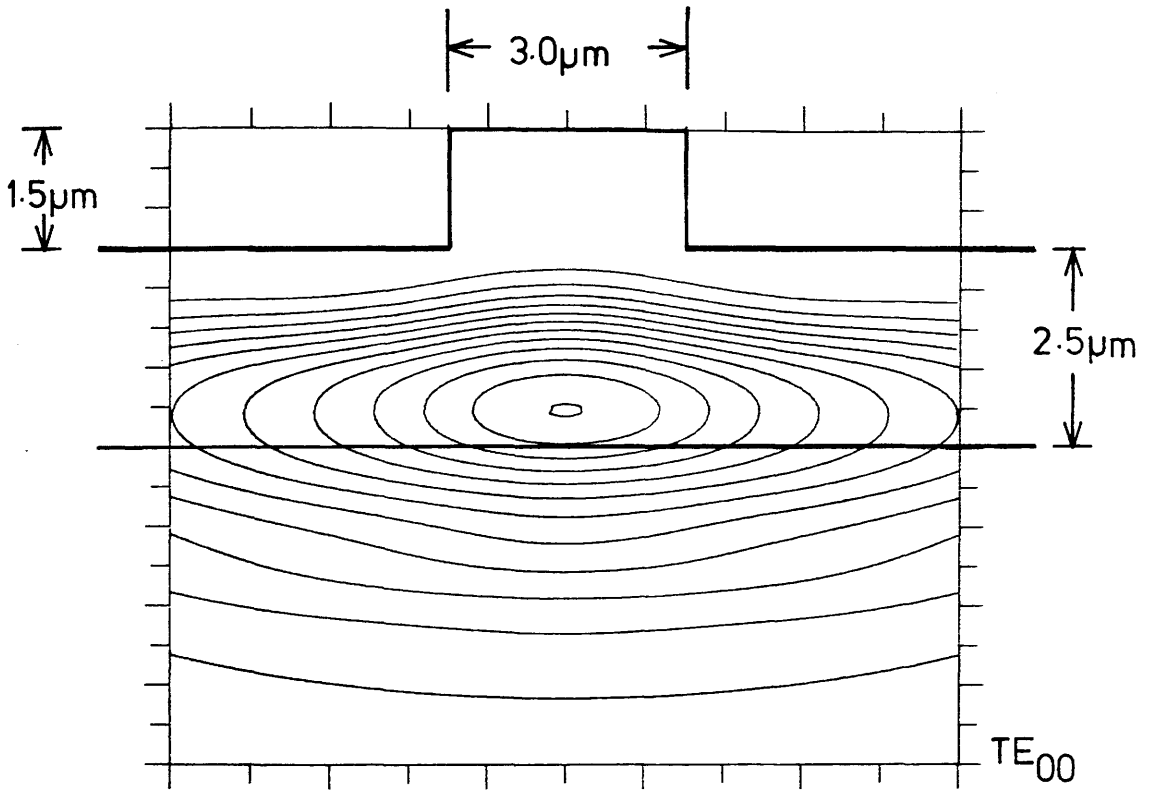


Fig 4-9 The modal intensity profile of the guided mode of a 3 μm wide rib waveguide in n/n⁺ sample VG42. As calculated by WAVE with $\lambda=1.15\mu\text{m}$.

As described in the previous chapter, dry etching had been chosen for the fabrication of semiconductor waveguides. At the time that this work was carried out, Ion Beam Etching (IBE) using the Oxford Applied Research model 2255 machine was the only dry etching technique available.

4.3.1 Etch Conditions and Procedure

The work of Webb and Wilkinson⁷ showed that well-defined ribs with rectangular profiles could be obtained in GaAs using IBE. They used ion beam current densities in the 0.3 to 0.5mAcm⁻² region, and ion beam voltages from 300 to 800 Volts. Within this range the etch rate of GaAs was found to be a slowly varying function of the beam voltage. Thus it was shown to be possible to work at relatively low power levels and still obtain a workable etch rate, thereby avoiding any problems of trying to dissipate heat away from the target being etched.

For the present work on n/n⁺ GaAs waveguides it was decided to use the etch conditions outlined in Table 4-1. At the start of an etch run these conditions were established and the system left to settle until the beam current density measured on the sample shutter was steady. Once the sample shutter was opened and the etch run commenced, the beam current density was held constant by varying the ion gun's filament current so that the indicated beam current was constant. This procedure ensured a constant etch rate throughout the run.

The sample mount was rotated and water cooled during every etch run.

4.3.2 Ridge Profile

As described in section 3.3.3, IBE must be carried out at some angle off from normal to obtain a rectangular ridge profile. Webb and Wilkinson⁷ determined that the optimum value for this angle is 22.5°. To test this value, a sample was etched at 22.5°. Fig 4-11 shows the resulting ridge profile. The apparent reduced etch rate at the corners of the rib walls would tend to suggest that 22.5° is too large an etching angle⁷. A second test at 20° (Fig 4-12) showed a much improved ridge profile. This angle was used for all further etch runs.

Beam Voltage	500 V
Accelerator Voltage	100 V
Discharge Voltage	50 V
Beam Current Density	0.2-0.5 mAcm ⁻²
Gas Pressure	4×10 ⁻⁵ mbar
Base Pressure	2×10 ⁻⁶ mbar
Etch Angle	20° to normal

Table 4-1 IBE etch conditions.

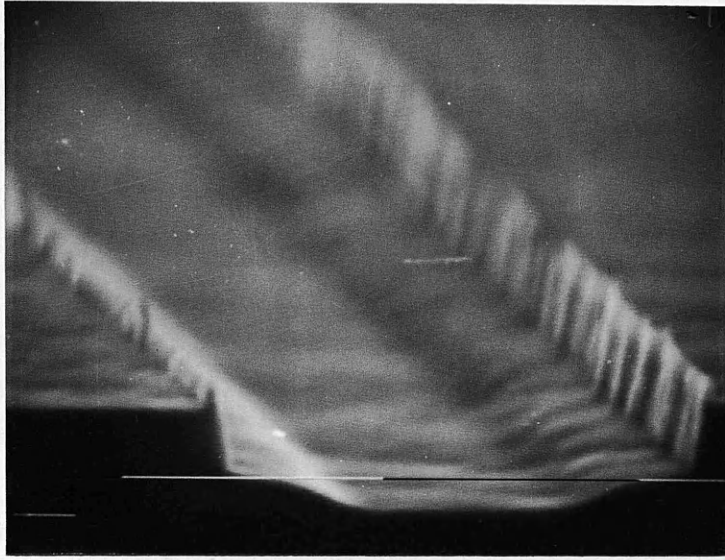


Fig 4-11 The ridge profile in GaAs sample VG42 resulting from IBE at 22.5° to normal incidence ($1\mu\text{m}$ markers).

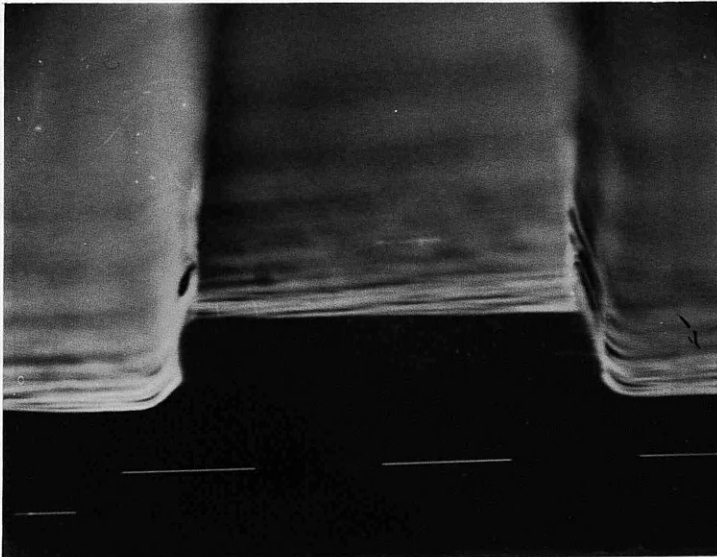


Fig 4-12 The ridge profile in GaAs sample VG42 resulting from IBE at 20° to normal incidence ($1\mu\text{m}$ markers).

Fig 4-11 also shows examples of another characteristic of IBE rib profiles, side walls on top of the rib⁸. These are formed from etched GaAs being redeposited on the edge of the photoresist stripes. When the resist is dissolved, this redeposited material remains as walls along the rib tops. It was found that reducing the photoresist thickness from 1.8 μm to 1.3 μm by increasing the resist spinning speed from 4000 to 8000 rpm stopped the formation of these walls as shown in Fig 4-12.

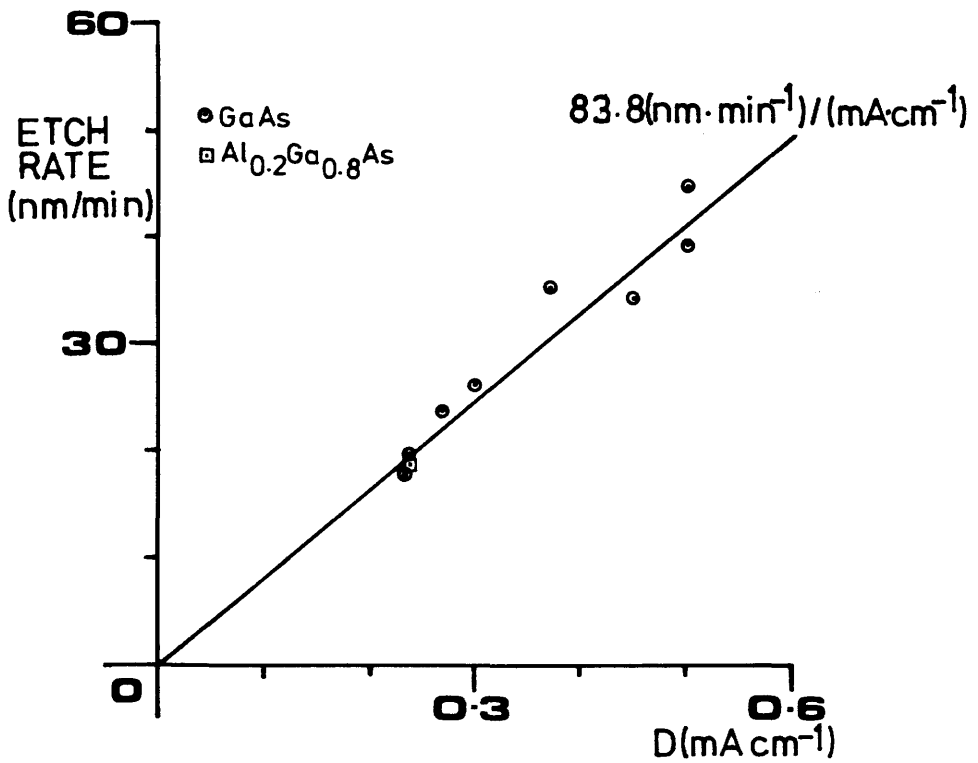
4.3.3 GaAs Etch Rate

To determine the etch rate of GaAs at a beam angle of 20°, a series of GaAs samples with waveguide photoresist patterns were etched. Each sample was etched at different beam current density to check the linearity of the relationship between etch rate and beam current density. Before etching, the height of the resist steps were measured, and after etching, the ridge heights before and after resist removal were measured - all step heights being measured using a Rank Taylor Hobson Talystep. This allowed the GaAs etch rate to be compared to the photoresist etch rate. Fig 4-13 plots the results. The etch rate is shown to have a linear dependence on beam current density with the best fit straight line having a gradient of 83.8(nm min⁻¹)/(mAcm⁻²), a result very close to that reported by Webb and Wilkinson⁷. The ratio between the etch rate of GaAs and that of the photoresist is shown to be independent of beam current density with a value $\langle\theta\rangle$ of $\theta = (2.9 \pm 0.3)$.

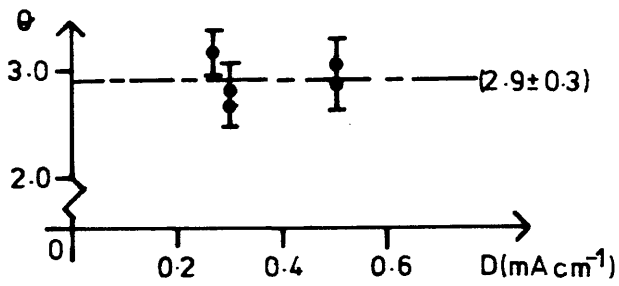
To compare the etch rate of GaAs with that of (Al,Ga)As, an Al_{0.2}Ga_{0.8}As sample grown by Liquid Phase Epitaxy was patterned and etched in an identical manner to the GaAs samples. The resulting etch rate, plotted in Fig 4-13, confirms the non-selectivity of IBE etch rates.

4.3.4 Waveguide Etch

Waveguide device sample VG42 was etched using the etch conditions shown in Table 4-1, with a 20° angle of incidence and a beam current density of 0.5mAcm⁻². An etch run of 35 minutes was predicted to give an etch depth of 1.5 μm . However, the resulting etch depth was measured by Talystep to be $(1.39 \pm 0.02)\mu\text{m}$.



(a)



(b)

Fig 4-13 (a) The etch rate of $(\text{Al,Ga})\text{As}$ versus beam current density (D), and (b) the GaAs to photoresist etch ratio (θ) versus beam current density (D).

Fig 4-14 shows s.e.m micrographs of the resulting waveguide structures of nominal width 3 and 10 μ m. It can be seen that the etched ridge wall is not vertical. Some edge roughness is also present. This roughness could have been transmitted through the resist from the mask or it could be a result of the nature of the dry etching process in GaAs. Whatever the cause, the relatively small size and vertical alignment of these striations is very similar to that observed by Webb and Wilkinson⁷.

The final rib widths at the base of the ridges were measured by s.e.m and found to be wider than the nominal line widths of the chrome shadow mask, with the 3 and 10 μ m nominal line widths resulting in 3.6 μ m and 11.2 μ m ridges respectively.

The ridge widths and profiles were thus different from that modelled in section 4.2, but the differences were such that the modal characteristics of the waveguides would not be significantly different from that predicted.

4.4 MODAL CHARACTERISTICS

The end-fire coupling system described in section 3.4.1 was used to couple 1.15 μ m NIR radiation into a planar waveguide and the rib waveguides described above. Using the IR camera, the near field pattern of the planar waveguide was found to consist of a single, bright horizontal line, consistent with the prediction of low-loss, single-mode propagation.

The near field patterns of the rib waveguides were also found to be consistent with theory. The 3 μ m rib guide exhibited a single bright spot in the near field. This is reproduced, together with a line scan in the x direction through the peak maximum, in Fig 4-15. Very little power was seen coupled into the planar guide mode, but, as predicted by WAVE, the mode is seen to spread out some distance from under the rib. The 50 μ m rib guide exhibited the highly structured near field pattern shown in Fig 4-16. The shape of this pattern, a complex superposition of the individual mode patterns of all the excited modes, was highly dependent on the position of the input beam on the waveguide.

The near field pattern of the 10 μ m wide rib guide is shown in Fig 4-17. At first glance the wide, single-peaked, intensity profile would seem to suggest a single-mode guide. However, careful analysis shows otherwise. Unlike the truly single-mode 3 μ m guide, the shape of the modal profile of this waveguide was seen to alter with input beam position - a clear indication of modal interference taking place in the near field pattern. A distinct twin-peaked near field pattern was not observed because the second mode, having a lower propagation constant and penetrating further into the substrate, has a higher propagation loss. Its contribution to the near field pattern was thus small.

Measurement of the coupling length (L_c) of the fabricated directional couplers was found to be impossible. The three micron spacing between the individual guides in the coupler structure continued to the sample's input facet. It was therefore difficult to excite one guide without exciting the other, causing the near field pattern of the directional couplers to vary depending on the input conditions. Hence no consistent coupling length could be found.

4.5 PROPAGATION LOSS

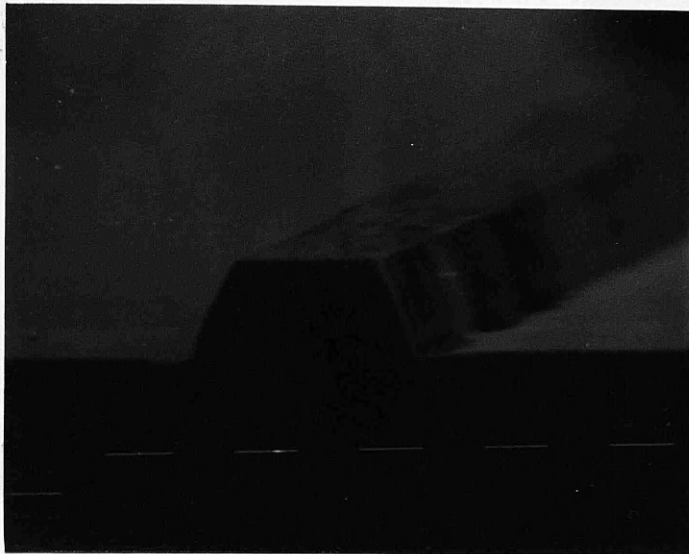
The modal characteristics having been investigated, it was decided to measure the propagation loss of the 3 and 10 μ m wide rib guides. Although a fundamental property of waveguides, the propagation loss is notoriously difficult to measure accurately. It can be measured in two ways, either by sequential cleaving⁹ or by using the Fabry-Perot effect¹⁰.

4.5.1 Theory

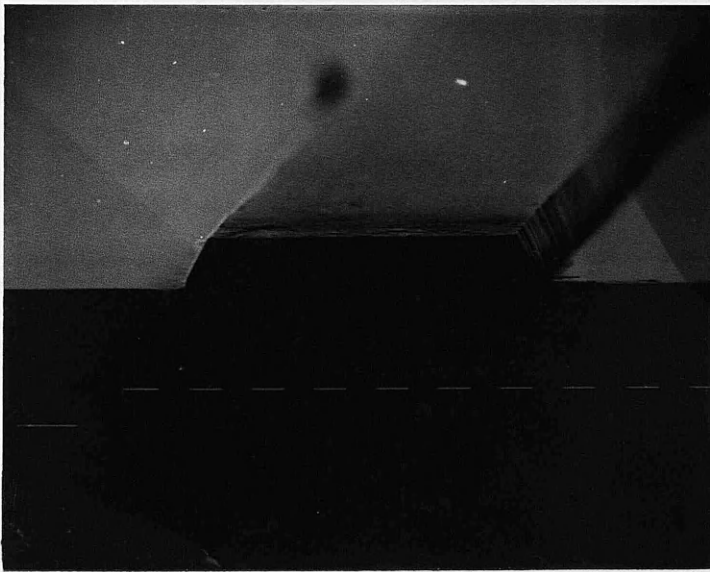
Sequential cleaving

In a cavity of length L , and the following properties:

	Intensity	Amplitude
Facet transmittance	T	t
Facet reflection	R	r
Material absorption	A	a



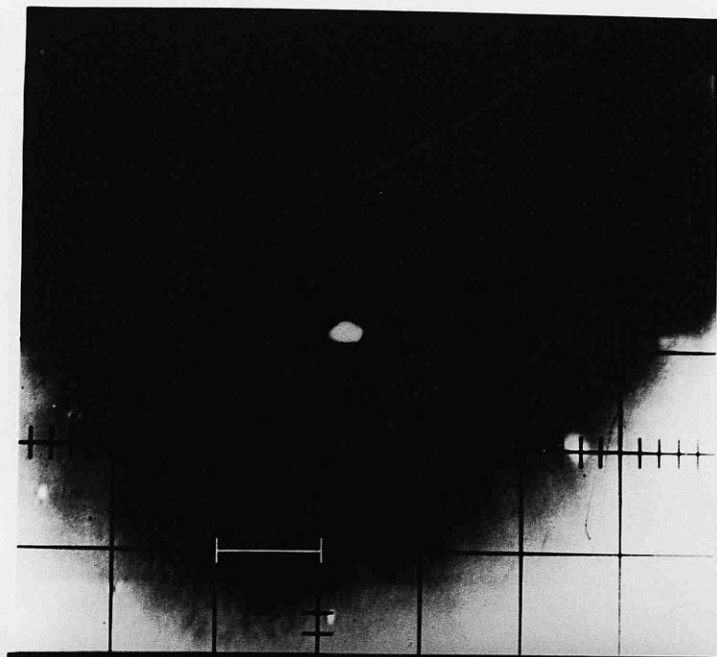
(a)



(b)

Fig 4-14 S.e.m. micrographs of ion beam etched rib waveguides in n/n^+ GaAs sample VG42. (a) $3\mu\text{m}$ nominal rib width; (b) $10\mu\text{m}$ nominal rib width ($1\mu\text{m}$ marker).

(a)
35 μ m
marker



(b)
9 μ m
marker

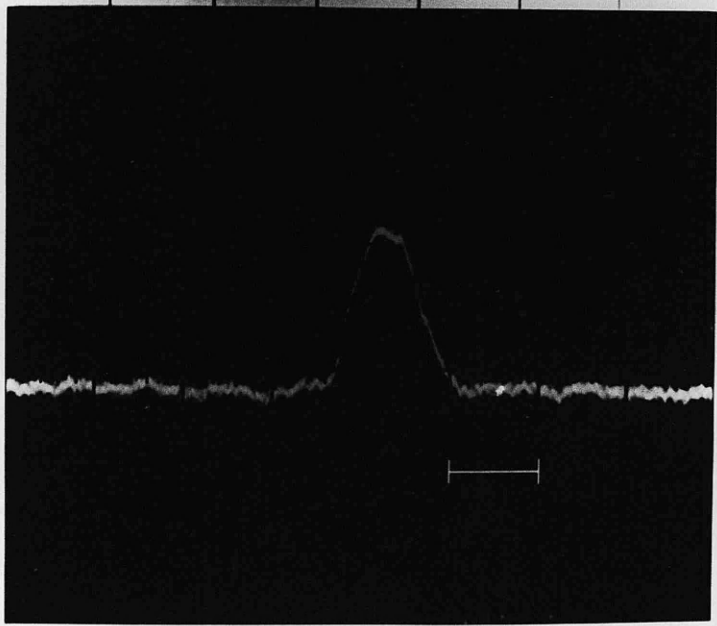
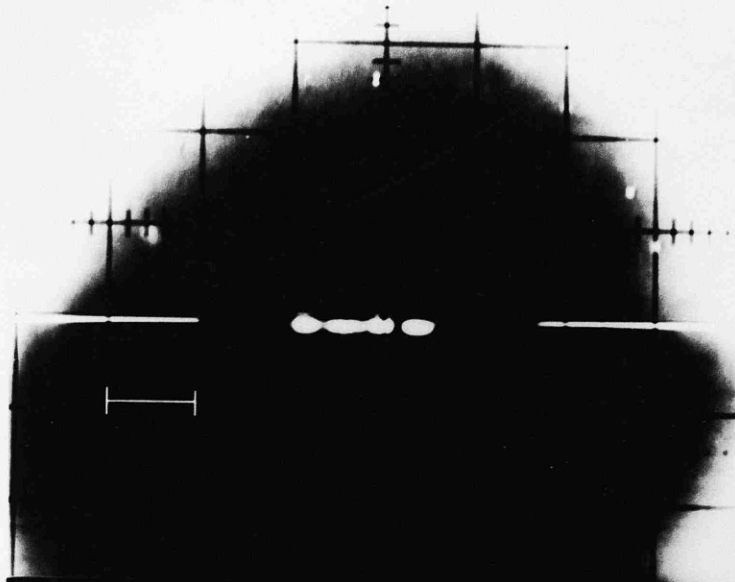


Fig 4-15 (a) The near field pattern, and (b) a x direction line scan of the nominally 3 μ m wide rib waveguide (The marker distances are only approximate).

(a)
35 μ m
marker



(b)
9 μ m
marker

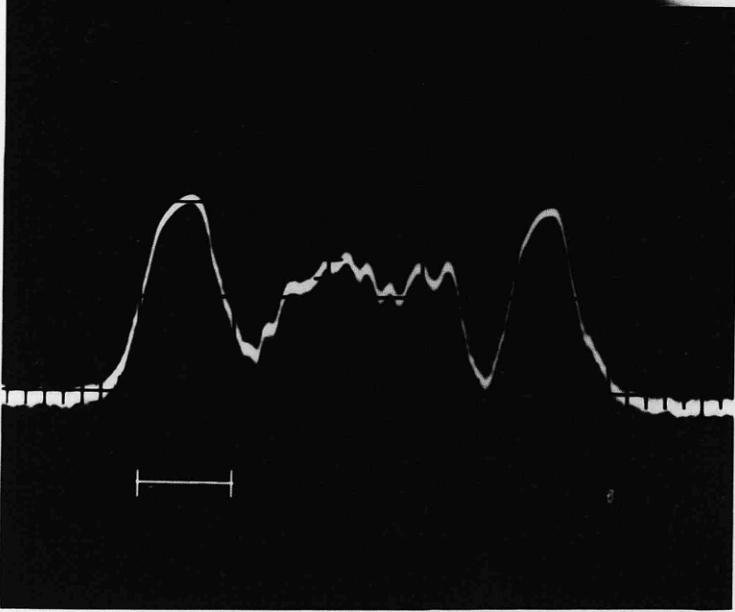
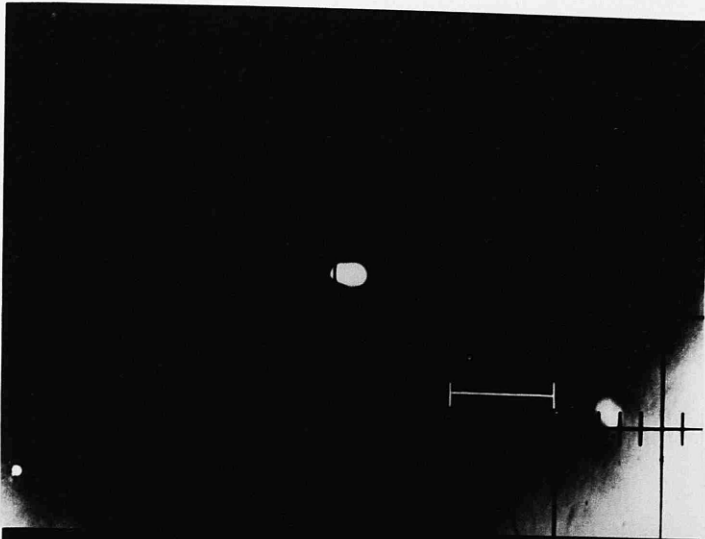


Fig 4-16 (a) The near field pattern, and (b) a x direction line scan of the nominally 50 μ m wide rib waveguide.

(a)
35 μ m
marker



(b)
9 μ m
marker

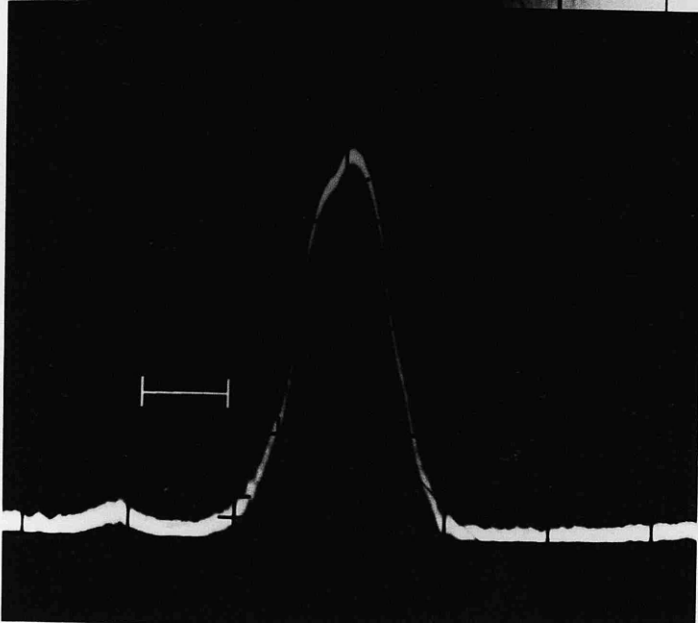


Fig 4-17 (a) The near field pattern, and (b) a x direction line scan of the nominally 10 μ m wide rib waveguide.

a ray will have a single-pass transmitted power of:

$$I = AT^2 = I_i A (1-R)^2$$

where I_i is the incident intensity and A can be expressed using the propagation loss (α) as:

$$A = \exp[-2\alpha L]$$

If we assume that A is large so that multiple reflections are small, then the transmitted intensity I through a waveguide is given by:

$$I(L) = I_i \gamma (1-R)^2 \exp[-2\alpha L] = I_o \exp[-2\alpha L] \quad (4.3)$$

where γ is the coupling coefficient between the incident laser beam and the waveguide.

Thus by measuring $I(L)$ for several waveguide lengths, L , and plotting $\ln(I)$ against L one should obtain a straight line of gradient $2\alpha_{PROP}$. In practice the units of decibels are often used with the propagation loss expressed in terms of power in dBcm^{-1} (see Appendix A).

Fabry-Perot effect

If A is not large enough to be able to neglect multiple cavity reflections, and one assumes a perfectly coherent, monochromatic light source, then the total optical power transmitted can be derived from the geometric series obtained by adding the wave amplitudes due to successive reflections¹¹. The transmitted power then becomes:

$$I = I_o A / (1 - 2AR \cos(\delta) + A^2 R^2)$$

where δ is the round trip phase change. This gives resonant (I_R) and anti-resonant (I_A) transmitted powers of

$$I_R = I_o [a / (1 - a^2 R)]^2 ; \quad I_A = I_o [a / (1 + a^2 R)]^2$$

whereas before $I_o = I_i \gamma (1-R)^2$.

If R is known, but not I₀, the single-pass loss Γ(dB) can be obtained by scanning through the F-P resonances and using the relationship:

$$\Gamma_K = -20\log_{10}a = -10\log_{10}[(1/R)((K-1)/(K+1))^{1/2}]$$

where K = I_R/I_A. If I₀ is known, but not R, the single-pass loss can be determined from the single-pass transmission (I_s) where:

$$\Gamma_T = 10\log_{10}(I_s/I_0) \quad \text{and} \quad I_s = I_0a^2 = 4[I_R^{-1/2} + I_A^{-1/2}]^{-2}$$

I₀ and R can thus be uniquely determined by cleaving the sample (sample 1) into two lengths (samples 2&3). R should be the same for all three samples so that

$$\Gamma_1 = \Gamma_2 + \Gamma_3$$

and so

$$I_0 = I_{s,2} \cdot I_{s,3} / I_{s,1} \quad \text{and} \quad R = F(K_2) \cdot F(K_3) / F(K_1)$$

where $F(K) = [(K-1)/(K+1)]^{1/2}$.

4.5.2 Sequential Cleave Measurements

After cleaving good end facets, the rib waveguides etched in n/n⁺ sample VG42 had a length of 5.40mm. The end-fire coupling system was used to couple 1.15μm light into these waveguides. The laser output was found to fluctuate when first switched on so the laser was left to stabilise for several hours before use. The laser beam was mechanically chopped at 3kHz and the transmitted signal, detected by a Ge photodiode, was preamplified, fed to a lock-in amplifier, and then recorded on chart paper. The transmitted power of the waveguides was found to be critically dependent on the laser input condition, indicating that the coupling coefficient (γ) was varying.

Using an estimated propagation loss of 5dBcm⁻¹ it was predicted that strong F-P effects would be observed in the waveguide. The F-P resonances could effect the propagation loss measured by the sequential cleavage method. It was thus decided to warm the sample radiatively from above and compensate for the F-P effects by taking

I(L) as the mean of the F-P peaks and troughs scanned as the guide cooled. Four guides of each width were thus examined.

The sample was then cleaved into two samples of length 1.70mm and 2.70mm, and the process repeated at these lengths. Fluctuations in the coupling coefficient were found to mask the small differences in loss between guides of a given width. For the analysis of propagation loss, the mean transmission of guides of a given width and length was used. The results are plotted in Fig 4-18. The gradients of the best fit lines were found to be:

nominal width	propagation loss
3 μ m	(6.7 \pm 0.9)dBcm ⁻¹
10 μ m	(4.0 \pm 1.4)dBcm ⁻¹

Discussion

The scatter in the experimental points in Fig 4-18 aptly demonstrates the difficulty in obtaining reliable results using the sequential cleaving method, the primary difficulty being that in removing and replacing the sample for cleaving, large changes in the coupling coefficient can occur. A further drawback is that the method is destructive.

The results, however, are close to that predicted by the free carrier loss approximation of section 4.2.3 which predicted a propagation loss for planar waveguides of 5dBcm⁻¹. The higher propagation loss of the 3 μ m guides compared with the 10 μ m guides is understood to be due to the increased penetration of the modal field of the 3 μ m guide into the substrate, and because of increased scattering from the ridge walls. The losses are slightly larger than that reported in the literature where 2-4dBcm⁻¹ loss is reported^{1,2} for different waveguiding conditions.

From these results it was concluded that it was possible, but difficult, to use the sequential cleaving method together with an end-fire coupling system to measure the propagation loss of rib waveguides. In addition, it was deduced that a standard of waveguide fabrication had been obtained which allowed relatively low-loss waveguides to be fabricated.

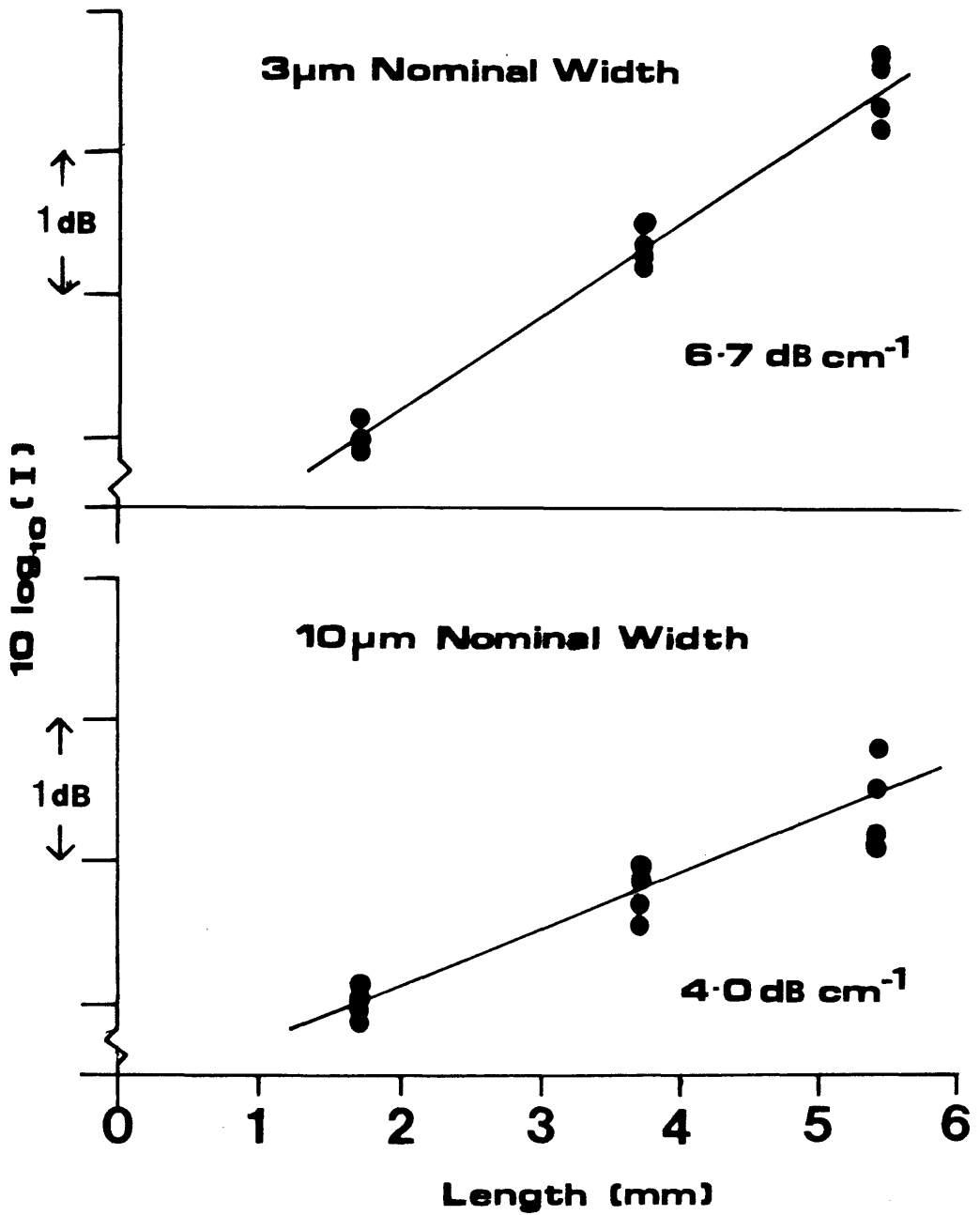


Fig 4-18 The propagation loss of the rib waveguides of nominal width 3µm and 10µm at $\lambda=1.15\mu\text{m}$.

4.5.3 Fabry-Perot Method

The difficulties inherent in the sequential cleaving method as demonstrated in section 4.5.2 (i.e. time consuming, destructive, etc.) led Walker¹⁰ to develop the method of calculating the propagation loss α outlined in section 4.5.1. Using F-P resonances in a waveguide to calculate α , he was able to obtain values which correlated very well with the values obtained from sample cleaving.

To investigate this model the 5.4mm, 10 μ m waveguide was radiatively heated from above, thus scanning the F-P resonances. Fig 4-19 plots the observed fluctuation in transmitted power from which a value of $K = 1.14$ was calculated. To be consistent with the sequential cleaving results this value of K demands an unrealistically low reflection coefficient R of 15.5%. Alternatively, if the value of R is assumed to be:

$$R = ((1-n)/(1+n))^2 \approx 0.30$$

the measured propagation loss should give $K = 2.09$.

The cause of this inconsistency was traced back to the Spectra-Physics HeNe laser. It was measured to have two transmission lines, one at the expected wavelength 1.153 μ m, and another at 1.162 μ m This latter line had an intensity one quarter of that of the former. This turns out to be standard for this laser. The effect of having two longitudinal modes present in the F-P cavity formed by the waveguide was calculated by Dr. S. Ritchie¹³. The shape of the F-P resonances observed on cooling was theoretically found to be critically dependent on the round trip phase difference between the two longitudinal modes. The presence of the second mode was calculated to reduce K , with even the observed 1:4 ratio between laser line intensities leading to large deviations from the single laser line model¹³. These theoretical results are in agreement with the above experimental observations. To be able to accurately measure propagation loss via the F-P method it would thus have been necessary to have placed a grating in front of the laser to spatially filter the second line. This task was not given a high priority since the important measurements involved in the investigation of MQW waveguides would not use this laser.

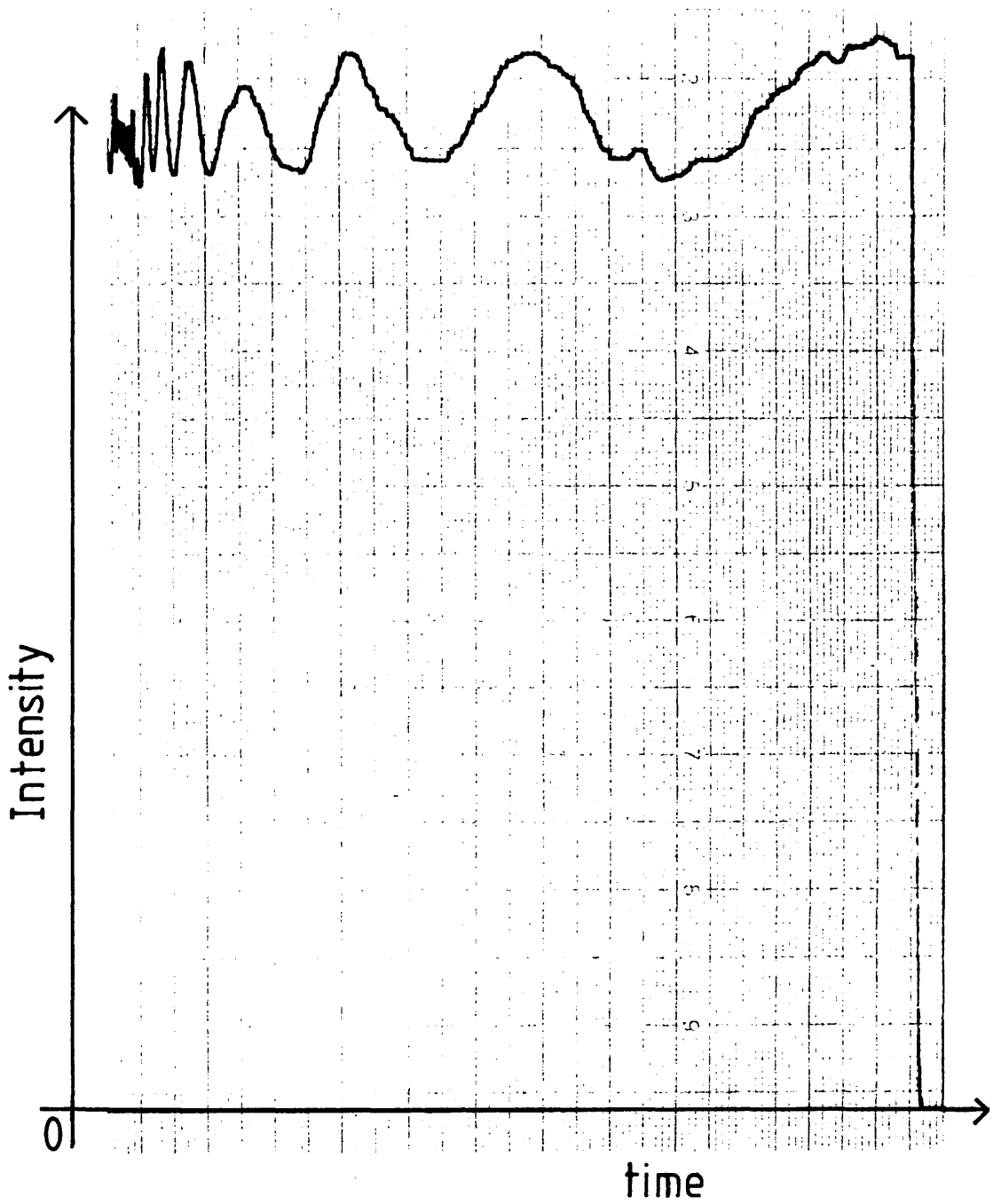


Fig 4-19 The Fabry-Perot oscillations observed during the cooling of the 10 μ m wide rib waveguide. The last few oscillations have a period of the order of seconds.

In summary, the F-P method of measuring the propagation loss of a waveguide was found to be potentially quick, reliable and non-destructive. However, the exact nature of the resonances observed is very dependent on the spectral nature of the light source.

4.6 THE ELECTRO-OPTIC EFFECT IN GaAs

The propagation loss of n/n⁺ waveguides having been measured, it was now necessary to measure the other main property of interest in GaAs at 1.15μm, the electro-optic effect. This was done by metallising the top and bottom of a planar n/n⁺ waveguide, and thus fabricating a planar phase modulator. This device was chosen because of its simplicity, with its one-dimensional electrical and optical fields simplifying the calculations involved in modelling the device.

4.6.1 Theory

The electro-optic effect, simply stated, is the effect that an externally applied electric field has on the refractive index of a material. It is usually expressed as a change in the indicatrix constant thus:

$$\Delta(1/n^2)_{ij} = r_{ijk}F_k + K_{ijkl}F_k \cdot F_l + \dots$$

where the indices i,j,k,l each cover a set of rectangular coordinates defined with respect to the crystallographic axes¹⁴, n is the refractive index, r is the linear electro-optic (LEO) tensor, K the quadratic electro-optic (QEO) tensor, and F the low frequency applied electric field.

The quadratic electro-optic effect is not significant in GaAs far from the band gap, so $\Delta(1/n^2)$ can be described by the linear term alone at $\lambda=1.15\mu\text{m}$. Taking advantage of symmetry arguments, the second rank indicatrix can be reduced to a one-dimensional, six-term vector describing the change in the index ellipsoid. In a similar way, the LEO tensor can be reduced to a two-dimensional matrix¹⁴ so that:

$$\Delta(1/n^2)_i = r_{ij}E_j^{(0)} \quad , \quad i=1, \dots, 6 \quad , \quad j=1, \dots, 3$$

with 1,2,3 being the principal dielectric axes.

This LEO matrix can be further simplified since GaAs has a crystal class of $\bar{4}3m$ for which the LEO matrix reduces to only three, non-zero equal terms; $r_{41}=r_{52}=r_{63}$.

Several models have been presented to predict the value of r_{41} in GaAs. These models fall into two distinct groups; models where the LEO is derived in terms of the properties of harmonic oscillators, and semi-empirical models where the LEO effect is determined by transforming an experimentally observed functional form of the band edge absorption.

Sugie and Tada¹⁵ applied the former type of model to GaAs, obtaining an expression for the dispersion of the LEO effect in GaAs that contained four fittable parameters. Adachi and Oe^{16,17} applied the latter type of model to GaAs close to the band gap, fitting their function to the experimental data of Sugie and Tada. Suzuki and Tada¹⁸ neatly summarise the work on the LEO effect in GaAs drawing together the relevant theoretical and experimental work, and state that the discrepancies in the published results for r_{41} could be due to residual strain in the samples, multiple reflection of light and photoconductivity. However, a general trend is discernable with the LEO coefficient decreasing slowly with decreasing λ in the range $1\mu m \leq \lambda \leq 10\mu m$, and then increase sharply close to the absorption edge.

It is important to note that some care must be taken when defining the experimental conditions under which the measurement of the electro-optic coefficient is made. If the GaAs crystal is mechanically free to move then a static electric field will cause a strain via the converse piezo-electric effect and this in turn will produce a change in the refractive index through the elasto-optic effect. The primary or "true" electro-optic coefficient r_{ij}^0 may only be observed in a clamped crystal. The relationship between the clamped (r_{41}^0) and unclamped (r_{41}^T) coefficients for GaAs is:

$$r_{41}^T - r_{41}^0 = p_{44}d_{14}$$

where p_{ij} = elasto-optic coefficient [dimensionless], and

d_{ij} = piezo-electric strain constant [m/v]

At $\lambda=1.15\mu m$ $r_{41}^T \approx -1.2 \times 10^{-12} m/V$, with $r_{41}^T - r_{41}^0 \approx 2 \times 10^{-13} m/V$ for GaAs¹⁸.

In the experimental work reported here it is the unclamped value, r_{41}^T , that is being measured.

4.6.2 Crystal Orientation

The relationship between Δn and r_{41} is determined by the direction of optical propagation in the crystal, the polarisation direction, and the orientation of the applied electric field¹⁴. As is normal practice, the GaAs waveguides used were epitaxially grown on $\langle 001 \rangle$ orientation crystals. In GaAs devices the electric field is applied by reverse biasing a Schottky barrier that has been evaporated onto the top surface. The electric field is thus applied perpendicular to the $\langle 001 \rangle$ plane. GaAs preferentially cleaves along the crystallographic $\langle 110 \rangle$ and $\langle -110 \rangle$ directions. Propagation will thus be normal to those directions and the $\langle 001 \rangle$ direction. The implication of these crystal orientations are¹⁴ that there will be no change of refractive index with applied electric field (F) for the TM mode but that the change in refractive index for the TE mode will be:

$$\Delta n = \pm(1/2)n^3 r_{41} F \quad \text{for } \langle \mp 110 \rangle \text{ propagation}$$

4.6.3 Variational Theorem for Dielectric Waveguides

The electro-optic effect is defined as a change in the refractive index of the bulk material constituting the waveguide. In actual waveguide experiments the property measured is $\Delta\beta$, the change in guided mode propagation constant. A relationship between $\Delta\beta$ and Δn is thus needed and this can be provided by the variational theorem for dielectric waveguides¹⁹. This theorem connects the variations δE and δH of the electromagnetic field solution to the perturbations $\delta(\omega\epsilon)$ and $\delta(\omega\mu)$ of the frequency and constants of the medium which are the cause of the variations. The theorem follows directly from Maxwell's equations. By assuming the form of E and H in a waveguide and assuming that $\delta\omega = \delta\mu = 0$, $\delta\epsilon = \Delta\epsilon$ one obtains:

$$\Delta\beta \cdot P = \omega \int_{-\infty}^{+\infty} \Delta\epsilon E \cdot E^* dx dz$$

where P = power carried by the mode. By applying the conditions pertaining to a planar waveguide one obtains the relationship for TE modes:

$$\Delta\beta = (\omega^2\mu/2\beta) \int_{-\infty}^{+\infty} \Delta\epsilon(z) E_x^2 dz / \int_{-\infty}^{+\infty} E_x^2 dz$$

which can be rewritten in the more useful form:

$$\Delta\beta = (k_0/n_e) \int_{-\infty}^{+\infty} n(z) \Delta n(z) E_x^2(z) dz / \int_{-\infty}^{+\infty} E_x^2 dz$$

Thus the relationship between $\Delta\beta$ and Δn in a slab waveguide involves a one-dimensional overlap integral between the waveguide's dielectric properties and the modal field. Substituting in the expression for $\Delta n(z)$ from section 4.6.2 one obtains:

$$\Delta\beta = (\pi/\lambda n_e) \int_{-\infty}^{+\infty} n^4(z) r_{41}(z) F(z) dz / \int_{-\infty}^{+\infty} E_x^2 dz \quad (4.4)$$

However, for the waveguides used, several simplifying assumptions can be made, namely that the variation in n and r_{41} with z is negligible and that $n_e \approx n_2$. Thus (4.4) becomes:

$$\Delta\beta = (\pi/\lambda) n_2^3 r_{41} \int_{-\infty}^{+\infty} F(z) E_x^2(z) dz / \int_{-\infty}^{+\infty} E_x^2 dz$$

It is normal to re-express $F(z)$ in terms of the total voltage (V_t) and the waveguide thickness (t_2) thus:

$$F(z) = (V_t/t_2) G(z)$$

to obtain:

$$\Delta\beta = (\pi/\lambda) n_2^3 r_{41} \cdot (V_t/t_2) \eta \quad (4.5)$$

where $\eta = \int_{-\infty}^{+\infty} G(z) E_x^2(z) dz / \int_{-\infty}^{+\infty} E_x^2(z) dz$

With $\eta=1$, expression (4.5) is the same expression one would obtain for a bulk GaAs modulator of thickness t_2 . So η can therefore be considered a correction factor for the waveguide geometry, and indeed for a perfectly confined mode in a highly resistive guide layer, $\eta=1$ is a good approximation.

4.6.4 Experimental Techniques

There are several methods of measuring the LEO effect in GaAs reported in the literature. They rely on the fact that light linearly

polarised at 45° to the x axis will emerge from the crystal as elliptical light due to the phase difference between TE and TM modes. For the crystal orientation of interest β_{TM} does not vary with applied electric field. The phase difference between TE and TM modes is thus:

$$\Gamma = L(\beta_{TM} - \beta_{TE}) = L \cdot \Gamma_0 \pm (\Pi/\lambda) L n_2^3 r_{41} (V_x/t_z) \eta \quad \text{for } \langle \pm 110 \rangle \text{ propagation}$$

where L is the waveguide length and Γ_0 is the phase difference due to the difference in propagation constants of the unperturbed waveguide and built-in strain.

The differences in the methods lie in the ways they measure this phase difference.

Crossed polarisers

Perhaps the simplest method is to place a polariser after the phase modulator at 90° to the input polariser. It can be shown¹⁴ that this will convert any phase modulation to an amplitude modulation with the output intensity being related to the input intensity via the relationship:

$$I(V_A)/I_0 = \sin^2[\Gamma(V_A)/2] = \sin^2[(\Pi/2) \langle (V_A - V_0)/V_\pi \rangle]$$

where V_π is the voltage needed to introduce a Π phase difference, and V_0 is a term to take account of the phase difference at $V_A=0$. By varying V_A and plotting $I(V_A)$, r_{41} may be determined from V_π .

This method has the disadvantages that any difference in the absorption of the TE and TM modes will introduce an error in the measured value of r_{41} , and that the relationship between $I(V_A)$ and $\Gamma(V_A)$ is not a linear one. This latter point makes the analysis of r_{41} for AC modulation, and the determination of the exact functional form of the dependence of Γ on V_A difficult.

Quarter-wave plate

In place of the crossed output polariser a quarter-wave plate can be placed parallel to the input polariser. After the quarter-wave

plate, a polariser set parallel to the z axis will result in an intensity dependence on phase of the form¹⁵:

$$I(V_A)/I_0 = (1 - \sin[\Gamma(V_A)])$$

so that for small Γ , ΔI is proportional to $\Delta\Gamma$.

This linear relationship between ΔI and $\Delta\Gamma$ allows r_{41} to be measured for an AC V_A . The method has the further advantage that small differences in absorption between the TE and TM modes will not affect the measured value of r_{41} .

Phase compensation

Placing a compensator after the phase modulator allows any phase difference introduced by the phase modulator to be compensated out, the amount of compensation needed exactly matching $\Gamma(V_A)$. The condition for exact compensation is that the light from the compensator be linearly polarised. This method is potentially the most versatile since differences in the absorption of TE and TM modes can be allowed for and the exact dependence of Γ on F can be measured. However, in practice the precision with which phase measurements can be made with the compensator is limited by the accuracy with which it can be determined that the light transmitted by the compensator is linear.

Due to its simplicity the crossed polariser technique was used for the GaAs work reported in this chapter.

4.6.5 Experimental Results

Mr J. Frost grew a new n/n⁺ sample VG119 by MBE for this work on the LEO coefficient. The epilayer thickness was accurately measured during growth to be 4.85 μm with a measured free carrier concentration of $2 \times 10^{15} \text{cm}^{-3}$. The substrate had a free carrier concentration of $2 \times 10^{18} \text{cm}^{-3}$. Fig 4-2 shows that this structure was predicted to sustain two modes, with the second mode being only weakly guided. This was reflected in the fact that although only 2.25% of the fundamental mode was calculated to be in the substrate, this rose to 17.89% for the second mode. Taking only the substrate loss into account, the complex

refractive index program of Mr D. F. Clarke returned $\alpha(\text{TE}_2)=3.8\text{dBcm}^{-1}$, $\alpha(\text{TE}_1)=34.6\text{dBcm}^{-1}$. Losses from an increased penetration into any top metal electrode would further increase the difference in propagation loss between the first and second modes.

Phase modulator fabrication

A simple planar phase modulator was fabricated. Firstly a suitably sized, rectangular, sample was cleaved off the wafer. A Au:Ge, ohmic contact (see section 3.3.4) was evaporated on the back of the n^+ substrate and annealed in the usual way. Then a Ti/Au Schottky contact was evaporated over the whole of the top surface. After cleaving off all four edges to avoid short-circuits across the device, the I-V characteristics were measured and found to be identical to those reported in section 3.3.4.

Crossed polariser measurements

Section 3.4 describes the end-fire coupling system used to couple light into the planar phase modulator. A half-wave plate and polariser were used to rotate the horizontally polarised HeNe laser beam round to $+45^\circ$. The output at the other end of the system was analysed using a polariser and found to be linearly polarised at $+45^\circ$, implying that the system did not introduce any amplitude or phase difference between vertically and horizontally polarised light.

IR radiation was coupled into the 2.46mm long sample using X20 objective lenses and the modal near field pattern observed to show only one mode for both TE and TM propagation. It was concluded that the propagation loss of the weakly guided second mode was too high for it to significantly contribute to the near field pattern, or to the detected transmission.

The laser beam was mechanically chopped at 3kHz and a Ge photodiode, preamplifier and lock-in amplifier used to detect the transmitted power. No significant difference was observed in the transmission of TE and TM modes implying that even with the top metal electrode, $\alpha_{\text{TE}} \approx \alpha_{\text{TM}}$.

With zero volts applied to the phase modulator, the built-in phase difference was measured by using a polariser to plot transmitted intensity as a function of polariser angle. This gave a built-in phase difference (Γ_B) of 0.37 radians.

The arm on which the sample rested was earthed, and the top Schottky contact reverse biased via a probe. The measured transmitted power through crossed polarisers as the DC applied voltage was varied between zero and 50 volts is plotted in Fig 4-20. The transmitted intensity can be seen to follow a roughly sinusoidal dependence on V_A , the non-zero intensity at $V_A=0$ being due to the built-in phase difference.

To obtain r_{41} from this curve the overlap coefficient $\eta(V_A)$ was calculated using the measured free carrier data on VG119. The modal field profile was assumed to be that of the passive waveguide structure with only the first mode contributing to the detected intensity. The Schottky barrier was assumed to be ideal. Fig 4-21 shows a plot of the optical and electric fields for a typical applied voltage, and Fig 4-22 shows the resulting value of η as a function of applied voltage. r_{41} can then be calculated from the value $V_A=V_P$ at which I/I_0 reaches a maximum using:

$$|r_{41}| n_2^3 = ((\Pi - \Gamma_B) / \Pi) \cdot (\lambda t_z / L) \cdot (1 / (V_P \cdot \eta(V_A=V_P)))$$

Using this expression the following values were obtained:

$$\begin{aligned} n_2^3 |r_{41}| &= 59.46 \times 10^{-12} \text{ m/v} \\ |r_{41}| &= (1.46 \pm 0.08) \times 10^{-12} \text{ m.v} \end{aligned}$$

Linear measurement

We have already seen that for crossed polarisers the relationship between transmitted intensity, I , and phase, Γ , is:

$$I/I_0 = \sin^2[\Gamma/2]$$

This implies that $\Delta I/I_0 = (1/2) \cdot \sin(\Gamma) \Delta \Gamma$.

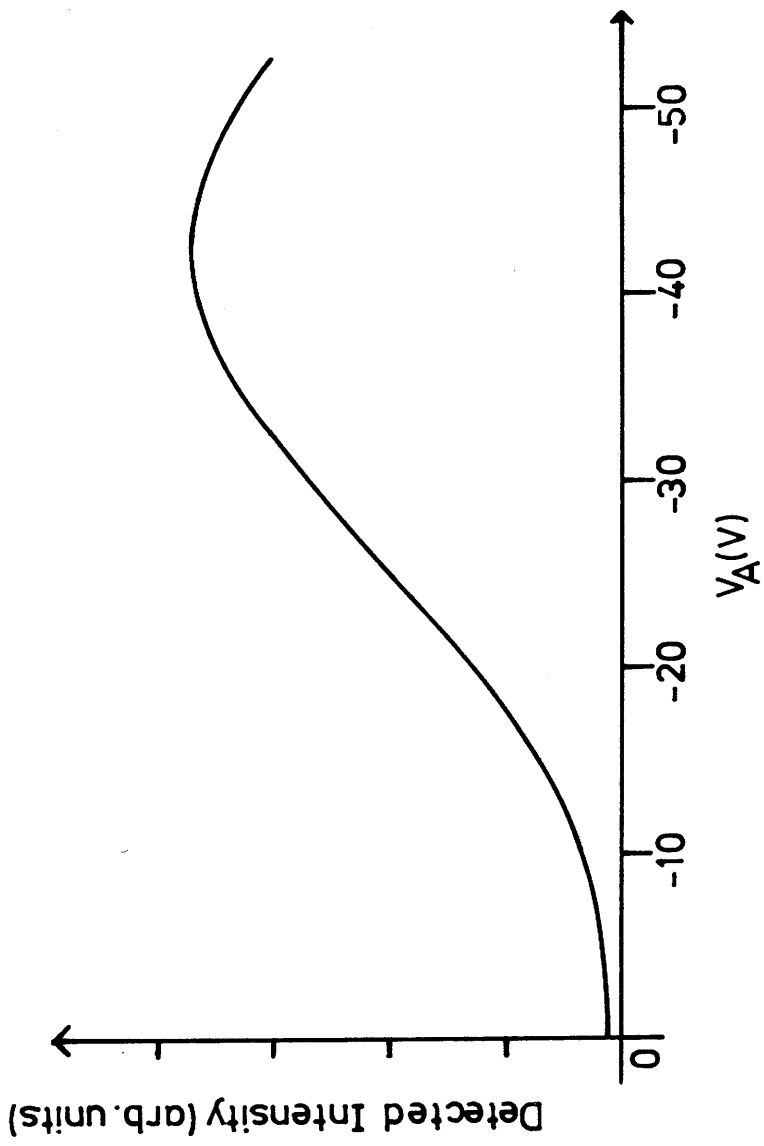


Fig 4-20 The detected intensity through the crossed polariser modulator as a function of applied voltage (V_A).

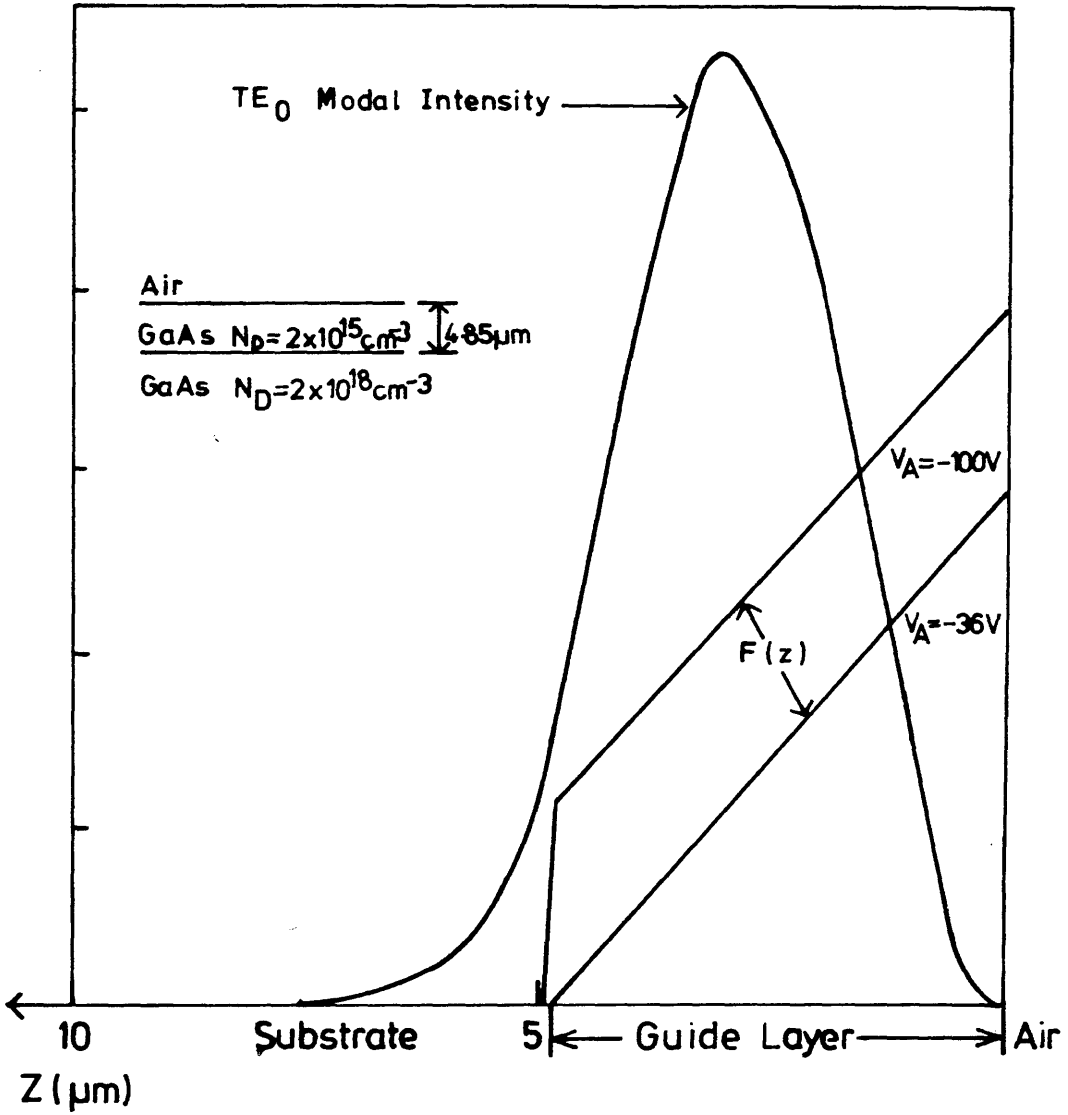


Fig 4-21 Typical optical and electrical fields in VG119 used to calculate the overlap integral. $\lambda = 1.15 \mu\text{m}$.

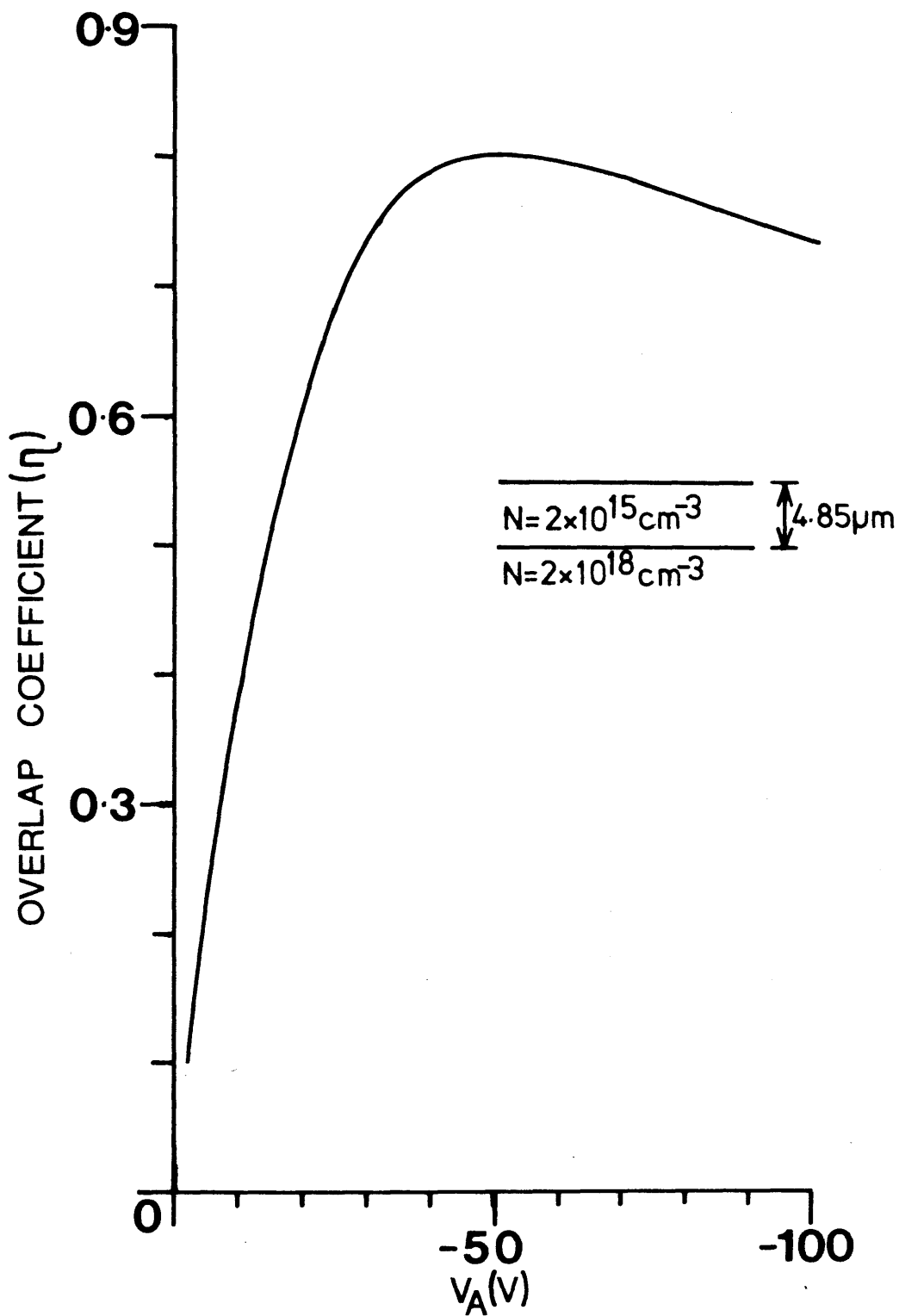


Fig 4-22 The overlap coefficient versus applied voltage (V_A) for VG119 at $\lambda = 1.15 \mu\text{m}$.

If a bias voltage is applied to the phase modulator such that $\Gamma = \pi/2$ then

$$\Delta I/I_0 \approx \Delta \Gamma/2$$

Using the measured values of Γ_0 and V_{π} and the calculated values of $n(V)$, it was deduced that the $\pi/2$ bias point would be obtained for $V_B \approx -22.5$ volts. Applying a selection of bias voltages, V_B , and then scanning a second, ramp voltage from $-2V$ to $+2V$, the transmitted intensity was found to vary linearly with voltage (Fig 4-23) with calculated values of r_{41}^T :

V_B (volts)	$ r_{41}^T $ (pm/v)	
20.5	1.42	
22.5	1.44	± 0.07
25.5	1.47	

in good agreement with the result obtained by the previous method.

4.6.6 Discussion

The LEO coefficient of GaAs for DC applied voltages had thus been measured by two methods, with good agreement between the two results. To place these results in context, the results of several workers have been summarised in Fig 4-24. It can be seen that the present results for r_{41}^T are some 18% higher in value than the result that would be predicted from the work of Walsh²⁰ and Suzuki and Tada¹⁸ on bulk GaAs devices. However, the present results compare very favourably with the result of Sugie and Tada²¹ and a recent measurement of r_{41}^T by Glick et al²² in a waveguide modulator. It can thus be said with some confidence that a reliable method has been found to measure r_{41}^T in waveguides.

4.7 CONCLUSIONS

Waveguide analysis techniques described in chapter three allowed the design of single-mode n/n^+ GaAs waveguides at $1.15\mu\text{m}$. Ion beam etching and standard photolithographic processes resulted in low-loss waveguides with good rib profiles and edge roughness with the end-fire coupling system being found to be adequate for the measurement of the

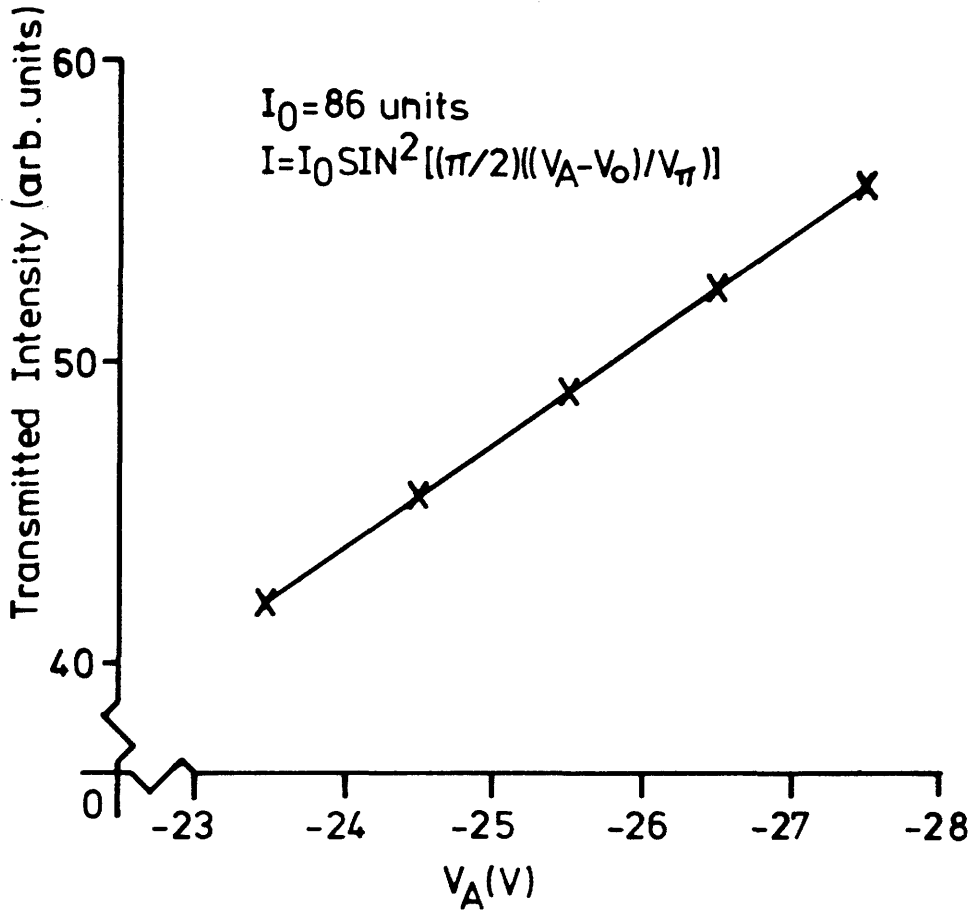


Fig 4-23 The transmitted intensity of a crossed polariser modulator versus applied voltage V_A for V_A about the $\pi/2$ bias point.

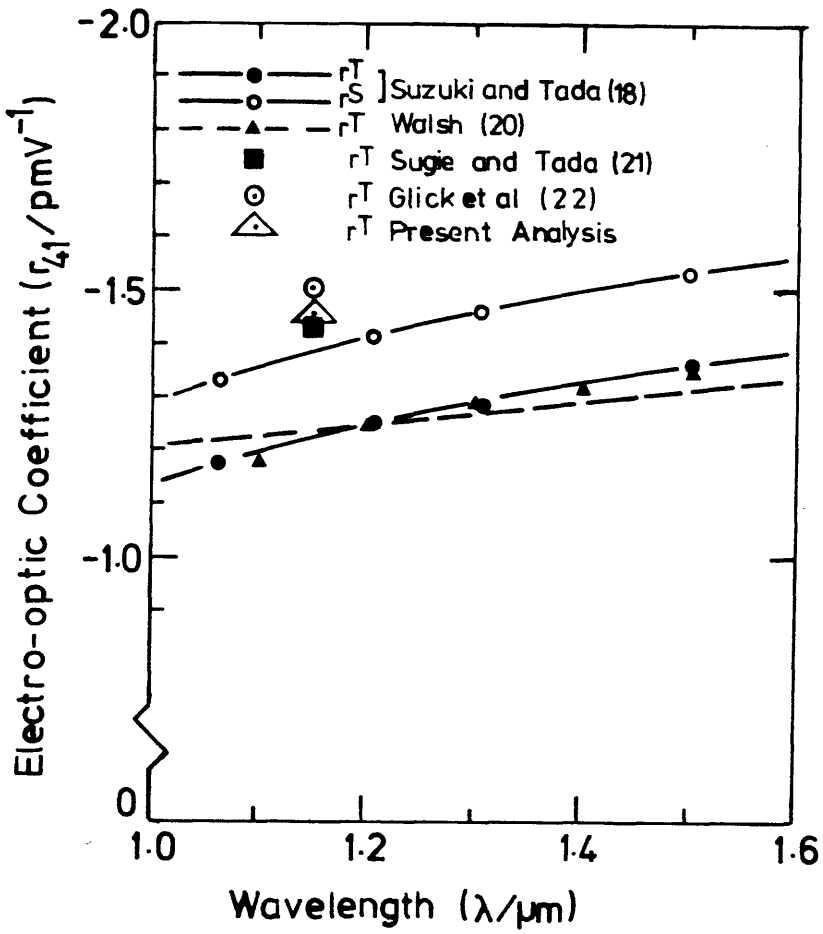


Fig 4-24 A comparison of the experimentally determined values of r_{41} for GaAs with those in the literature.

propagation loss. The metal semiconductor contacts outlined in chapter three allowed a planar waveguide phase modulator to be fabricated and used to measure the linear electro-optic (LEO) effect in GaAs at $\lambda=1.15\mu\text{m}$. The techniques used in the measurement were verified by the close agreement between the results obtained and those published in the literature. The accurate determination of the LEO coefficient was found to depend critically on the accurate calculations of the overlap between the electrical and optical fields in the modulator.

References to Chapter Four

- 1 E.Garmire;
in *Topics in Applied Physics, Vol. 7: Integrated Optics*, ed. T.Tamir (Springer-Verlag, New York, 1975).
- 2 J.S.Blakemore;
"Semiconducting and other major properties of gallium arsenide", *J. Appl. Phys.* **53**, R123 (1982).
- 3 V.Evtuhov and A.Yariv;
"GaAs and GaAlAs Devices for Integrated Optics", *IEEE Trans. Microwave Theory Tech.* **MTT-23**, 44 (1975).
- 4 D.Hall, A.Yariv and E.Garmire;
"Optical guiding and electro-optic modulation in GaAs epitaxial layers", *Opt. Comm.* **1**, 403 (1970).
- 5 Y.Suematsu, M.Hakuta, K.Furuta, K.Chiba and R.Hasumi;
"Fundamental transverse electric field (TE_0) mode selection for thin-film asymmetric light guides", *Appl. Phys. Lett.* **21**, 291 (1972).
- 6 *Properties of Gallium Arsenide*, emis. Datareviews Series No2 (Inspec, London).
- 7 A.P.Webb and C.D.W.Wilkinson;
"Ion beam etching GaAs for integrated optical applications", *Vacuum* **34**, 159 (1984).
- 8 W.Kern and C.A.Deckert;
Thin Film Processes (Academic Press, New York, 1978).
- 9 A.J.N.Houghton, D.A.Andrews, G.J.Davies and S.Ritchie;
"Low-loss optical waveguides in MBE-grown GaAs/GaAlAs heterostructures", *Opt. Comm.* **46**, 164 (1983).
- 10 R.G.Walker;
"Simple and accurate loss measurement techniques for semiconductor optical waveguides", *Electron. Lett.* **21**, 581 (1985).

- 11 R.G.Walker and C.D.W.Wilkinson;
"Integrated optical ring resonators made by silver ion-exchange in glass", *Appl. Optics* **22**, 1029 (1983).
- 12 P.Buchmann, H.Kaufmann, H.Melchior and G.Guekos;
"Reactive ion etched GaAs optical waveguide modulation with low loss and high speed", *Electron. Lett.* **20**, 295 (1984).
- 13 S.Ritchie;
British Telecom Research Laboratories, Martlesham Heath, Suffolk;
private communication.
- 14 J.F.Nye;
Physical Properties of Crystals (Clarendon Press, Oxford, 1957).
- 15 M.Sugie and K.Tada;
"Generalized theory of nonlinear susceptibilities and linear electrooptic coefficients based on a three-dimensional anharmonic oscillator model", *Jpn. J. Appl. Phys.* **12**, 215 (1973).
- 16 S.Adachi and K.Oe;
"Linear electro-optic effects in zincblende-type semiconductors: Key properties of InGaAsP relevant to device design", *J. Appl. Phys.* **56**, 74 (1984).
- 17 S.Adachi and K.Oe;
"Quadratic electro-optic (Kerr) effects in zincblende-type semiconductors: Key properties of InGaAsP relevant to device design", *J. Appl. Phys.* **56**, 1499 (1984).
- 18 N.Suzuki and K.Tada;
"Elasto-optic and electro-optic properties of GaAs", *Jpn. J. Appl. Phys.* **23**, 1011 (1984).
- 19 H.Kogelnik;
in *Topics in Applied Physics, Vol. 7: Integrated Optics* ed. T.Tamir (Springer-Verlag, New York, 1975).
- 20 T.E.Walsh;
"Gallium-arsenide electro-optic modulators", *RCA Review* **27**, 323 (1966).
- 21 M.Sugie and K.Tada;
"Measurements of the Linear Electrooptic Coefficients and Analysis of the Nonlinear Susceptibilities in Cubic GaAs and Hexagonal CdS", *Jpn. J. Appl. Phys.* **15**, 421 (1976).
- 22 M.Glick, F.K.Reinhart and G.Weimann;
"Optical Waveguide Properties of Multiquantum Wells", *Proc. 3rd Euro. Conf. Integrated Opt.* 99 (1985).

CHAPTER FIVE
THE DESIGN, GROWTH AND INITIAL TESTING OF MQW-DH

5.1 INTRODUCTION

The design techniques developed and tested on n/n^+ GaAs waveguides were now combined with the MQW properties outlined in chapter two to design MQW waveguides. As emphasised in chapter two, many of the parameters involved in the design of MQW waveguides (for example, refractive index) have not been extensively investigated in the literature, so certain working assumptions had to be made to facilitate the design.

The growth of multi-layer semiconductor structures by Vapour Phase Epitaxy or Molecular Beam Epitaxy is a whole field of research in its own right. The MQWS used in this project were therefore grown by others. However, in order to design and analyse MQWS, a certain basic understanding of the growth processes is necessary. The basic principles of VPE and MBE are therefore outlined.

Once grown, a MQWS must be analysed for quality and closeness to design. Due to the very small dimensions of the MQWS, analysis techniques are limited in number, and some analysis techniques influence the design of the waveguide structure itself. A brief description of the various analytical techniques used is given, together with a summary of the results obtained from the structures grown.

Obtaining good quality MQW material became a major difficulty during this project, and finally limited the conclusions that could be drawn from the waveguide experiments. This has important consequences for future research at Glasgow University on the one hand, and in more general terms for the practical use of MQW waveguides. These are emphasised in the concluding section of this chapter.

5.2 DESIGN

The ideas presented in this section on the design of multiple quantum well double heterostructure optical waveguides were developed over the full three years of this project. Therefore, although the waveguide design is presented in a finalised form, some aspects of the design - for instance the number of well/barrier periods and the p-i-n diode doping - have changed over the years. This will become apparent in later chapters when several broadly similar structures are analysed.

5.2.1 Design Requirements and Assumptions

The requirements of MQW waveguides fall conveniently into three sets, each of which had to be satisfied by each waveguide grown if it was to be of use.

Quantum properties

The actual MQWS had to be designed so that the strong quasi-two-dimensional excitonic effects described in chapter two would be maximised. In this way it was hoped to maximise the novel properties of the MQWS waveguides. In addition, the structure was designed to be such that the wells were isolated from each other so that no coupling/decoupling effects would mask the multiple quantum well opto-electronic properties. The rectangular potential models of chapter two were used for the design.

Waveguide properties

It was planned to undertake experiments with lasers at a variety of wavelengths from $1.15\mu\text{m}$ to $0.85\mu\text{m}$. The waveguides were therefore required to sustain only one planar mode over this wavelength range. The working assumption was made that the refractive index of the MQWS for TE modes was equal to the weighted rms average of the bulk refractive indices of the constituent layers.

The waveguides also had to be low-loss, with the propagation loss from any deposited electrode being minimised.

Electronic properties

To observe the unique opto-electronic properties of MQWS it is necessary to apply a uniform electric field across the MQWS. It was desirable to be able to test the opto-electronic properties at fields up to the breakdown field of approximately 3×10^{15} V/cm. It was assumed that the electric field across the MQWS could be adequately described within the depletion layer approximation.

5.2.2 Quantum Properties

The design of the actual MQWS followed the work of Chemla et al' outlined in section 2.3.2. Chemla argues that to maximise the excitonic effects at the MQW absorption edge, the 2D binding energy must be maximised and that this occurs in (Al,Ga)As waveguides for wells of width 75-110Å. However, the width of these excitonic peaks also has to be less than the binding energy of the excitons for distinct peaks to be observed. In MQWS substantial inhomogeneities in such parameters as well thickness and barrier height broaden the excitonic peak, with further broadening occurring in poor quality material due to coulombic impurities i.e. donors and acceptors. However, the broadening due to well width fluctuations can be reduced if larger wells are used, since the shift in the i^{th} energy level is related to variation in well width (a) by the expression

$$(\Delta E_i / E_i) \propto (\Delta a / a)$$

The binding energy of an exciton in a well 75-110Å wide is approximately 8.5 to 12.5 meV'. Using the infinite well model for a 100Å well and the condition that the width of the exciton peak should be less than the exciton binding energy, one obtains an upper limit on well thickness fluctuations of 3-4 atomic layers. Therefore to maximise the excitonic effects one must:

- (1) grow material as pure as possible,
- (2) minimise MQWS inhomogeneities to $\Delta a \approx 3-4$ atomic layers,
- (3) grow wells in the 100-110Å range.

Obviously the first two requirements are beyond the control of the designer, except through his ability to choose the growth process. In the case of this project it was planned to use both MOVPE and MBE

grown material with MBE being favoured because of its superiority with respect to pureness and homogeneity. The last requirement was satisfied by designing for 100Å wells.

The aluminium concentration (x) of the barriers was designed to be 0.3 since MQWS with barriers in the $x=0.25$ to $x=0.35$ range had been shown to perform well²⁻⁴, and MQWS of this form had already been successfully grown at the SERC Central Facility for III-V Semiconductors⁵. With a designed barrier width of 100Å it was calculated that the first bound minibands would not be significantly broadened through interaction with neighbouring wells, and could therefore be adequately described by the tight binding approximation. The relatively small ratio of well to barrier width would also allow a large number of wells to be present for a given thickness of MQWS, thus maximising the effect of the quantum wells on the waveguide properties.

Fig 5-1 and 5-2 show the energy band structure for this MQWS using the Krönig-Penney model with an assumed conduction band mismatch to valance band mismatch ($Q=\Delta E_c/\Delta E_v$) of 0.65 and hole masses⁶ $m_{lh}^*(z)=0.34m_0$, $m_{lh}^*(z)=0.094m_0$. From this it can clearly be seen that two bound electron minibands, two bound light hole minibands, and four bound heavy hole minibands are predicted to exist, with the deepest bands being very narrow.

The number of well/barrier periods in the MQWS was limited by the patience of the material growers. To allow the structure to be grown on a manually controlled MBE system, the number of periods was limited to a maximum of approximately 25 periods. In fact, to produce a symmetrical structure, a MQWS of 26 wells and 25 barriers was requested.

5.2.3 Waveguide Properties

The first step in designing a planar MQW waveguide structure that would be single-mode from 1.15 μ m to 0.85 μ m was to determine the refractive index of the MQWS. As discussed in section 2.3.2 it was assumed that the refractive index of a MQWS for TE modes could be adequately modelled by using the rms model⁷. To calculate the refractive indices of the constituent layers for photon energies

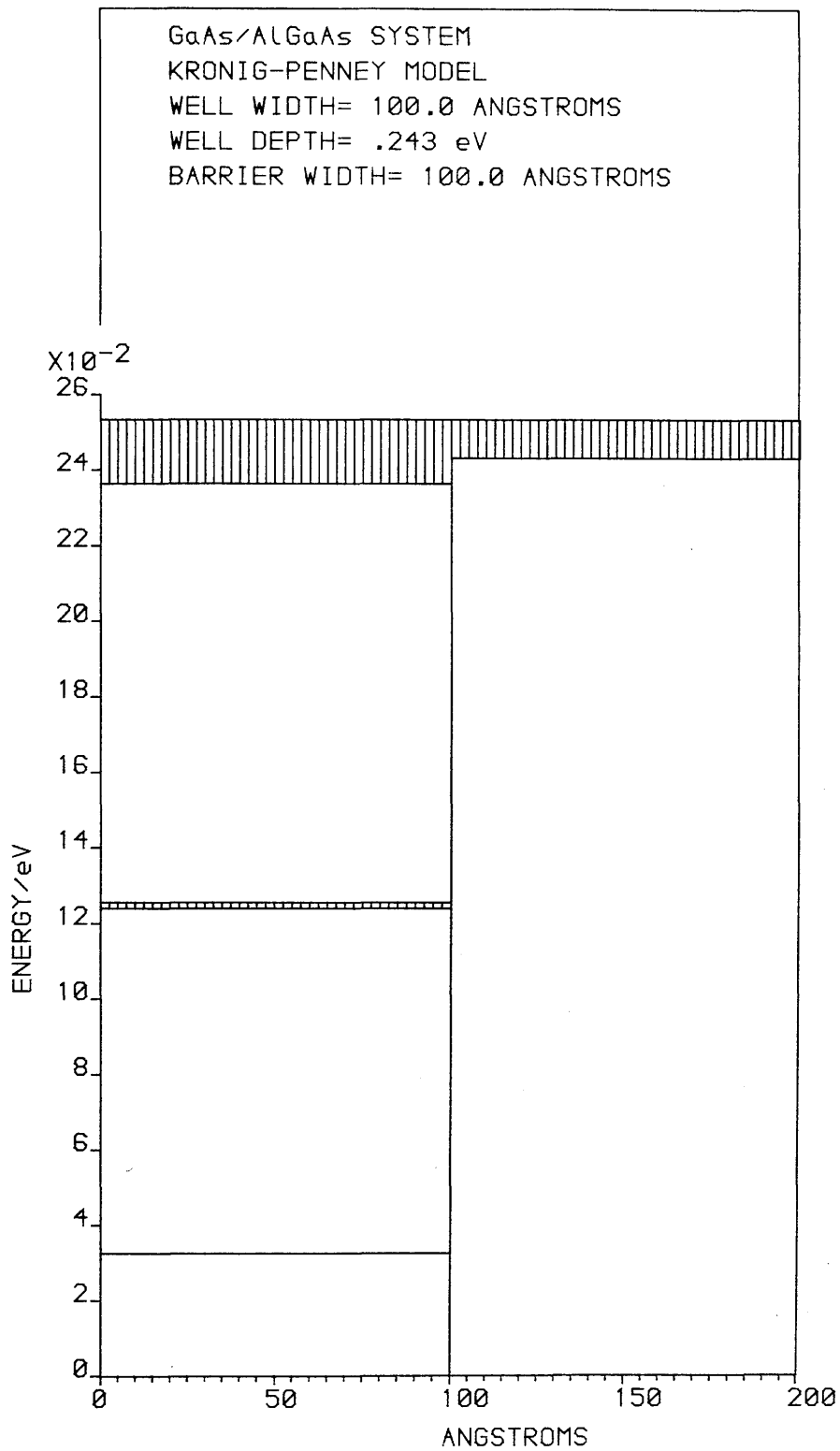


Fig 5-1 A real space, energy diagram of the electron band structure in the designed MQWS. Results from the Krönig-Penney model.

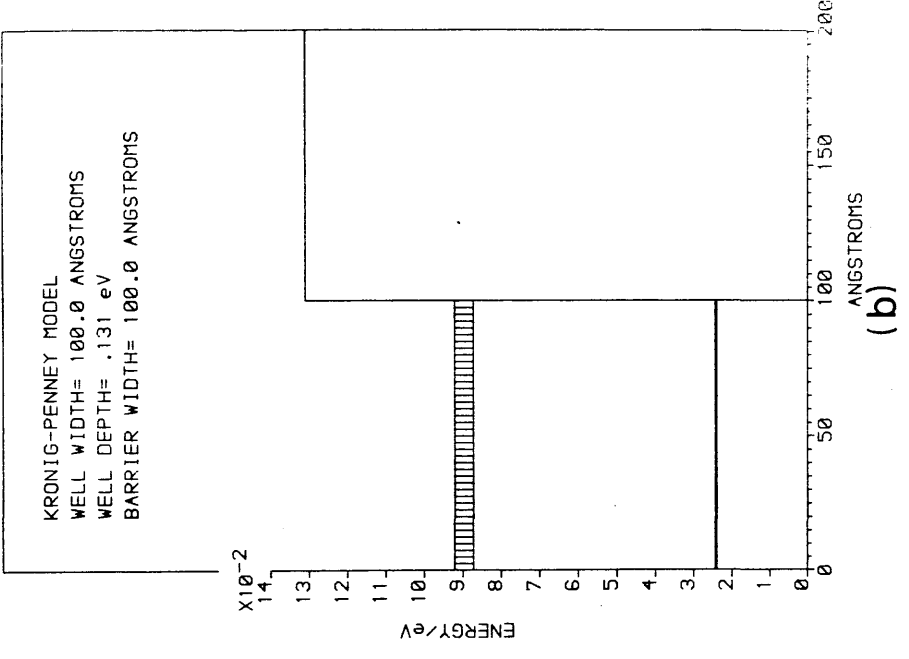
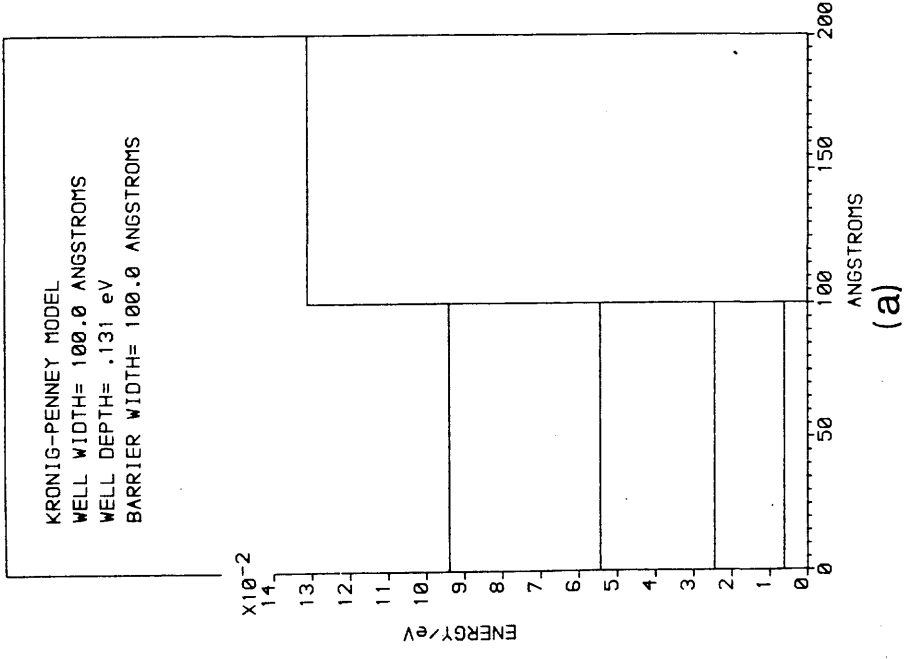


Fig 5-2 A real space, energy diagram of the hole band structure in the designed MQWS for (a) heavy holes, and (b) light holes. Results from the Kronig-Penney model.

below their band gap, the expression for the refractive index of (Al,Ga)As given by Adachi⁹ was used. The refractive index of Al_xGa_{1-x}As is thus given by:

$$n^2(\hbar\omega, x) = A_0(F(\chi) + (1/2)[E_0/(E_0+\Delta_0)]^{3/2}F(\chi_0)) + B_0$$

with

$$\begin{aligned} F(\chi) &= \chi^{-2}[2-(1+\chi)^{1/2}-(1-\chi)^{1/2}] \\ \chi &= \hbar\omega/E_0, \quad \chi_0 = \hbar\omega/(E_0+\Delta_0) \\ E_0 &= 1.425 + 1.115x + 0.37x^2 \\ E_0+\Delta_0 &= 1.765 + 1.115x + 0.37x^2 \end{aligned}$$

The parameters A_0 and B_0 were determined by fitting this function to the experimental data of Casey et al⁹ for $x=0$ to $x=0.38$, and Fern and Anton¹⁰ for $x=1$ giving:

$$\begin{aligned} A_0 &= 6.0 + 17.8x \\ B_0 &= 9.5 + 9.8x \end{aligned}$$

results somewhat different from Adachi's.

For photon energies above the band gap of GaAs, the experimental data of Casey et al⁹ was used to calculate the refractive index of GaAs.

Experiments were planned in which it would be necessary to propagate TM modes in both active and passive MQW waveguide structures. The propagation loss induced in a TM mode from a top surface electrode was minimised by using a double heterostructure.

The general structure of the waveguide and the MQWS (100Å wells and barriers, $x=0.3$) having been settled, it was possible to combine the rms model with the three layer planar waveguide model to determine cladding region aluminium compositions that would ensure that only a single planar mode was sustained over the desired wavelength range.

Fig 5-3 plots the value of MQW layer thickness at which the second planar mode is cut-off in a symmetrical double heterostructure waveguide with cladding layer composition (x) as the free space

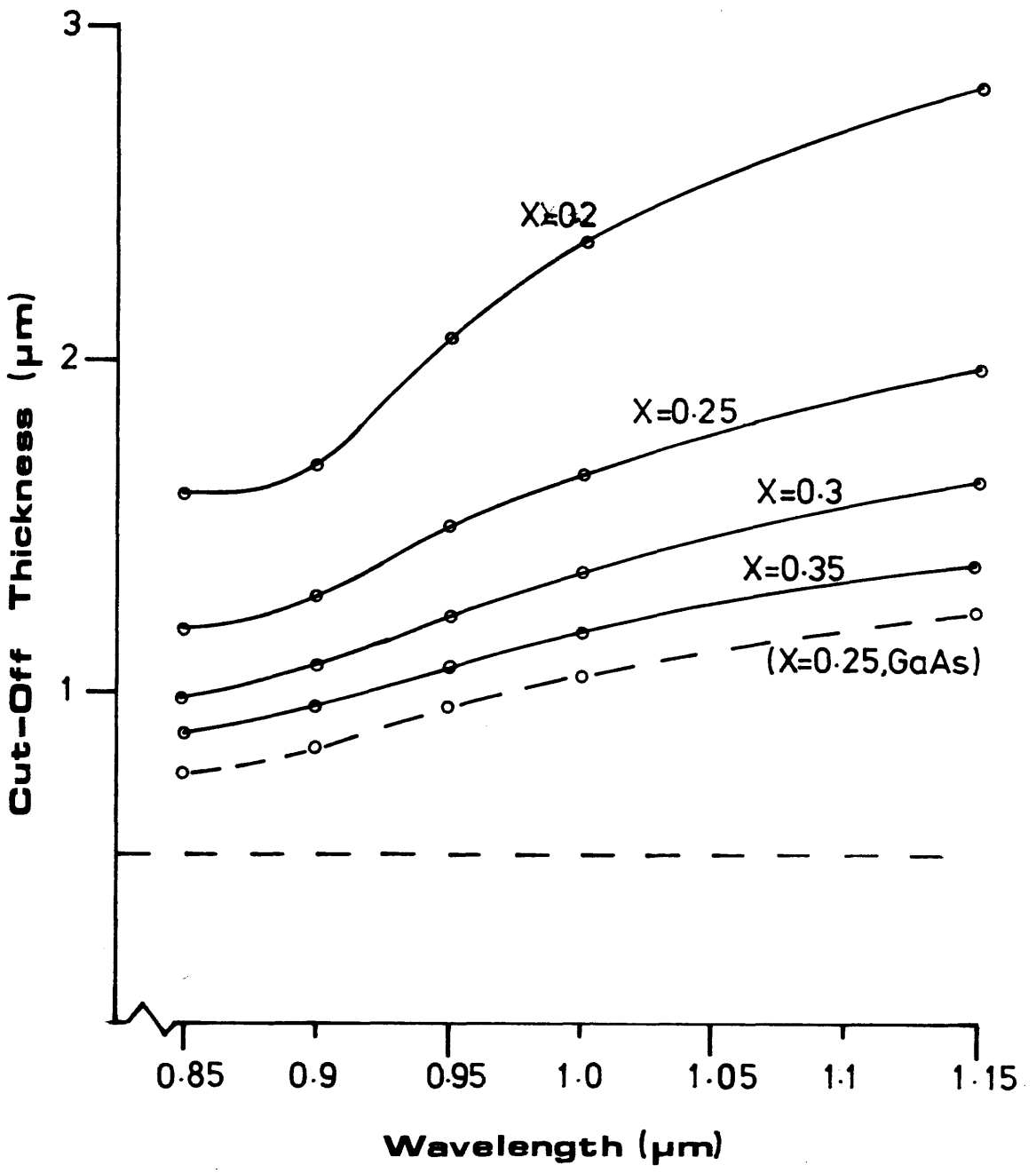


Fig 5-3 The cut-off thickness of the MQW guide layer against wavelength for several cladding layer compositions.

wavelength is varied. The cut-off thickness is seen to increase slowly with wavelength and decrease with x . For cladding compositions as high as $x=0.35$, Fig 5-3 suggests that a MQW layer $0.51\mu\text{m}$ thick would sustain only one mode right up to the band gap. However, in one of the few experimental investigations of the refractive index of MQWS it has been shown that the refractive index can be far larger than that predicted by the rms model¹¹. Using the refractive index of GaAs as an upper bound on the MQWS refractive index, Fig 5-3 shows that an $\text{Al}_{0.25}\text{Ga}_{0.75}\text{As}$ cladding layer would still allow single-mode propagation up to the band gap. The initial waveguide design therefore had this cladding composition.

The top cladding thickness was now chosen so that the absorption due to a deposited electrode would be small. Using the complex dielectric constant waveguide program of Mr D. F. Clark, the propagation loss shown in Fig 5-4 was calculated assuming the rms refractive index model and a gold top electrode. A top cladding thickness (t_3) of $2\mu\text{m}$ completely isolates the propagating mode from the metal and results in a propagation loss of approximately $\alpha \approx 5.6 \times 10^{-7} \text{dBcm}^{-1}$ and a modal intensity with an exponential decay term ($q \cdot t_3$) of 6.6 at $\lambda=0.9\mu\text{m}$. Fig 5-5 shows that at this cladding thickness the modal effective index is independent of cladding thickness for all wavelengths of interest and the waveguide can thus be treated as a three layer planar waveguide.

The final waveguide structure together with a plot of the intensity profile using the rms model at $\lambda=0.9\mu\text{m}$ is shown in Fig 5-6.

5.2.4 Electronic Properties

It was a requirement of the electronic properties of the waveguide structure that it be possible to apply a uniform electric field across the MQWS, and perpendicular to the layers. The novel opto-electronic properties close to the band edge of a MQWS rely on the fact that the strong room temperature exciton peaks can be shifted using a perpendicular electric field by up to 2.5 times the zero field binding energy before they are broadened by field ionisation¹². However, two factors tend to further increase the broadening of the excitonic peaks. Firstly, a MQWS which for zero applied field is perfectly homogeneous, will show excessive exciton peak broadening if

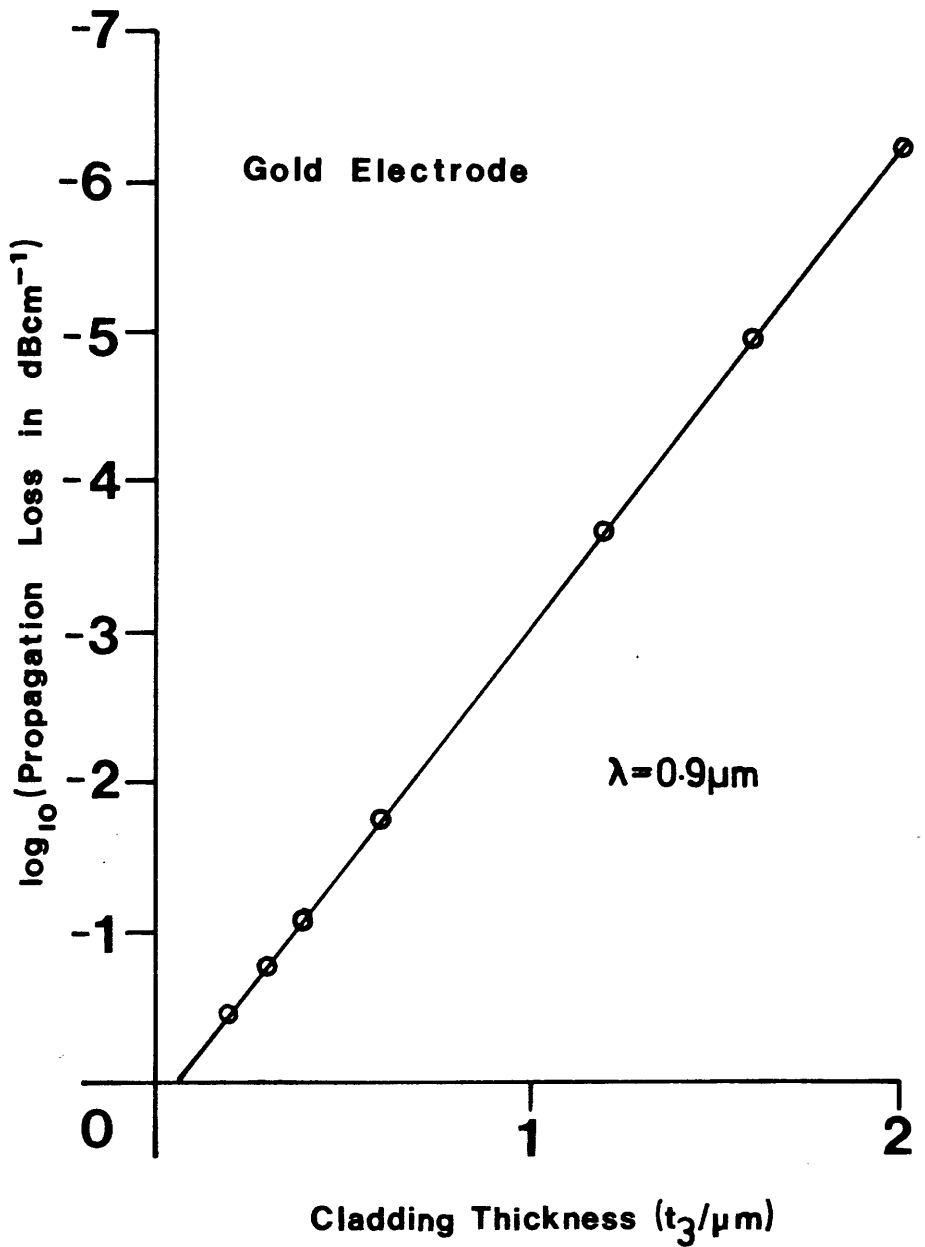


Fig 5-4 The propagation loss of the MQW-DH design versus upper cladding layer thickness for a gold top electrode.

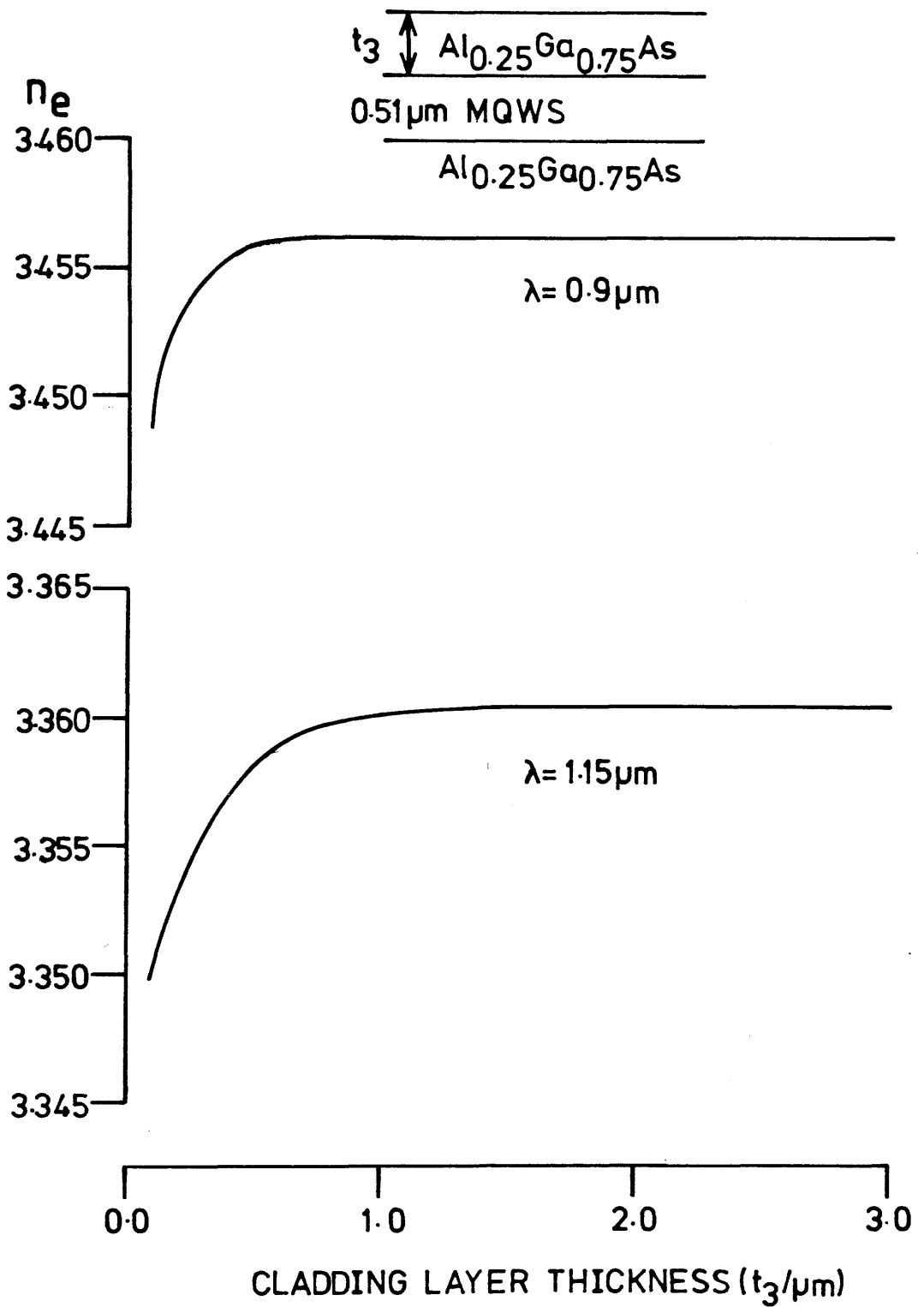


Fig 5-5 The modal effective index versus upper cladding layer thickness at two wavelengths.

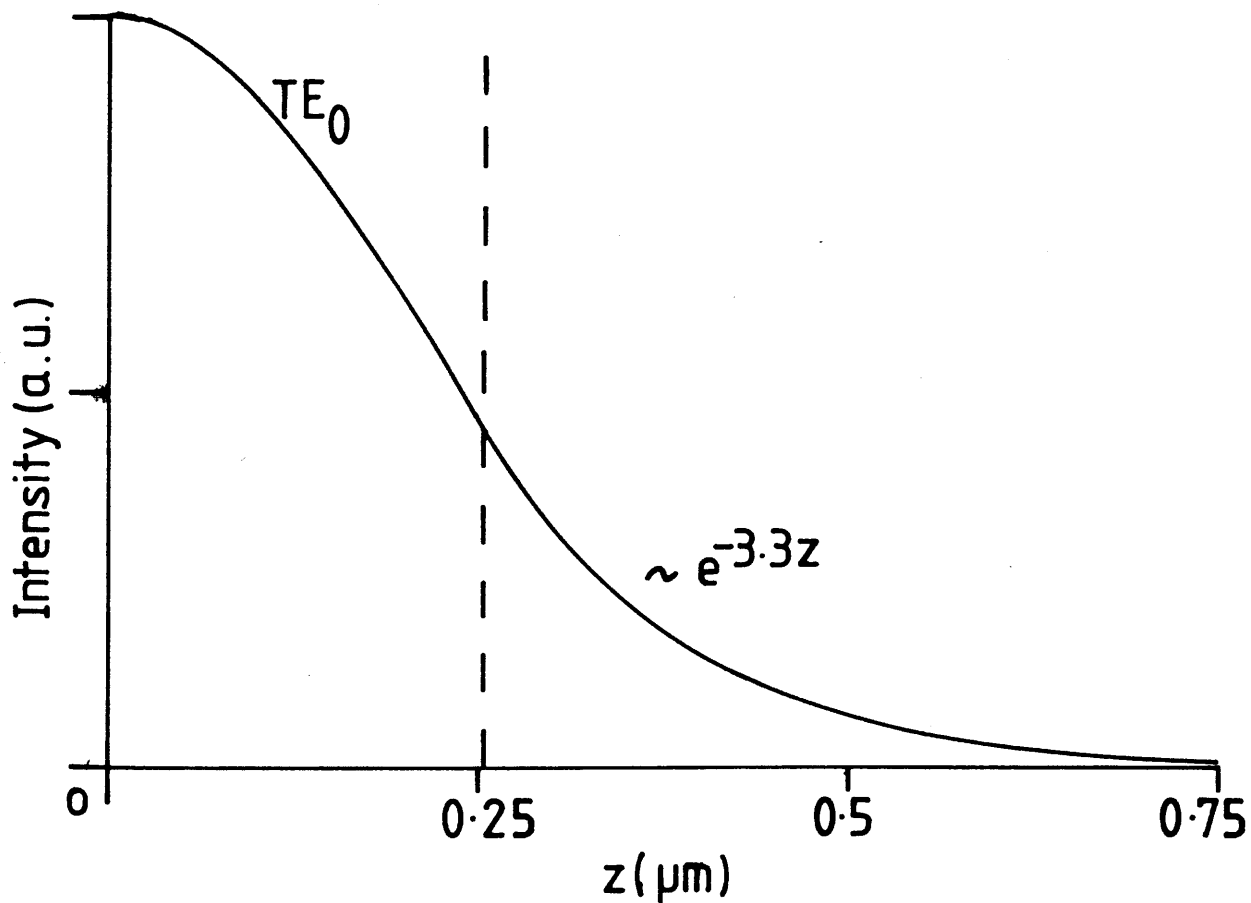
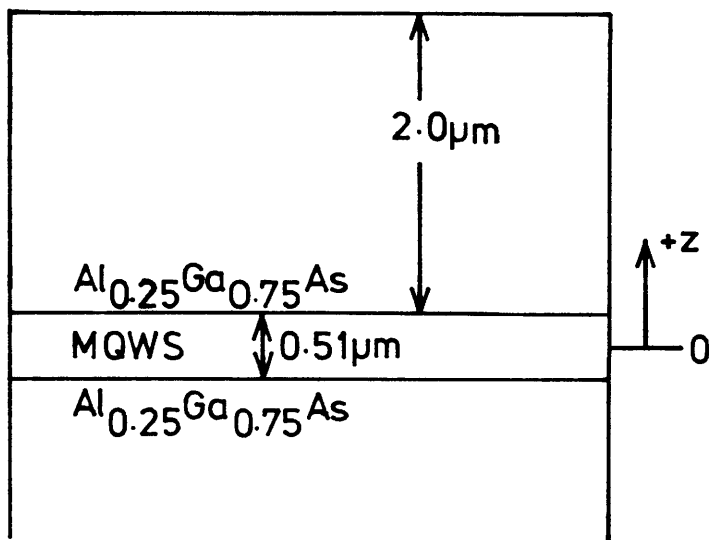


Fig 5-6 The final waveguide design together with a plot of the guided mode profile at $\lambda=0.9\mu\text{m}$.

a non-uniform applied field perturbs all the individual wells away from resonance. This non-homogeneous field broadening could easily mask the Stark-type exciton shift at the band edge. Secondly, ionised impurities will exist in any real MQWS. Once the MQW is depleted by the applied field, these coulombic impurities will cause a local random electric field component which will perturb the wells from resonance with any field component parallel with the layers further broadening the excitonic peak in a manner similar to the bulk Franz-Keldysh effect (see section 2.4.1).

This ionised impurities broadening may broaden the excitonic peaks at $V_A=0$, since with a low doped MQWS, the built-in voltage of the structure used to apply the field will fully deplete the MQW region. This effect can only be reduced by choosing the semiconductor growth technique and growth conditions that minimise impurity introduction.

The former effect, inhomogeneous broadening, can be minimised by the design of the diode structure used to apply the electric field across the MQWS. There are two common ways of applying an electric field across a waveguide. The first, commonly used for single heterostructure waveguides, is to form a Schottky contact on top of the uniformly low n-doped epitaxial layers. This method was described in chapter four when it was used to form an n/n⁺ GaAs phase modulator. By reverse biasing the Schottky contact, an electric field can be applied across the depletion region. It will be shown in chapter seven that this method could not be used with the MQW-DH structure because Schottky contacts that could withstand the voltages needed to deplete through the top cladding layer could not be fabricated.

It was therefore necessary to design a p-i-n diode within the MQW-DH waveguide (see the insert in Fig 5-7). As with the Schottky barrier, reverse biasing the p-i-n diode allows an electric field to be applied across the depletion region. The p-i-n diode structure has several disadvantages. Firstly, the introduction of high doping levels to the cladding layers will inevitably cause free carrier absorption of the guided mode. In addition, the field produced across the "intrinsic" region can never be totally uniform due to the presence of a finite background doping. It was necessary to obtain a quantitative limit on the required uniformity of this electric field,

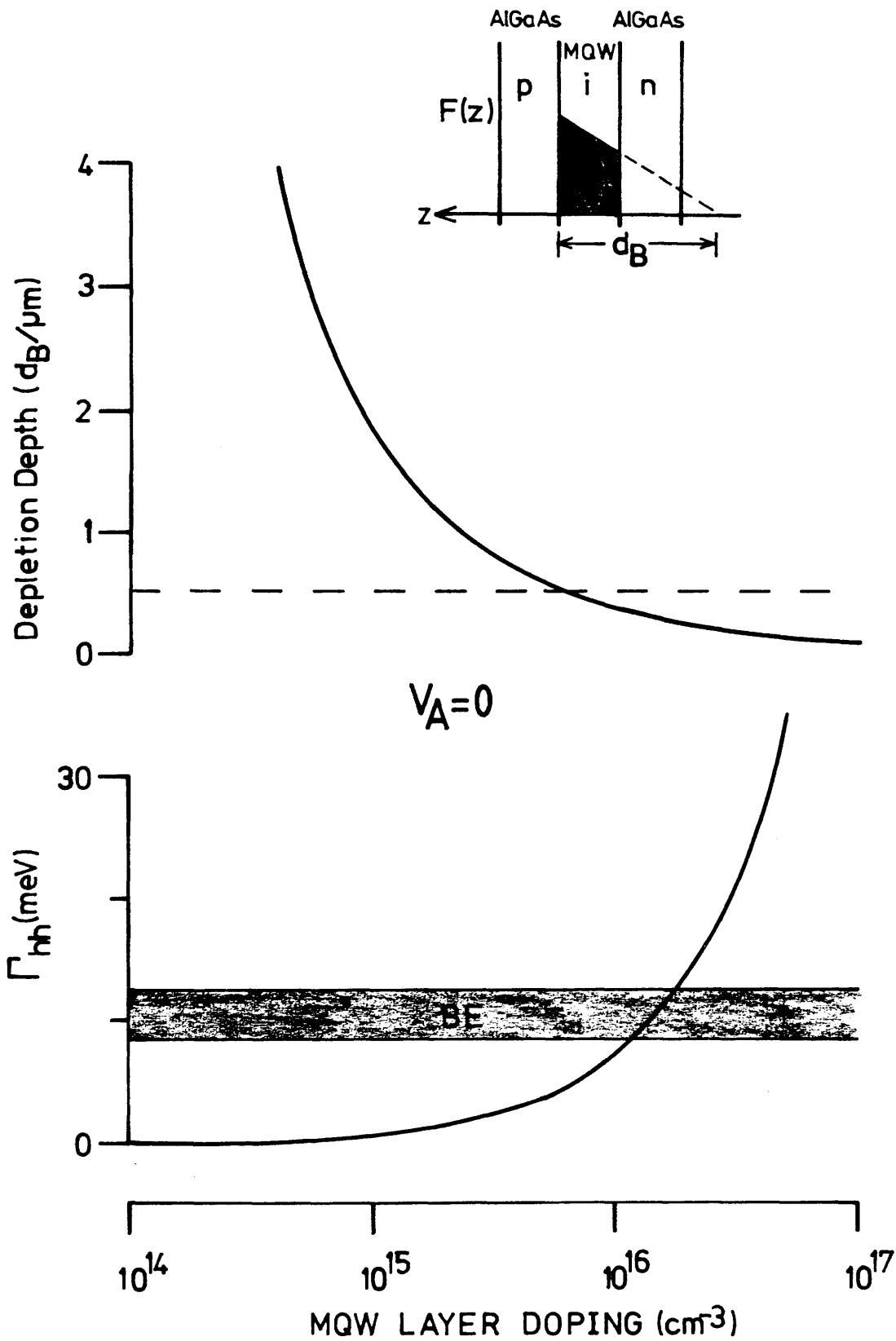


Fig 5-7 The difference in excitonic peak positions of the outer wells (Γ_{hh}) and the built-in depletion depth (d_B) versus MQW layer doping level.

and hence an upper limit to the acceptable background doping of the "intrinsic" layer. Such a suitable limit would be to require that the background doping was such that the two outer wells of the MQWS had exciton peak energies that differed due to the built-in voltage by less than, say, one quarter of the exciton binding energy (BE). At room temperature the designed MQWS has a binding energy of approximately 10meV¹. Using the data of Miller et al^{12,13}, it will be shown in chapter seven that the heavy hole exciton peak shift (ΔE_{hh}) in a structure similar to that designed is quadratically dependent on the applied field (F) thus:

$$\Delta E_{hh}(\text{meV}) = 0.199 \times 10^{-12} F^2$$

where F is in V/m.

Using the standard depletion layer approximation and assuming a p-doped layer of $5 \times 10^{17} \text{cm}^{-3}$ the difference in peak positions for the two outer wells (Γ_{hh}) was found to vary with intrinsic layer doping as shown in Fig 5-7. From this it is clear that to have well-defined exciton peaks ($\Gamma_{hh} < BE/4$) at zero applied volts, the intrinsic doping layer must be $N_D < 3 \times 10^{15} \text{cm}^{-3}$. It can also be seen that for this doping level the MQW region at 0.51 μm thick will be completely depleted with no external voltage applied. Since ΔE_{hh} varies quadratically with the applied field, Γ_{hh} increases with F (see Fig 5-8). However, this reduction in peak visibility will be countered by the increased shift in the peak position away from the 2D density of states edge. These conclusions are confirmed by Miller et al^{12,13} who observed distinct exciton peaks for applied fields up to 10⁵V/cm using an intrinsic region with $N_D \approx 2 \times 10^{15} \text{cm}^{-3}$.

Fig 5-8 shows the calculated maximum, minimum and average electric fields within the MQW "intrinsic" region with a background doping of $3 \times 10^{15} \text{cm}^{-3}$. It shows that to obtain an average applied electric field of $3 \times 10^5 \text{V/cm}$, an applied voltage of approximately 15 Volts is needed. However, for this applied voltage the broadening due to field inhomogeneity has increased to $\Gamma_{hh} \approx 3 \times BE_0$.

Fig 5-9 plots the applied electric field as a function of position in the MQWS for two applied voltages to give an indication of the

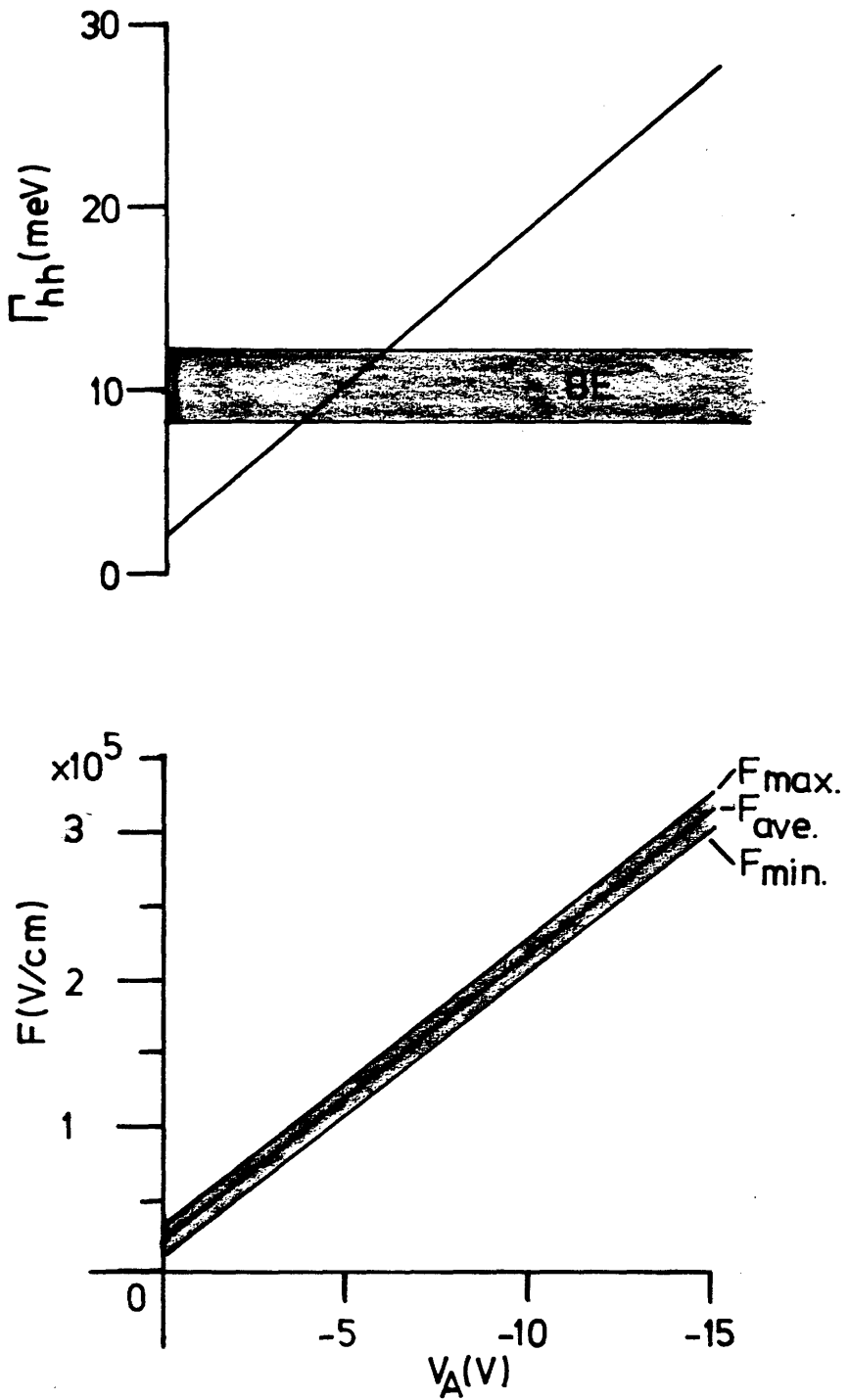


Fig 5-8 The difference in excitonic peak positions of the outer wells (Γ_{hh}) and the applied field (F) versus applied voltages (V_A).

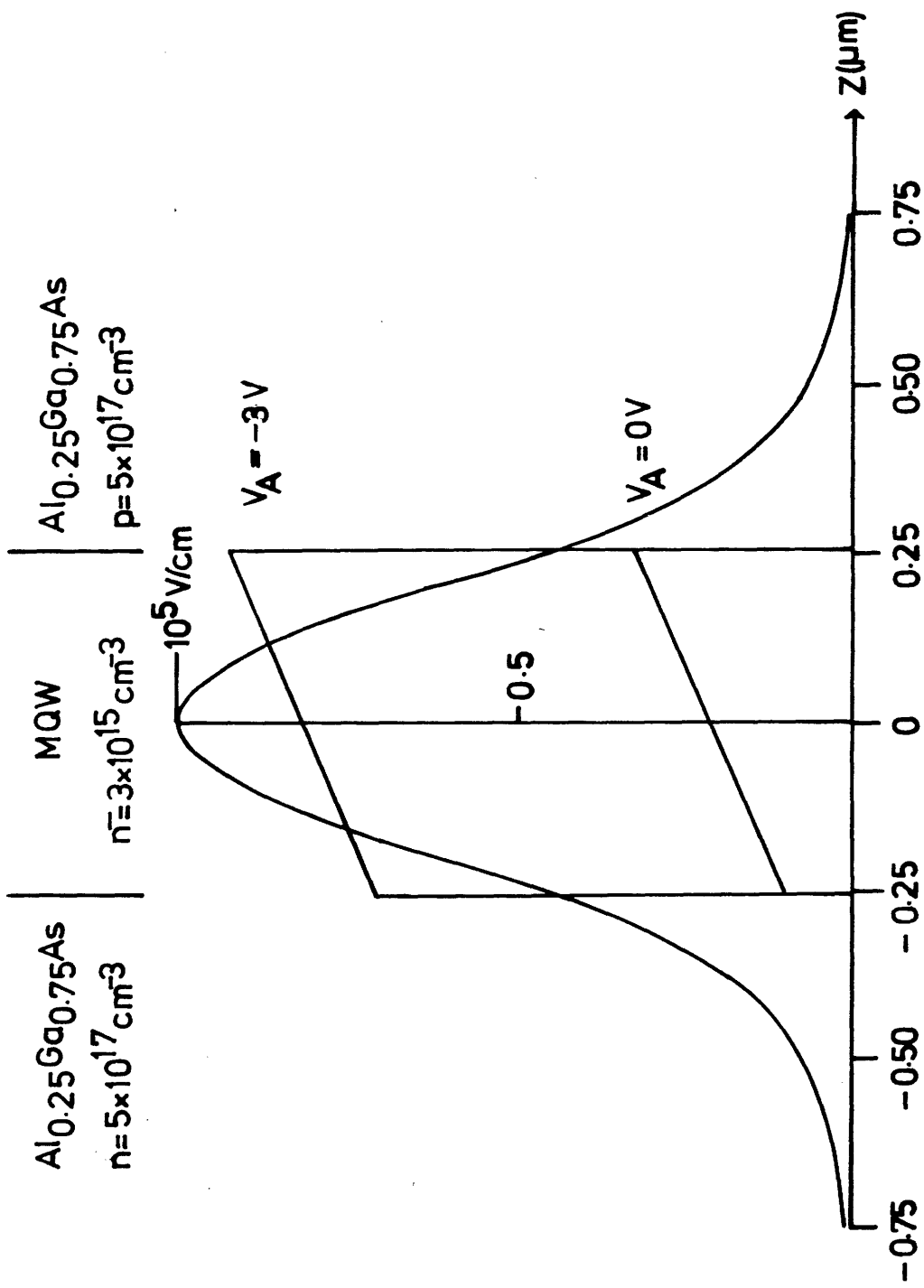


Fig 5-9 The applied electric field and optical mode

intensity in the final MQW-DH design at $\lambda = 0.9 \mu\text{m}$.

overlap between the optical and electrical fields in the structure at $\lambda=0.9\mu\text{m}$.

5.2.5 Miscellaneous

Several other considerations influenced the design. Firstly a very thin capping layer of p^+ GaAs was specified as the very top layer to aid the fabrication of ohmic contacts to the structure. A thick $\text{Al}_{0.5}\text{Ga}_{0.4}\text{As}$ etch stop layer was placed below the bottom cladding layer to allow selective etches to remove the substrate, and a n^+ GaAs buffer layer was specified to be grown as the very first epitaxial layer to smooth out any substrate imperfections.

The final structure thus had the form shown in Fig 5-10.

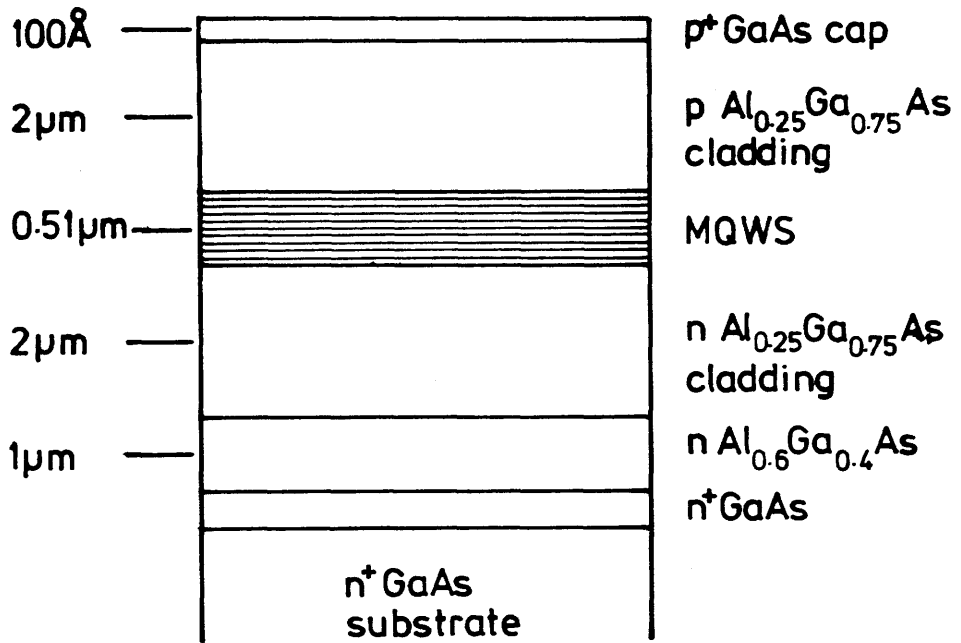
5.3 GROWTH OF MQWS

The growth of MQWS has only become possible with the recent development of the epitaxial growth techniques of Vapour Phase Epitaxy (VPE) and Molecular Beam Epitaxy (MBE) to the stage where material parameters such as layer thickness, composition, and impurity concentration can be well controlled. The growth of multi-layer semiconductor structures by VPE or MBE is a highly skilled task, and so the actual growth of MQW waveguides was left to others.

Epitaxial growth is the growth of a thin crystalline layer on a single crystalline substrate where the atoms in the growing layer mimic the arrangement of the substrate. Epitaxy allows lower growth rates and temperatures than bulk growth techniques, which ensures higher purity and perfection in the epitaxial layer, with the growth of compound semiconductors being simplified. Epitaxy is nearly the exclusive growth technique for alloys such as (Al,Ga)As.

The requirements on any technique for growing MQWS can be summarised as:

- (1) The ability to grow several materials with abrupt heterojunctions between them, with fluctuations in well width being less than 3-4 atomic layers.



$p^+ \gg 10^{18} \text{ cm}^{-3}$
 $p \approx 5 \times 10^{17} \text{ cm}^{-3}$
 $n \approx 5 \times 10^{17} \text{ cm}^{-3}$
 $n^+ \gg 10^{18} \text{ cm}^{-3}$

MQWS: 25 wells of GaAs and 25 barriers
 of Al_{0.3}Ga_{0.7}As with well and
 barrier thickness = 100 Å.
 Doping $n^- \ll 3 \times 10^{15} \text{ cm}^{-3}$.

Fig 5-10 Details of the final MQW-DH waveguide design.

- (2) The ability to grow high purity material with background concentration less than approximately $3 \times 10^{15} \text{cm}^{-3}$ and few interface defects.
- (3) The ability to grow layers doped over a wide range of impurity concentrations with abrupt doping changes between layers.
- (4) The ability to grow ultrathin layers interspersed with thicker layers in the same structure.

Liquid Phase Epitaxy (LPE) can produce very high quality material but the morphology of LPE material is difficult to control; both long range and short range uniformity is low; and abrupt interfaces are difficult. The growth of MQWS is therefore limited to VPE and MBE.

5.3.1 Metal Organic Vapour Phase Epitaxy (MOVPE)

MOVPE, a subcategory of VPE, uses an organometallic transport mechanism. MOVPE is the simplest VPE system mechanically, requiring only an envelope to preserve the high purity ambient and an RF heated substrate holder. MOVPE has also been shown to be versatile with the growth of thin layers for MQWS having been demonstrated^{5,14}.

A schematic diagram of the MOVPE system used to grow MQWS waveguides at the SERC Central Facility for III-V Semiconductors is shown in Fig 5-11. To grow (Al,Ga)As, liquid trimethylgallium (TMG) is held in a bubbler at -10°C , and hydrogen is passed through it to transport the vapour to a horizontal reactor cell which is at atmospheric pressure. In a similar way, trimethylaluminium is held in a bubbler at 20°C for introduction to the chamber, and arsine (AsH_3) gas is held in a cylinder as a 10% mixture in hydrogen. On reaching the chamber, reactant molecules have to pass through a boundary layer of stagnant gas over the sample. For temperatures between 600 and 850°C this mass transport through the boundary layer is the growth rate determining step, with the rate being linearly dependent on TMG concentration and independence of temperature or AsH_3 concentration. The TMG is completely decomposed before reaching the boundary layer, with the AsH_3 only decomposing slowly unless catalysed by solid GaAs. The reactions involved are:

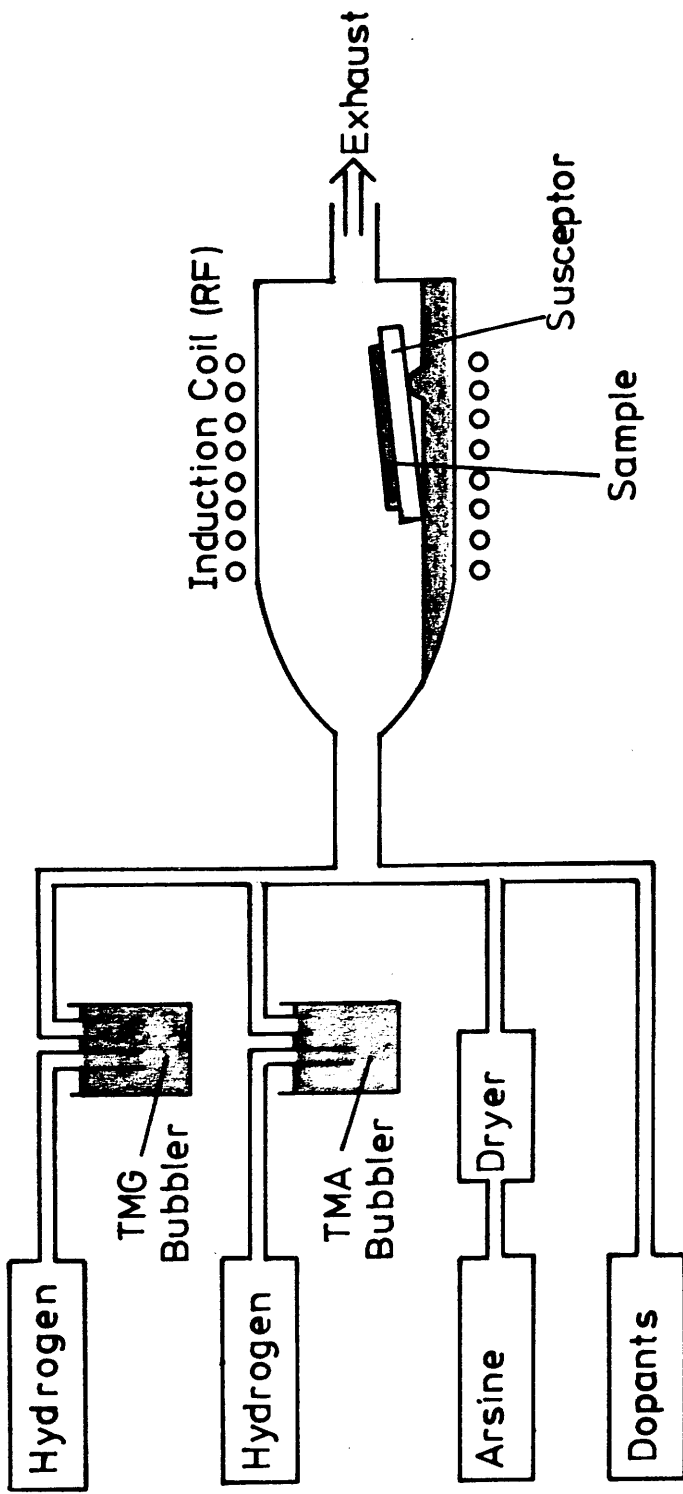


Fig 5-11 A schematic diagram of a MOVPE system.



To introduce n-type dopants, silane (SiH_4) is held at 4ppm in H_2 . Dimethylezinc (DMZ) is used to introduce a p dopant and is held at 700ppm in H_2 . Before entering the chamber the silane is dried using a bubbler containing an AlInGa ternary melt.

A complex gas handling system using mass-flow controllers is needed to reduce gas transients and minimise the system's response time and hence allow abrupt material and doping transitions to take place. During growth, the group V / group III gas ratio is kept at approximately seven with the GaAs growth being continuous and TMA being switched in to grow (Al,Ga)As. Growth rates between 1 and $5\mu\text{m}/\text{hour}$ can be obtained, but with a reactor response time of approximately 1 second, a slow growth rate is used to allow abrupt transitions. The growth conditions used for MQWS could, in an ideal reactor, produce monolayer transitions. However, practical problems such as turbulence in the reactor is thought to significantly degrade the abruptness of the transitions. SIMS profiling of double well structures grown by MOVPE show interface abruptness at least as good as the resolution of the measurement (20\AA)⁵.

MOVPE material suffers from two major impurities. The first is carbon which is obviously present in large quantities in the reaction zone in the form of methyl groups. Some of this can become elemental carbon and be incorporated into the growth layer, where it acts as a donor, making the background n-type¹⁵. The carbon incorporation in GaAs can be reduced by reducing the growth temperature to around 600°C , but even here a background doping of approximately 10^{15}cm^{-3} n-type will remain due to the carbon. The problem is worse in (Al,Ga)As growth because the Al-C bond is strong, leading to higher incorporation. In addition, (Al,Ga)As has to be grown at high (800°C) temperatures to prevent epitaxial problems (see below). So the growth temperature of (Al,Ga)As is something of a compromise with carbon concentrations of 10^{16}cm^{-3} usually being the lowest concentration obtainable (compared with $7 \times 10^{14}\text{cm}^{-3}$ of LPE). When growing MQWS, the growth temperature must be a further compromise between 600°C for GaAs and 800°C for (Al,Ga)As. 720°C was used for the growth of the

MQW waveguides, a growth temperature which had previously resulted in good quality (Al,Ga)As lasers¹⁶. Although incorporated carbon is found to reduce electron mobility in devices, it does not appear to act as a significant non-radiative recombination centre¹⁷.

Unintentional incorporation of oxygen in MOVPE (Al,Ga)As is a severe problem because of the strong Al-O bond. This causes O₂ and H₂O(V) to be incorporated into the growing surface. Oxygen incorporation results in a wide variety of problems such as heavy compensation and poor PL efficiency. To reduce the incorporation of oxygen, the whole reactor must be leak free, and chemicals like silane must be dried using the eutectic liquid AlInGa. The use of a horizontal, Bass, growth chamber has itself been shown to reduce oxygen incorporation because of gettering of the oxygen containing species to the reactor wall.

This gettering process has been further enhanced in the MR100 by using a new design of chamber, the Cambridge Instruments 1x2 reactor. This chamber is much longer than the Bass chamber, with a flat geometry and tapered gas inlet that allows incoming gases to gradually expand. This reduces the turbulence in the growth chamber and has allowed 23Å quantum wells to be grown with a low temperature photoluminescence FWHM of 6.35meV¹⁸ i.e. as good as that produced by MBE¹⁸.

5.3.2 Molecular Beam Epitaxy (MBE)

MBE is conceptually a very simple crystal growth technique being essentially a highly controlled evaporation in an ultra-high-vacuum (UHV). The advantages of MBE are:

- (1) The use of high-impurity elemental sources rather than less pure compounds results in the highest purity.
- (2) Growth occurs at UHV (10⁻¹⁰tor) apparatus where background concentrations of undesirable gases are very low.
- (3) Extreme control of growth rate and composition leads to very abrupt changes in composition and/or doping level.

However, although conceptually simple, MBE is very sophisticated in terms of the apparatus used. Fig 5-12 is a schematic diagram of

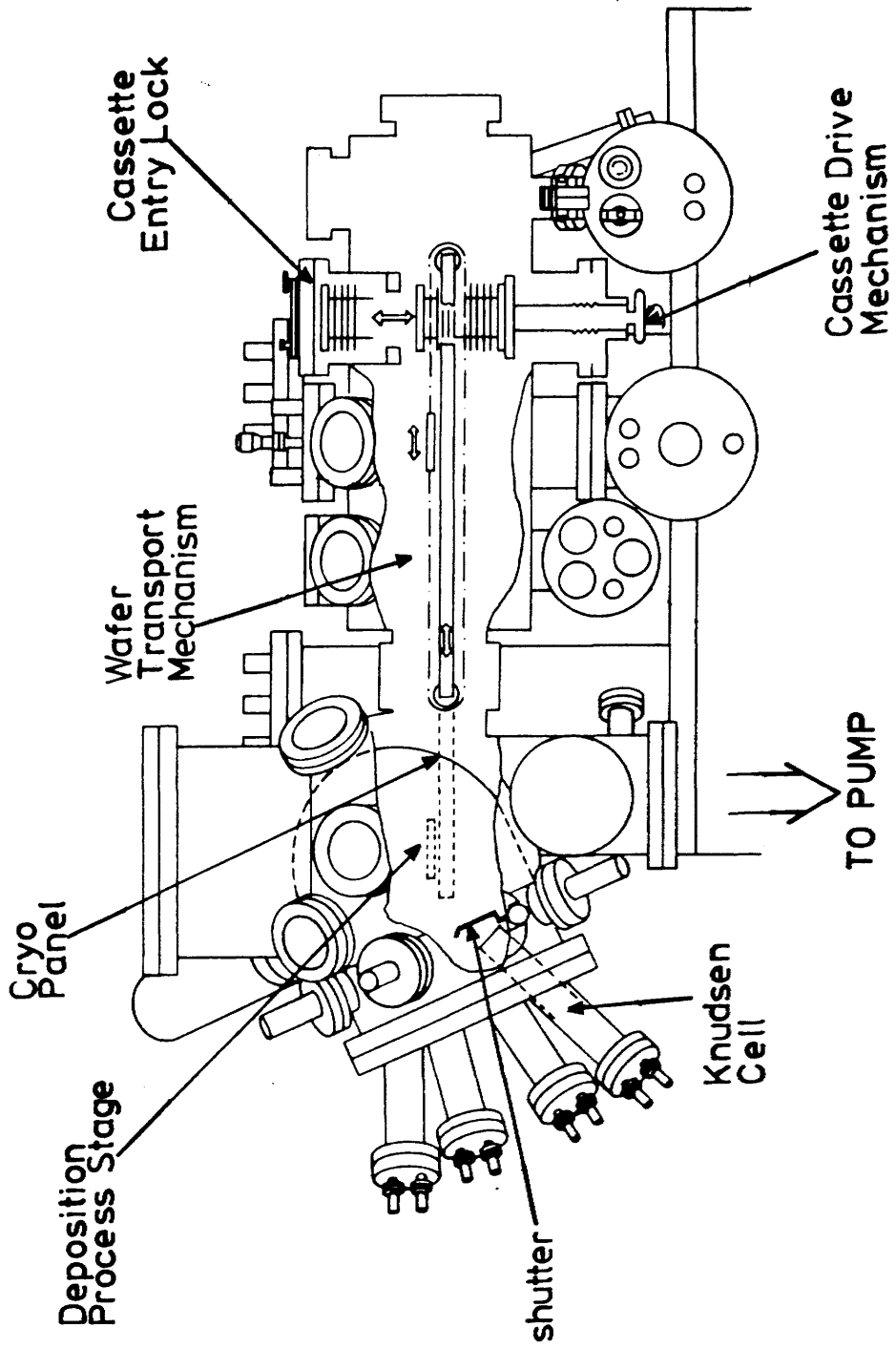


FIG 5-12 A schematic diagram of a V80H MBE system.

the V80H MBE system used to grow MQWS at Glasgow. It is based on a three chamber UHV system which is cryo-pumped, and includes large areas of liquid nitrogen cooled panels. The provision of a vacuum interlock to enable substrates to be introduced into the chamber without breaking vacuum is essential if high quality layers are to be grown.

The atomic or molecular beams used in MBE are formed in heated Knudsen effusion cells. The material to be evaporated is contained in a crucible which is radiatively heated from a separate winding. In the cell, the liquid or solid phase are in equilibrium, with the mean free path of the vapour atoms or molecules being much larger than the cell orifice, ensuring molecular flow (Knudsen effusion). Beam intensities are controlled by the cell temperatures. Individual cells are thermally isolated by heat shields and the flux is regulated by a shutter operating in front of each aperture.

Fluxes are monitored by an ion gauge which can be rotated in and out of the beams. Other analytical facilities include a mass spectrometer for residual gas analysis and leak checking, and a reflection high energy electron diffraction (RHEED) arrangement for assessing the surface quality before and during growth.

A RHEED arrangement consists of a 5-20keV electron gun and fluorescent screen. The electron beam is incident at a very shallow angle to the substrate surface. The diffracted electron beams form a characteristic pattern on the fluorescent screen which provides information on the morphology. The intensity of the RHEED pattern is a maximum as each monolayer is complete, and it can thus be used to monitor deposition monolayer by monolayer if the layer is not too thick, or calibrate growth rates.

Highly uniform growth can be obtained using MBE by rotating the specimen at a rate slower than the growth rate of one monolayer¹⁹, with fluctuations in composition and growth rate being kept to <1% over 5cm.

Growth is initiated by bringing the substrate to the appropriate temperature (600-700°C) in a beam of arsenic, and then opening the shutter of the group III element source. Growth rates are in the

range 2-3 μ m/hr. The arsenic flux is typically some 3-5 times greater than that of the group III element, the latter determining the growth rate. The actual growth mechanism is complex, but RHEED patterns show that GaAs and (Al,Ga)As films grow predominantly by a process of two-dimensional nucleation of new monolayers¹⁹.

Source material is usually elemental, with the group III elements producing monoatomic beams and the arsenic producing As₄ or As₂ molecules. Dopant beams are also produced from Knudsen cells with the elements used being: Be for p-type films, and Si for n-type, all of which evaporate as monomers. Free carrier concentrations in GaAs can be controlled between 10¹⁴ and 10¹⁹cm⁻³ with the lower limit being due to background impurities, carbon being a main contaminant¹⁹.

The achievement of high quality GaAs layers has been rather slow. The first MBE layers were grown in 1968²⁰, with background impurity concentrations of less than 10¹⁵cm⁻³ only obtained in 1979²¹. The growth of high quality (Al,Ga)As is much more difficult due to the effects of minute quantities of O₂ or H₂O at the very low MBE growth rates. Good quality (Al,Ga)As was obtained in 1979²² with present "state of the art" MBE (Al,Ga)As being as good as that grown by LPE.

However, it is in the production of thin and/or multi-layer structures that MBE excels²³, with multi-layer GaAs/AlAs structures having been grown to unit cell dimensions (10\AA). MBE has therefore led the way in the growth of many new semiconductor structures outlined in the general introduction to this thesis.

5.3.3 Comparison

The following table is included to allow a comparison between epitaxial growth techniques.

	LPE	MOVPE	MBE
background			
GaAs doping	10^{14} n-type	5×10^{14} n-type	10^{14} n-type
impurity sources	III melt container	MO sources C contamination	Vacuum sources System (walls)
AlGaAs $N_D + N_A$	7×10^{14}	approx. 10^{16}	approx. 10^{15}
morphology	poor	good	good
complexity	simple	complex	very complex
inherent advantages	simple high purity	large scale most versatile	most abrupt (2-10Å)
inherent disadvantages	limited volume inflexible morphology	C contamination	Expensive slow growth

This comparison would suggest that if possible MBE should be used to produce MQW waveguide structures since the background doping of the (Al,Ga)As in MOVPE MQWS would be outwith the desired doping level specified in section 5.2.4 that was necessary to minimise inhomogeneous broadening. In addition, the large amount of carbon impurities in MOVPE (Al,Ga)As would make ionised impurity broadening a problem. MBE produces the most abrupt interfaces, thus aiding the use of rectangular well models.

5.4 ANALYSIS

Now that the waveguide design and the methods of growing the structure have been described, an analysis will be made of the quality of the structures that were actually grown. At this stage, the chronology of events cannot be ignored and so a brief history will be given indicating when and where given structures were grown. Then a brief outline of the various analysis techniques used will be given, followed by the results of the analyses of specific samples.

5.4.1 History

From the start it was perceived that obtaining suitable MQWS would be a difficult and important part of this project. With this in mind, three sources of high quality epitaxial (Al,Ga)As were secured. The higher quality of material obtainable from MBE would be available from the cooperating industrial body, British Telecom Research Laboratories, and from the MBE group within the Department of Electronics and Electrical Engineering, University of Glasgow. MOVPE material would be available from the SERC Central Facility for III-V Semiconductors. Unfortunately, only a few months into the project the direction of research at BTRL moved away from (Al,Ga)As, and no MQWS layers were obtainable from this source over the whole project period. The aim at this stage in the project was to obtain MQW-DH waveguide structures that were uniformly low n-doped throughout for depletion by a top Schottky contact. The SERC Centre was first to supply a sample (NJ177) but this differed substantially from design requirements. The MBE group at Glasgow then produced a series of samples grown by Mr J. Frost which provided useful data but showed that the Schottky depletion technique would not work (VG200 and 215). After the design was changed to a p-i-n diode structure, Glasgow's MBE group failed to produce a sample that fulfilled the requirements of

- (1) having a clear, single planar mode,
- (2) showing bright PL, and
- (3) having good diode electrical characteristics.

Dr. O. Mikami, on sabbatical from NTT, Japan, obtained a MBE layer from NTT (NTT203) which was an example of how high the quality of MBE MQWS can be. Unfortunately the sample did not include a p-i-n diode.

At this stage (June-November 1985) considerable effort was being put into obtaining acceptable performance from the Styryl-9 dye-laser described in section 3.4.2 so that an earlier sample from Glasgow's MBE group (VG215) could be used to test the passive waveguide characteristics of MQW-DH. What was really needed, however, was a series of consistent runs on a growth system where each sample could be quickly checked and the results used to alter the design or change growth conditions. Thus a single structure would be obtained on which both passive and active tests could be made. This series of runs was only achieved after a personal visit to the SERC Central Facility for

III-V Semiconductors. Although only a partial success, this series of MOVPE grown samples (CPM57, 68, 96) produced the only sample to satisfy all three of the requirements mentioned above. It was thus only in February 1986 that a suitable laser source and sample were available with which to investigate the passive and active, planar and rib waveguide characteristics of MQW-DH close to the two-dimensional band edge.

5.4.2 Methods

The methods available to investigate the quality of MQWS are limited by the very high resolution required. Such techniques as Auger electron spectrometry and secondary ion mass spectrometry (SIMS) are limited to resolutions of 10Å at very best¹⁹. The available methods of obtaining structural/compositional information with the necessary level of spatial resolution are limited to transmission electron spectroscopy (TEM) and optical techniques (eg. photoluminescence (PL) and etalon absorption). TEM involves long sample preparation times and was not readily available, but a method was developed to use a s.e.m. to image the MQWS directly. Optical techniques were available, but it will be seen that their usefulness was limited by the need to use models to relate the optical data to the actual physical structure of the MQWS.

S.e.m. imaging of the MQWS

Samples were cleaved and a s.e.m. used to image the facet. The contrast between GaAs and $Al_{0.3}Ga_{0.7}As$ was found to be too low to allow the cross-sectional image of the MQWS to be observed. A selective etch ammonia:hydrogen peroxide was used in an attempt to increase the contrast but was found to be too strong, destroying edge definition as it selectively etched away the GaAs wells. However, by immersing the sample in a 5:95 (v/v) deoxidising solution of ammonia (25% solution): H_2O for eight seconds, it was found that the contrast was increased without any deterioration in edge definition. $(Al,Ga)As$ has a deeper oxide than GaAs, so when removed, the oxide leaves a very slightly stepped surface, thus improving the contrast by producing surface relief.

Etalon transmission data

The nature of the absorption edge of some samples was investigated using a spectrophotometer at both room and low temperature for beam propagation perpendicular to the MQWS layers. For this to be possible it was necessary to remove the GaAs substrate since in the (Al,Ga)As system the MQW absorption edge is above the GaAs absorption edge. Initially this was done by cementing a sample face down onto a glass slide, and selectively etching off the whole back surface. A standard spectrophotometer in the Department of Chemistry, University of Glasgow, was then used to measure the etalon's absorption as a function of wavelength for propagation perpendicular to the MQW layers. The sensitivity of this method was severely limited by the large beam sizes of the spectrophotometer used.

Later, Mr J. Isaac, Department of Electronics and Electrical Engineering, University of Glasgow, used a procedure set out by Mr W. S. Mackie et al²⁴ to etch away a selected area of the GaAs substrate leaving the epitaxial layers as a free-standing membrane. The procedure was as follows:

- (1) a thick photoresist layer was painted onto the front and back of the sample,
- (2) a suitable mask was used to open a 1mm x 2mm window in the bottom resist layer,
- (3) a fast non-selective etch (1:8:1, H₂SO₄:H₂O₂:H₂O, V:V:V, 15µm/min) was used to etch off the substrate to within 20µm of the (Al,Ga)As etch stop layer,
- (4) a slow selective etch (1:19, NH₄OH(35% solution):H₂O₂, 2µm/min in GaAs, 3nm/min in Al_{0.5}Ga_{0.4}As) was used to clear a flat window down to the etch stop layer.

These etched membranes were sent to Dr. R. A. Taylor at the Clarendon Laboratories, Oxford, where absorption measurements were made using an Oxford Instruments CF204 cryostat situated in one arm of a Perkin-Elmer Lambda 9 spectrophotometer. This allowed the absorption spectrum to be measured at 3.8K and room temperature.

Photoluminescence data

A standard PL system (Fig 5-13) was used to measure the PL spectrum of the samples at approximately 19K and room temperature. A sample of structure VG215 was sent to Dr. N. Balkan, Department of Physics, University of Essex, for more detailed studies at 18K, 65K and 293K. To relate the PL peak positions to compositional/structural information requires the use of some model. All of the available models in turn rely on parameters such as carrier effective masses and (Al,Ga)As/GaAs Γ valley offsets over which there is still much debate. Electrical measurements using C-V profiling and other techniques are inconsistent but seem to have converged to a conduction band to valance band offset ($Q = \Delta E_c / \Delta E_g$) in the 0.6 - 0.65 range²⁵ far below the traditional "Dingle's rule" which gave $Q = 0.85$ ²⁶. These electrical measurements also throw some doubt on the energy gap versus aluminium concentration for $Al_xGa_{1-x}As$ at room temperature given by Casey and Panish²⁷ as $E_g(x)/eV = 1.44 + 1.25X$.

The results from optical experiments show even greater inconsistency. Each model seems to require its own values of Q to be consistent with experiment^{6, 28-30}. Recently even the hole effective masses have become almost fittable parameters^{6, 30, 31} with the more complicated Kane models (see chapter two) being reported as systematically underestimating the well widths, and the simpler Krönig-Penney model retaining a good predictive value²⁹. Most of the difficulties encountered in the literature involve the modelling of transitions higher than that of the first electron to first heavy hole state. The PL data obtained from MQW-DH structures usually exhibited the first, heavy hole and light hole transitions only, and so, faced with this uncertainty in the literature, it was decided to use a very simple, single finite well model to interpret the PL peak positions.

By comparing the full width half maximum (FWHM) values of the PL lines obtainable from the MQW-DH structures with the results in the literature, it was also possible to make an assessment of the homogeneity and interface roughness of the MQWS grown.

Following the work of Duggan et al⁶, a set of contour diagrams was used to find the combinations of Q and hole effective masses that

Photoluminescence System Schematic

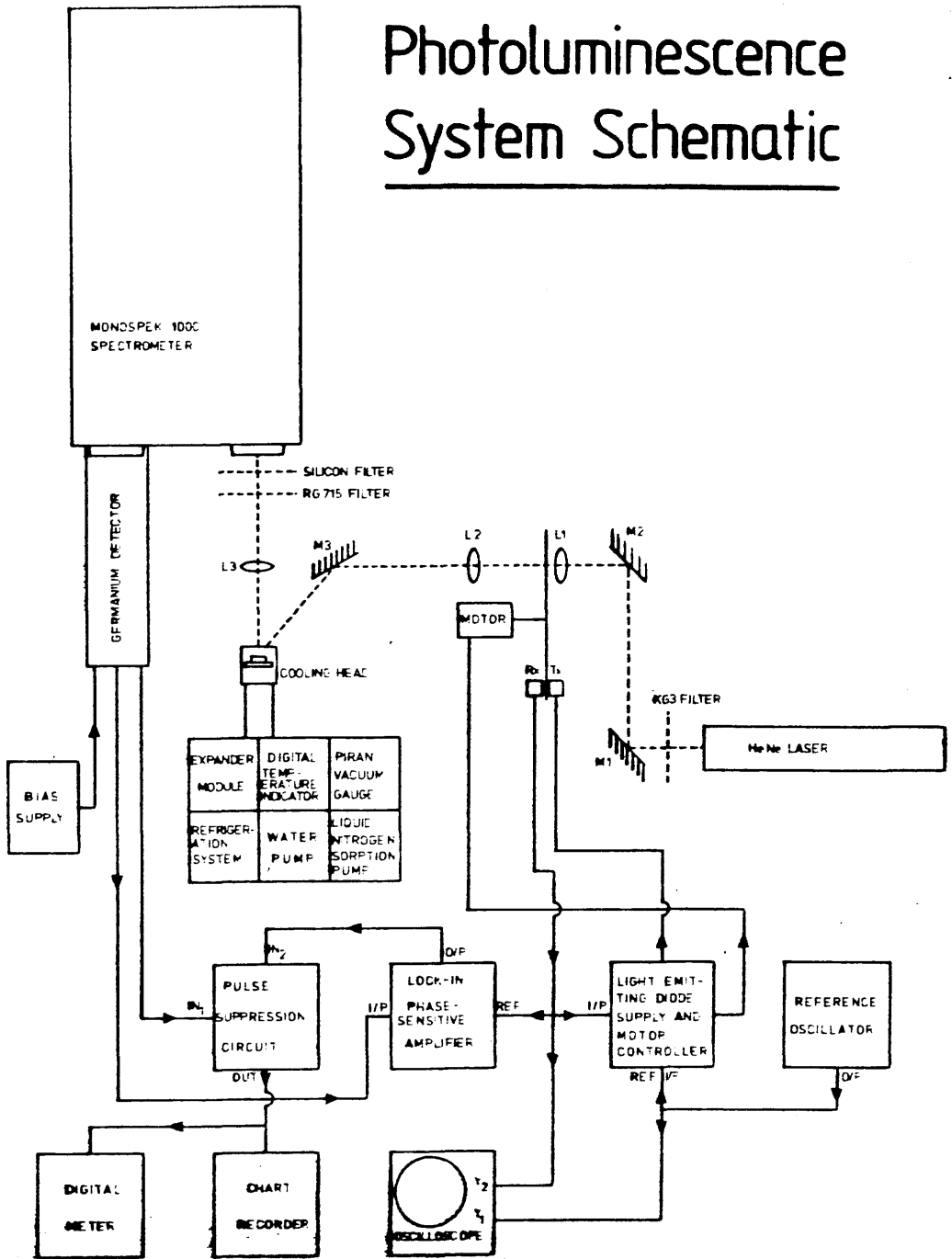


Fig 5-13 A schematic diagram of the photoluminescence system.

would self-consistently model the MQWS PL data. The low temperature PL data of MBE (Glasgow) sample VG215 (Fig 5-14) showed two distinct peaks at 1.546meV and 1.558meV which were interpreted as being the first electron to first heavy hole state (1e-hh) excitonic transition, and the first electron to first light hole (1e-lh) excitonic transition respectively. Fig 5-15(a) shows the result of using conventional hole effective masses²⁶ and a variety of values of Q and binding energies (BE) to calculate the well width from the 1e-hh and 1e-lh transitions. It can be seen that the well width obtained from the 1e-hh transition is very weakly dependent on Q , with a value for Q around that of "Dingle's rule" being required for consistency between the 1e-hh and 1e-lh results. Recently different hole effective masses of $m_{hh}=0.34$, $m_{lh}=0.094$ or $m_{lh}=0.12$ have been proposed in the literature^{29,31}. The contour diagram using these hole masses is shown in Fig 5-15(b). No significant difference was observed between $m_{lh}=0.094$ or 0.12 with a value of Q from 0.67 to 0.75 being required for consistency. The revised effective masses and a value of $Q=0.75$ were chosen to model the MQWS since these values had been successfully used by Chomette et al²⁹ with the Krönig-Penney model. An exciton binding energy of 12meV was assumed. This is close to the value used by Duggan et al⁶ and that predicted by Chemla et al', but smaller than that obtained from recent magneto-optical experiments⁶. Table 5-1 lists the parameter values used in the finite single well model.

5.4.3 Results

A summary of the PL, s.e.m. and optical absorption data from the main MQWS obtained from Glasgow University's MBE group (denoted VG), the SERC Central Facility for III-V Semiconductors (denoted NJ and CPM) and from NTT, Japan (denoted NTT) is given in Table 5-2. A fuller description of the main samples is given in Appendix B.

VG200

VG200 was an early MBE sample grown to be low n-doped throughout. S.e.m. micrographs of the structure suggested wells of widths $(97\pm 4)\text{\AA}$. The low temperature photoluminescence (PL) spectrum shown in Fig 5-16(a) exhibits several characteristic features of all the MQWS, PL spectrum measured. The peak at 1.810eV is due to an excitonic

transition from a free excitonic state to a carbon acceptor excitonic state (FB transition) in the (Al,Ga)As cladding layer³³. The small height of this transition implies good quality (Al,Ga)As. The very small shoulder at 1.836eV is due to a donor bound excitonic transition (DX transition) from which the Al concentration of the (Al,Ga)As cladding can be estimated as $x=0.26^{33}$. This line is more prominent in later PL spectra and is a convenient method of determining the carrier Al concentration to $\pm 1\%$. The peaks at 1.492eV and 1.514eV are due to transitions within the GaAs capping layer. Identical transitions (see Fig 5-16(b)) in bulk GaAs are assigned to a GaAs FB transition and a GaAs DX transition³⁴. The broad band of transitions around $1\mu\text{m}$ are due to deep impurities and are present in all but the purest material. The final transition at 1.551eV was assigned to the 1e-hh MQW transition. Using the single well model, this MQW transition implied a well width of 96.3Å, consistent with the s.e.m. data and less than the 100Å requested. Its FWHM value of 12meV at 16k is larger than that of recently published MQWS results and is consistent with well fluctuations of $\pm a_0$ (where a_0 is a lattice constant)¹⁹.

NJ117

This MOVPE sample was also grown to be low doped throughout its epitaxial layers. The characteristic GaAs DX and FB excitonic transitions are again observed in the low temperature PL spectra (Fig 5-17) with a broad impurity band at $0.93\mu\text{m}$. The line at 1.541eV was interpreted as the 1e-hh MQW transition and resulted in a predicted well width of 108.8Å. The FWHM of 8meV at 16k is low for MOVPE material and implies well fluctuations of less than $\pm a_0/2$, as good as MBE material. Twenty nine periods of MQW were grown with a barrier Al concentration of 0.25, somewhat different from that requested.

VG215

The PL spectrum of VG215 is shown in Fig 5-14. The small peaks at 1.499eV in the 18k spectrum are the GaAs transitions from the cap. The main peak at 1.546eV was assigned to the 1e-hh excitonic transition and the shoulder at 1.558eV to the 1e-lh transition. The former transition was used to fit the model parameters and gave a

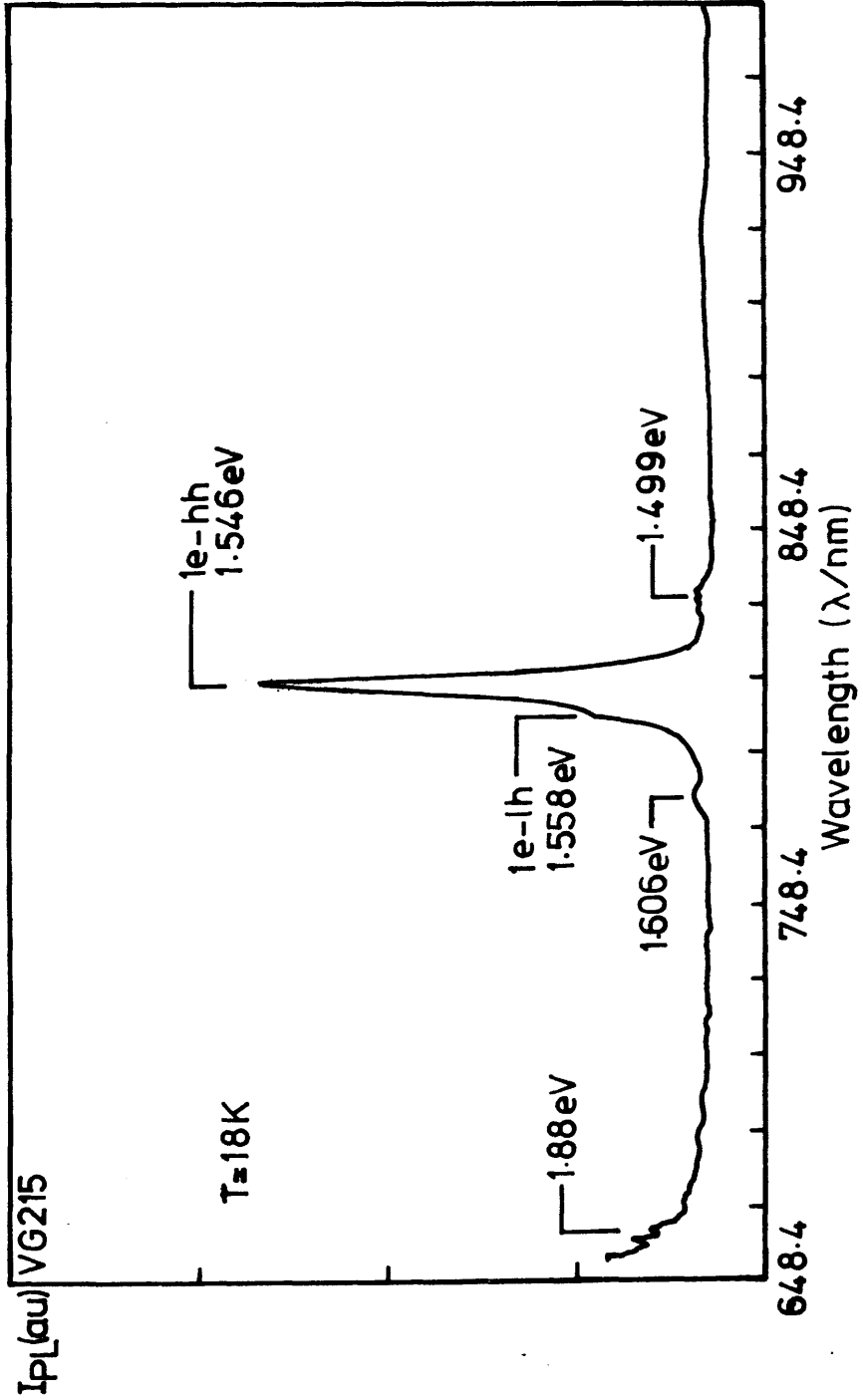
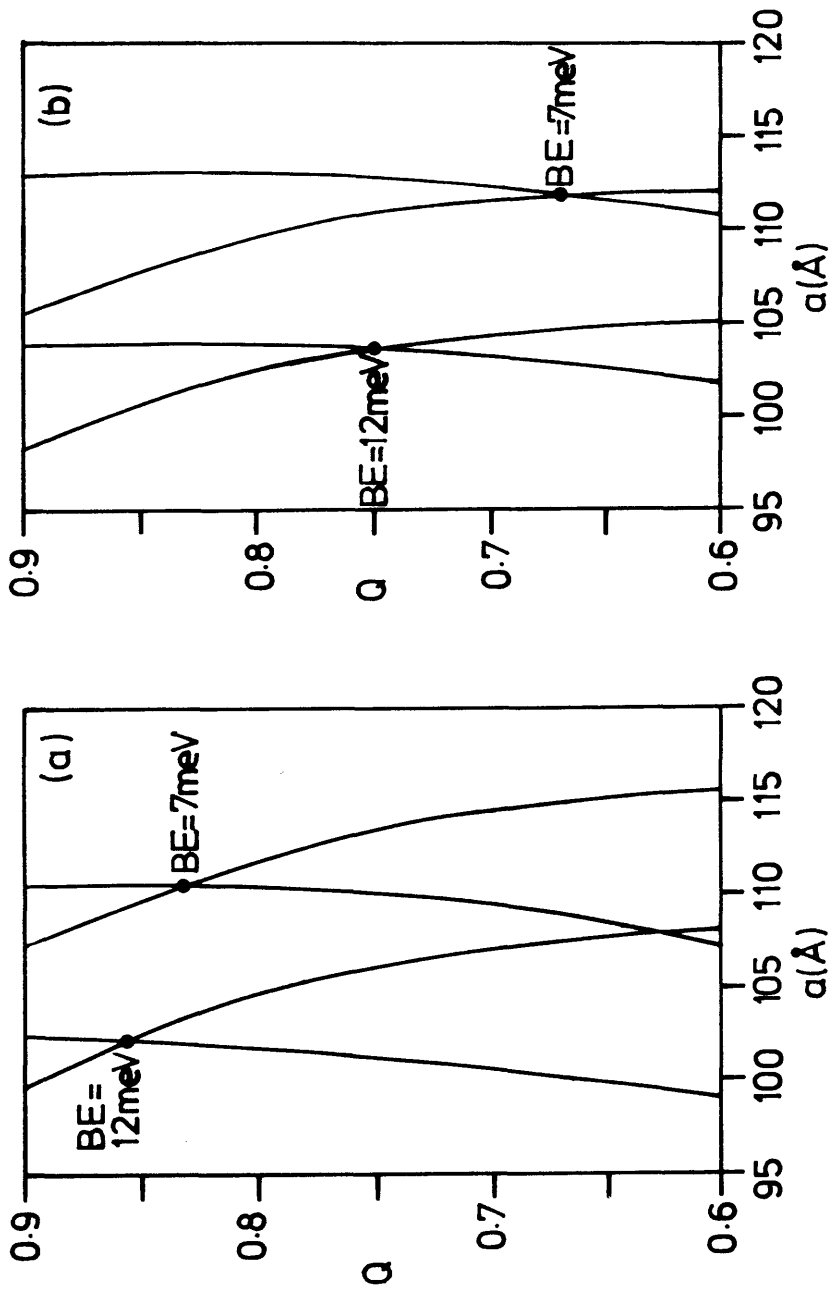


Fig 5-14 The PL spectrum of MBE (Glasgow) sample VG215.



$T = 18\text{K}, m_e^* = 0.067$
 $m_{hh}^* = 0.45, m_{lh}^* = 0.082$

$T = 18\text{K}, m_e^* = 0.067$
 $m_{hh}^* = 0.34, m_{lh}^* = 0.094$

Fig 5-15 Contour plots of conduction to valance band mismatch ratio (Q) against well width (a) for the 1e-hh transition of VG215.

GaAs	
$E_g = 1.519 - 5.405 \times 10^{-4} T^2 / (T + 204)$	
T in Kelvin	
E_g in eV	
(Ref.31)	
$E_g(X) = E_g(X=0) + 1.247X$	
(Ref.28)	
$m_e^* = 0.067m_0$	
$m_{hh}^* = 0.34m_0$	(Ref.30)
$m_{lh}^* = 0.094m_0$	
$Q = 0.75$	(Ref.28)

Table 5-1 The parameter values used in the finite single well model.

SAMPLE	TEP./K	TRANSITION ENERGY (eV)	FWHM (meV)	CLADDING COMPOSITION (x)	BARRIER COMPOSITION (x)	a/λ (sem)	a/λ (PL/E)
--- (a) ---							
VG215	18	1.546 (hh) 1.558 (lh)	14	0.25 (PL)	0.33 (g)	104±4	103.6
NJ117	16	1.541 (hh)	8	0.30 (g)	0.25 (g)	-	108.8
VG200	16	1.551 (hh)	12	0.26 (PL)	0.33 (g)	97±4	96.3
CPM57	17	1.538 (hh)	7	0.25 (g)	0.3 (g)	-	117.8
CPM66	18	1.539 (hh)	13	0.20 (PL)	0.3 (g)	105±2	115.4
CPM68	19	1.528 (?) 1.555 (lh)	-	0.18 (PL)	0.3 (g)	114±4	105.8
CPM96	16	1.528 (?) 1.548 (hh)	-	0.17 (PL)	0.3 (g)	97±3	99.0
--- (b) ---							
CPM96	3.8	1.561 (lh)	-	0.17 (PL)	0.3 (g)	97±3	98.9
MTT203	3.8	1.560 (lh)	-	0.33 (PL)	0.33 (PL)	100±2	100.8

g = growth data
 PL = PL data
 E = etalon data

Table 5-2 A summary of the characteristics of the MQWS grown. Transition energies in (a) from photoluminescence data, and in (b) from etalon transmission data.

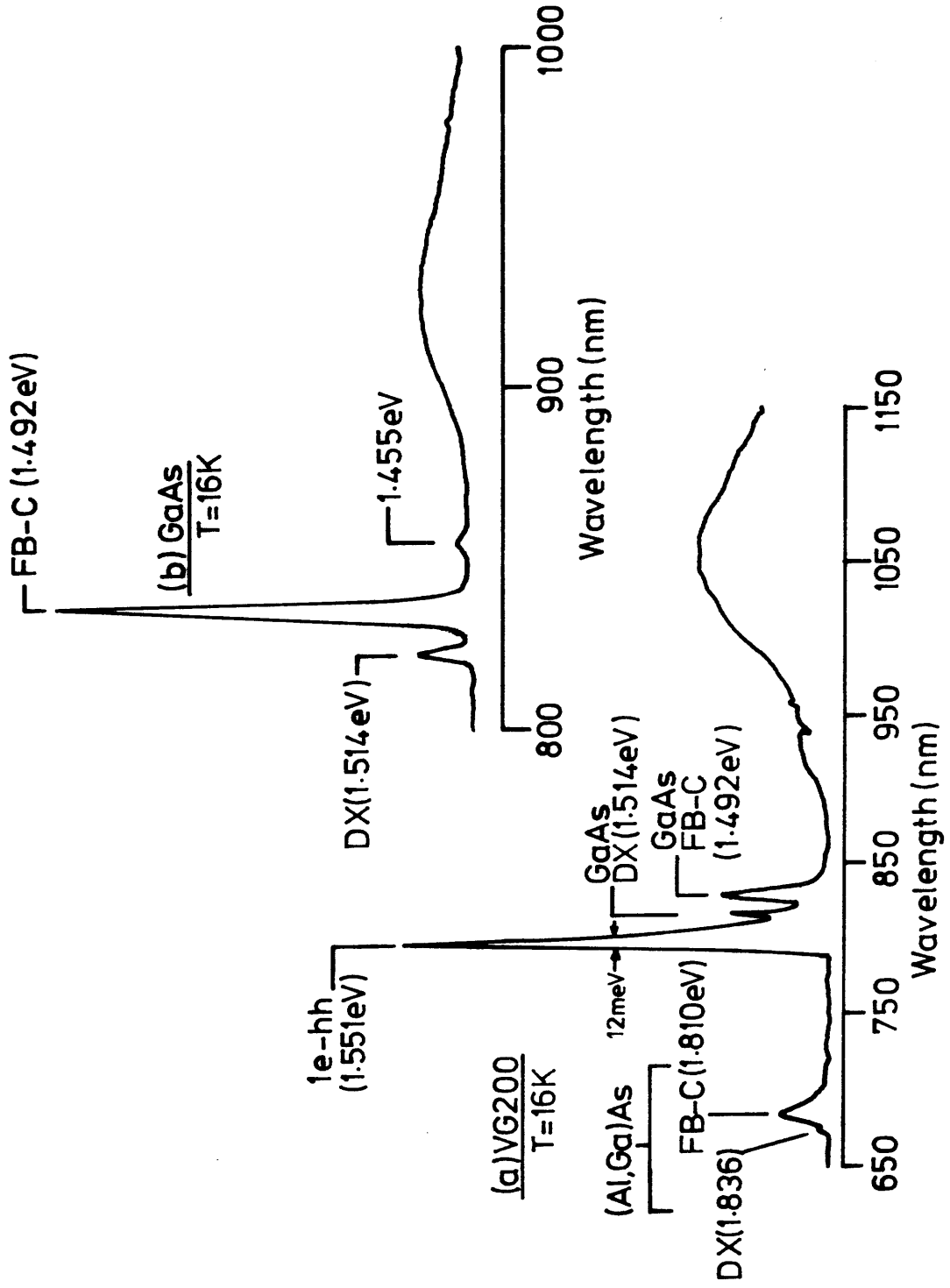


Fig 5-16 The PL spectra of (a) MBE (Glasgow) MQWS VG200, and (b) MOVPE (Sheffield) GaAs.

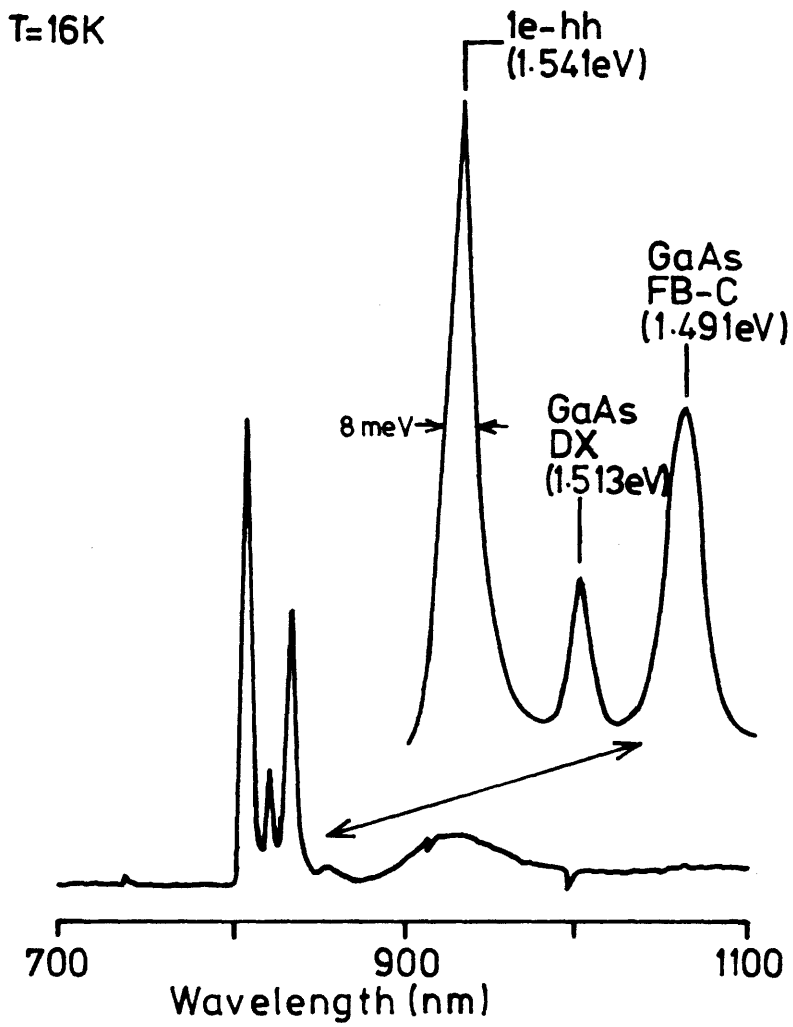


Fig 5-17 The PL spectrum of MOVPE (Sheffield) MQWS NJ117.

well width of 103.6Å. The broader peak at 1.606eV may be the 2e-hh transition but a firm assignment of this line will require further work. The lines at 1.88eV are due to transitions in the AlGaAs cladding layer which place the Al concentration at $x=0.25$. The very low peak intensity of the deep level transitions at $\lambda=930\text{nm}$ reflects the high purity of the sample. The FWHM of 14meV is similar to that of VG200.

CPM57 and CPM66

These samples were grown by MOVPE to have low n-doped epitaxial layers. Fig 5-18 shows their PL spectra. CPM57 shows an 1e-hh transition at 1.538eV implying a well width of 117.8Å, with the 1e-hh transition in CPM66 at 1.539eV resulting in 115.4Å wells, larger than that predicted by s.e.m. data. The FWHM of CPM57 (7meV) is even less than that of NJ117, and both the DX and FB GaAs transitions appear in the PL. However, CPM66 shows signs of poorer quality with the relative intensity of the deep transitions much higher, and the DX GaAs centre being masked by the 1e-hh peak with a FWHM of 13meV.

CPM68

So far, well widths derived from the PL model and s.e.m. data had correlated well given the assumptions involved in obtaining the well width from the PL data. However, with the PL data of CPM68, interpretation became more difficult. CPM68 was the first MOVPE sample to be grown to include a p-i-n diode structure, and s.e.m. data (Fig 5-19(a)) suggested well widths of 114Å. The PL spectrum of CPM68 (Fig 5-19(b)) shows weaker PL than previous samples (the intensity scale is expanded approximately five times compared to that on the PL spectrum of CPM66), with the relative intensities of the deep level transitions and the (Al,Ga)As FB transition being much greater. The shoulder at 1.513eV is the GaAs DX transition in the cap layer. If the main transition at 1.529eV is interpreted as the 1e-hh transition, the resulting well width is 147.6Å, too large to be consistent with the s.e.m. data. Alternatively, if the small peak at 1.555eV is interpreted as the 1e-lh transition, the finite well model results in a well width of 105.9Å. Using this well width, the 1e-hh transition would be predicted at 1.544eV where, if it were a weak transition, it could be masked by the broad 1.529eV peak. Following

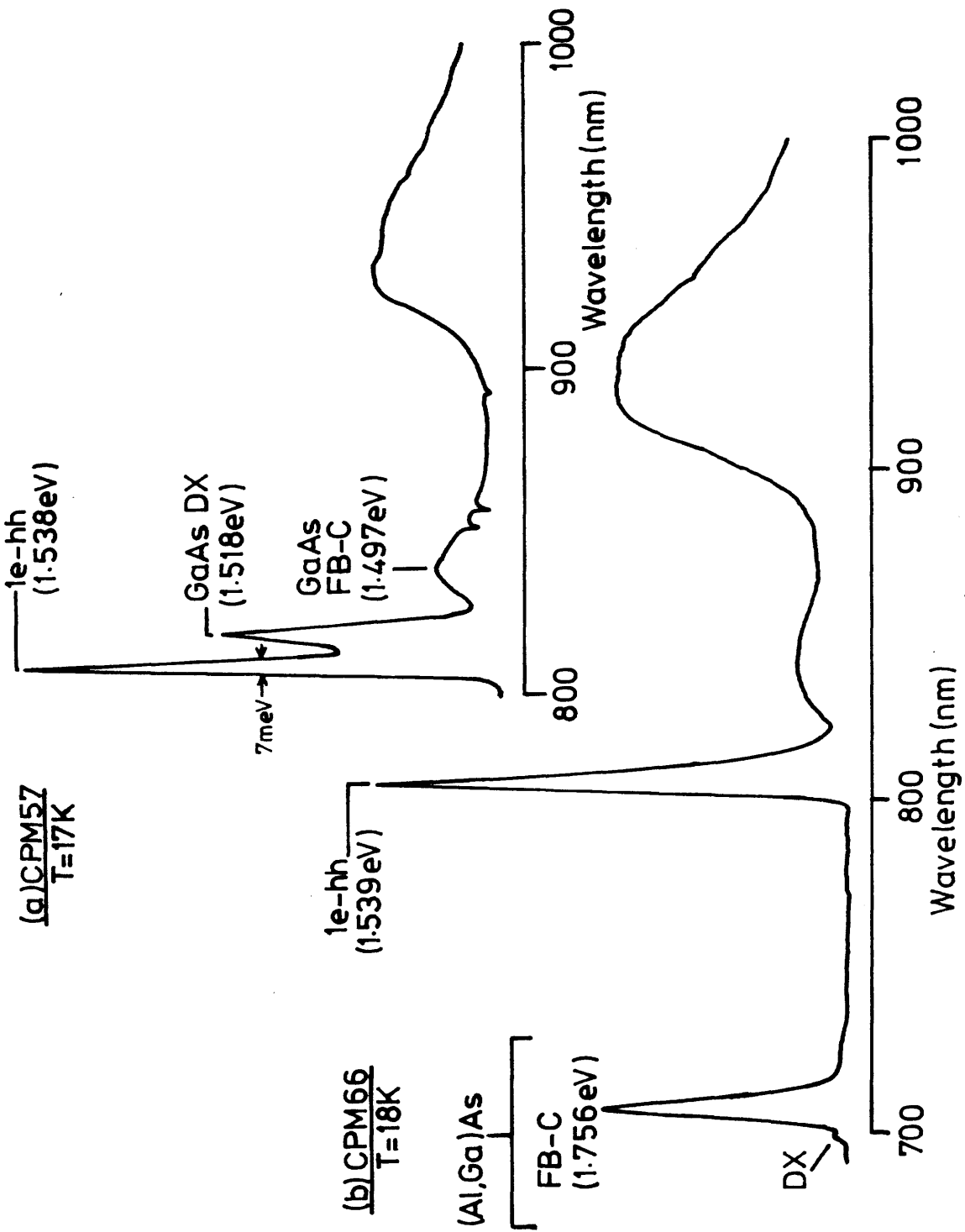


Fig 5-18 The PL spectra of MOVPE (Sheffield) MQWS (a) CPM57, and (b) CPM66.

(a)

|MQWS|



(b) CPM68

T=19K

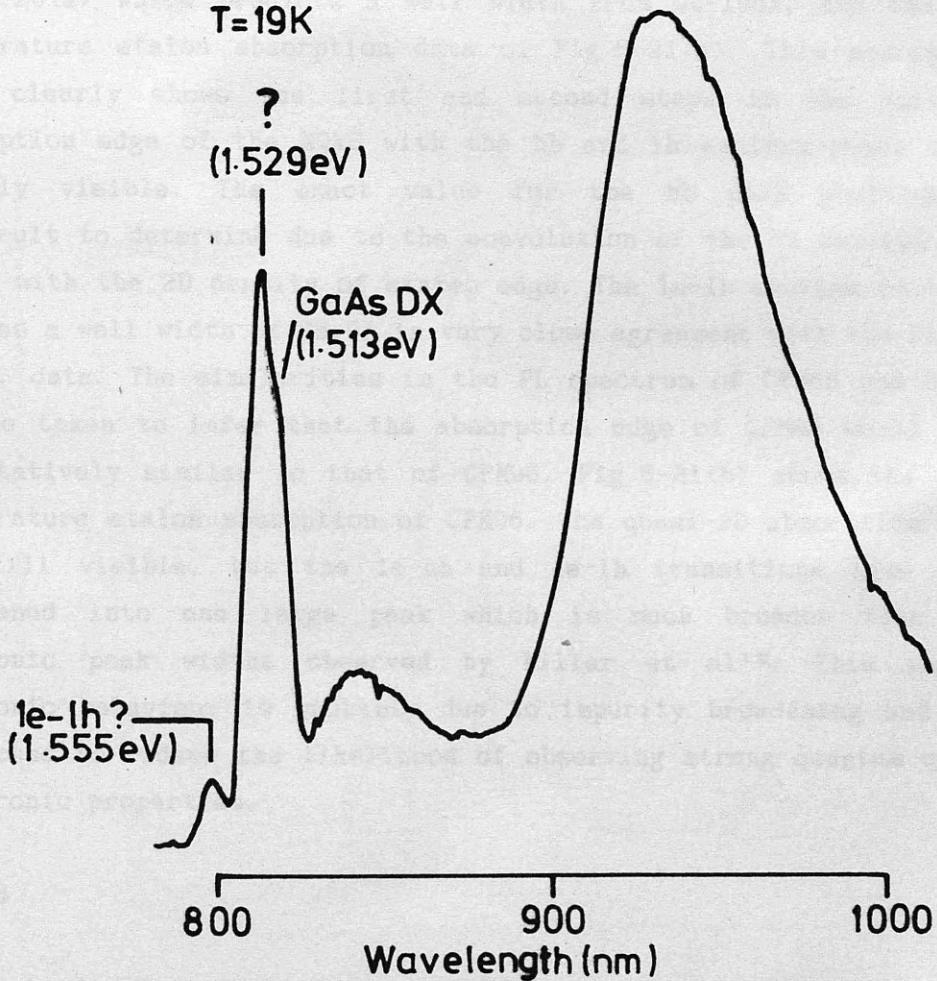


Fig 5-19 A s.e.m. micrograph (a), and PL spectrum (b) of MOVPE (Sheffield) MQWS CPM68.

this interpretation the peak at 1.529eV must be assigned to some impurity transitions in the MQWS since its energy is greater than the band gap of GaAs but less than that of the predicted 1e-hh transition.

CPM96

This interpretation of the PL spectrum of CPM68 is supported by the PL spectrum obtained from CPM96 (Fig 5-20). The relative intensity of the deep level transitions is lower in this spectrum, possibly due to the larger number of wells in the sample, but the anomalous peak at 1.529eV remains. In this spectrum, however, a shoulder appears at 1.528eV. Interpreting this shoulder as the 1e-hh transition masked in the previous spectrum, a well width for CPM96 of 99.0Å is returned from the single finite well model. Further support for this well width results from an inspection of the s.e.m. data of Fig 5-20(a) which predicts a well width from 94-100Å, and the low temperature etalon absorption data of Fig 5-21(a). This absorption data clearly shows the first and second steps in the quasi-2D absorption edge of the MQWS with the hh and lh exciton peaks being clearly visible. The exact value for the hh peak position is difficult to determine due to the convolution of the hh exciton line shape with the 2D density of states edge. The 1e-lh exciton position implies a well width of 98.9Å in very close agreement with the PL and s.e.m. data. The similarities in the PL spectrum of CPM68 and CPM96 can be taken to infer that the absorption edge of CPM68 would look qualitatively similar to that of CPM96. Fig 5-21(b) shows the room temperature etalon absorption of CPM96. The quasi-2D absorption edge is still visible, but the 1e-hh and 1e-lh transitions have been broadened into one large peak which is much broader than the excitonic peak widths observed by Miller et al¹². This weaker excitonic behaviour is probably due to impurity broadening and was predicted to reduce the likelihood of observing strong quantum optoelectronic properties.

NTT203

To obtain absorption data on a MBE structure for comparison with CPM68, NTT203 was back etched. NTT203 was grown to have undoped epitaxial layers. S.e.m. data had predicted 100Å wells and low

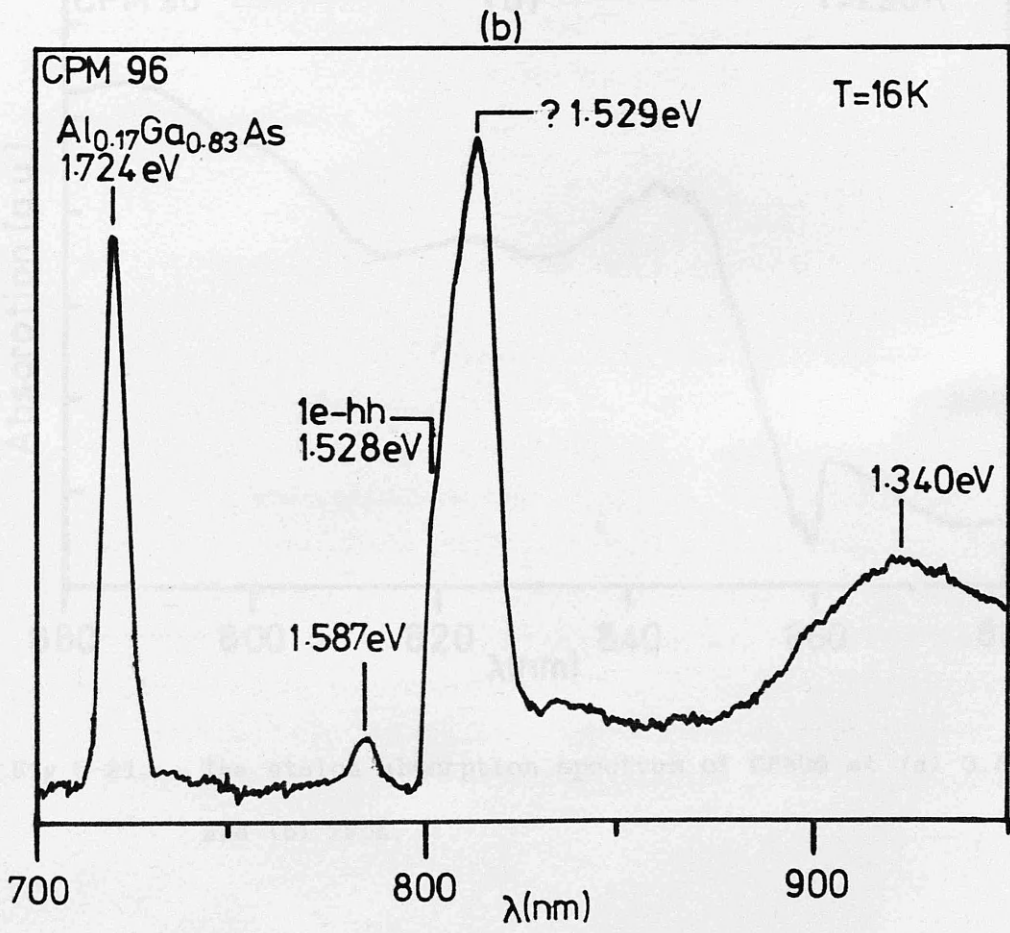
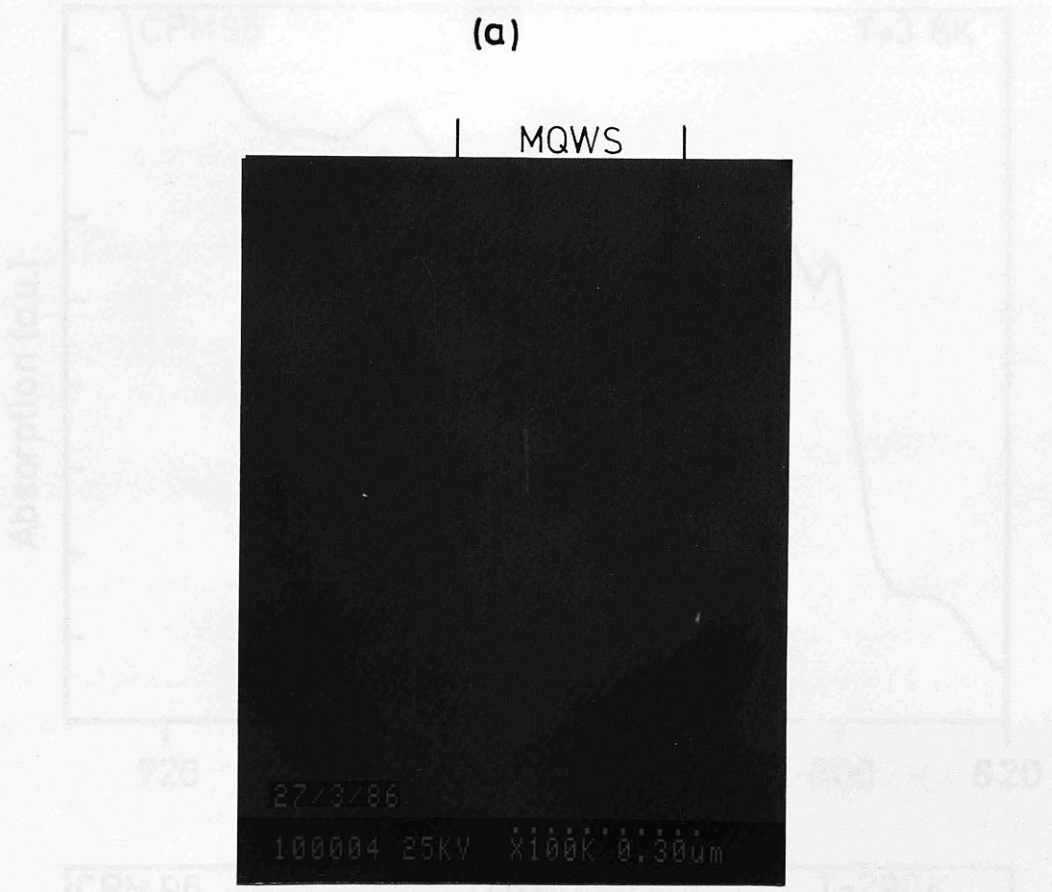


Fig 5-20 A s.e.m. micrograph (a), and PL spectrum (b) of MOVPE (Sheffield) MQWS CPM96.

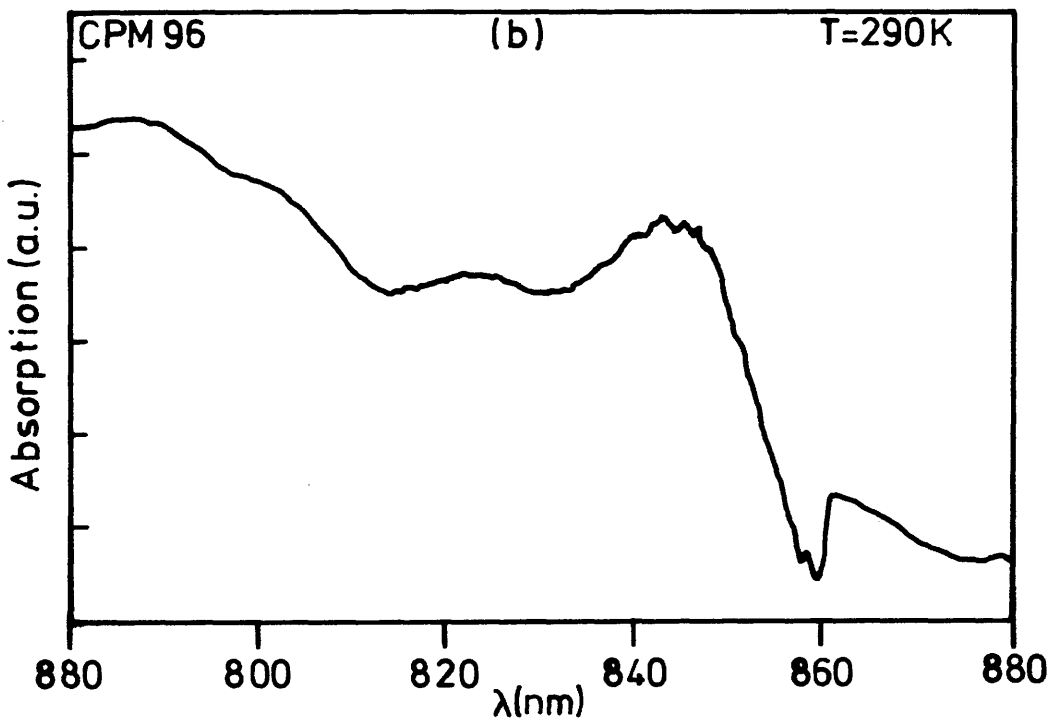
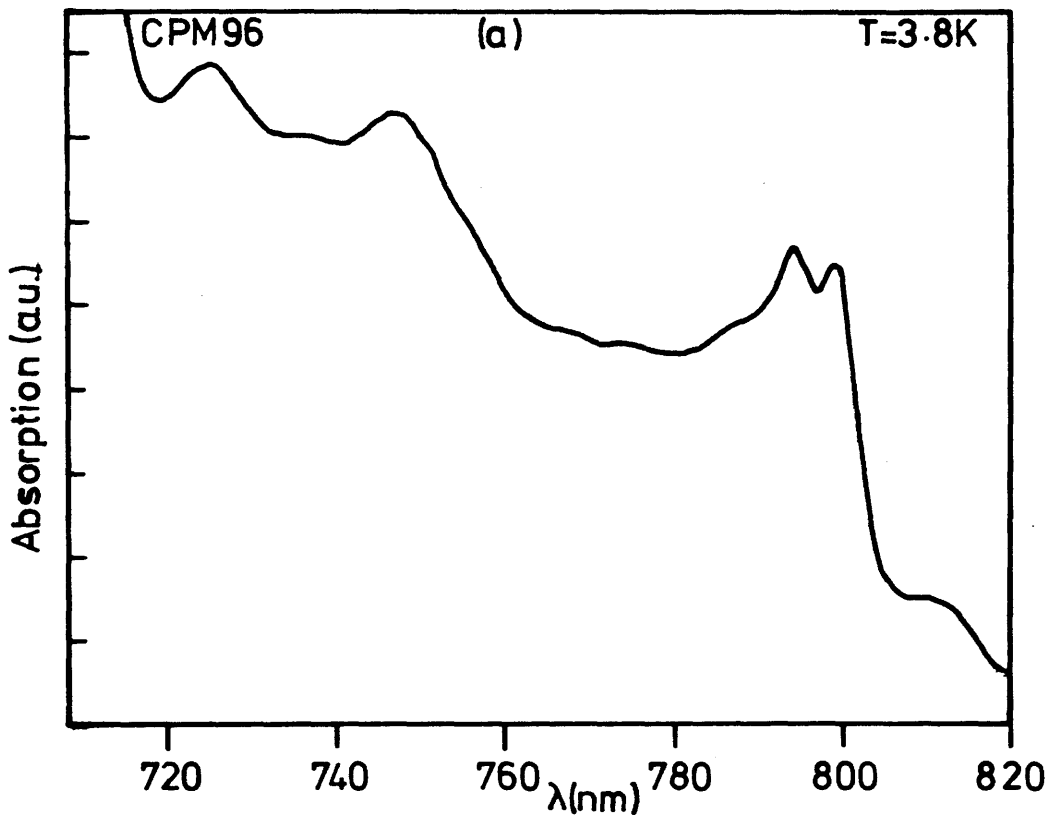


Fig 5-21 The etalon absorption spectrum of CPM96 at (a) 3.8K and (b) 290K.

temperature PL data gave a FWHM at 17k of 6.4 meV, implying well fluctuations of ± 1 monolayer. The low temperature etalon absorption shows the 1e-hh and 1e-lh exciton peaks very clearly (Fig 5-22(a)) and the single finite well model was used to predict a well width of 100.8Å. At room temperature (Fig 5-22(b)) only the 1e-hh is distinguishable from the F-P resonances, but its width is much narrower than that observed in CPM96, implying that CPM96 had significantly greater interface roughness, well homogeneities and impurity broadening.

5.4.4 Conclusions

Low temperature photoluminescence spectra, etalon absorption data and s.e.m. micrographs can be used to investigate the compositional and structural characteristics of MQW waveguide structures. A simple, single finite well model of the MQWS was found to adequately model the position of the 1e-hh and 1e-lh transitions in the MQWS and return well widths consistent with those calculated from s.e.m. micrographs. Some difficulty was found in interpreting the PL data of p-i-n structure MQW waveguides, but etalon absorption data resolved the difficulties. The inclusion of an $\text{Al}_{0.6}\text{Ga}_{0.4}\text{As}$ etch stop in any MQW waveguide structure to allow substrate removal is thus recommended.

The results showed that the undoped MOVPE material obtained had, in practice, interfaces as pure and smooth as the MBE material available. However, the only structures that were to prove useful as active MQW waveguides (see chapter six) and which were grown by MOVPE with p-i-n doping, showed an anomalous PL transition, with room temperature etalon absorption data showing very indistinct excitonic characteristics in comparison with good quality MBE material. This broadening was probably due to field inhomogeneity and ionised impurity effects due to the practical limits of the MOVPE growth technique. The broad room temperature excitonic characteristics would reduce the general validity of any conclusions derived from this material on the general opto-electronic properties of MQW waveguides.

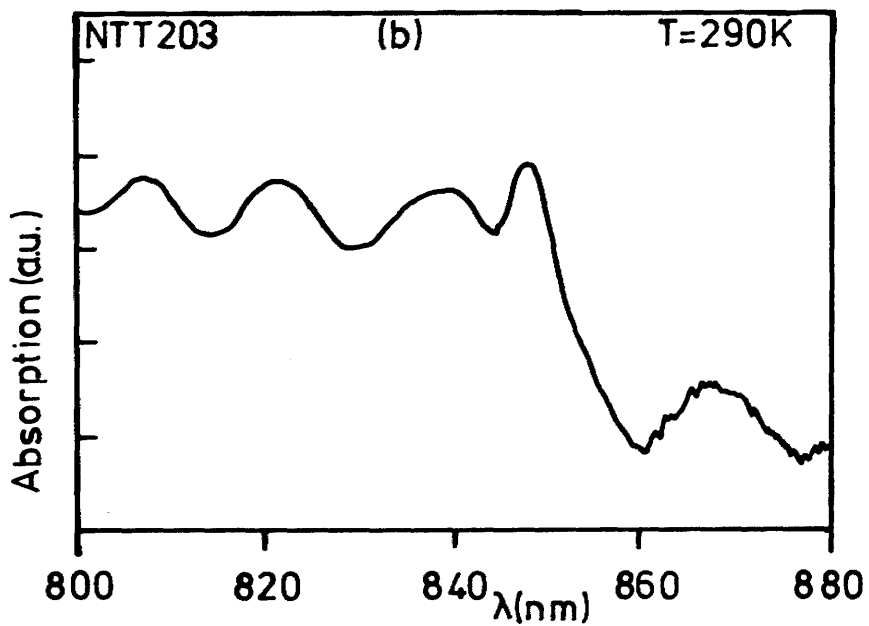
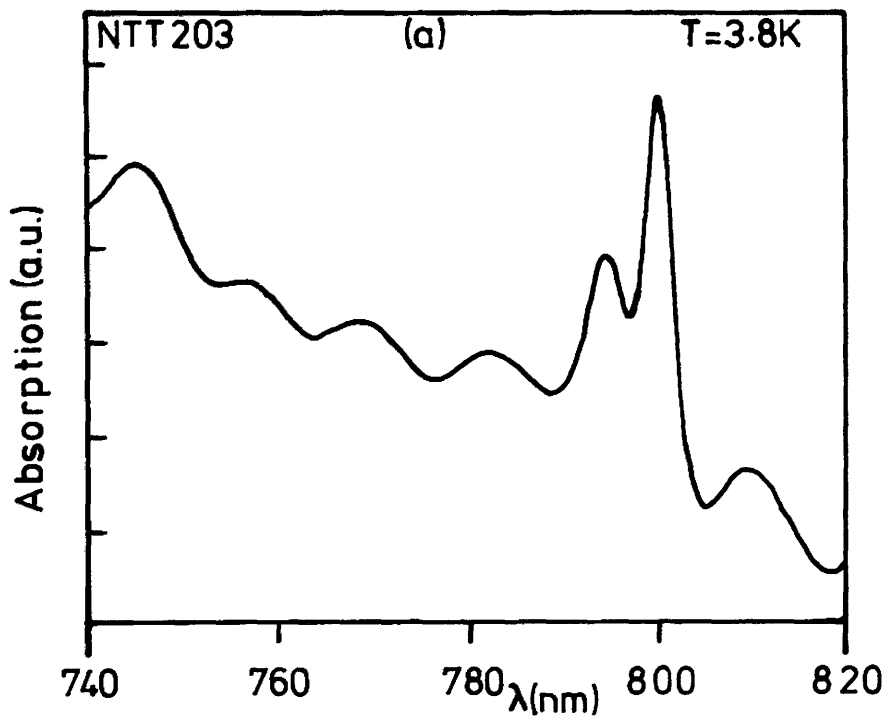


Fig 5-22 The etalon absorption data of MBE (NTT, Japan) MQWS NTT203 at (a) 3.8K and (b) 290K.

5.5 CONCLUSIONS

A MQW waveguide structure was designed using the rms refractive index model to sustain a single planar mode for propagation wavelengths in the range 1.15-0.85 μ m. The MQWS was designed to maximise the excitonic nature of the quasi-2D absorption edge. Well homogeneity and material purity were found to be important if strong MQW effects were to be observed. Well width fluctuations would need to be limited to less than three atomic layers with MQW background doping held to less than $3 \times 10^{15} \text{cm}^{-3}$. Examining the epitaxial growth techniques available it was noted that MBE would be the preferred technique due to the abrupt interfaces, low background doping levels and lower carbon impurity levels obtainable in comparison with the alternative growth technique, MOVPE. A short history was given of the difficulties met in trying to obtain MQW material of suitable quality and to the desired design, before the techniques used to analyse the compositional and structural quality of the MQWS were described. The results of these techniques showed that in practice good low doped MOVPE MQW had interface roughness no worse than similar MBE grown structures. However, the only p-i-n diode structures available, grown by MOVPE, were shown to have very poor excitonic characteristics at room temperature in comparison with structures reported in the literature. The scope of any conclusions as to the general properties of MQW waveguides will thus be limited by the quality of the MOVPE material available.

It is hoped that the description given of the difficulties met in trying to obtain good quality MQW material will emphasise the fact that any future work involving MQW waveguides should not be undertaken without the full and dedicated support of one or more suitable growth facilities.

References to Chapter Five

- 1 D.S.Chemla, D.A.B.Miller, P.W.Smith, A.C.Gossard and W.Wiegmann; "Room Temperature Excitonic Nonlinear Absorption and Refraction in GaAs/AlGaAs Multiple Quantum Well Structures", IEEE J. Q. Electron. **QE-20**, 265 (1984).

- 2 P. Blood, E. D. Fletcher, P. J. Hulyer and P. M. Smowton;
"Emission wavelength of AlGaAs-GaAs multiple quantum well lasers",
Appl. Phys. Lett. **48**, 1111 (1986).
- 3 Y. Arakawa, A. Larsson, J. Paslaski and A. Yariv;
"Active Q switching in a GaAs/AlGaAs multiquantum well laser with
an intracavity monolithic loss modulator", Appl. Phys. Lett. **48**,
561 (1986).
- 4 H. Nakashima, S. Semura, T. Ohta, Y. Uchida, H. Saito, T. Fukuzawa,
T. Kuroda and K. L. I. Kobayashi;
"Device Characteristics of GaAlAs Buried-Multiquantum-Well Lasers
Fabricated by Zn-Diffusion-Induced Disordering", IEEE J. Q.
Electron. **QE-21**, 629 (1985).
- 5 J. S. Roberts, N. J. Mason and M. Robinson;
"Factors Influencing Doping Control and Abrupt Metallurgical
Transitions During Atmospheric Pressure MOVPE Growth of AlGaAs and
GaAs", J. Cryst. Growth **68**, 422 (1984).
- 6 G. Duggan, H. I. Ralph and K. J. Moore;
"Reappraisal of the band-edge discontinuities at the $Al_xGa_{1-x}As$ -
GaAs heterojunction", Phys. Rev. B **32**, 1 (1985).
- 7 S. Okhe, T. Umeda and Y. Cho;
"Optical waveguides using GaAs- $Al_xGa_{1-x}As$ multiple quantum well",
Opt. Comm. **56**, 235 (1985).
- 8 S. Adachi;
"GaAs, AlAs, and $Al_xGa_{1-x}As$: Material parameters for use in
research and device applications", J. Appl. Phys. **58**, R1 (1985).
- 9 H. C. Casey, D. D. Sell and M. B. Panish;
"Refractive index of $Al_xGa_{1-x}As$ between 1.2 and 1.8 eV", Appl.
Phys. Lett. **24**, 63 (1974).
- 10 R. E. Fern and A. Anton;
"Refractive Index of AlAs", J. Appl. Phys. **42**, 3499 (1971).
- 11 Y. Suzuki and H. Okamoto;
"Refractive index of GaAs-AlAs superlattice grown by MBE", J.
Electron. Mat. **12**, 397 (1983).
- 12 D. A. B. Miller, D. S. Chemla, T. C. Damen, A. C. Gossard, W. Wiegmann,
T. H. Wood and C. A. Burrus;
"Electric field dependence of optical absorption near the band gap
of quantum-well structures", Phys. Rev. B **32**, 1043 (1985).

- 13 D. A. B. Miller, D. S. Chemla, T. C. Damen, A. C. Gossard, W. Wiegmann, T. H. Wood and C. A. Burrus;
"Band-Edge Electroabsorption in Quantum Well Structures: The Quantum-Confined Stark Effect", Phys. Rev. Lett. **53**, 2173 (1984).
- 14 P. D. Dapkus, H. M. Manasevit, K. L. Hess, T. S. Low and G. E. Stillman;
J. Cryst. Growth **55**, 10 (1981).
- 15 N. J. Mason;
"MOVPE (and Assessment)", Low Dimensional Structures summer school, Nottingham, 1985.
- 16 J. S. Roberts;
SERC Central Facility for III-V Semiconductors, Sheffield, private communication.
- 17 G. B. Stringfellow;
"Epitaxy", Rep. Prog. Phys. **45**, 469 (1982).
- 18 B. Deveaud, A. Regreny, J.-Y. Emery and A. Chomette;
"Photoluminescence study of interface defects in high-quality GaAs-GaAlAs superlattices", J. Appl. Phys. **59**, 1633 (1986).
- 19 B. Joyce;
"Molecular Beam Epitaxy Growth", Low Dimensional Structures summer school, Nottingham, 1985.
- 20 J. E. Davey and T. Pankey;
"Epitaxial GaAs Films Deposited by Vacuum Evaporation", J. Appl. Phys. **39**, 1941 (1968).
- 21 H. Morkoc and A. Y. Cho;
"High-purity GaAs and Cr-doped GaAs epitaxial layers by MBE", J. Appl. Phys. **50**, 6413 (1979).
- 22 W. Tsang;
"Infrared-visible (0.89-0.72 μ m) $Al_xGa_{1-x}As/Al_yGa_{1-y}As$ double-heterostructure lasers grown by molecular beam epitaxy", J. Appl. Phys. **51**, 917 (1980).
- 23 A. C. Gossard;
Thin films: Preparation and properties, ed. K. N. Tu and R. Rosenberg (Academic Press, New York, 1983).
- 24 W. S. Mackie, S. P. Beaumont, C. D. W. Wilkinson and J. S. Roberts;
"High Resolution Lithography on Thin Active Semiconductor Membranes", 10th Electron and Ion Beam Science and Technology Conference, Montreal, May 1982.
- 25 H. Kroemer;
"Band Offsets at Heterointerfaces: Theoretical Basis, and Review, of Recent Experimental Work", Surface Sci. **172**, 1 (1986).

- 26 R. Dingle;
in *Festkörperprobleme/Advances in Solid-State Physics*, ed. H.J. Queisser, Vol. 15, pp.21-48 (Vieweg, Braunschweig, 1975).
- 27 H.C. Casey and M.B. Panish;
Heterostructure Lasers (Academic Press, New York, 1978).
- 28 J. Batey and S.L. Wright;
"Energy band alignment in GaAs:(Al,Ga)As heterostructures: The dependence on alloy composition", *J. Appl. Phys.* **59**, 200 (1986).
- 29 A. Chomette, B. Deveaud, M. Baudet, P. Auvray and A. Regreny;
"Band discontinuities and calculations of GaAs-AlGaAs superlattice structures", *J. Appl. Phys.* **59**, 3835 (1986).
- 30 K. Yamanaka, T. Fukunaga, N. Tsukada, K.L.I. Kobayashi and M. Ishii;
"Photocurrent spectroscopy in GaAs/AlGaAs multiple quantum wells under a high electric field perpendicular to the heterointerface", *Appl. Phys. Lett.* **48**, 840 (1986).
- 31 R.C. Miller, D.A. Kleinman and A.C. Gossard;
"Energy-gap discontinuities and effective masses for GaAs-Al_xGa_{1-x}As quantum wells", *Phys. Rev. B* **29**, 7085 (1984).
- 32 J.S. Blakemore;
"Semiconducting and other major properties of gallium arsenide", *J. Appl. Phys.* **53**, R123 (1982).
- 33 G. Wicks, W.I. Wang, C.E.C. Wood, L.F. Eastman and L. Rathbun;
"Photoluminescence of Al_xGa_{1-x}As grown by molecular beam epitaxy", *J. Appl. Phys.* **52**, 5792 (1981).
- 34 *Properties of Gallium Arsenide. i, emis. Datareviews Series No2* (Inspec, London).

CHAPTER SIX
PASSIVE MQW-DH WAVEGUIDES

6.1 INTRODUCTION

With the structural properties of the MQWS having been tested as outlined in the previous chapter, it was possible to move on to test the planar waveguide characteristics of the MQW-DH. Only if these characteristics were found to be suitable would further processing into stripe waveguides be considered. The simplest device after the straight, stripe waveguide is the synchronous directional coupler. Fabrication of such a device in a MQW-DH would further verify the design rules used for the MQW-DH, and demonstrate the feasibility of fabricating more complex integrated optical devices in MQWS.

6.2 PLANAR WAVEGUIDES

Recently leaky mode waveguides with one or two quantum wells within a superlattice waveguide structure have been used to observe the anisotropic absorption edge of quantum wells^{1,2}. These structures were used for experimental purposes. Actual integrated optical devices will have to support truly guided modes in many quantum wells. Such waveguide structures have been reported³⁻⁵. The present MQW-DH structure was designed to be a general purpose structure that would sustain only one truly guided mode up to the absorption edge, with the difference in propagation loss between the TE mode and TM mode under a metal electrode being negligible.

6.2.1 Near Field Pattern

To investigate the modal near field pattern a sample of each structure grown was cleaved to form a planar waveguide. The end-fire coupling system described in chapter three was then used to couple laser radiation of the desired wavelength into the structures with the output microscope focusing the modal near field pattern onto the IR camera. Incident power was limited to less than $30\mu\text{W}$ to prevent non-linear effects. Initially the lasing range of the Styryl-9 dye-laser had a long wavelength limit of 880nm. The near field pattern was thus studied at $1.15\mu\text{m}$, $0.88\mu\text{m}$ and various wavelengths down to a

wavelength limit (λ_c) determined by the absorption edge of the waveguide. The first structure to be tested was the MBE sample VG200 (see Appendix B). At $\lambda=1.15\mu\text{m}$ and $\lambda=0.88\mu\text{m}$ to λ_c , this structure showed a near field pattern that consisted of a single, bright horizontal line for both TE and TM excitation. Varying the input conditions did not alter this modal pattern, implying that only one planar mode was sustained as predicted by the MQW waveguide model of the previous chapter. A similar structure, VG215, showed identical characteristics.

MOVPE sample NJ117 was next to be tested. This sample had been grown with a structure different from that desired (see Appendix B) with twenty nine periods in the MQWS, and the designed aluminium concentration in the MQW buffers and DH cladding layers being transposed. At $\lambda=1.15\mu\text{m}$, this structure exhibited a single line in the near field pattern for both TE and TM propagation. At $\lambda=0.88\mu\text{m}$, however, the near field pattern consisted of two bright, parallel, horizontal lines implying bimodal propagation. Both these observations are consistent with results obtained from the four layer planar waveguide model assuming the refractive index of the MQWS for TE propagation is the rms mean of the bulk refractive indices of the constituent layers (the rms model).

Although VG200 and 215 had satisfied the design criterion that they be single-mode up to the absorption edge, it was necessary to test further structures which included a p-i-n diode to allow the fabrication of active waveguide devices. MBE sample VG285 was such a sample. At both $\lambda=1.15\mu\text{m}$ and $\lambda=0.880\mu\text{m}$ the near field pattern of this structure consisted of two distinct horizontal lines, even though this structure was grown very close to the original design (see Appendix B). Initially the near field pattern was interpreted as implying bimodal propagation similar to NJ117. But this interpretation at $\lambda=1.15\mu\text{m}$ would lead to a value for the MQWS refractive index far above that of GaAs. Such a high value seems unlikely, and no such anomalously high refractive index has been reported. It proved impossible to conclusively determine the actual cause of this anomalous near field pattern. However, scanning the input beam across the waveguide in a direction perpendicular to the epitaxial layers was observed to excite the top line in the near field pattern first, then, as the scan continued, both lines became

visible, and finally the top line disappeared leaving only the bottom line excited. These characteristics are more consistent with two planar guides being present in the structure than one bimodal guide being present.

Following the initial interpretation that the structure was bimodal, it was decided to do a series of growth runs using the MOVPE system at the SERC Central Facility for III-V Semiconductors, reducing the confinement of the waveguide grown on each run until single-mode propagation was observed.

First, a low n-doped sample CPM57 was grown with the nominal guide layer thickness reduced to 21 wells and 20 barriers (i.e. $0.41\mu\text{m}$ thick). This structure showed identical near field characteristics to VG285, i.e. two horizontal, bright lines. CPM66 was thus grown to have 21 wells, 20 barriers, and $\text{Al}_{0.2}\text{Ga}_{0.8}\text{As}$ cladding. When tested, this low n-doped structure had $\text{Al}_{0.18}\text{Ga}_{0.82}\text{As}$ cladding layers, and its near field pattern exhibited a single horizontal line. It was therefore attempted to re-grow this structure with p-i-n doping (CPM68). Unfortunately growth of CPM68 stopped after just 12 wells due to a reactor malfunction, with just the top cladding layer being grown upon restarting the reactor. The resulting waveguide layer was thus much thinner than designed, but it did exhibit just one bright line in its near field pattern (see Fig 6-1) at $\lambda=1.15\mu\text{m}$ and $\lambda=0.88\mu\text{m}$ to λ_g . This structure was the only MQW-DH obtained during the project that had a single line near field pattern and a good p-i-n diode structure to allow active waveguide fabrication.

In a further attempt to repeat the structure of CPM66 with p-i-n diode doping, CPM96 was grown. PL and s.e.m. studies of the grown layers revealed a structure of 21 wells, 20 barriers and $\text{Al}_{0.17}\text{Ga}_{0.83}\text{As}$ cladding. However, despite the similarities with CPM66, this structure exhibited the anomalous, two lines in its near field pattern (Fig 6-2) at $\lambda=0.88\mu\text{m}$. In contrast, NTT529, grown by MBE with 21 wells, 20 barriers and $\text{Al}_{0.2}\text{Ga}_{0.8}\text{As}$ cladding showed just one line at $\lambda=0.88\mu\text{m}$ to λ_g .

In conclusion then, although initial planar waveguide results were consistent with the rms model of MQWS and resulted in single planar mode propagation, some later results could not be explained by the

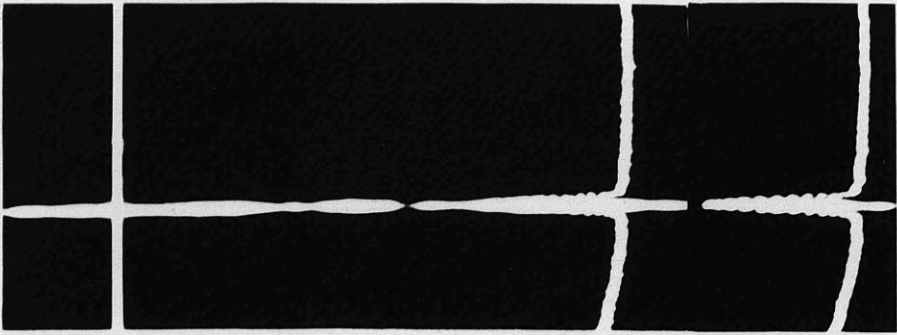
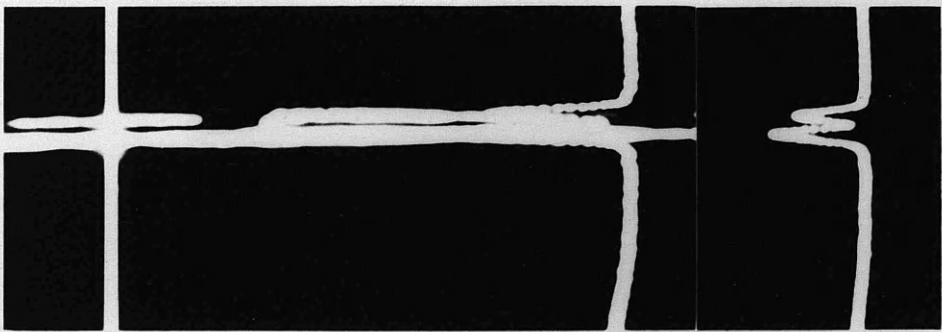
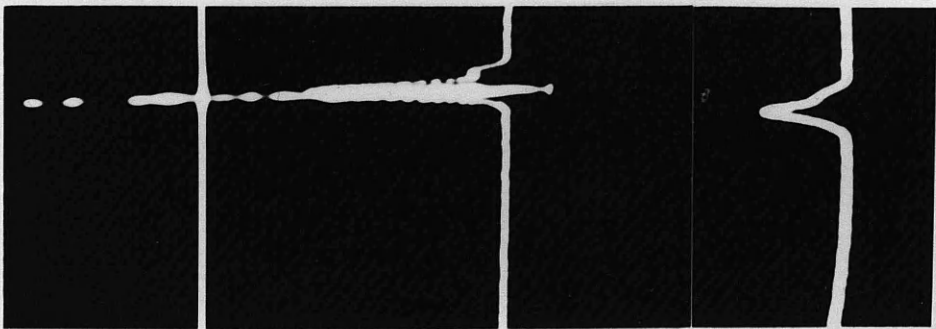


Fig 6-1 The near field pattern of planar waveguide CPM68.



(a)



(b)

Fig 6-2 The near field pattern of planar waveguide CPM96 for two different input conditions.

rms model due to the very high value that would have to be assigned to the refractive index of the MQWS. No conclusive explanation could be found for these anomalous near field patterns, but the rms model was still considered to be valid since it was consistent with the earlier waveguide results and the modal properties of published MQW waveguide structures³⁻⁵.

Further, it had been shown that two p-i-n diode samples (CPM68 and NTT529) exhibited the desired single-mode propagation. Due to the lack of time remaining when CPM68 was delivered, it was decided to concentrate all passive and active waveguide work on CPM68.

6.2.2 Absorption Edge

Propagation loss measurements were made in sample CPM68 to observe the quasi-2D absorption edge of the MQWS. Planar waveguides from 0.5 to 5mm long were cleaved and placed on the end-fire coupling rig described in chapter three. The dye-laser amplitude stabiliser was used to hold the power incident on the waveguides at a constant level of less than 30 μ W over the dye scanning range of $\lambda=905\text{nm} - 870\text{nm}$. A large area Si photodiode was used to ensure that the whole width of the propagated mode could be focused onto the detector using the output microscope. The laser beam incident on the waveguide was mechanically chopped at 3kHz to allow the detected signal to be selectively amplified using a lock-in amplifier and fed to a chart recorder. A significant amount of stray, chopped light was found to fall on the photodetector. This came from unguided light skimming over the sample surface. This light was blocked by placing a piece of 0.5mm diameter Al wire on top of the guide and using a horizontal slit placed before the detector to spatially filter the detected light.

Recalling expression (4.3), if multiple cavity reflections can be ignored, the relationship between transmitted intensity and propagation loss (α) can be written:

$$I(L, \lambda) = I_0 \gamma (1-R)^2 \exp[-2\alpha L] = I_0 \exp[-2\alpha L]$$

where γ = coupling efficiency, I_i = incident intensity,
 L = device length, R = facet reflection coefficient,
 α = propagation loss in nepers per unit length.

To take account of the transmission of the system and wavelength dependence of the detector, the detected signal, I_D , can be written:

$$I_D(L, \lambda) = I(L, \lambda) \cdot T_s \cdot D$$

where T_s and D are respectively the system transmission (which can be wavelength and polarisation dependent) and the detector sensitivity (which can be wavelength dependent).

A waveguide of a given length (L_0) was placed on the end-fire coupling system, and $I_D(L_0, \lambda)$ measured from 905nm into the absorption edge for both TE and TM propagation. This measurement was then repeated without the sample, thus determining:

$$I_s(\lambda) = I_i \cdot T_s \cdot D$$

Clearly I_s and I_D cannot be measured absolutely but by dividing $I_D(L_0, \lambda)$ by $I_s(\lambda)$ it is possible to remove the system's wavelength and polarisation dependence. γ and R were assumed to be independent of wavelength, so that $\alpha(\lambda)$ could be calculated in dBcm^{-1} for both polarisations, relative to some constant $\alpha(\lambda_0)$ thus:

$$\alpha(\lambda) = \Delta\alpha(\lambda) + \alpha(\lambda_0)$$

$$\Delta\alpha(\lambda) = (-10/L_0) \{ \log_{10}[I_D(L_0, \lambda) / I_s(\lambda)] - \log_{10}[I_D(L_0, \lambda_0) / I_s(\lambda_0)] \}$$

The resulting curves are shown in Fig 6-3. To obtain the absolute value of propagation loss in dBcm^{-1} , sequential cleaving was used at four wavelengths using four guide lengths. The results are shown as points in Fig 6-3. One of the points was used as the value for $\alpha(\lambda_0)$. The other points were used to check the consistency of the two measurement methods. The two sets of results are seen to be in excellent agreement.

From Fig 6-3 it can be seen that far from the absorption edge the propagation loss of the TE mode (α_{TE}) is equal to that of the TM mode (α_{TM}) with $\alpha_{TE} \approx \alpha_{TM} \approx 12\text{dBcm}^{-1}$. This propagation loss is rather

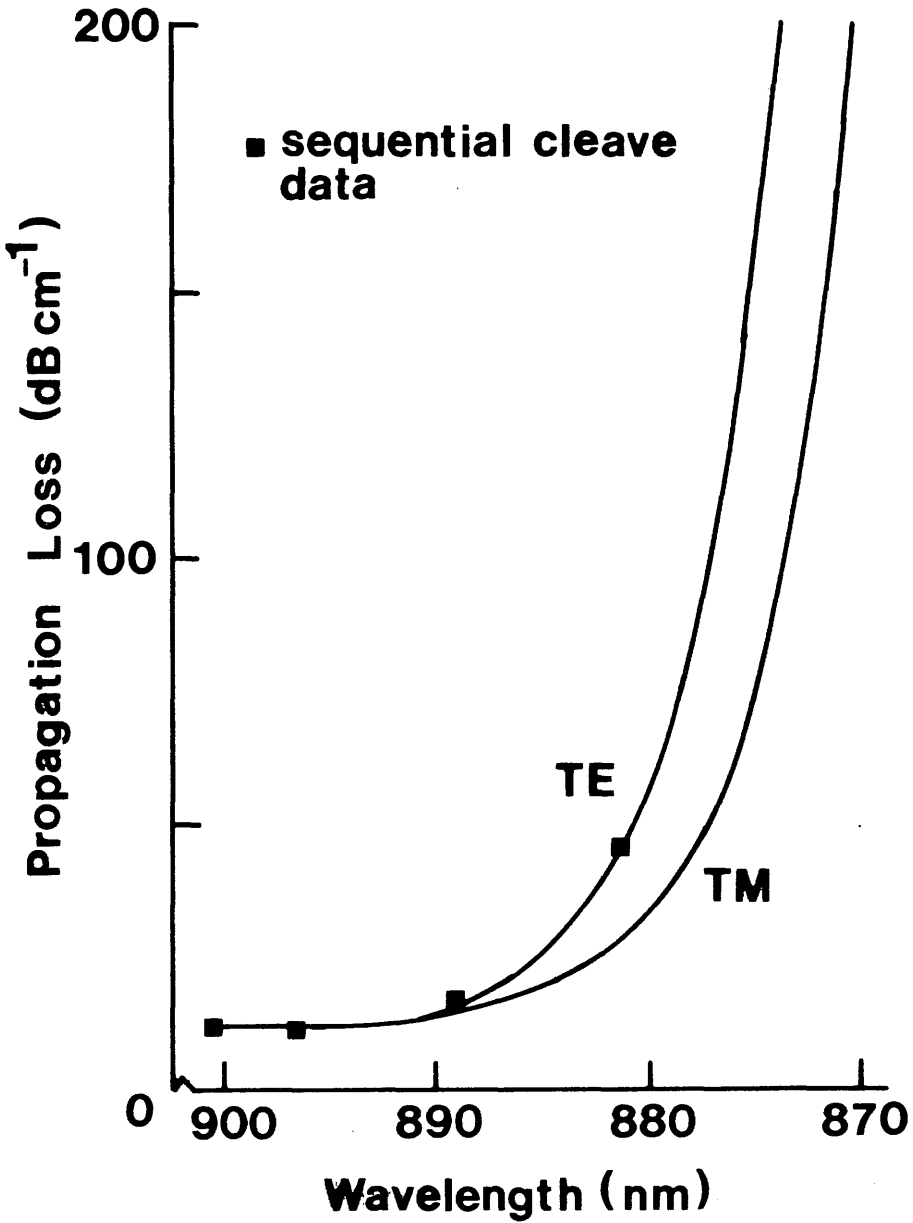


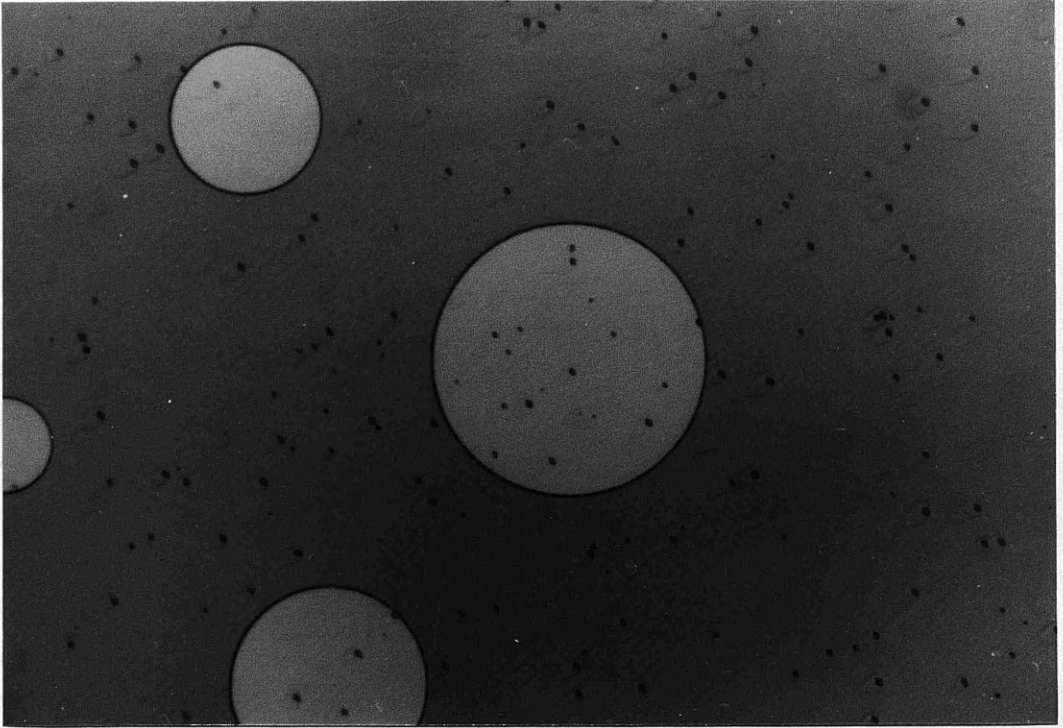
Fig 6-3 The propagation loss of CPM68 versus wavelength. The continuous lines, obtained by continuously scanning the dye-laser, were calibrated using the longest wavelength sequential cleave data point.

large but can be accounted for by several contributing loss terms. Firstly, because the MQWS is much thinner than planned (0.263 μm consisting of 12 wells and 11 barriers), the confinement of the mode is low with 63% of the modal power actually in the guide layer at $\lambda=0.9\mu\text{m}$. There will therefore be a large free carrier loss due to the high doping levels of the (Al,Ga)As cladding layers. This free carrier loss term was estimated using a four layer complex refractive index waveguide model to be 7.7dBcm⁻¹. The deeper penetration of the modal field out into the cladding will also introduce a loss term due to absorption in the GaAs substrate. This term was included in the complex refractive index program, and brought the calculated propagation loss to approximately 8.4dBcm⁻¹. The remainder of the measured propagation loss is due to radiation loss into the GaAs substrate, and scattering loss from the large number of defects observed on the surface of the sample.

This defect scattering term could be large. Fig 6-4 shows the "as received" surface of CPM68. The large density of defects consisted of pits in the surface. These defects are probably due to poor preparation of the surface of the substrate prior to growth at the SERC Central Facility for III-V Semiconductors. The defects may therefore propagate down through the epitaxial layers, in which case their effect on the waveguide, quantum mechanical and electrical characterisation of the sample could be severe.

Closer to the 2D absorption edge α_{TE} is larger than α_{TM} , with $\alpha_{TE} \approx 2\alpha_{TM}$ for $\lambda \approx 875\text{nm}$. This anisotropic absorption is due to the different oscillator strengths of the exciton transitions at the quasi-2D band edge. As described in chapter two, the heavy hole excitonic transition is not allowed for TM modes. The absorption edge for TM modes therefore occurs at a higher energy than for TE modes. This anisotropic absorption edge has previously been observed in single and double well leaky guides by Weiner et al^{1,2}.

From the room temperature etalon absorption data of CPM96 and similar data by others^{1,2,6}, the absorption edge of a MQWS with 100Å wells would have been expected to occur at $\lambda \approx 860\text{nm}$. The observed TE absorption edge at $\lambda \approx 880\text{nm}$ is therefore at a longer wavelength than expected, but is still shorter than the absorption edge observed in GaAs-DH⁶. The longer wavelength edge is an indication that broadening



(a)



(b)

Fig 6-4 The surface defects of sample CPM68. (a) An optical micrograph of a sample with photolithographically developed windows in a coating of photoresist. The largest circle has a diameter of 80 μ m. (b) A s.e.m. close-up of the defects.

of the exciton peaks has occurred due to the inhomogeneities in the MQWS. However, it must also be remembered that the absorption edge observed in these MQW waveguide experiments is the very tail of the absorption edge and may not accurately reflect the position of the fundamental absorption edge of the structure.

The observed absorption anisotropy for TE and TM modes is consistent with that observed by Weiner et al². Glick et al⁴ found that a similar anisotropy could be induced at $\lambda=888\text{nm}$ by applying 8V reverse bias to their p-i-n diode waveguide structure.

6.3 DESIGN OF PASSIVE STRIPE WAVEGUIDES

For many device structures of interest in integrated optics (for example, directional couplers and Y-junctions) it is necessary to confine light in the lateral direction. To demonstrate a reliable method of fabricating stripe waveguides in MQW-DH, single, double and multi-mode stripe waveguides were fabricated in CPM68.

Two forms of ridge waveguide are possible in a MQW-DH. If the outer slab region (Fig 6-5) is etched down into the MQW layer or beyond, then a very strongly confined rib waveguide can be formed. This form of guide has been demonstrated in MQW-DH by Tarucha and Okamoto⁷ who used it to form a monolithic laser-modulator structure. However, the very strong lateral confinement of this waveguide structure would have made the formation of single lateral mode guides and the fabrication of directional couplers very difficult using the photolithographical techniques developed. If the outer slab region is etched down to a depth no further than the bottom of the upper cladding layer (Fig 6-5) then a strip loaded waveguide is formed in which the lateral confinement can be easily controlled by the etch depth. In this way, single-mode stripe waveguides of 2-3 μm width and directional couplers can be formed.

The composition and structure of sample CPM68 had previously been studied by s.e.m. and PL as described in section 5.4.3, the results being summarised in Fig 6-6. The rms model was used together with the Effective Index Method to calculate the ridge width at which a strip loaded waveguide with a given outer cladding thickness, t , would sustain two TE modes in the lateral direction. The curves thus

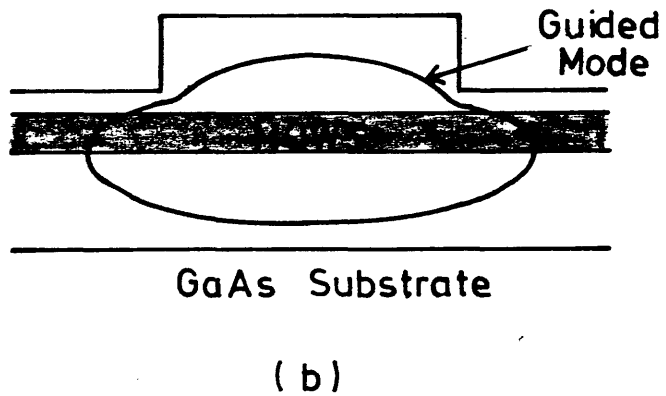
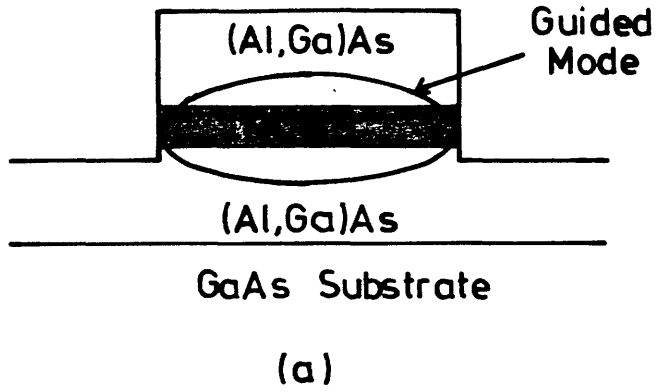
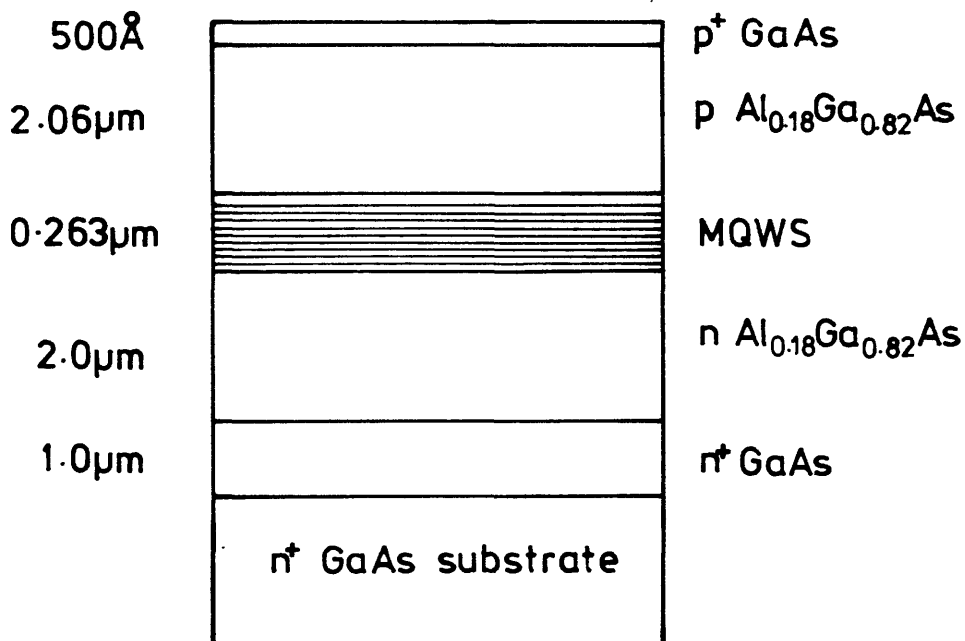


Fig 6-5 Two forms of ridge waveguide in MQW-DH: (a) the rib waveguide, and (b) the strip loaded waveguide.



$$p^+ \approx 5 \times 10^{17} \text{ cm}^{-3}$$

$$p \approx 5 \times 10^{17} \text{ cm}^{-3}$$

$$n \approx 4 \times 10^{16} \text{ cm}^{-3}$$

$$n^+ \approx 10^{18} \text{ cm}^{-3}$$

12 wells of GaAs and
 11 barriers of Al_{0.3}Ga_{0.7}As
 average doping $n \approx 2 \times 10^{16} \text{ cm}^{-3}$

Fig 6-6 A schematic diagram of CPM68. The data was obtained from s.e.m., PL and C-V investigations.

obtained for two excitation wavelengths (900 and 875nm) are plotted in Fig 6-7. Also plotted for comparison are curves obtained from the Effective Index Method assuming that the refractive index of the MQWS is that of the (Al,Ga)As alloy with the same average aluminium concentration (see section 2.3.2) or that of GaAs. From Fig 6-7 it was decided to cut a chrome light field shadow mask that consisted of 3, 5 and 10 μ m wide lines. Etching waveguides of various outer cladding thicknesses between 0.4 μ m and 0.8 μ m would therefore allow single and bimodal waveguides to be fabricated and some conclusions about the validity of the rms model to be made.

6.4 FABRICATION OF PASSIVE STRIPE WAVEGUIDES

Substrate preparation and photoresist patterning followed the standard procedures described in chapter three. Several samples of epitaxial (Al,Ga)As were patterned together with several samples of CPM68 to allow the dry etching process to be characterised before the final devices were made.

As described in chapter three, dry etching had been chosen for the fabrication of semiconductor waveguides. Work by Dr. G. Doughty using a Plasma Technology RIE80 reactive ion etching system with SiCl₄ had resulted in a set of etch conditions which produced smooth vertical walls in GaAs. It was decided to apply these etch conditions to the MQW-DH and thus obtain information on the etching characteristics of (Al,Ga)As, as well as producing novel MQW-DH waveguide structures by RIE.

6.4.1 Etch Conditions and Procedure

A common difficulty with RIE dry etching is the formation of cones of unetched material on the surface of the sample (see Fig 6-8), the cones often occurring in tight groups and swirls around etched features. One reason for their formation is the improper drying of the sample after development of the photolithographic pattern. Impurities left on the sample surface mask the sample, leaving cones. Another mechanism is the sputtering of mask material onto the surface. To reduce the possibility of contamination, samples for RIE were carefully dried in the clean-room immediately prior to etching,

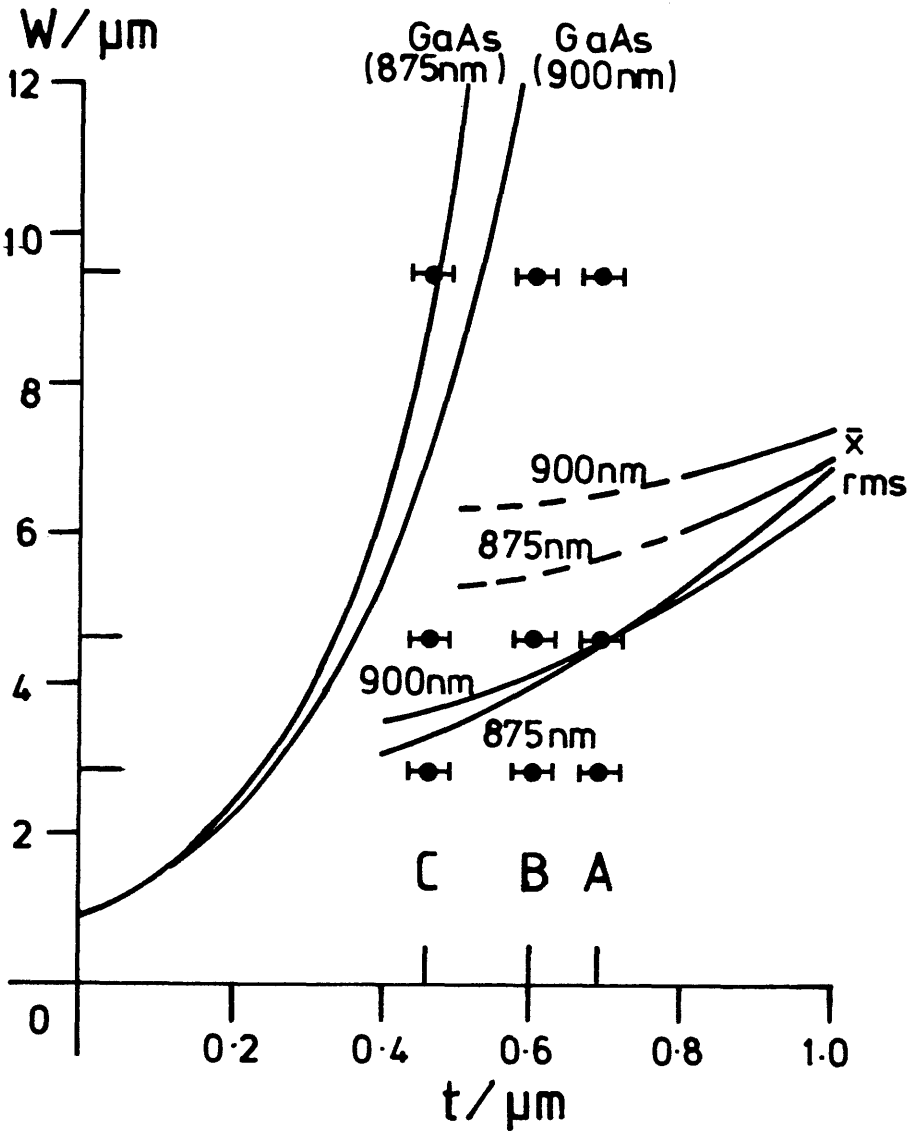


Fig 6-7 The TE₁₀ cut-off width (W) against outer cladding thickness (t) at $\lambda=900\text{nm}$ and 875nm assuming the refractive index of the MQWS to be that of: (i) GaAs, (ii) the alloy with identical Al concentration (\bar{x}), (iii) the weighted rms mean of the bulk indices of the constituent layers (rms). The sets of data points A, B and C correspond to the fabricated samples of section 6.5.

and carried, covered, to the RIE. In this way, the sample surface was kept under approximately 10^{-10} Torr.

The plasma chamber was pumped down to a base pressure of 10^{-10} Torr before SiCl_4 was introduced to establish an etching process. The chamber temperature was normally controlled via a fan in contact with the sample. The gas flow was set to 100 sccm which gave a DC self-bias voltage of about 100V when striking the plasma. The impedance matching was regularly monitored to minimize reflected power. Each time was automatically controlled to a 100% of a second. The etch conditions are summarized in Table 6-1.

Several different etching rates were obtained for different etching times. The resulting etch rates are plotted in Fig 6-9. The etch rate is dependent on the concentration of SiCl_4 in the gas and with a predictable manner. The results suggest, with

6.4.2 Ridge

The results found to be

resulting in

Fig 6-10(b)

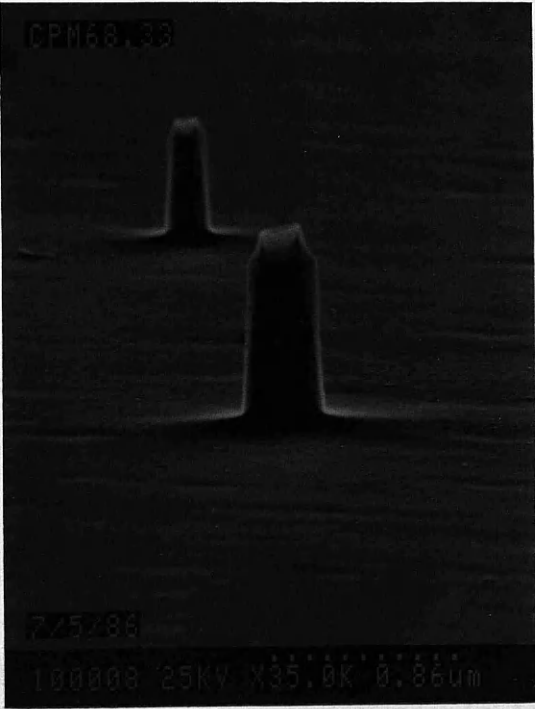
the tapered sidewall slope over the cones. The tapered sidewall slope over the cones is consistent with the higher RF power density used in the present work. The tapered sidewall slope over the cones is consistent with the higher RF power density used in the present work.

appear to be greater in the present results. With the tapered sidewall slope over the cones is consistent with the higher RF power density used in the present work.

sample this roughness is caused by ripples in the photoresist. The surface texture evident in this RIE process will have to be determined whether the edge roughness of the CPMS sample is due to the original mask preparation or whether it is the result of the RIE process.

shows that this edge roughness has an amplitude of less than 100nm. The edge roughness of the CPMS sample is due to the original mask preparation or whether it is the result of the RIE process.

Fig 6-8 shows cones formed on sample CPM68 by RIE. The edge roughness of the CPMS sample is due to the original mask preparation or whether it is the result of the RIE process.



CPMS were etched for different etching times. The resulting etch rates are plotted in Fig 6-9. The etch rate is dependent on the concentration of SiCl_4 in the gas and with a predictable manner. The results suggest, with

under a 5.0 a 200 W

show examples of the

Fig 6-10(a) and (b)

the tapered sidewall slope over the cones. The tapered sidewall slope over the cones is consistent with the higher RF power density used in the present work.

appear to be greater in the present results. With the tapered sidewall slope over the cones is consistent with the higher RF power density used in the present work.

sample this roughness is caused by ripples in the photoresist. The surface texture evident in this RIE process will have to be determined whether the edge roughness of the CPMS sample is due to the original mask preparation or whether it is the result of the RIE process.

shows that this edge roughness has an amplitude of less than 100nm. The edge roughness of the CPMS sample is due to the original mask preparation or whether it is the result of the RIE process.

Fig 6-8 shows cones formed on sample CPM68 by RIE. The edge roughness of the CPMS sample is due to the original mask preparation or whether it is the result of the RIE process.

and carried, covered, to the RIE80. In this way, the cone density was kept under approximately $10\text{-}100\text{cm}^{-2}$ on most samples.

The plasma chamber was pumped down to a base pressure of 0.2mr before SiCl_4 was introduced to establish an etch pressure of 11mr. Temperature was manually controlled via a tap to $(45\pm 1)^\circ\text{C}$. RF power was set to 100W which gave a DC self-bias voltage of 420V. After striking the plasma, the impedance matching was regularly checked to minimise reflected power. Etch time was automatically controlled to a 100^{th} of a second. The etch conditions are summarised in Table 6-1.

Several samples of GaAs, $\text{Al}_{0.3}\text{Ga}_{0.7}\text{As}$ and CPM68 were etched for different lengths of time over a period of several weeks. The resulting etch depths were measured by Talystep and are plotted in Fig 6-9. The etch rate was found to be independent of aluminium concentration at $(0.21\pm 0.01)\mu\text{m min}^{-1}$. This etch rate is almost three times that observed by Stern and Liao⁸ using SiCl_4 . On a given day and with a given structure the etch rate was found to be more predictable than the error bars of 5% on the above etch rate would suggest, with etch depths being predictable to $\pm 2\%$.

6.4.2 Ridge Profile

The resulting ridge profiles were observed under a s.e.m and were found to be highly rectangular. Fig 6-10 shows examples of the resulting profiles in $\text{Al}_{0.3}\text{Ga}_{0.7}\text{As}$ (Fig 6-10(a)) and CPM68 (Fig 6-10(b)). In both cases the sample is left very clean with few cones. The improved sidewall slope over that observed by Stern and Liao⁸ is consistent with the higher RF power density (and resulting DC bias) used in the present work. Edge roughness does, however, appear to be greater in the present results. With the $\text{Al}_{0.3}\text{Ga}_{0.7}\text{As}$ sample this roughness is caused by ripples in the photoresist due to the surface texture evident in this MBE grown sample. Further investigation of the RIE etch process will have to be made to determine whether the edge roughness of the CPM68 sample is due to resist mask preparation, roughness in the original shadow mask lines, or some effect related to the etch mechanism. Fig 6-10(b) shows that this edge roughness has an amplitude of less than 20nm. This improvement in edge roughness over that produced by IBE is to be expected due to the chemical nature of RIE and, together with the

Etch Pressure	11m τ
RF Power	100W
DC Self Bias	420V
RF Frequency	13.56MHz
Temperature	45°C
Plate size	top: 280mm \emptyset bottom: 170mm \emptyset
Plate separation	50mm

Table 6-1 A summary of the RIE etch conditions used.

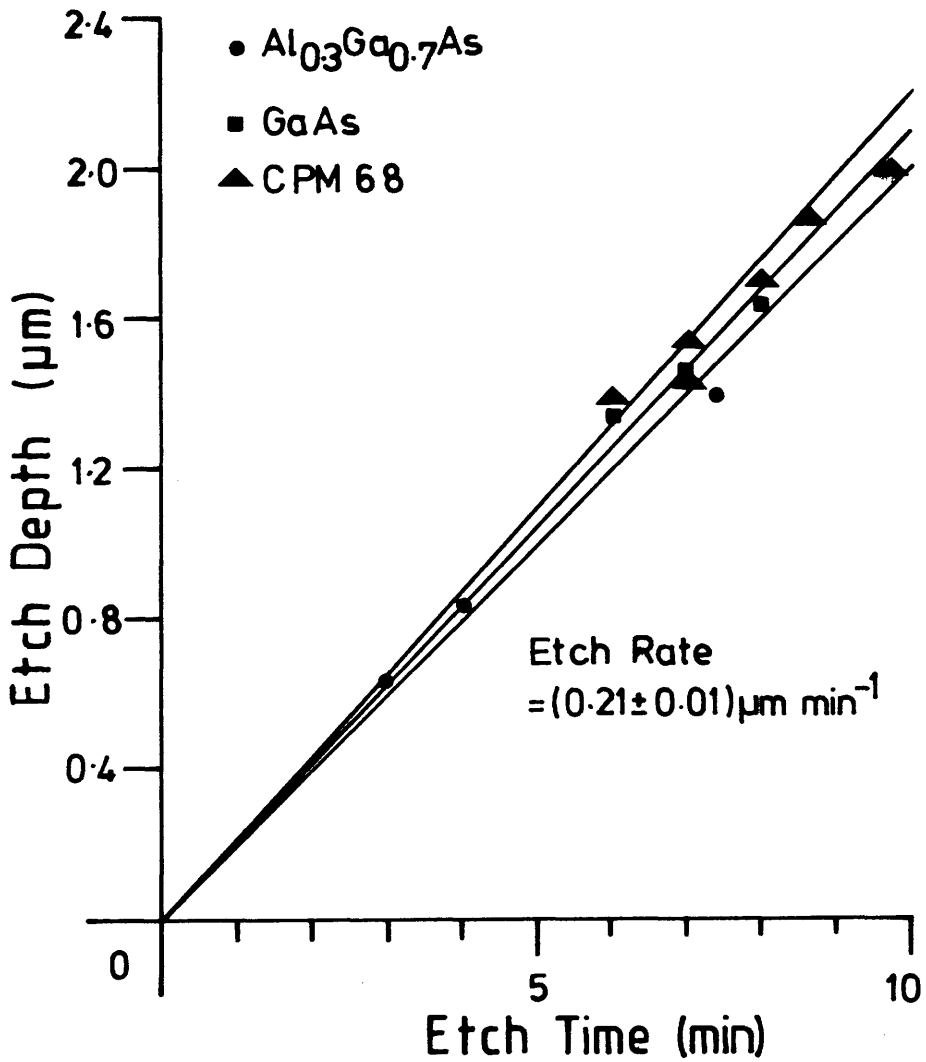
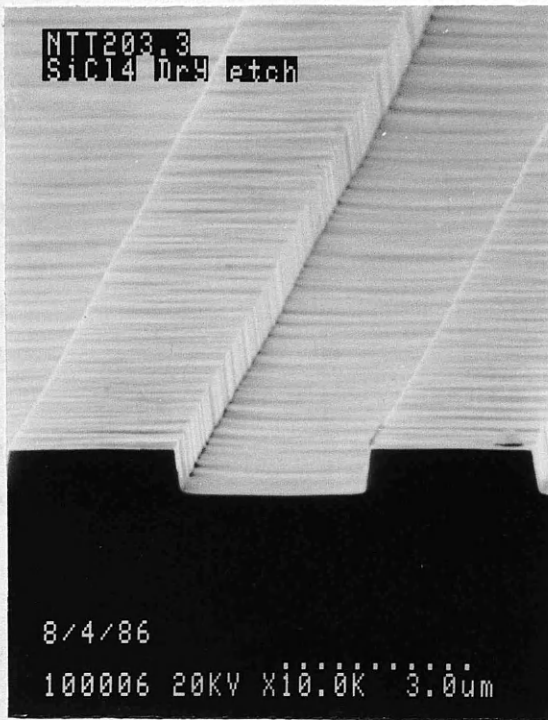
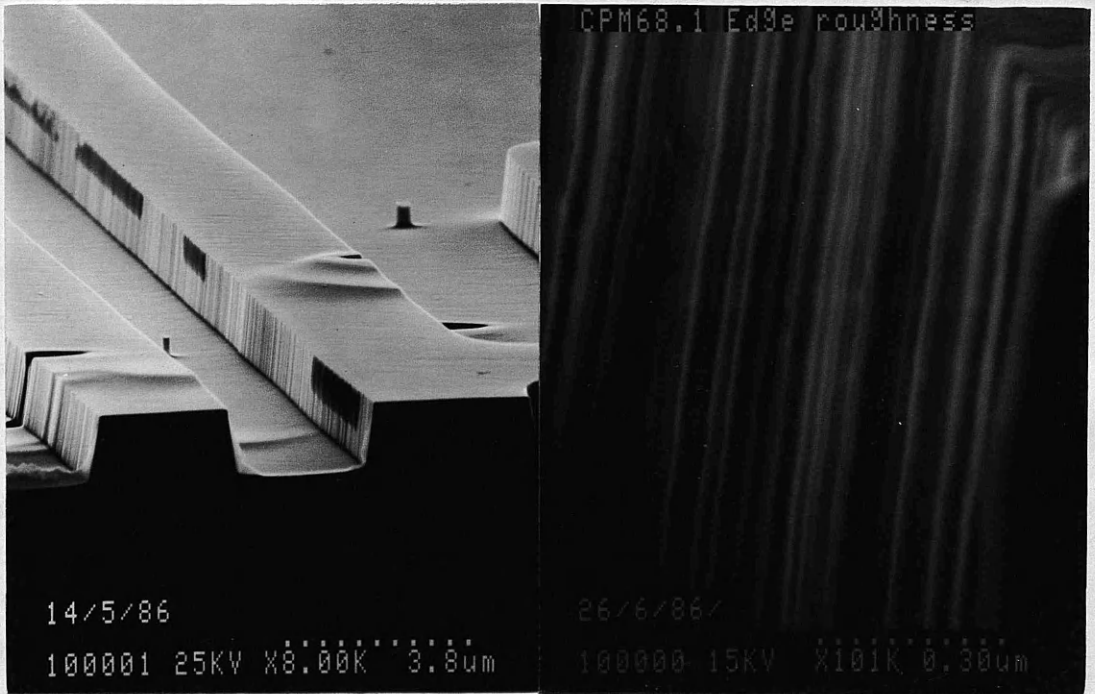


Fig 6-9 Etch depth versus etch time for several (Al,Ga)As structures using RIE.



(a)



(b)

Fig 6-10 Typical ridge profiles resulting from the RIE process in: (a) $\text{Al}_{0.3}\text{Ga}_{0.7}\text{As}$, and (b) MQW-DH CPM68.

observed improvement in wall angle and reported reduction in surface damage⁹, made SiCl_4 RIE the preferred alternative to IBE for the fabrication of the MQW-DH waveguides.

6.4.3 Waveguide Etch

Three samples of CPM68 were etched for 7, 7 and 8 minutes resulting in etch depths of A: $(1.42 \pm 0.02) \mu\text{m}$, B: $(1.51 \pm 0.02) \mu\text{m}$ and C: $(1.65 \pm 0.02) \mu\text{m}$ respectively. Fig 6-11 shows s.e.m. micrographs of the resulting ridges of nominal width 3, 5 and $10 \mu\text{m}$. In fact, measurement using the s.e.m. put the widths of the ribs at their base as:

nominal width / μm	measured width / μm
3	2.86 ± 0.03
5	4.58 ± 0.05
10	9.48 ± 0.10

The difference between nominal and measured width is due to slight errors in the shadow mask line width rather than any process related effect.

At this point it is worth noting again the large defects present on the surface of CPM68 evident in Fig 6-11, many of which intersect the ridges to become potential scattering centres for the guided mode.

By using the de-oxidising technique described in section 5.4.2 to increase the contrast between epitaxial layers, it was possible to use the s.e.m. to obtain Fig 6-12. In this micrograph both the $(\text{Al,Ga})\text{As}$ ridge and the MQW layers (in the form of a faint, light band) are visible allowing detailed measurement of the waveguide structure to be made.

6.5 MODAL CHARACTERISTICS

Fig 6-7 in section 6.3 plots the curves of maximum rib width against outer cladding thickness calculated together with experimental points representing the three waveguide structures etched. It can be seen that both the rms and the alloy models for the

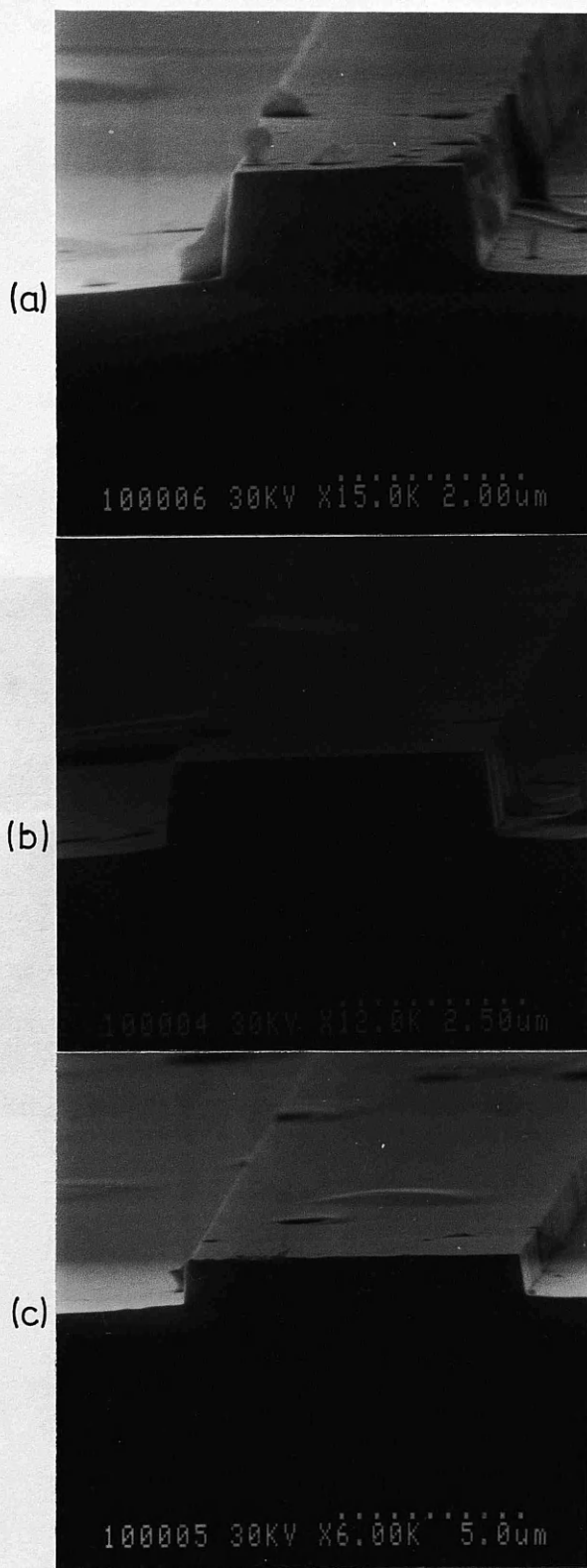


Fig 6-11 Micrographs of a set of RIE etched waveguide structures in MQW-DH CPM68 with nominal widths: (a) 3 μ m, (b) 5 μ m, and (c) 10 μ m.

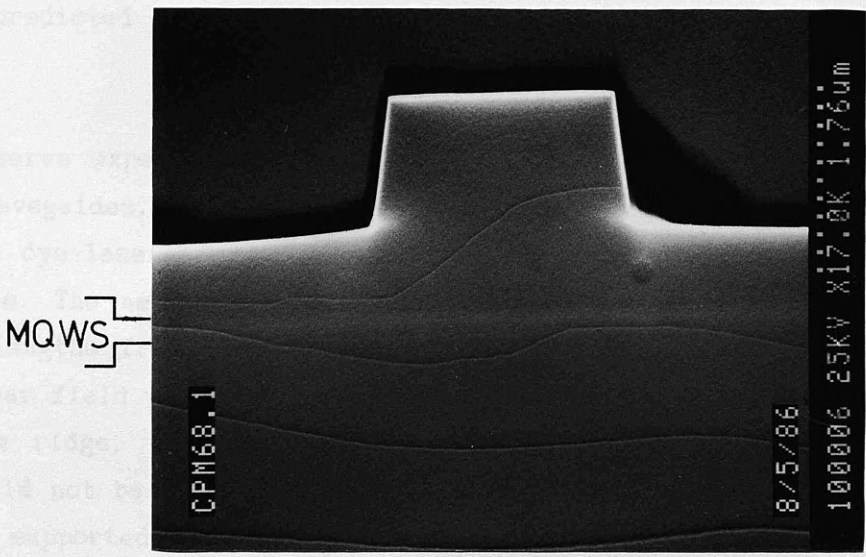


Fig 6-12 A detailed micrograph of a strip loaded waveguide of nominal width $3\mu\text{m}$ in CPM68 showing the MQW layer as a faint, light band.

refractive index of MQWS predict that all the $10\mu\text{m}$ waveguides will be multi-mode. However, the alloy approximation ($n_x=n_s$) predicts that all the 3 and $5\mu\text{m}$ waveguides will be single-mode while the rms model ($n_x=n_{\text{rms}}$) predicts that the two deeper etched $5\mu\text{m}$ guides will be bimodal with the shallowest etched $5\mu\text{m}$ guide being on the second mode cut-off point.

The WAVE variational method had some difficulty modelling the second mode of the strip loaded waveguide structures as can be seen from the convergence results in Fig 6-13. However, using 7×12 basis functions and the rms model, the shallowest etched $5\mu\text{m}$ guide was calculated to sustain only one mode at $\lambda=875$ and 900nm . The modal profile predicted by WAVE for this structure at $\lambda=900\text{nm}$ is shown in Fig 6-14.

To observe experimentally the modal characteristics of the strip loaded waveguides, the end-fire coupling system was used with the Styryl-9 dye-laser to couple TE polarised radiation into the waveguides. The near field pattern was observed using the IR camera for wavelengths from 875 to 900nm . Any change observed in the shape of the near field pattern, as the input beam was translated laterally under the ridge, would be due to modal interference and thus the guide would not be single-mode. This method of determining the number of modes supported in a stripe waveguide is not infallible since a second mode close to cut-off would be too highly absorbed to cause modal interference at the guide output.

The results are tabulated in Table 6-2 with Fig 6-15 showing examples of the near field patterns obtained from samples A and C. All the $3\mu\text{m}$ guides were clearly single-mode. It was found that a distinct double peak near field pattern could be induced in the $5\mu\text{m}$ wide guides of sample C by asymmetrically exciting the waveguide, indicating that a second transverse mode was being sustained. A much less intense double peaked pattern could be observed in sample B, indicating that the second mode was much closer to cut-off. The near field pattern of the $5\mu\text{m}$ guides of sample A showed no dependence on input condition, implying single-mode propagation. The near field pattern of all the $10\mu\text{m}$ guides was found to be complex, implying multi-mode propagation.

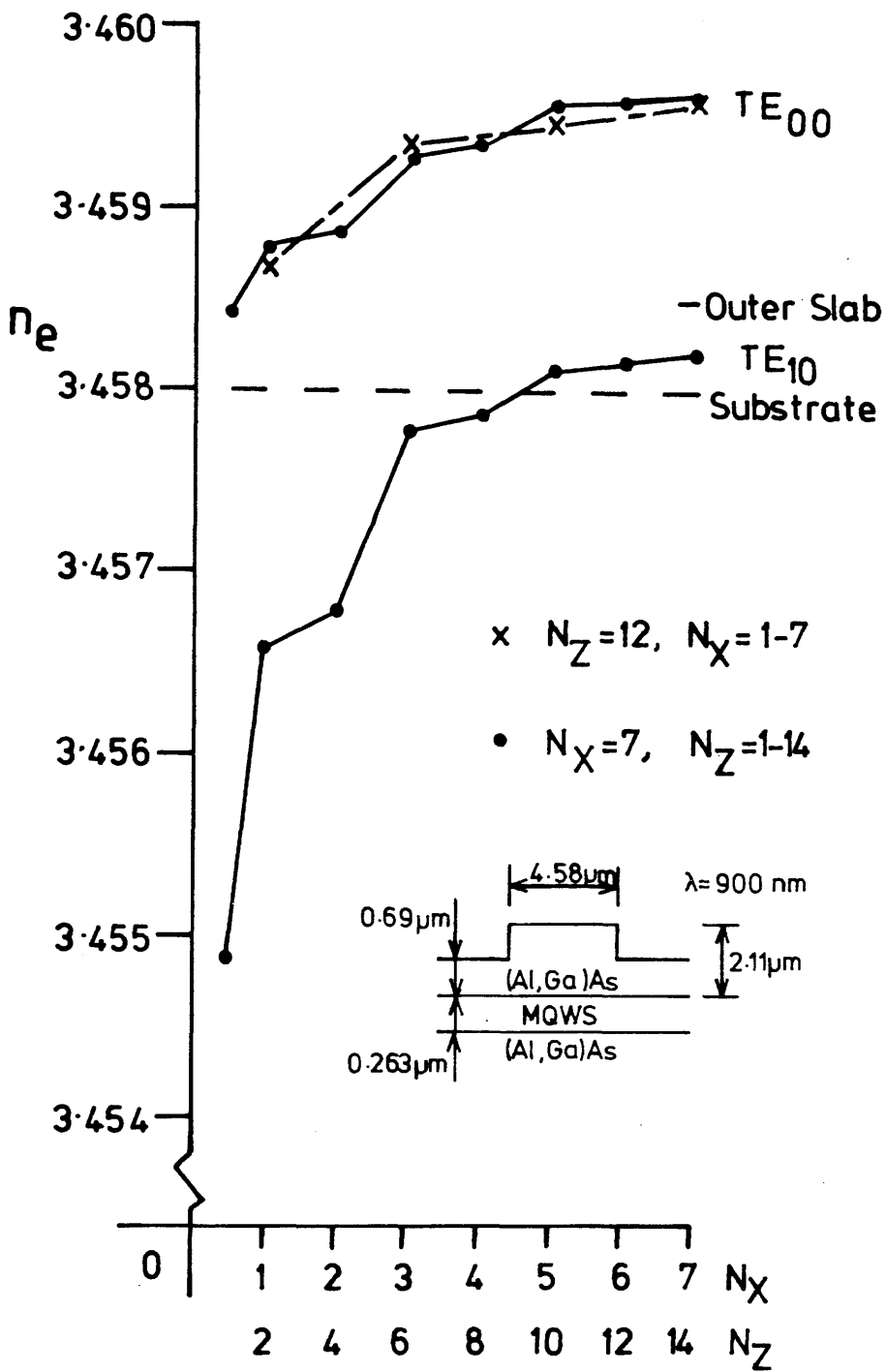
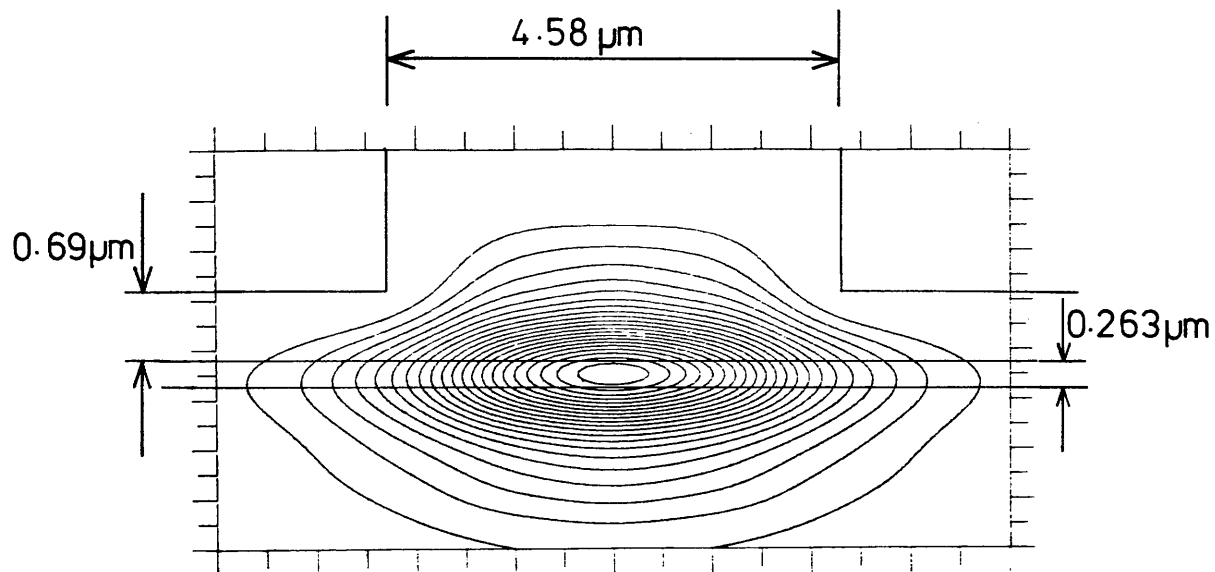


Fig 6-13 Convergence of the WAVE solution to the strip loaded waveguide problem as the number of basis functions in the x (N_x) and z (N_z) directions is varied.

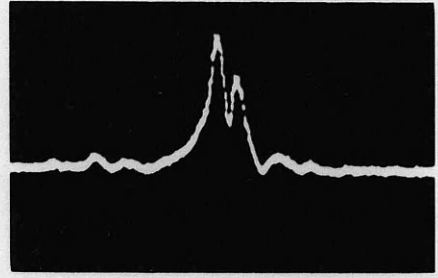
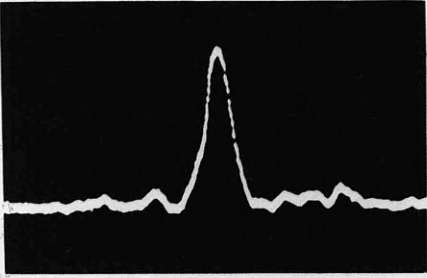
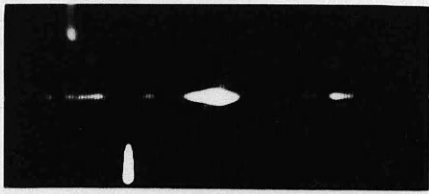


CPM68 Guide A5, $\lambda=900\text{nm}$

Fig 6-14 The modal field profile predicted by WAVE for strip loaded sample A5 at $\lambda=900\text{nm}$.

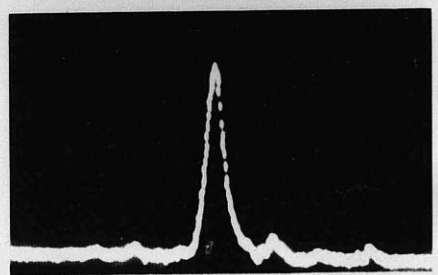
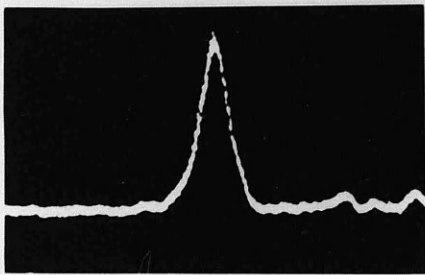
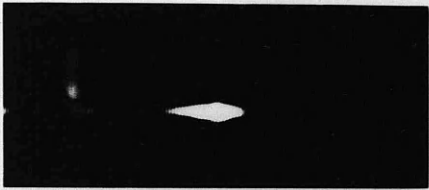
Etch Depth	Guide Width / μm		
	3	5	10
A	Single - Mode	Single- Mode	Multi- Mode
B	Single- Mode	Weak Second Mode	Multi- Mode
C	Single- Mode	Two Modes	Multi- Mode

Table 6-2 A summary of the modal characteristics of the strip loaded waveguides in CPM68.



A5

C5



A3

C3

Fig 6-15 The near field patterns observed in strip loaded samples of nominal width $3\mu\text{m}$ (3) and $5\mu\text{m}$ (5), and etch depths $1.42\mu\text{m}$ (A) and $1.65\mu\text{m}$ (C).

These results are consistent with the rms model for the refractive index of a MQWS, but not the alloy model, and demonstrate the use of a reliable dry etching process to fabricate strip loaded waveguides in MQW-DH.

6.6 PROPAGATION LOSS

A detailed study of the transmission loss of the 3 and 5 μ m waveguides was undertaken at a wavelength of 905nm. The sequential cleave method described in chapter four was used. At each of four lengths, the transmission of six 3 μ m wide and three 5 μ m wide guides was measured using a small area Si photodiode and a lock-in amplifier. Spatial filtering ensured that only power remaining in the laterally guided mode was detected. Fig 6-16 plots the results and shows a significant difference in both the coupling loss and the propagation loss of the 3 μ m and 5 μ m wide guides with:

$$3\mu\text{m guide propagation loss} = 17.0 \text{ dBcm}^{-1}$$

$$5\mu\text{m guide propagation loss} = 15.3 \text{ dBcm}^{-1}$$

Although high, this propagation loss is consistent with the high propagation loss measured in the planar structure. The additional propagation loss in the ridge structures is due to defects scattering light from the laterally confined mode into the planar mode which is still above cut-off. Further, the lower propagation constant of the laterally guided mode in comparison with the unetched slab will enhance free carrier, GaAs and radiation loss due to the weaker confinement of the mode. Ridge roughness will introduce an additional loss term.

The difference in propagation loss between the 3 and 5 μ m waveguides is due to the stronger lateral confinement in the 5 μ m guide, making it more difficult for light to be scattered into the planar mode and the higher propagation constant reducing the other loss terms.

6.7 PASSIVE DIRECTIONAL COUPLER

Having demonstrated the fabrication of single-mode strip loaded waveguides and measured their propagation loss it was decided to

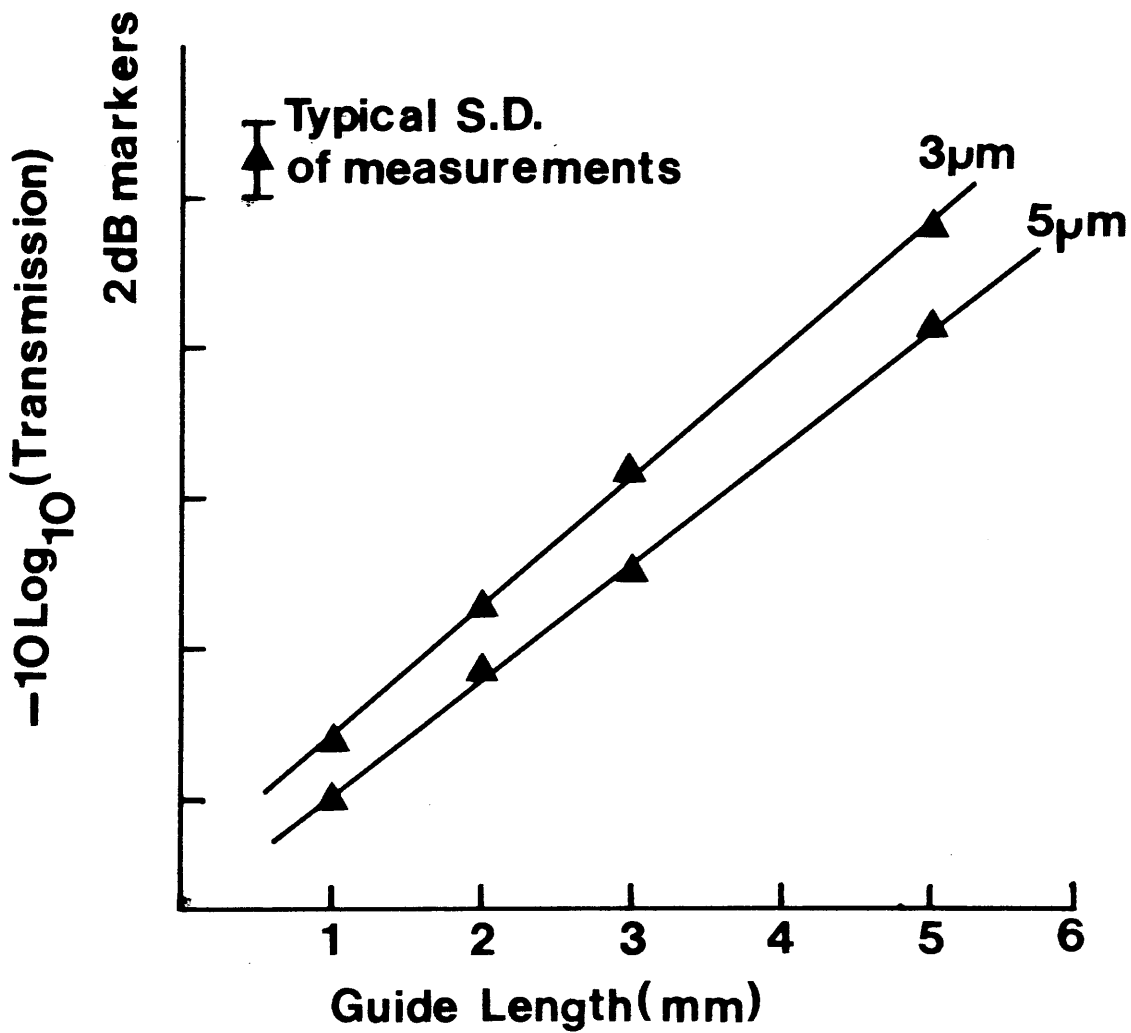


Fig 6-16 The results of sequential cleaving loss measurements on sample A3 (nominal width $3\mu\text{m}$) and A5 (nominal width $5\mu\text{m}$).

demonstrate the fabrication of a passive directional coupler in a MQW-DH. Directional couplers had been demonstrated in MQW single heterostructure waveguides by Kam Wa et al⁵ who produced lateral confinement using photo-elastic waveguides. However, to allow a full range of devices such as Y-junctions, curves and couplers to be made in MQWS using conventional semiconductor integrated optics technology, a strip loaded waveguide geometry would be useful.

6.7.1 Design and Fabrication

The shadow mask used to fabricate the strip loaded waveguides described in section 6.3 had been designed to have a set of five coupler structures as well as straight waveguides. The couplers consisted of 3 μ m lines separated by 3 μ m spaces. At intervals along each guide in the coupler, short branches connected 80 μ m square pads with the guides to allow the eventual fabrication of active, directional coupler switches. The work reported in chapter four with directional couplers in n/n⁺ GaAs waveguides had shown that it could be very difficult to excite one arm alone of a directional coupler. Consequently the couplers were designed so that only one guide extended to the edge of the mask. As schematically depicted in Fig 6-17, the second guide started some distance in from the edge of the mask, with the interaction length of each coupler differing in steps of 0.25mm.

Assuming a power P₀ is coupled into guide B of a lossless coupler at y=0, coupled mode theory¹⁰ states that the power in guides A and B will vary with interaction length L as:

$$P_A(L) = P_0 \left(\frac{K^2}{K^2 + \delta^2} \right) \cdot \sin^2 \left[(K^2 + \delta^2)^{1/2} L \right]$$

$$P_B(L) = P_0 - P_A(L)$$

so that:

$$P_B/P_0 = 1 - (P_A/P_0) = 1 - \left(\frac{K^2}{K^2 + \delta^2} \right) \cdot \sin^2 \left[(K^2 + \delta^2)^{1/2} L \right]$$

where K is the coupling coefficient between waveguides, and δ is the mismatch between the propagation constant in guides A and B.

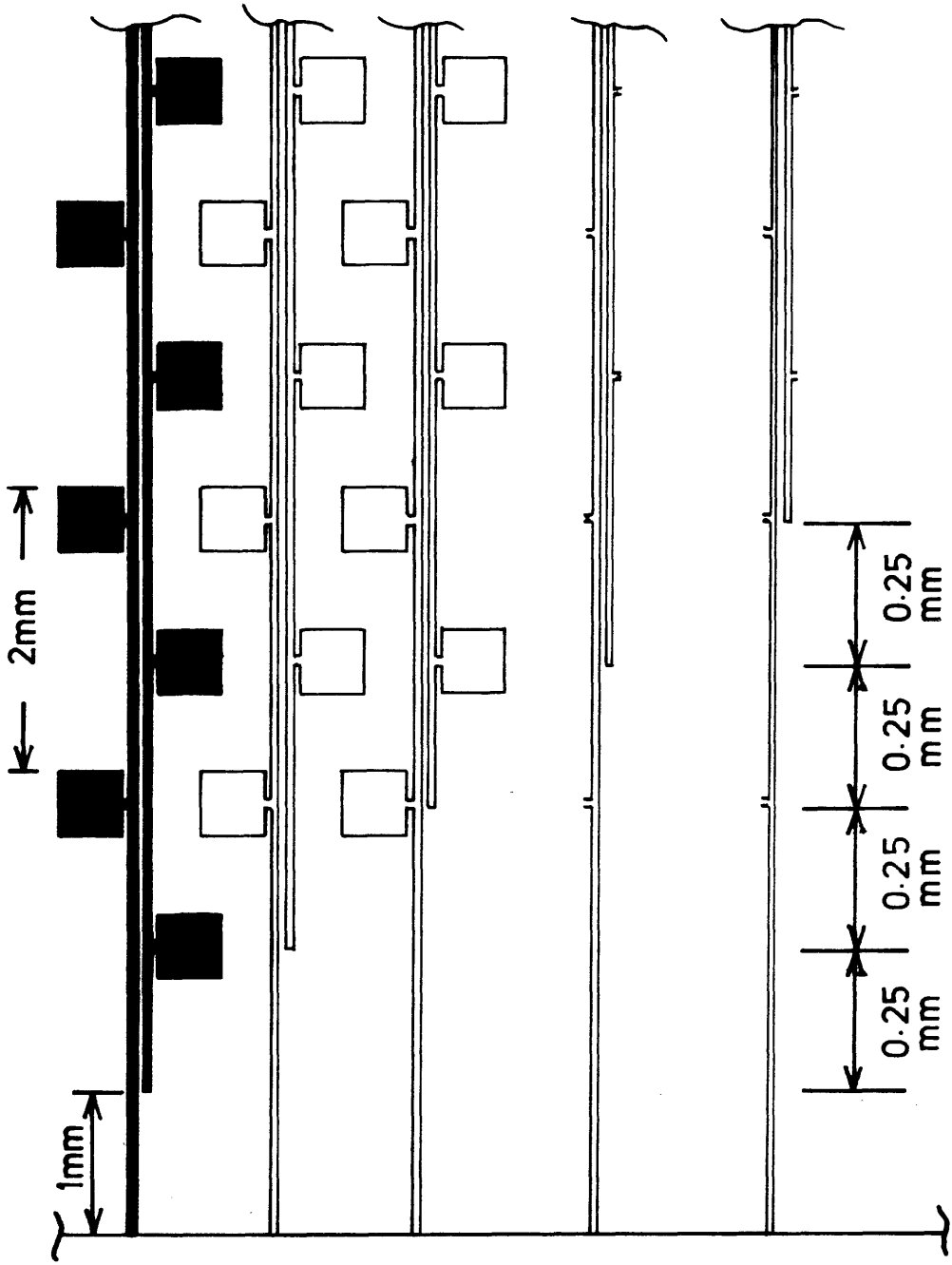


Fig 6-17 A schematic diagram of the directional coupler mask.

Power will transfer from guide B to A with distance, with maximum power transfer occurring for $\delta \approx 0$ at the coupling length $L_c = \pi / (2K)$.

The designed structure uses identical guides so that $\delta \approx 0$. Thus:

$$P_B/P_0 \approx \cos^2[(K^2 + \delta^2)^{1/2}L] \approx \cos^2KL$$

The coupling length, L_c , can be calculated from both the WAVE variational method and the MEIM as outlined in section 3.2.2 by calculating the propagation constant of the even and odd modes of the coupler structure. Initial design work on the couplers was carried out at $\lambda = 880\text{nm}$ using WAVE and the MEIM. Fig 6-18 shows that WAVE fails to satisfactorily converge even with a large basis set. With such a large basis set, calculations are very time consuming. Fig 6-19 plots the variation of L_c with outer cladding thickness t as calculated by the MEIM and WAVE using a 15×6 basis set. At large etch depths L_c is large because the strong confinement of the individual guides reduces the coupling between guides. At small etch depths the odd mode of the combined coupler structure is close to cut-off. Its propagation constant does not therefore change as fast with etch depth as the even mode's propagation constant does. Their values thus converge, lengthening L_c . For t greater than $0.9\mu\text{m}$ the odd coupler mode is below cut-off.

As was discussed in chapter three the two methods give a very similar minimum coupling length point which in this case is at $t \approx 0.7\mu\text{m}$ with $L_c \approx 2\text{mm}$. This is approximately the etch depth of the previously examined sample A. Fig 6-20 shows examples of the coupler structures fabricated in sample A. They exhibit very good ridge profiles similar to those of the straight guides. Note the large contact pad connected to the furthest ridge in Fig 6-20(b).

The actual guide widths and spacings of the coupler structures were measured by a s.e.m. and due to imperfect mask cutting and photolithography were found to vary slightly across the sample with values:

waveguide width	$(2.95 \pm 0.05)\mu\text{m}$
waveguide separation	$(3.00 \pm 0.05)\mu\text{m}$

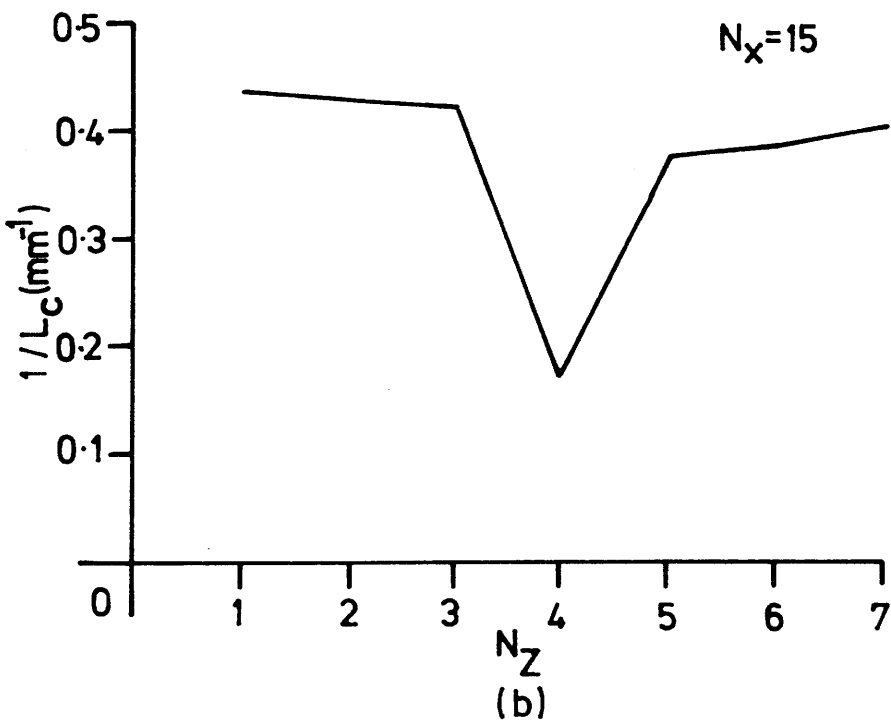
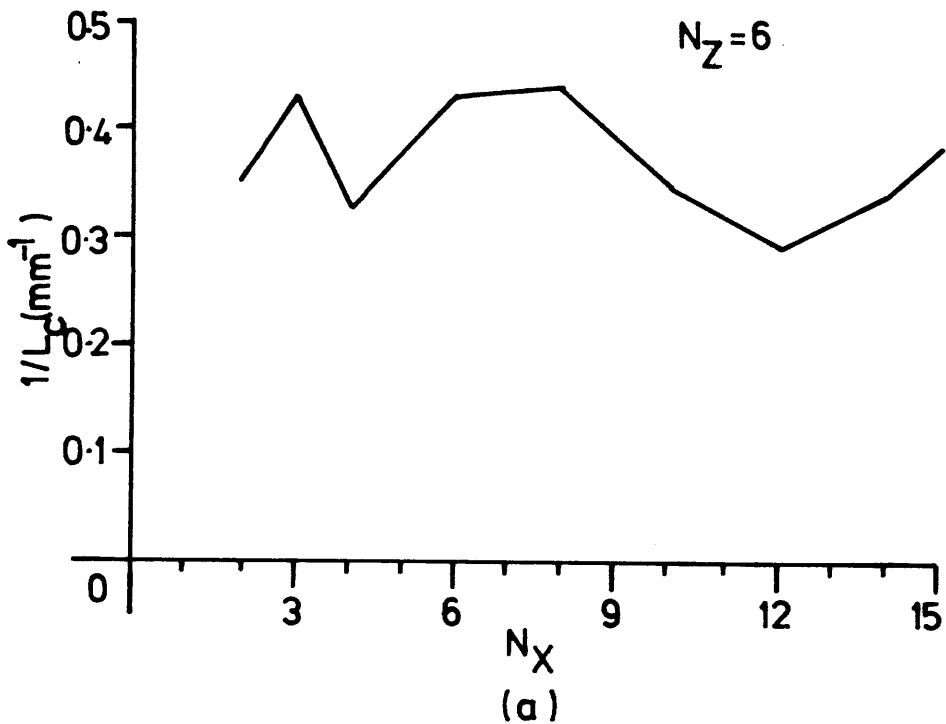


Fig 6-18 The convergence of the WAVE solution to the directional coupler problem as the number of basis functions (a) in the x direction and (b) in the z direction is varied. The outer cladding thickness is $0.8\mu\text{m}$ and $\lambda=0.88\mu\text{m}$.

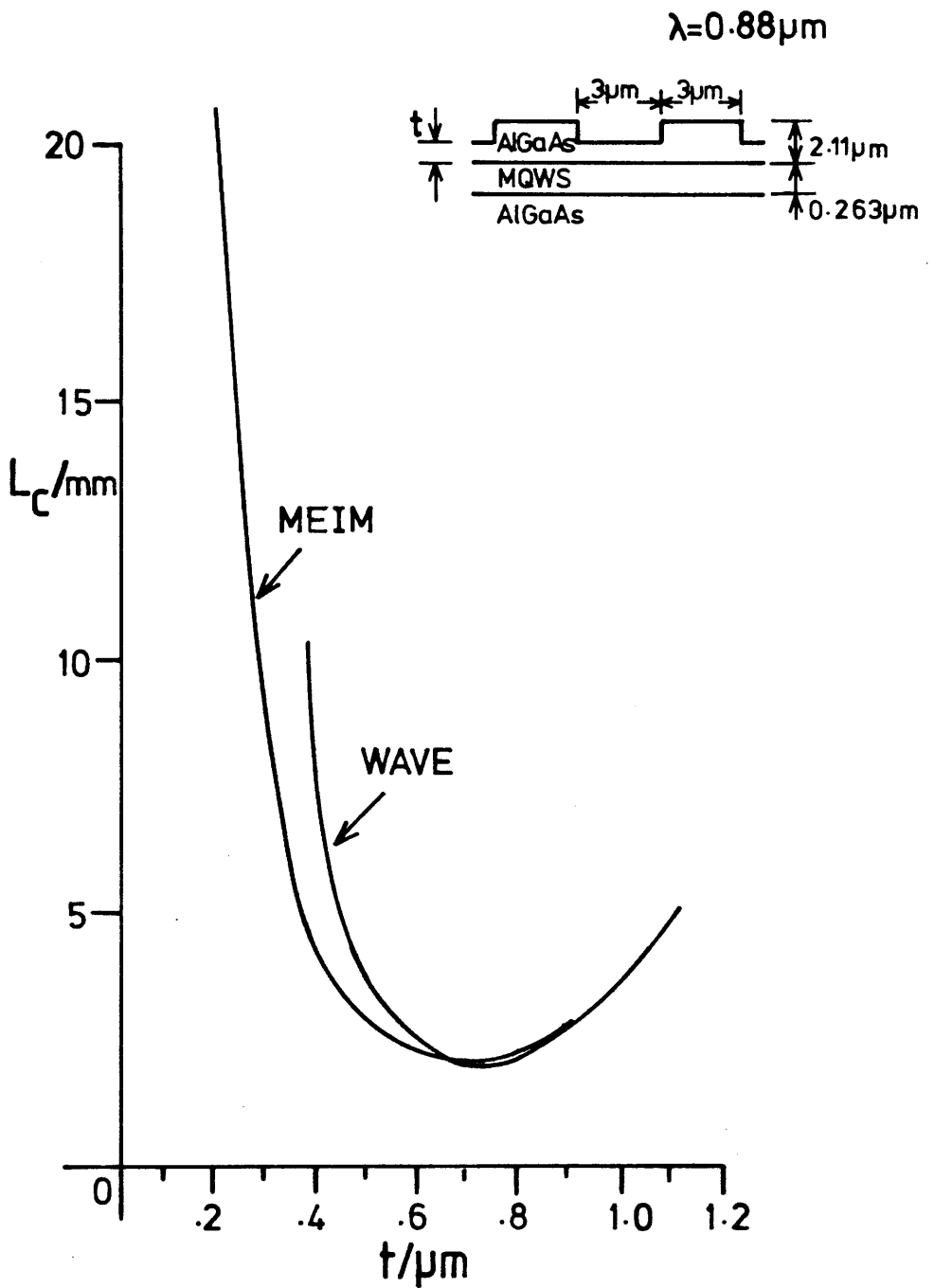
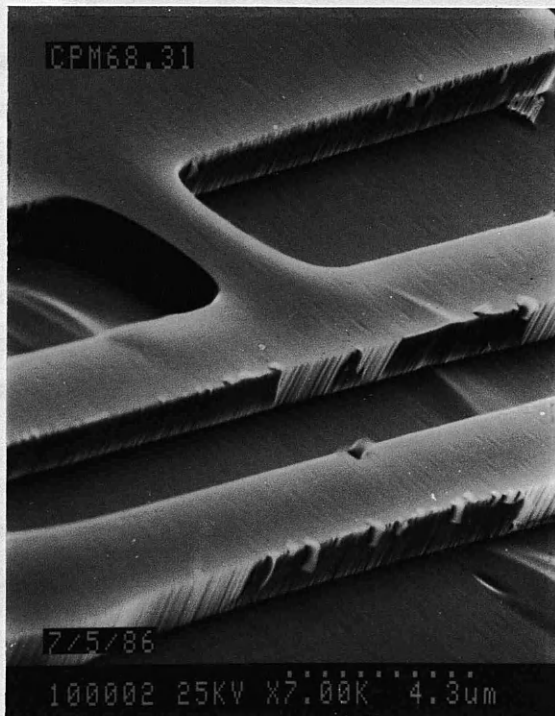


Fig 6-19 The variation of coupling length (L_c) with outer cladding thickness (t). The results are for the designed coupler structure and are calculated by WAVE and the MEIM .



(a)



(b)

Fig 6-20 S.e.m. micrographs of the directional couplers etched by RIE in CPM68 sample A.

This measured variation in coupler structure across the sample was estimated to produce approximately $\pm 3\%$ fluctuations in the coupling lengths of the structures.

6.7.2 Experimental Results

Sample A was first cleaved so that the central interaction length was (2.10 ± 0.02) mm. At $\lambda = 880$ nm the propagation loss in the structures made precise measurement of the coupling intensity difficult, so the experiment was carried out at $\lambda = 900$ nm. Fig 6-21 shows that using the measured coupler dimensions in the MEIM at this wavelength results in a coupling length of 1.96mm being predicted.

A membrane beam splitter was placed after the output microscope of the end-fire coupling system to direct the near field pattern of the couplers onto both a Si photodiode and an IR camera. The image on the IR camera was then used to position a pin hole before the beam splitter so that the power in each guide could be measured in turn. The power transmitted by each guide of each coupler was measured several times and the mean value used in further calculations. The sample was then cleaved so that the central coupler had a coupling length of (1.05 ± 0.02) mm and the process was repeated.

Fig 6-22 shows a typical near field pattern of the coupler structures. It was found to be difficult to precisely filter the near field pattern to measure the power in an individual guide because the guides were still only $3\mu\text{m}$ apart at the output facet. It is recommended that in any future coupler design the guides are curved away from each other before they reach the end facet. For each interaction length, L , P_o was calculated as:

$$P_o(L) = P_A(L) + P_B(L)$$

Plotting P_B/P_o against L , Fig 6-23 was obtained. A least squares fit of a \cos^2 function to the data points gave a value for L_c of $L_c = (2.17 \pm 0.15)$ mm.

The large errors placed on this value are due to the difficulty found in accurately measuring the output power of the waveguides which fluctuated slightly with input condition. It is therefore

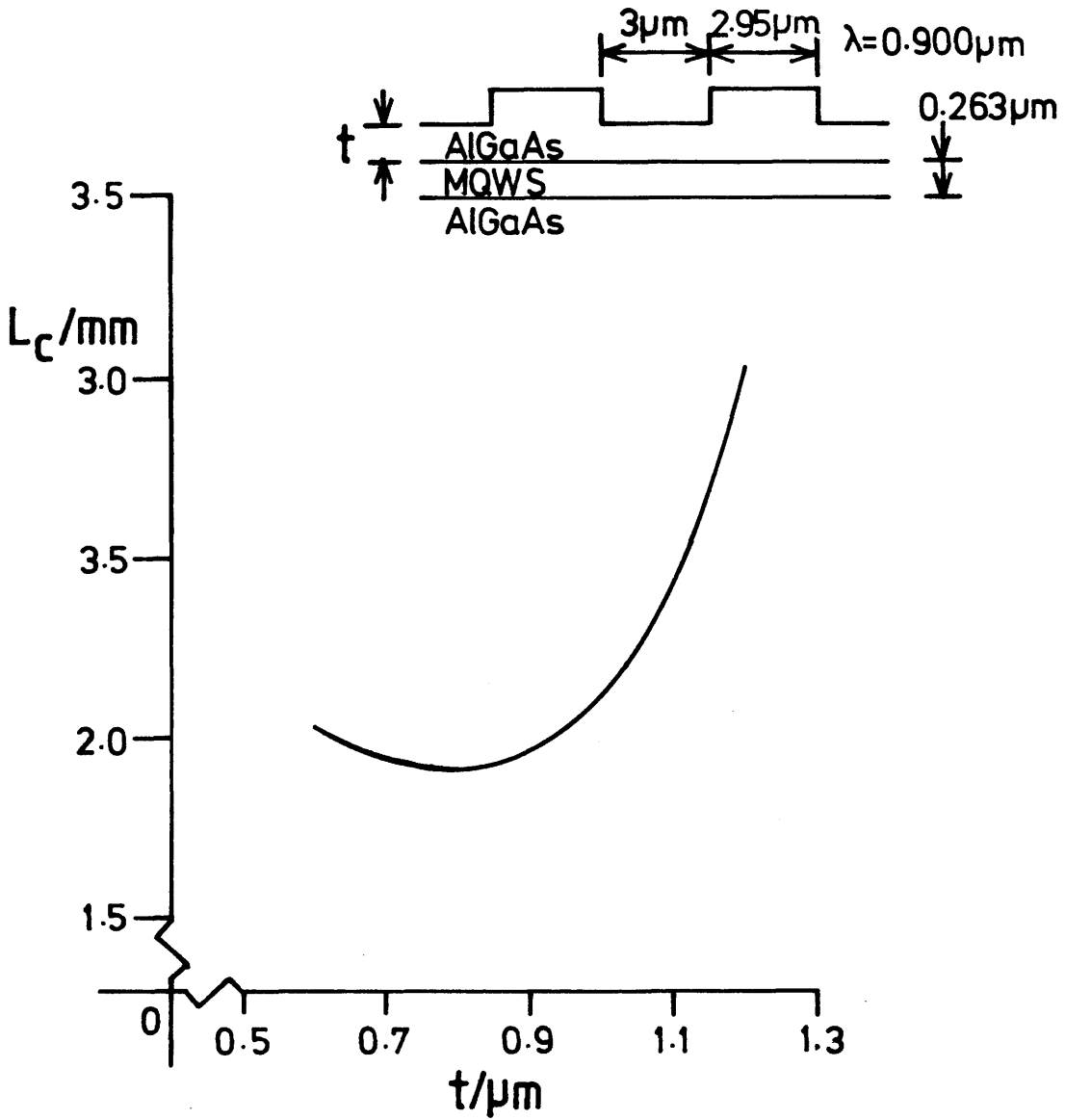


Fig 6-21 The variation of coupling length (L_c) with outer cladding thickness (t) for the measured coupler dimensions.

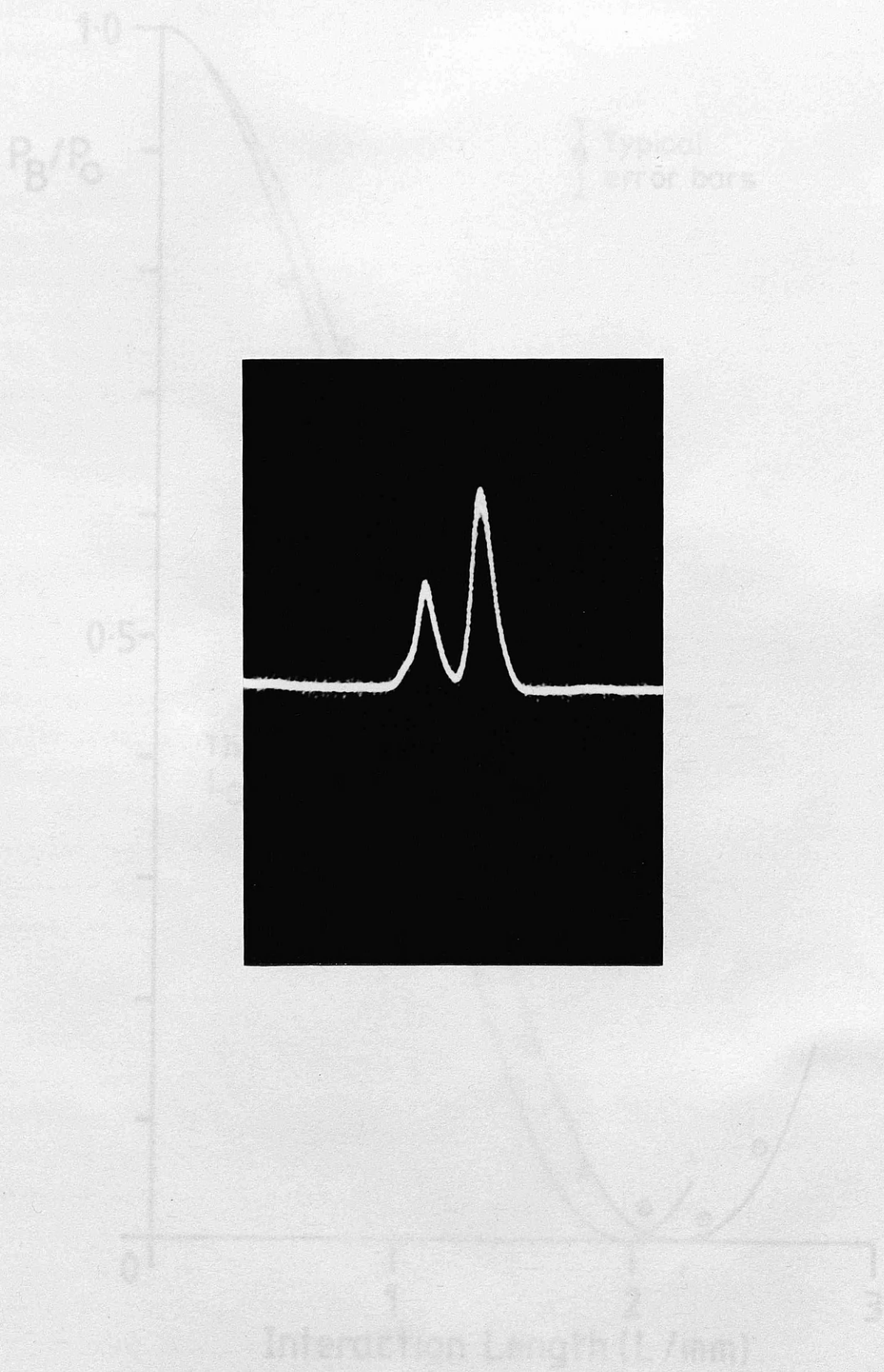


Fig 6-22 A typical near field pattern of the etched directional couplers.

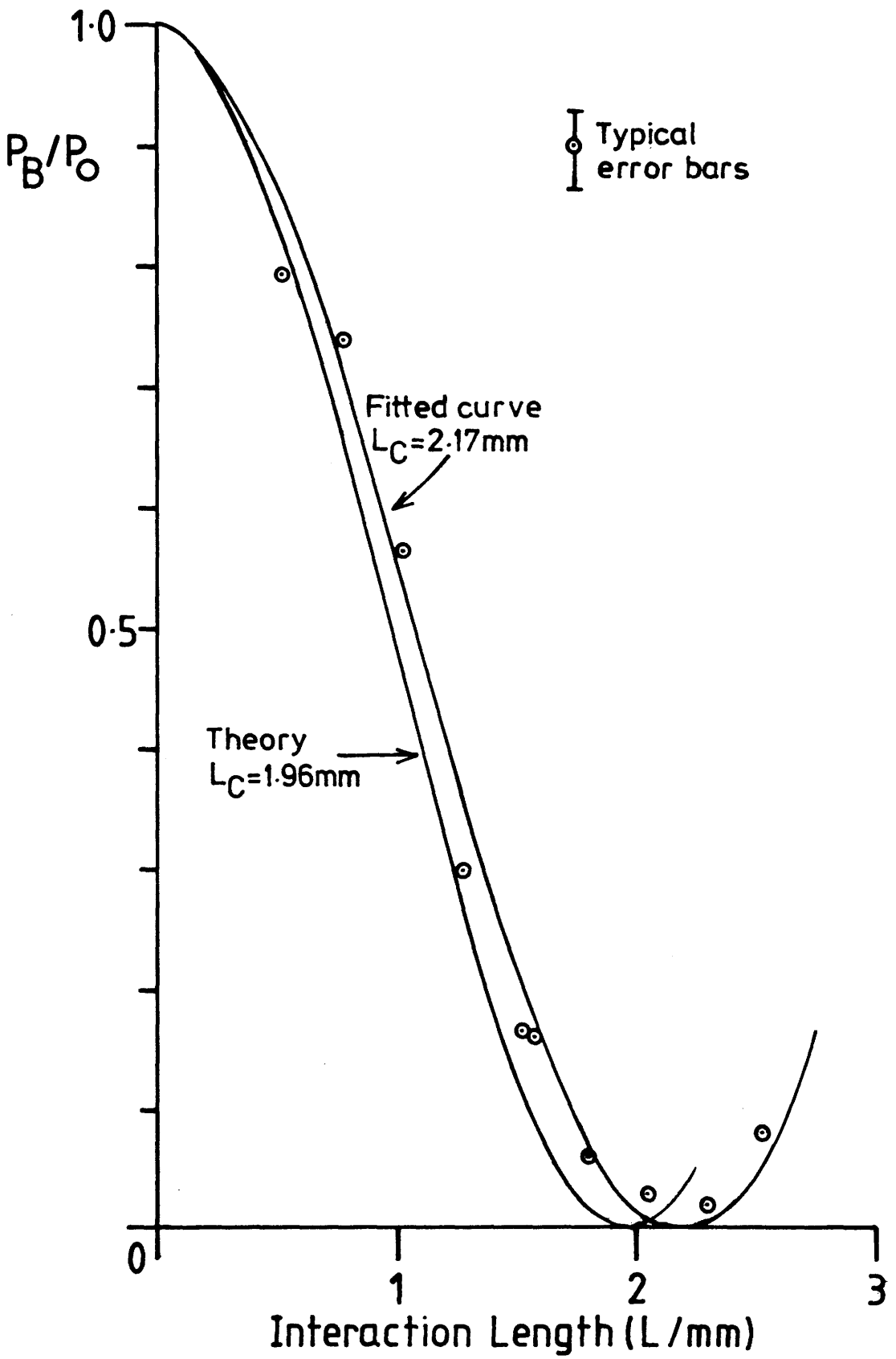


Fig 6-23 A plot of the ratio of uncoupled power to total power (P_B/P_O) in the directional couplers as a function of the interaction length (L).

difficult to draw any firm conclusions from the difference between measured and predicted coupling lengths.

What can be said is that once again the rms model has proved a useful and accurate model for the design of MQW-DH waveguide devices. The passive coupler structure thus demonstrated has many potential applications. Its ridge structure would make monolithic integration with a MQW laser straightforward providing a passive power divider. Alternatively, it could be used as an all optical switch similar to than demonstrated by Kam Wa et al in photo-elastic waveguides⁵. The inclusion of ohmic contacts on top of the ridges would also allow the creation of an electro-optic directional coupler modulator or switch for monolithic integration with MQW lasers.

6.8 CONCLUSIONS

The planar waveguide characteristics of MQW-DH have been shown to be confusing, with similar structures supporting different near field patterns. Several of the samples grown exhibited the desired single bright planar mode, including two p-i-n doped samples. It was decided to concentrate on one of these samples. The variation of propagation loss with wavelength close to the absorption edge of this MQW-DH was measured and found to be anisotropic with $\alpha_{TE} > \alpha_{TM}$. The absorption edge was observed at a higher wavelength than expected, due to broadening of the 2D absorption edge.

The rms model was used to fabricate novel strip loaded waveguides in MQW-DH, and the observed near field patterns were consistent with the rms model. Strip loaded passive directional couplers were then fabricated in MQW-DH and found to have coupling lengths close to that predicted by using the rms refractive index model and the MBIM waveguide model.

The use of the demonstrated directional couplers as all optical and electro-optical switches and modulators was highlighted as a fruitful area of further research.

References to Chapter Six

- 1 J.S.Weiner, D.S.Chemla, D.A.B.Miller, H.A.Haus, A.C.Gossard, W.Wiegmann and C.A.Burrows;
"Highly anisotropic optical properties of single quantum well waveguides", Appl. Phys. Lett. **47**, 664 (1985).
- 2 J.S.Weiner, D.A.B.Miller, D.S.Chemla, T.C.Damen, C.A.Burrows, T.H.Wood, A.C.Gossard and W.Wiegmann;
"Strong polarization-sensitive electroabsorption in GaAs/AlGaAs quantum well waveguides", Appl. Phys. Lett. **47**, 1148 (1985).
- 3 G.J.Sonek, J.M.Ballantyne, Y.J.Chen, G.M.Carter, S.W.Brown, E.S.Koteles and J.P.Salerno;
"Dielectric Properties of GaAs/AlGaAs Multiple Quantum Well Waveguides", IEEE J. Q. Electron. **QE-22**, 1015 (1986).
- 4 M.Glick, F.K.Reinhart, G.Weimann and W.Schlapp;
"Quadratic electro-optic light modulation in a GaAs/AlGaAs multiquantum well heterostructure near the excitonic gap", Appl. Phys. Lett. **48**, 989 (1986).
- 5 P.Li Kam Wa, J.H.Marsh, P.N.Robson, J.S.Roberts and N.J.Mason;
"Nonlinear propagation in GaAs/GaAlAs multiple quantum well waveguides", SPIE vol.578 Int. Opt. Circ. Engineering II, 110 (1985).
- 6 S.Tarucha, Y.Horikoshi and H.Okamoto;
"Optical Absorption Characteristics of GaAs-AlGaAs Multi-Quantum-Well Heterostructure Waveguides", Jpn. J. Appl. Phys. **22**, L482 (1983).
- 7 S.Tarucha and H.Okamoto;
"Monolithic integration of a laser diode and an optical waveguide modulator having a GaAs/AlGaAs quantum well double heterostructure", Appl. Phys. Lett. **48**, 1 (1986).
- 8 M.B.Stern and P.F.Liao;
"Reactive ion etching of GaAs and InP using SiCl₄", J. Vac. Sci. Tech. B **1**, 1053 (1983).
- 9 G.Doughty;
Department of Electronics and Electrical Engineering, University of Glasgow, private communication.
- 10 S.E.Miller;
"Coupled Wave Theory and Waveguide Applications", The Bell Syst. Tech. Journal **661** (1954).

CHAPTER SEVEN
THE ELECTRO-ABSORPTION EFFECT IN MQW-DH

7.1 INTRODUCTION

A great deal of interest has been shown in the use of quantum well structures to enhance the electro-optic properties of semiconductors as outlined in chapter two. The fabrication of leaky waveguides containing two quantum wells by Weiner et al¹ and Wood² allowed a detailed study of the strong polarisation-sensitive electro-absorption in (Al,Ga)As quantum wells to be made. Glick et al³ have also observed this anisotropic electro-absorption in more practical MQW double heterostructures. The strong and fast electro-absorption demonstrated in MQW etalons⁴ has also been used in waveguides at wavelengths very close to the band edge to produce monolithic modulators/laser structures^{5,6}.

It was the aim of the work reported in this chapter to investigate the theoretical and practical aspects of fabricating electro-absorption modulators in MQW-DH. To fulfil this aim, a semi-empirical model was developed and used to describe the excitonic Stark shift observed when an electric field is applied across quantum wells. This allowed comparisons to be made between MQWS and GaAs electro-absorption modulators. Attention then turned to the practical aspects of applying an electric field across a MQW-DH, with I-V and C-V measurements being used to probe the electrical characteristics of the fabricated devices. Finally planar and stripe waveguide electro-absorption modulators were fabricated and tested.

7.2 THEORETICAL MODEL

7.2.1 Model Description

The semi-empirical model of Chemla et al⁷ for the absorption edge of a MQWS was described in chapter two. This takes into account the temperature and crystal imperfection broadening of the excitons by fitting Gaussian line shapes to the experimental peaks. The absorption due to the 2D density of states edge is fitted with a single smoothed out step. The following expression is obtained:

$$\alpha(\hbar\omega) = \alpha_h \exp[-(\hbar\omega - \hbar\Omega_h)^2 / 2(\hbar\Gamma_h)^2] + \alpha_l \exp[(\hbar\omega - \hbar\Omega_l)^2 / 2(\hbar\Gamma_l)^2] \\ + \alpha_c / (1 + \exp((\hbar\Omega_c - \hbar\omega) / \hbar\Gamma_c)) \times 2 / (1 + \exp\{-2\pi[|\hbar\Omega_c - \hbar\omega| / R_V]^{-1/2}\})$$

where subscript **h** = heavy hole exciton peak
l = light hole exciton peak
c = continuum edge

and

$\alpha(\hbar\omega)$ = total absorption
 α_i = peak height or continuum height at edge
 $\hbar\omega$ = photon energy
 $\hbar\Omega_i$ = peak or edge position
 $\hbar\Gamma_i$ = peak or edge width
 R_V = Rydberg's constant

This function gives a very good fit to the observed absorption edge of a MQWS as demonstrated by Chemla et al⁷. However, it is the leading edge of the absorption that is of interest in modelling the electro-absorption of MQWS and this was found to be satisfactorily modelled by a single Gaussian fitted to the hh peak for TE radiation or lh peak for TM. In the following analysis only TE radiation will be modelled.

On the application of an electric field all three terms defining the Gaussian absorption edge may vary (α_i , $\hbar\Omega_i$ and $\hbar\Gamma_i$). The magnitude of this variation was determined from experimental results quoted in the literature for MQWS with structures similar to the designed MQW-DH.

Ω_h variation

The experimental data of Miller et al⁸ was used to find a simple function form for the variation of $\hbar\Omega_h$ with electric field (**F**). The work of Miller et al⁸ has shown that a fundamental quantum mechanical analysis of MQWS yields a dependence of $\hbar\Omega_h$ and $\hbar\Omega_l$ on **F** that is very close to that experimentally observed (using no fitted parameters). However, in the present analysis, it was assumed that $\hbar\Omega_h$ would principally vary quadratically with **F** as predicted by quantum mechanical perturbation theory.

It was described in chapter two how an electric field F applied across an MQWS perturbs the wells, changing the position of the confined states. The new eigenenergy (E_n) of a state can be written as a power series thus:

$$E_n = E_n^{(0)} + \lambda E_n^{(1)} + \lambda^2 E_n^{(2)} + \dots$$

where λ is an arbitrary constant, $E_n^{(0)}$ is the unperturbed eigenenergy and $E_n^{(i)}$ the i^{th} order correction. $E_n^{(1)}$ is then given by¹⁰:

$$E_n^{(1)} = \langle n | H^{(1)} | n \rangle$$

where $H^{(1)}$ is the first order correction to the Hamiltonian, and $|n\rangle$ is the unperturbed eigenfunction. For a constant uniform field F , $H^{(1)}(z)$ is proportional to both F and z , and is therefore an anti-symmetrical function of z . Since $|n\rangle$ is strictly symmetrical or anti-symmetrical $E_n^{(1)} = 0$. However, the second order perturbation $E_n^{(2)}$ is non-zero and given by:

$$E_n^{(2)} = \sum_{i \neq n} \frac{\langle n | H^{(1)} | i \rangle \langle i | H^{(1)} | n \rangle}{E_n^{(0)} - E_i^{(0)}} \propto F^2$$

giving a quadratic dependence of E_n on F .

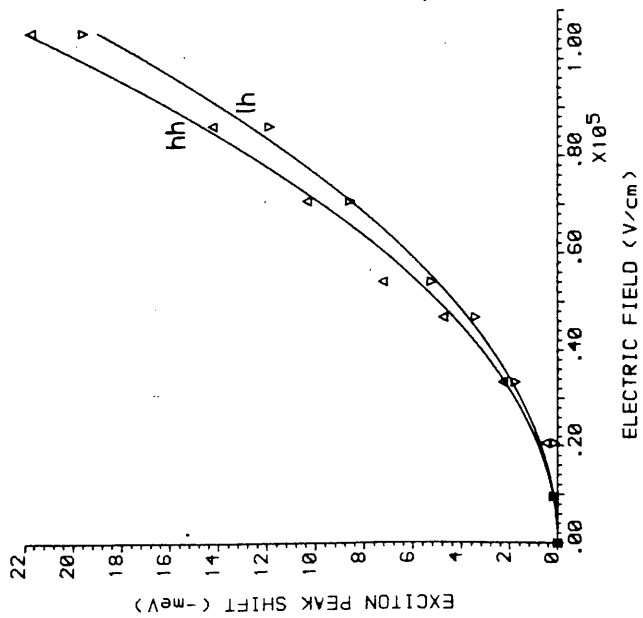
For small F , reduction in the binding energy of the exciton may introduce a small linear component to $\chi Q_n(F)$. However, a least squares fit of the function :

$$\chi Q_n = A + B \cdot F^2$$

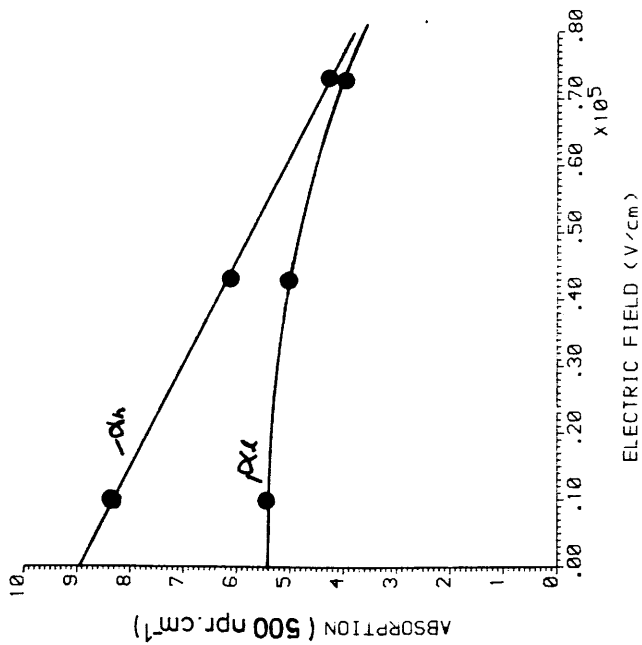
to the published data⁸ resulted in the values:

$$A = 1.457 \text{ eV}; \quad B = 0.199 \times 10^{-8} \text{ meV}/(\text{V/cm})^2$$

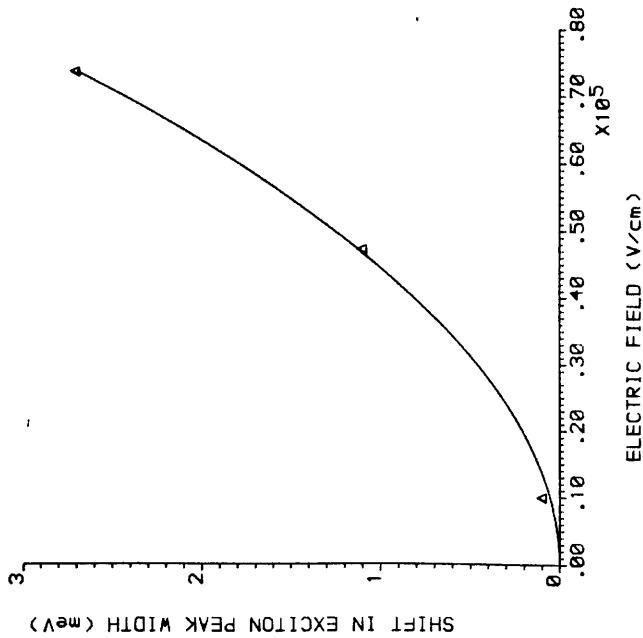
and a very good fit to the experimental data (see Fig 7-1(a)).



(a)



(b)



(c)

Fig 7-1 The variation with applied electric field of the parameters defining the excitonic peak: (a) the shift in peak position, (b) the shift in peak height, (c) the change in peak width.

α_n variation

A functional form for the variation of maximum peak height with F was obtained in a similar way by fitting a linear function to data from the same sample⁹. This resulted in the function (see Fig 7-1(b)):

$$\alpha_n = C + D \cdot F$$

where $C=4.48 \times 10^{23} \text{ npr. cm}^{-1}$; $D=-3.16 \times 10^{-2} \text{ npr. V}^{-1}$. The experimental data of Wood² confirmed the conclusion that α_n varies linearly with F until $F \approx 10^{15} \text{ Vcm}^{-1}$. Above this field the rate of change of α_n with F seems to saturate as the wells become strongly perturbed.

Γ_n variation

Using the same data as above⁹ the best fit of the variation of $\hbar\Gamma_n$ with F was found to be (see Fig 7-1(c)):

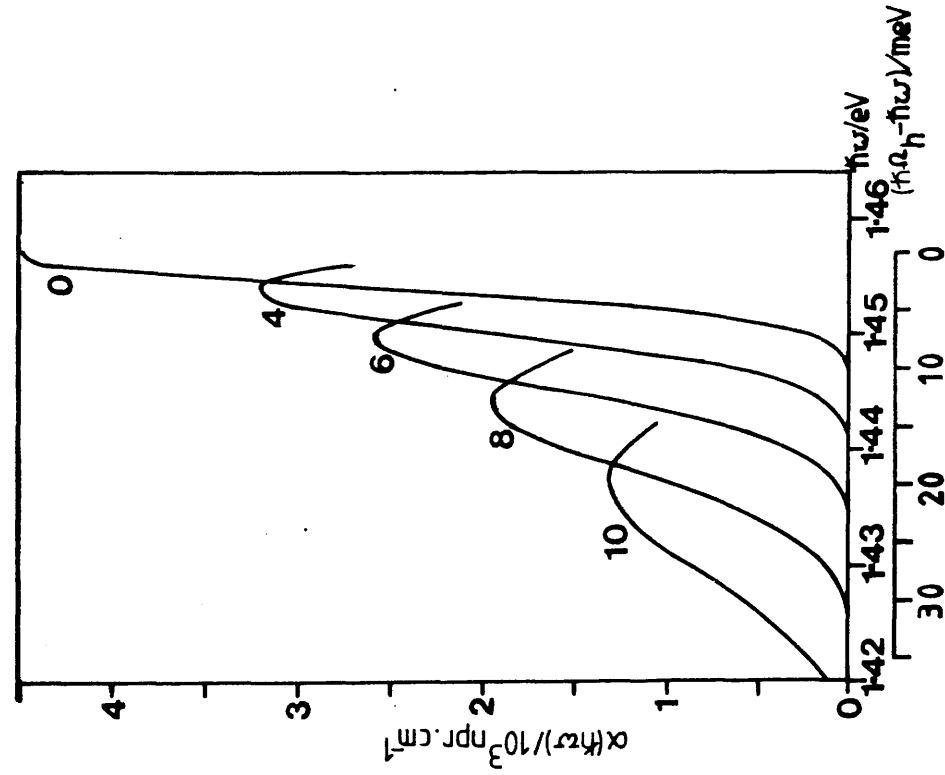
$$\hbar\Gamma_n = G + H \cdot F + K \cdot F^2$$

where $G=2.9 \text{ meV}$; $H=4.708 \times 10^{-7} \text{ meV/(V/cm)}$; $K = 4.989 \times 10^{-10} \text{ meV/(V/cm)}^2$.

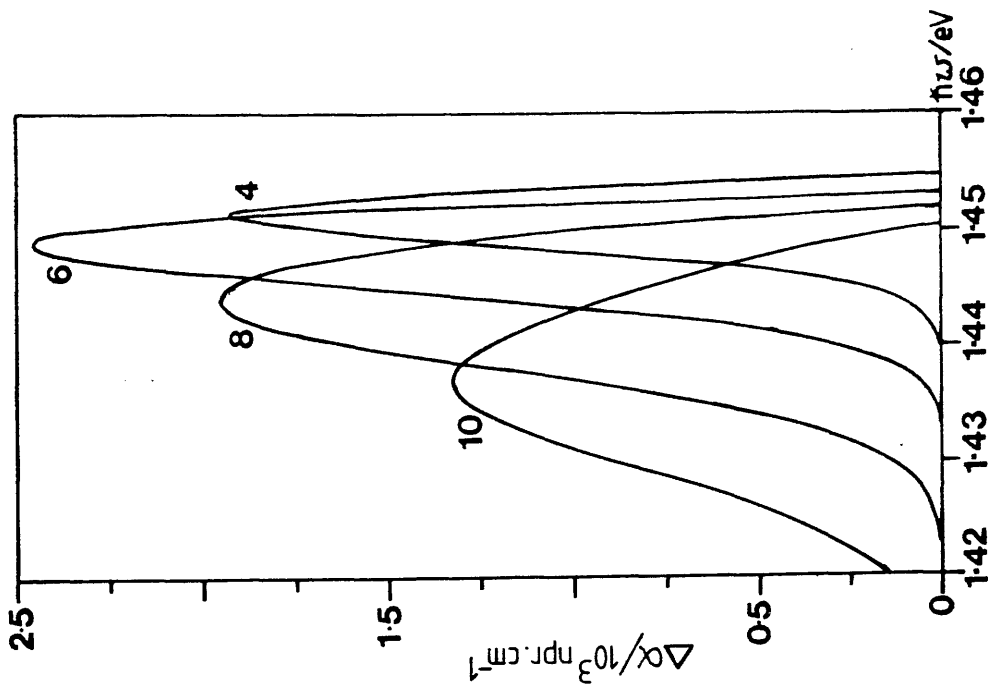
7.2.2 Results of Model

The functional forms of $\hbar\Omega_n$, α_n and $\hbar\Gamma_n$ were combined with the single Gaussian absorption edge model in a simple computer program. The shift in exciton peak with F is shown in Fig 7-2(a). As F increases there is a distinct Stark shift of the peak to lower energies with a decrease in peak height and increase in peak width. It is evident that the exciton peak will be greatly flattened before the avalanche breakdown limit of approximately $3 \times 10^{15} \text{ Vcm}^{-1}$ is achieved¹¹.

To calculate $\Delta\alpha$ it was assumed that at photon energies far below the absorption edge $\alpha(\hbar\omega)$ tended towards a value limited by free carrier loss. Assuming that the free carrier loss values for GaAs apply and that a background free carrier concentration of $1 \times 10^{18} \text{ cm}^{-3}$ n-type exists, one obtains a background free carrier loss of:



(a)



(b)

Fig 7-2 (a) The effect of an applied field on the position and shape of the heavy hole excitonic peak, and (b) the resulting absorption change for applied fields of 0, 4×10^4 , 6×10^4 , 8×10^4 and $10 \times 10^4 \text{ V/cm}$.

$$\alpha_0 = 3 \times 10^{-3} \text{ npr. cm}^{-1}.$$

Inspecting Fig 7-2(a) it is evident that at a given wavelength, varying F will cause the absorption to rise until the exciton peak passes. The absorption will therefore go through a distinct maximum. To maximise $\Delta\alpha$ the highest photon energy possible should be used to maximise the Gaussian peak height as it passes. However, as the photon energy becomes close to the absorption edge, $\alpha(F=0)$ begins to increase faster than the maximum absorption peak height. The optimum photon energy to maximise $\Delta\alpha$ will thus be on the shoulder of $\alpha(\hbar\omega, F=0)$. $\Delta\alpha = \alpha(\hbar\omega, F) - \alpha(\hbar\omega, 0)$ was calculated for various F and the results are plotted in Fig 7-2(b). They show the optimum photon energy as $\hbar\omega \approx 1.449$, with an optimum switching field of approximately $6 \times 10^4 \text{ Vcm}^{-1}$. A realistic figure of merit for an absorption modulator² is $\Delta\alpha/\alpha$. This function is even more dependent than $\Delta\alpha$ on $\alpha(\hbar\omega, F=0)$. To maximise the figure of merit $\hbar\omega$ should be as large as possible but still hold $\alpha(\hbar\omega) \approx \alpha_0$. This is calculated to occur at $(\hbar\omega_0, (F=0) - \hbar\omega) \approx 17 \text{ meV}$, i.e. $\hbar\omega = 1.44 \text{ eV}$. Indeed when $\Delta\alpha/\alpha$ was calculated for various F (Fig 7-3(a)) it was found to be a maximum for $\hbar\omega \approx 1.44 \text{ eV}$ with an optimum switching field of approximately $8 \times 10^4 \text{ Vcm}^{-1}$. Fig 7-3(b) replots the data as a function of F . This shows that at $\hbar\omega = 1.44 \text{ eV}$ and with a switching field of $8.6 \times 10^4 \text{ Vcm}^{-1}$, $\Delta\alpha/\alpha$ can reach the maximum of approximately 5.3×10^5 with $\Delta\alpha/\alpha$ being a strong function of the applied electric field.

7.2.3 Results Compared with Published MQW

These results are qualitatively very similar to the experimental results of Wood² who observes the same Gaussian type peaks in double well leaky waveguides as V_A is varied. In a similar way to that described above, he also finds that a maximum in $\Delta\alpha/\alpha$ is obtained at photon energies significantly less than that at which $\Delta\alpha$ is maximised. Since the light hole, TM band to band transition strength is 4/3 that of the heavy hole TE transition, Wood finds that $\Delta\alpha/\alpha$ is maximised for TM radiation. However, due to a very large background absorption of approximately $2.5 \times 10^{-2} \text{ npr. cm}^{-1}$ the measured $\Delta\alpha/\alpha$ is only 21. If the theoretical absorption data obtained above is reduced to "loss per well" for comparison with Wood's data and a similar background absorption is used as that observed by Wood, then the simple theory results in $\Delta\alpha/\alpha \approx 20$. This result emphasises the

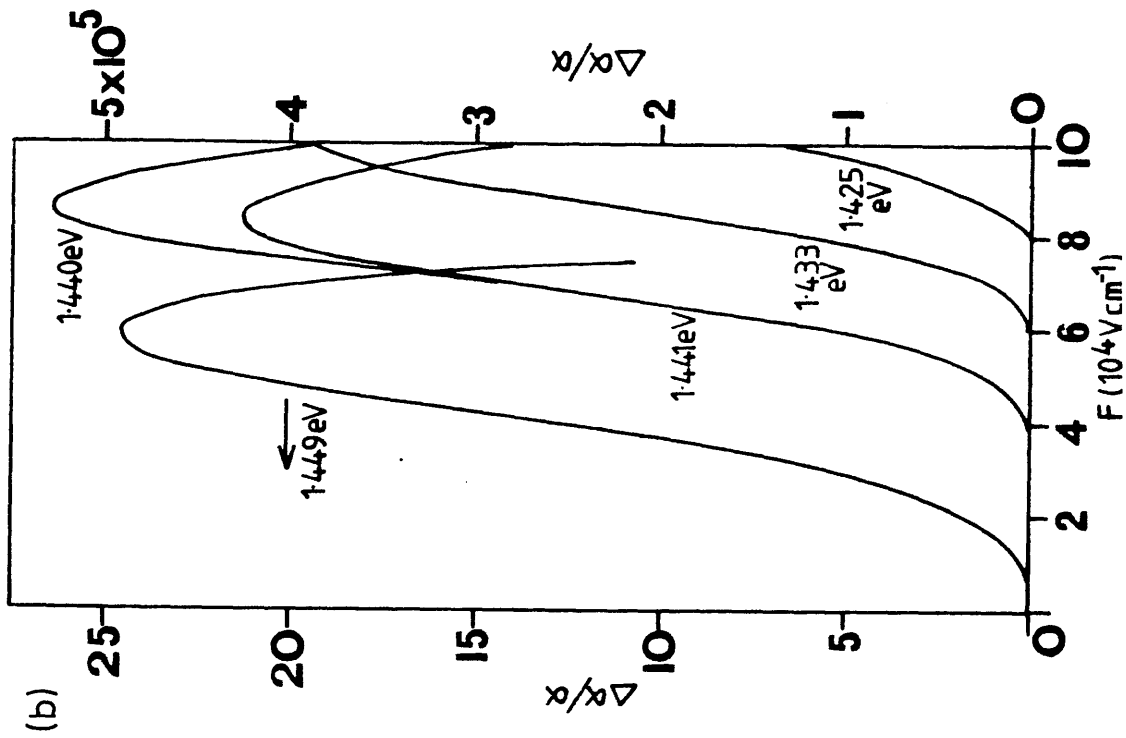
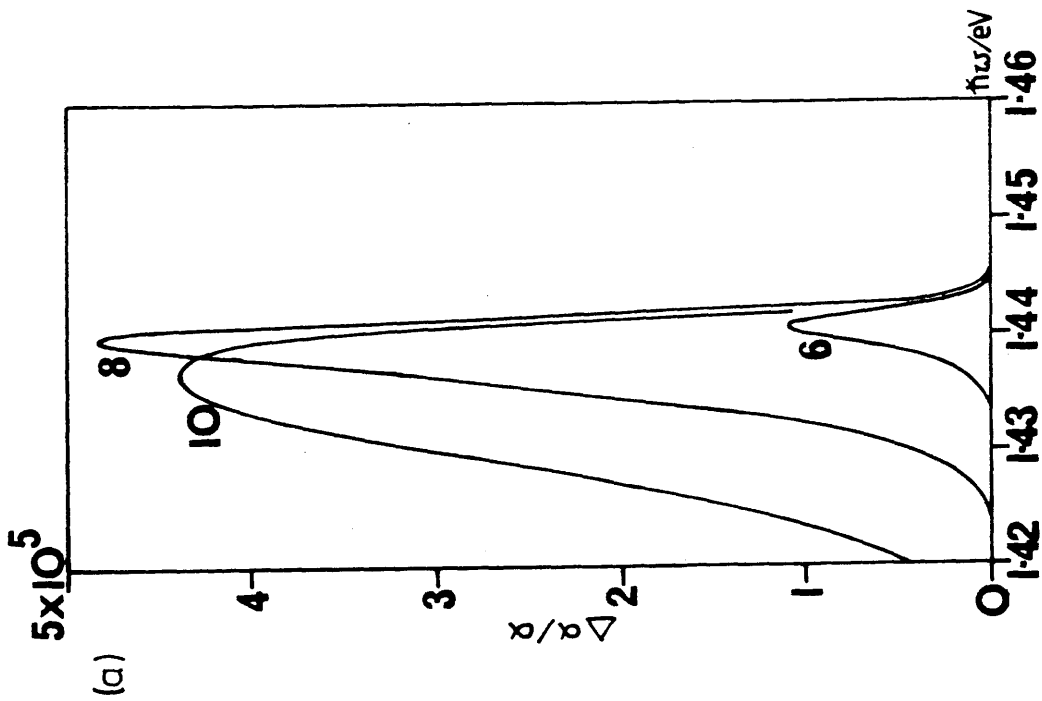


Fig 7-3 The variation of the electro-absorption figure of merit, $\Delta\alpha/\alpha$: (a) as a function of photon energy for applied fields of 6×10^4 , 8×10^4 and 10×10^4 V/cm, and (b) as a function of applied field for several photon energies.

practical importance of minimising the background free carrier loss to obtain the maximum theoretical figure of merit, and also demonstrates that the simple model outlined above models the electro-absorption effect in quantum wells reasonably well.

7.2.4 Comparison Between Electro-Absorption in MQWS and Bulk GaAs

Several theoretical and experimental analyses of electro-absorption in GaAs have been made and published in the literature¹². They show that the room temperature electro-absorption in GaAs is dominated by the Franz-Keldysh effect¹³ with a small polarisation dependence being observed due to applied field induced splitting of the degenerate valance bands. This anisotropic absorption in GaAs causes light polarised along the applied field direction to be absorbed more strongly than light polarised normal to the field.

Ignoring the anisotropic absorption for simplicity, the electro-absorption in GaAs can be described by¹³:

$$\alpha(\hbar\omega, F) = C \cdot F^{1/3} [|Ai'(\eta)|^2 - \eta |Ai(\eta)|^2] / \hbar\omega$$

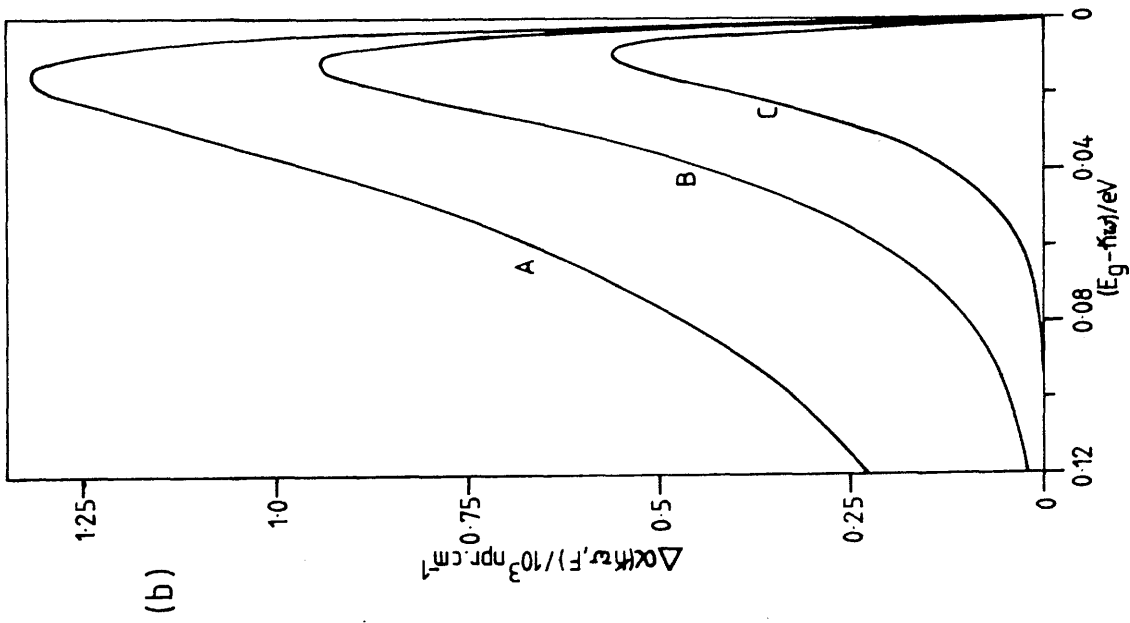
$$\eta = (E_g - \hbar\omega) / \hbar\theta \quad , \quad \theta^3 = e^2 F^2 / 2\mu\hbar$$

where $Ai(\eta)$ is an Airy function, μ is the reduced mass, F is in V/cm, $\hbar\omega$ in eV and $C=298.9eV(Vcm^{-1})^{-1/3}npr.cm^{-1}$. Using a similar expression Stillman et al¹⁴ have shown a reasonable fit of theory with experiment. An even simpler model of the Franz-Keldysh effect results in the expression¹⁵:

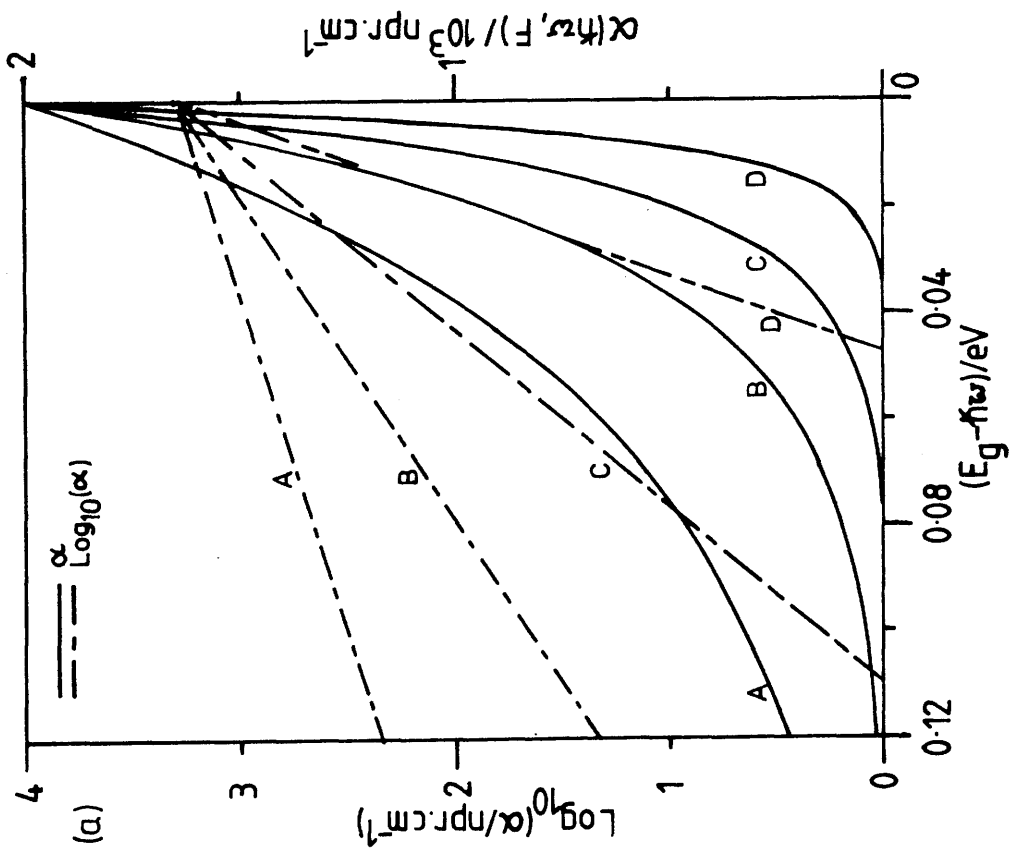
$$\alpha(\hbar\omega, F) = A \cdot \exp(-(E_g - \hbar\omega) / \Delta E) \quad (7.1)$$

where $\Delta E = 3/2(m^*)^{-1/3}(e\hbar F)^{2/3}$ and A is a fittable parameter.

To obtain plots of $\Delta\alpha/\alpha$ analogous to those obtained for MQWS, the simple expression (7.1) was used (with ΔE as well as A as a fittable parameter) to fit and extrapolate the results of Stillman et al¹⁴. Fig 7-4(a) shows how the band edge is calculated to change as an electric field (F) is applied. In the case of bulk GaAs, the electric field is seen to broaden the exponential tail of the absorption edge. For a given photon energy, α will steadily increase with applied field in contrast to the MQWS where an optimum applied field was



(b)



(a)

Fig 7-4 The effect of an applied field on (a) the absorption edge of bulk GaAs, and (b) the resulting absorption change. For applied fields of 3×10^5 , 1×10^5 , 4×10^4 and 0 V/cm (A - D respectively).

predicted above which the absorption decreased. To allow direct comparison with the MQW theory a background doping of $1 \times 10^{15} \text{cm}^{-3}$ was again assumed and the breakdown field was taken as being approximately $3 \times 10^5 \text{Vcm}^{-1}$. $\alpha(F=0)$ was obtained from Blakemore¹⁶.

Fig 7-4(b) and 7-5(a) plot the resulting values for $\Delta\alpha$ and $\Delta\alpha/\alpha$ as functions of photon energy and applied field with the optimum photon energy appearing to be $E_g - \hbar\omega \approx 0.100 \text{eV}$. This is much further from the absorption edge than was found to be optimum for MQWS. Fig 7-5(b) plots $\Delta\alpha(F)/\alpha$ for this optimum photon energy. $\Delta\alpha/\alpha$ steadily increases to a value at $F=3 \times 10^5 \text{Vcm}^{-1}$ of 9.4×10^4 compared with the MQW optimum value of 5.3×10^5 at $8.6 \times 10^4 \text{Vcm}^{-1}$. MQWS therefore show a clear advantage over bulk GaAs for the modulation of light by electro-absorption with a higher figure of merit by a factor of 5-6. The optimum switching field for the MQWS is also very low, the equivalent of approximately 3V using the diode calculations of chapter five compared to the 14V required to obtain $3 \times 10^5 \text{Vcm}^{-1}$. MQWS devices will thus use substantially less power to achieve the same modulation depth. In addition, practical devices may not always be able to achieve a field of $3 \times 10^5 \text{Vcm}^{-1}$ due to such effects as surface breakdown. Fig 7-5(b) shows that even a small reduction in the maximum field applicable will substantially reduce a bulk device's figure of merit without altering that of the MQWS.

7.2.5 Conclusions and Model Limitations

Theoretically MQWS show a substantial improvement over bulk GaAs in the figure of merit for electro-absorption modulators. They also exhibit a greatly reduced switching voltage. However, this theoretical analysis does not take into account the anisotropy of the electro-absorption effect in GaAs, nor does it model the TM electro-absorption effect in MQWS which may show even larger values of $\Delta\alpha/\alpha$.

It was the aim of this analysis to compare the fundamental material properties of MQWS and GaAs. No account was taken therefore of the waveguide nature of the proposed modulators. However, the factors affecting GaAs and MQW waveguide modulators are identical and will not alter the general conclusions of the above comparison. Bottka and Hutcheson¹³, when modelling GaAs DH p-i-n diode electro-absorption modulators, came to the conclusion that the net donor

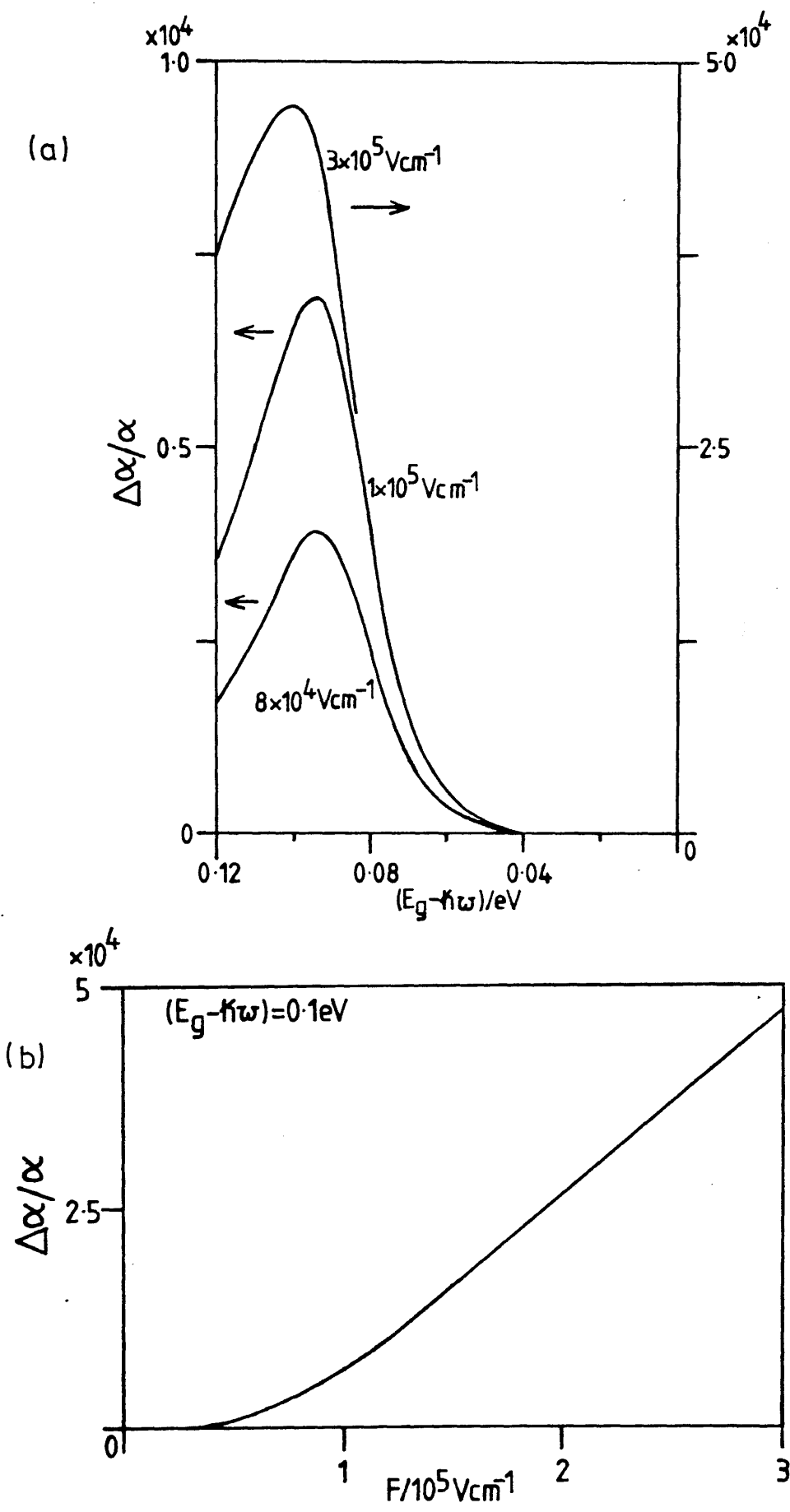


Fig 7-5 The variation of the electro-absorption figure of merit, $\Delta\alpha/\alpha$, in bulk GaAs: (a) as a function of photon energy, and (b) as a function of applied field at the optimum photon energy.

concentration in the intrinsic region was optimum at a value of 10^{15}cm^{-3} (thus allowing waveguide depletion by the built-in junction field) and that the material should be homogeneous and defect-free to minimise broadening of the absorption edge. These conclusions equally apply to MQW-DH and have been independently arrived at elsewhere in this thesis.

7.3 I-V AND C-V TESTS

To fabricate an electro-absorption modulator it is necessary to apply an electric field across the waveguide layer. In integrated optics this is usually done by depleting the waveguide via a reverse biased rectifying junction. This junction can either be a surface evaporated Schottky contact or a doped p-i-n structure. Both were used in the present work in an attempt to fabricate MQW-DH electro-absorption modulators. The relevant metal contacts used were described in chapter three, and the p-i-n diode design was described in chapter five. In this section, the methods used to test the quality of the fabricated diodes will be described and the results presented.

7.3.1 I-V Tests

The simplest way to test the quality of a diode is to apply DC bias (V_A) and measure the resulting current flow. This was carried out using a Hewlett-Packard digital parameter analyser as described in chapter three.

Following on from the work on n/n⁺ GaAs phase modulators, MQW-DH were fabricated in which all the epitaxial layers were low n-doped on an n⁺ substrate. This was designed to allow depletion of the MQW layer by a Schottky barrier evaporated on the surface of the semiconductor. Experience with n/n⁺ GaAs suggested that a reverse bias of up to -70V would be applicable via a Ti/Au contact evaporated onto the GaAs capping layer of the MQWS-DH, easily depleting the waveguide layer.

Using the standard sample preparation and evaporation procedures outlined in chapter three, Au:Ge ohmic contacts were evaporated onto n/n⁺ sample VG119 and MQW-DH VG215, and annealed in the usual way.

Ti:Au Schottky contacts were then simultaneously evaporated onto the top of both samples. The n/n⁺ sample exhibited identical characteristics to those reproduced in section 3.3.4. Sample VG215 exhibited very poor I-V characteristics. Fig 7-6 shows that the reverse leakage current was very high with reverse breakdown occurring at the very low value of approximately -2.5 Volts. These characteristics were not due to poor sample preparation or evaporation conditions since the VG119 sample exhibited ideal characteristics.

To explain this behaviour, the self-consistent Monte Carlo method briefly described in section 2.2.2 was used by Dr. M. A. R. Al-Mudares, Department of Electronics and Electrical Engineering, University of Glasgow, to model the complete diode quantum mechanically. The resulting I-V plot (Fig 7-7) shared many features in common with the experimental results with reverse breakdown at approximately -2.5 Volts, and forward current switch-on at +0.5 Volts. This confirmed that the poor reverse characteristics were not due to some fabrication problem. The sheer complexity of the Monte Carlo method made it difficult to determine the exact reason for the poor reverse characteristics, but the calculated potentials within the structure (see Fig 7-7) showed that the peak electric fields could have been above the avalanche threshold for $V_A > -2.5V$, and this is tentatively suggested as the breakdown mechanism.

Due to this fundamental inability to use Schottky barriers to deplete the MQWS, the emphasis shifted to p-i-n diode structures. Work concentrated on the two p-i-n diode structures, CPM68 and NTT529, that had been shown to satisfy the condition that they sustain only one planar mode. Again standard sample preparation and evaporation techniques were used to evaporate and anneal a Au:Ge ohmic contact to the back of each sample. Au:Zn:Ni contacts were then evaporated and annealed onto the p-doped GaAs capping layers of these MQW-DH as described in section 3.3.4.

The I-V characteristics of CPM68 were the first to be tested and exhibited good diode characteristics (Fig 7-8) with a very low reverse bias leakage current, and breakdown at -15 to -16V. The forward characteristics were exponential over almost four decades of current.

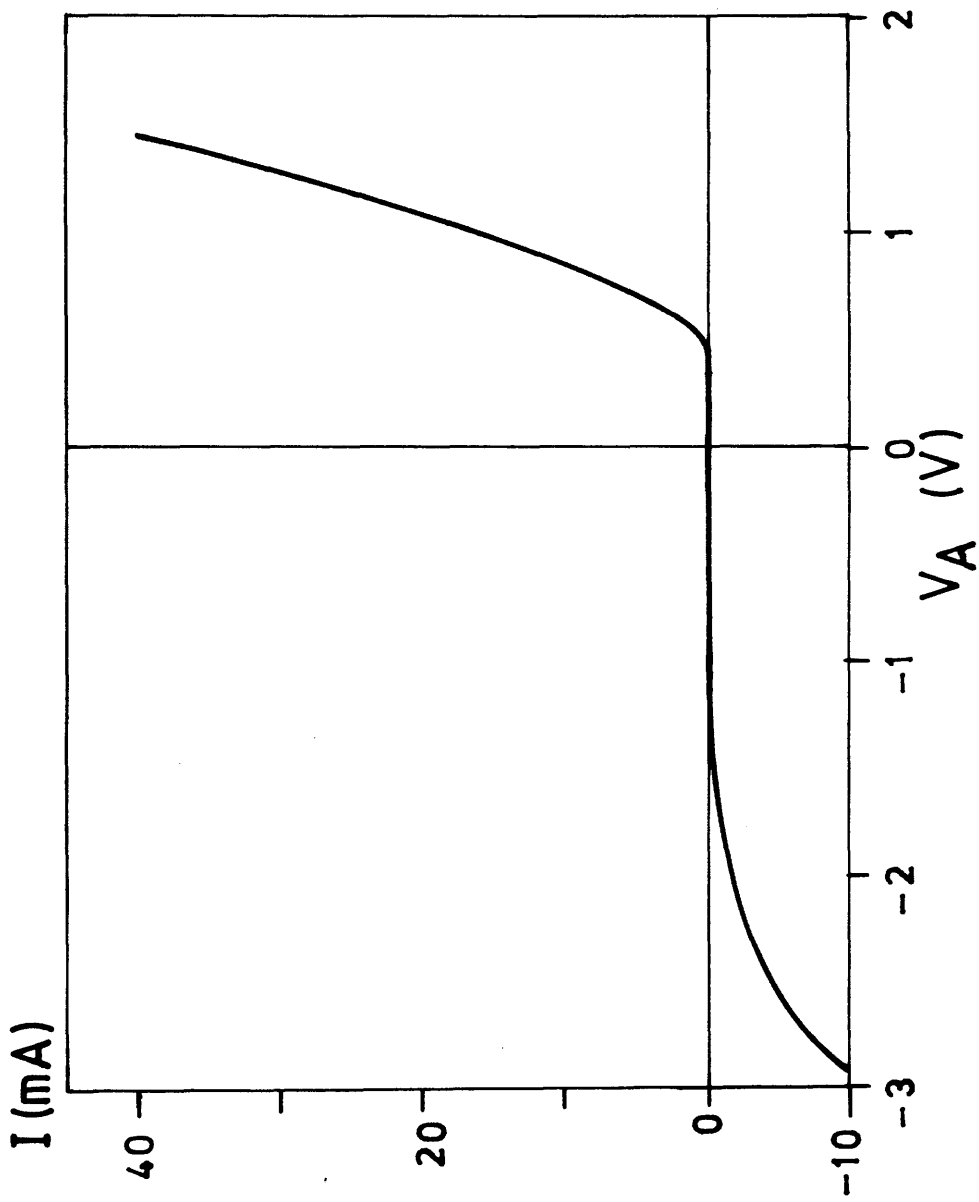


Fig 7-6 The I-V characteristics of an Al Schottky contact to MQWS VG215.

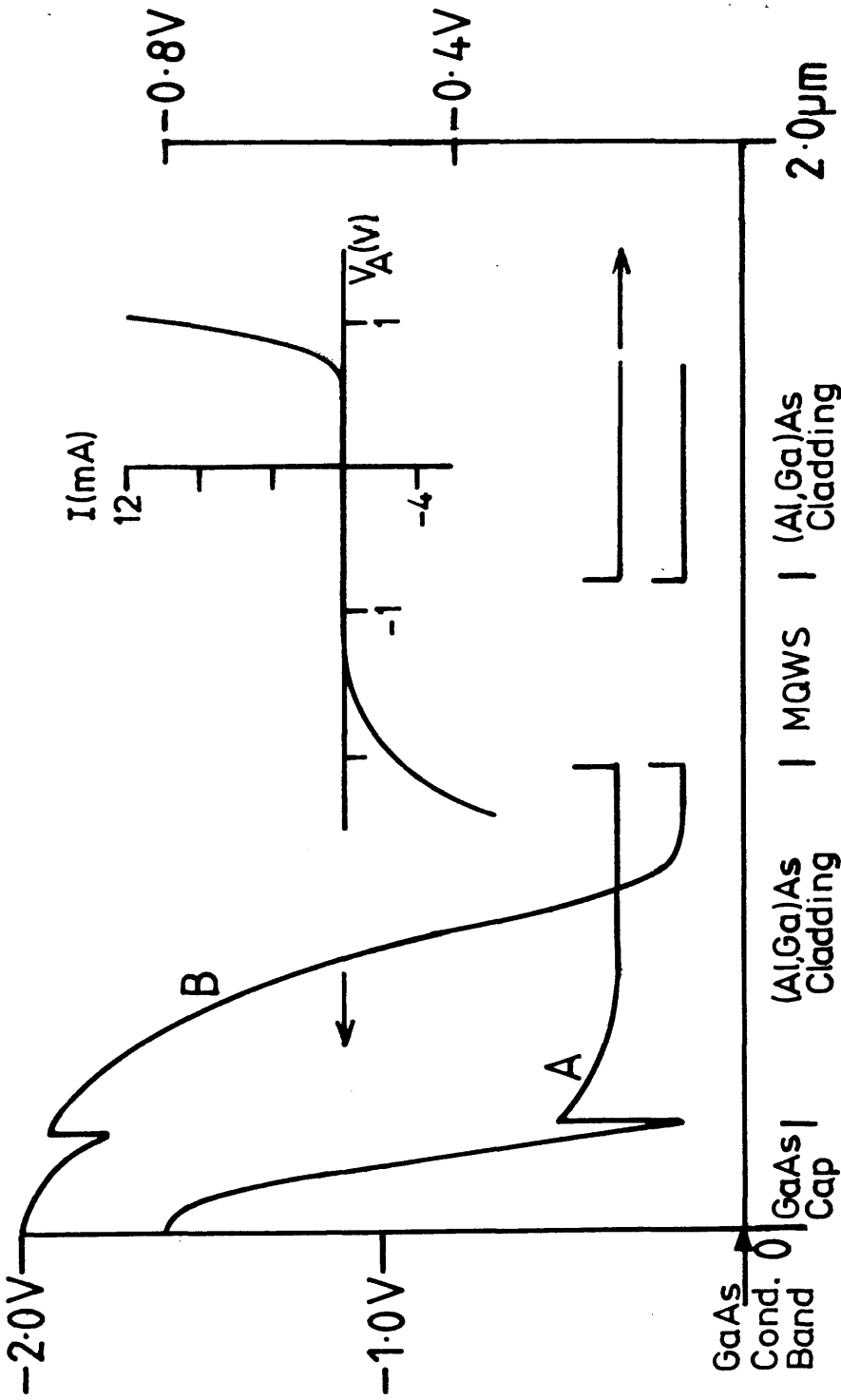


Fig 7-7 The theoretically derived I-V curve and the conduction band potential under a reverse bias of 0V (A) and -1.2V (B).

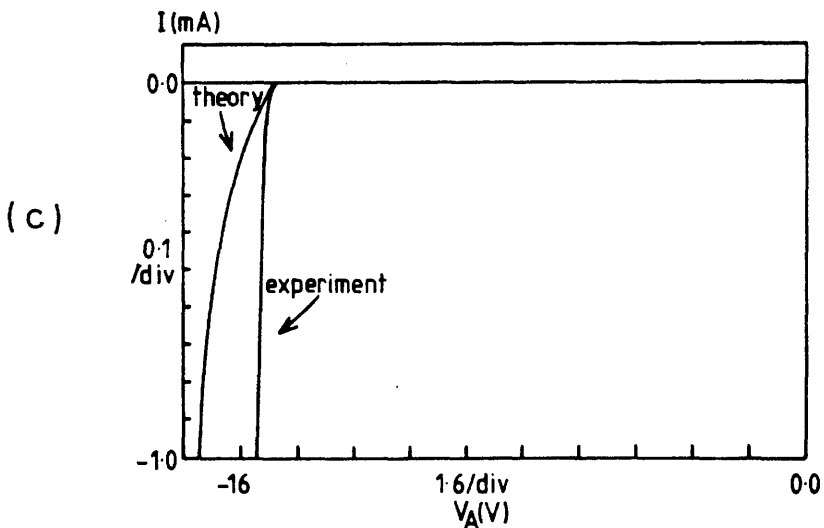
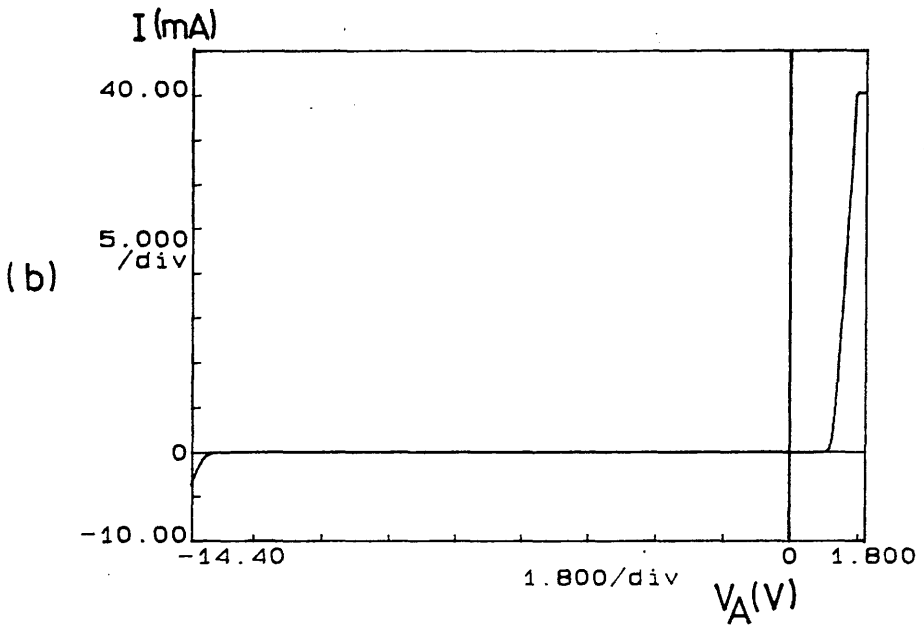
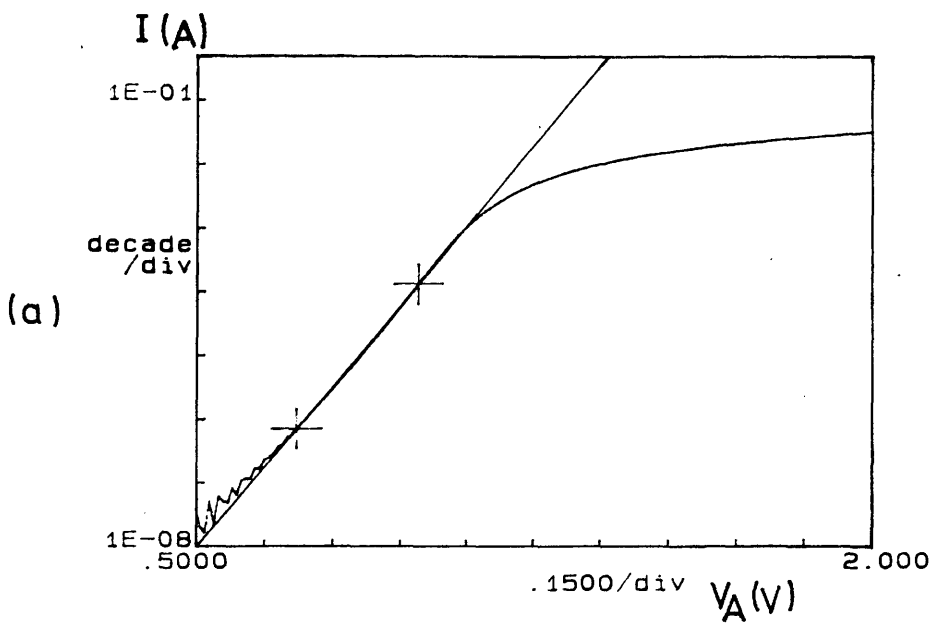


Fig 7-8 The I - V characteristics of MQW-DH CPM68: (a) the forward characteristics, (b) the full rectifying characteristics, and (c) a comparison between the experimental and theoretical reverse characteristics.

The plotted forward characteristics are close to that expected with a semi-log gradient given by $e/\eta kT$. For low forward voltages ($V_A < +0.5V$) the diffusion current in the junction is small and the depletion layer is relatively wide, and the generation-recombination (G-R) current dominates'' giving a value of $\eta=2$. Above $V_A \approx +0.5V$ the diffusion current starts to dominate over the G-R current. If the diffusion current completely dominated η would be 1. The measured value of $\eta=1.8$ is higher than the value of 1.5 generally obtained in Si p-n diodes, and shows that the G-R current is still contributing to the forward current. For $V_A > 1.1V$ the diode moves into a region where ohmic drops across the sample contacts and bulk semiconductor become dominant and current becomes proportional to voltage. The Monte Carlo model was used to reproduce the reverse characteristics of this structure. Fig 7-8(c) plots the theoretical and experimental results, with the Monte Carlo method accurately modelling the breakdown voltage but underestimating the reverse current after breakdown.

The characteristics of NTT529 were completely different from CPM68 showing no diode characteristics whatsoever. For applied voltages up to ± 100 Volts the sample behaved as an insulator with no breakdown in either direction being observed. This behaviour was attributed to poor growth conditions resulting in an (Al,Ga)As layer being undercompensated, and thus producing a complicated sequence of p and n doped layers.

CPM68 was therefore the only sample to satisfy the photoluminescence and waveguide criteria of the previous chapter and show good p-i-n diode characteristics. Active waveguide fabrication subsequently concentrated on this sample.

7.3.2 C-V Tests

I-V characterisation allowed the general quality of the p-i-n diodes to be assessed. To obtain more detailed information on CPM68, C-V measurements were made using a Hewlett-Packard multi-frequency LCR meter which utilised the same probes as the Hewlett-Packard parameter analyser. The LCR meter was controlled using an Olivetti personal computer using software written by Mr C. Reeves, Department of Electronics and Electrical Engineering, University of Glasgow.

Theory

If the reverse voltage V_A applied to a p-n junction is increased by ΔV_A , the depletion layers on the p and n sides of the junction will widen by Δd_p and Δd_n respectively. This will increase the space charge by $-\Delta Q$ and $+\Delta Q$ on either side of the junction where:

$$|\Delta Q| = |eN_D\Delta d_n| = |eN_A\Delta d_p|$$

and N_D , N_A are the donor and acceptor densities.

The junction capacitance C_j can thus be defined as the differential capacitance:

$$C_j = (dQ/dV_A)_{V_A}$$

For an abrupt homojunction this definition results in the expression:

$$C_j = A(\epsilon\epsilon_0(N_A+N_D)/2V_t)^{1/2}[(N_D/N_A)^{1/2}+(N_A/N_D)^{1/2}]^{-1}$$

where A = area of device

ϵ = dielectric constant of semiconductor

V_t = total junction voltage = $V_B - V_A$, ($V_A < 0$ for reverse bias)

N_A = acceptor density on p side

N_D = donor density on n side

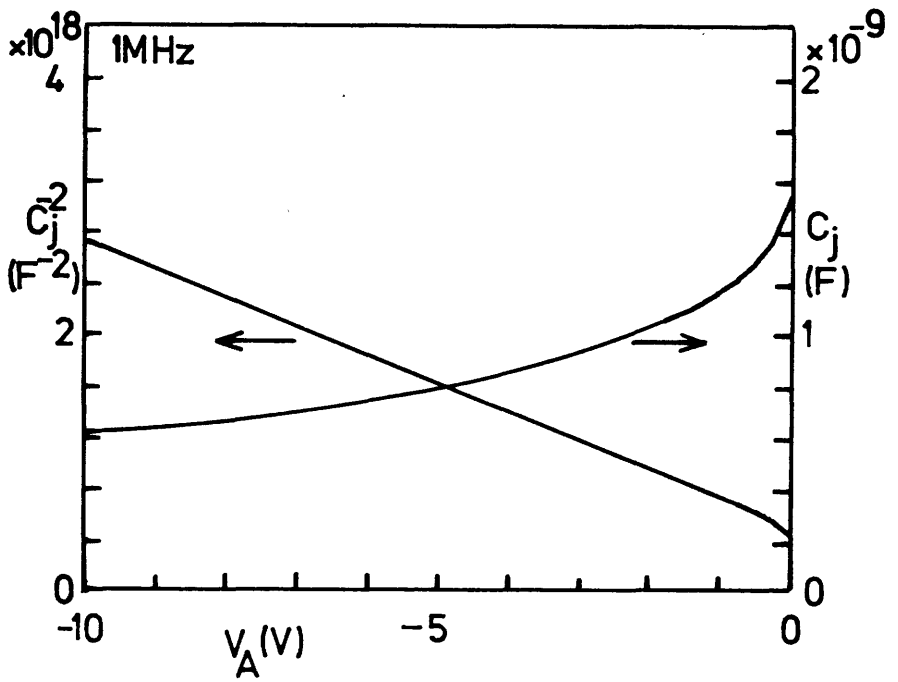
If $N_A \gg N_D$ then:

$$C_j = A(\epsilon\epsilon_0 N_D / 2V_t)^{1/2} \quad (7.2)$$

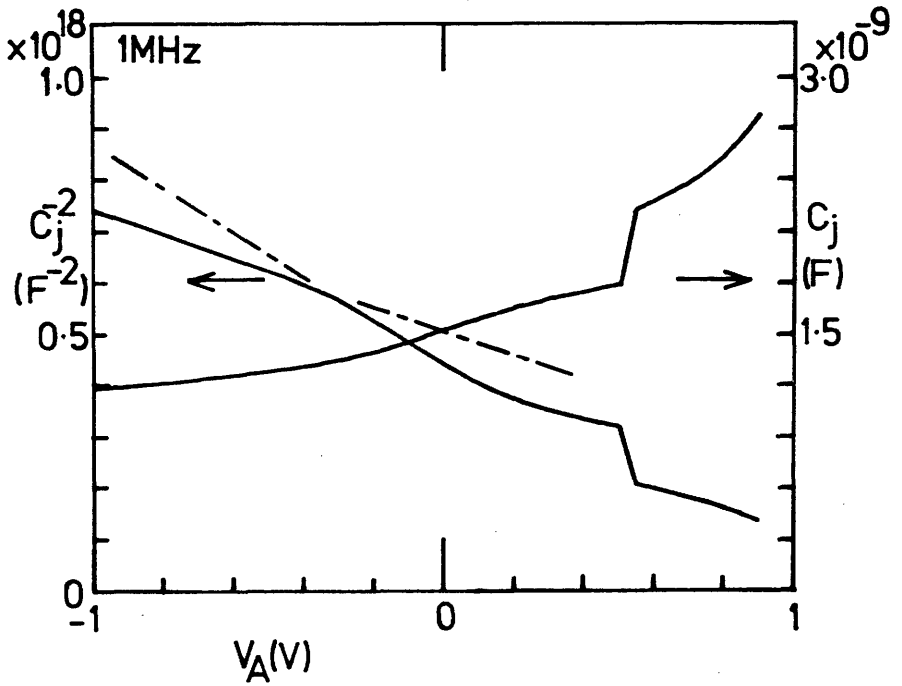
Thus as shown in Fig 7-9 plotting $1/C_j^2$ against $-V_A$ one obtains a straight line with a gradient inversely proportional to the donor density on the low doped n side. Projecting the straight line backwards, the built-in voltage V_B may be obtained.

In the case of an abrupt p-n heterojunction where the higher band gap material is p-type with dielectric constant ϵ_2 the junction capacitance becomes¹¹:

$$C_j = [eN_D N_A \epsilon_1 \epsilon_2 \epsilon_0 / 2(\epsilon_1 N_D + \epsilon_2 N_A) V_t]^{1/2}$$



(a)



(b)

Fig 7-9 The C-V characteristics of MQW-DH CPM68: (a) at large reverse bias voltages, and (b) around the zero volts bias point.

For the one-sided junction ($N_A \gg N_D$) this expression reduces to (7.2), and so to the first order a one-sided heterojunction can be treated as a homojunction when interpreting measured C-V characteristics.

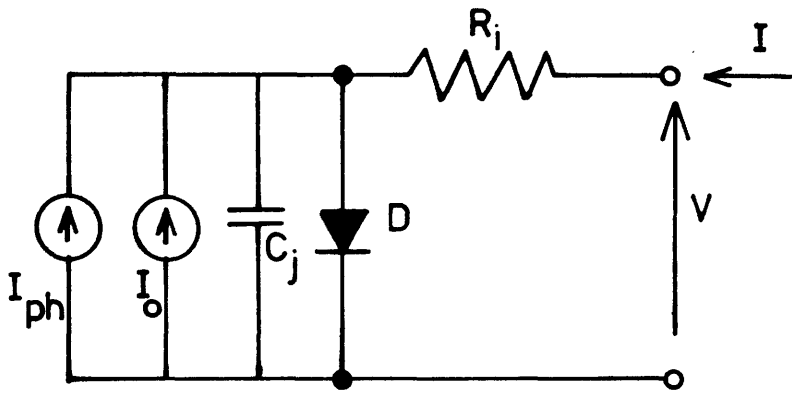
Experiment

C-V measurements of sample CPM68 were made at 1MHz on a diode with a junction area of 3.6mm^2 . Fig 7-9 reproduces the resulting curves. It can be seen that $1/C_j^2$ decreases linearly with V_A for $V_A < -1$ Volt. Using expression (7.2) the measured gradient results in a calculated donor concentration of $3.9 \times 10^{16}\text{cm}^{-3}$, below the $6 \times 10^{16}\text{cm}^{-3}$ estimated from growth conditions and far below the designed value of approximately $5 \times 10^{17}\text{cm}^{-3}$. For $V_A > -0.3\text{V}$ there is a distinct change in gradient to a value consistent with a doping of $2.0 \times 10^{16}\text{cm}^{-3}$. This value is close to that predicted for the MQWS from growth conditions. This slope continues until $V_A \approx 0.1\text{V}$, and if extrapolated back to find the x axis intercept, a built-in voltage of 1.04V is obtained compared with the 1.2V obtained from simple p-n junction theory. For $V_A > 0.1\text{V}$ interpretation becomes difficult with the plot of $1/C_j^2$ against V_A showing an upward trend followed by a sharp drop. This result was repeatable but interpretation was complicated by the fact that in this region the diode is beginning to conduct.

The C-V results therefore suggest that CPM68 consists of MQW region with an average effective doping level of $2 \times 10^{16}\text{cm}^{-3}$ n-type with a lower cladding layer of $4 \times 10^{16}\text{cm}^{-3}$ n-type and a built-in voltage of 1.04V . Using the upper cladding layer doping of 6×10^{17} p-type these results imply a built-in depletion depth of $0.264\mu\text{m}$ i.e. the waveguide layer is just depleted. The continuation of the $2 \times 10^{16}\text{cm}^{-3}$ gradient until $V_A \approx -0.3\text{V}$ thus implies that a small part (approximately $0.1\mu\text{m}$) of the lower cladding layer next to the MQWS is doped to this level.

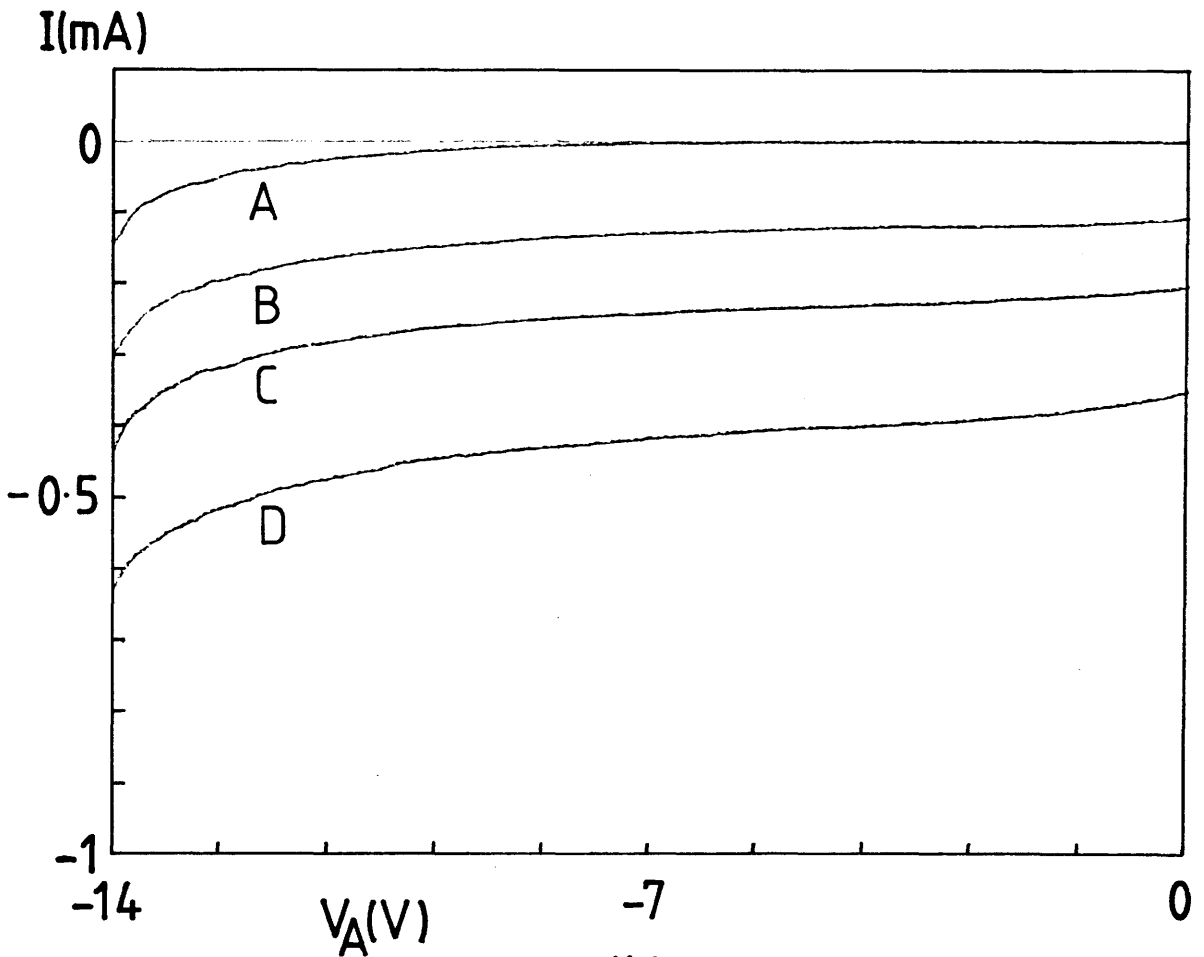
7.4 PHOTOCURRENT SPECTROSCOPY

Even under the light of a microscope, CPM68 was observed to be a very good photodetector. As Fig 7-10 shows, different light settings of the white light source produced very different reverse voltage characteristics. This result motivated this work on investigating



D =ideal diode, R_i =internal resistance, C_j =junction capacitance.

(a)



(b)

Fig 7-10 MQW-DH CPM68 as a photodetector: (a) the equivalent circuit, and (b) the third quadrant characteristics for four power settings of a white light source (A = room lights only).

CPM68 as a photodetector. By measuring the photocurrent as a function of incident wavelength it was found possible to investigate the absorption edge of the MQWS using photocurrent (PC) spectroscopy^{2,9,17}. This analysis technique has the major advantage over etalon transmission experiments that it does not involve any substrate removal, and consequently also does not require an $\text{Al}_{0.6}\text{Ga}_{0.4}\text{As}$ etch stop layer in the sample.

7.4.1 Description of Method

A p-i-n diode may be used as a detector by operating it in the third quadrant of its characteristics. It is operated at a reverse bias smaller than the breakdown voltage, and its detection capability stems from the sharp increase in the reverse current with light as demonstrated by CPM68 in Fig 7-10. If the dark current is I_0 then the detected current will change from I_0 to $I_0 + I_{ph}$ on the detection of light, where I_{ph} is the detected photocurrent. This photocurrent is due to absorbed photons which generate free hole-electron pairs. These pairs would normally recombine within a diffusion length, but within the depletion region they are immediately swept apart by the depletion region field, thus contributing to the total current.

If the diode is illuminated perpendicular to the layers then the total carrier collecting volume is $A \cdot W$, where W is the total depletion depth and A the junction area. The total photocurrent is then²:

$$I_{ph}(\hbar\omega, F) = P_0 (e\lambda/hc) (1-R)^2 \eta(v) \cdot (1 - \exp(-2\alpha(\hbar\omega, F)W))$$

where P_0 = incident power

R = surface reflection coefficient

η = internal quantum efficiency

$e\lambda/hc$ = conversion from watts to amps.

In a p-i-n diode certain conditions are fulfilled which allow I_{ph} to accurately follow $\alpha(\hbar\omega)$ and thus allow photocurrent spectroscopy to take place. Firstly $\eta(v)$ will rapidly increase with reverse voltage until η becomes independent of voltage at $\eta \approx 1$. This occurs because initially when the intrinsic region is not fully depleted, some absorption will take place in low field regions where the

carriers may not be swept out before recombination. At higher V_A the whole of the depletion region is subject to high fields. Secondly, when the intrinsic region is fully depleted, the depletion depth, W , becomes independent of voltage with a value equal to that of the intrinsic region thickness. Thus with an intrinsic layer thickness of approximately $1\mu\text{m}$, absorption coefficients up to $5 \times 10^{23} \text{pr.cm}^{-1}$ leave $2\alpha W < 1$ so that $I_{ph}(\hbar\omega, F)$ is approximately proportional to $\alpha(\hbar\omega, F)$.

This very technique has been used by Miller et al⁹ and Yamanaka et al¹⁷ to investigate MQW p-i-n diodes at a variety of values of V_A with the former work experimentally demonstrating a very clear proportional relationship between I_{ph} and $\alpha(\hbar\omega)$. $\eta(V_t)$ was also shown to be the same whether absorption was taking place at an exciton peak or within the inter-band absorption region. MQW-DH p-i-n diode structures have thus the capability of acting as both very efficient electro-absorption modulators and photodetectors. This fact which has already produced novel non-linear optical devices¹⁸ and offers intriguing practical applications in monolithic laser, modulator, waveguide and detector integration.

Wood² has also shown that photocurrent spectroscopy can be used in waveguide photodetectors. In this case the photocurrent is related to the total propagation loss thus:

$$I_{ph}(\hbar\omega, F) = P_0(e\lambda/hc)\gamma(1-R)^2\eta(V_t)[\alpha_{abs}(\hbar\omega, F)/\alpha_{tot}(\hbar\omega, F)] \times (1 - \exp(-2\alpha_{tot}(\hbar\omega, F)L)) \quad (7.3)$$

where L = waveguide length

α_{tot} = total propagation loss i.e. absorption and radiation etc.

α_{abs} = contribution to α_{tot} from absorption

γ = coupling coefficient.

Assuming $\alpha_{abs} \approx \alpha_{tot}$, (7.3) reduces to:

$$I_{ph}(\hbar\omega, F) = I(\infty)(1 - \exp(-2\alpha(\hbar\omega, F) \cdot L))$$

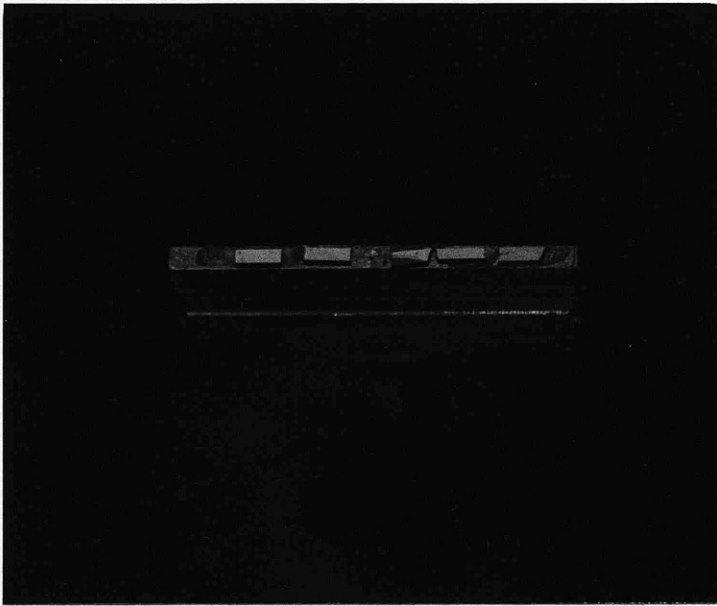
Sample CPM68 did not contain an etch stop. It had therefore not been possible to measure the MQW material absorption using etalon transmission. Photocurrent spectroscopy was thus an ideal way of obtaining some idea of the position of the exciton peak in CPM68.

7.4.2 Experimental Method and Results

To measure the PC spectra it was decided to use MQW p-i-n diode CPM68 as a waveguide photodetector since this would also give useful information on its potential use as an integrated optical detector. A sample of CPM68 was back-polished with a bromine methanol solution until it was approximately $150\mu\text{m}$ thick to allow cleaving of waveguides of various lengths down to $200\mu\text{m}$. Au:Ge ohmic contacts were then evaporated onto the back of the samples before they were mounted with silver epoxy onto aluminium blocks (see Fig 7-11) which could be easily handled and securely located on the translation stage assembly of the end-fire coupling rig. The arm that supported the sample block was earthed and a probe used to apply the required DC bias to the detector. Fig 7-12(a) schematically depicts the electrical circuit used. The incident laser light was TE polarised and mechanically chopped at 3kHz and the detected signal voltage (V_o) was preamplified, then processed by a lock-in amplifier and displayed on a chart recorder.

The measured dark current was very low, being less than 10pA at $V_A=0$ compared to photocurrents of the order of $10\mu\text{A}$. Incident light intensity was kept below $30\mu\text{W}$ using the dye-laser stabiliser and the laser initially scanned over the wavelength range 880 to 825nm. Later the laser was able to scan out beyond 880nm to 905nm and the results in this range were obtained.

The detected photocurrent is shown in Fig 7-12(b). Interpretation of these waveguide results was more difficult than the results of Miller et al⁹ and Yamanaka et al¹⁷ since the length of the waveguide detector in this case meant that for part of the wavelength range $2\alpha L > 1$. $I_{ph}(\hbar\omega)$ was thus no longer simply proportional to $\alpha(\hbar\omega)$. Infact as the photon energy increased $I_{ph}(\hbar\omega, F) \rightarrow I_{ph}(\omega)$ and the results are best understood by recognising that the transmission (T) of the modulator is proportional to $(I_{ph}(\omega) - I_{ph}(\hbar\omega, F))$. Due to uncertainties about the exact value of $I(\omega)$ it was impossible to calculate T, but changes in detected photocurrent (ΔI) will be proportional to changes in MQW transmission ($-\Delta T$). The C-V results indicated that the MQW layer was fully depleted at $V_A=0$, so the quantum efficiency (η) will be close to 1 over the whole range of V_A .



Photocurrent (a.u)

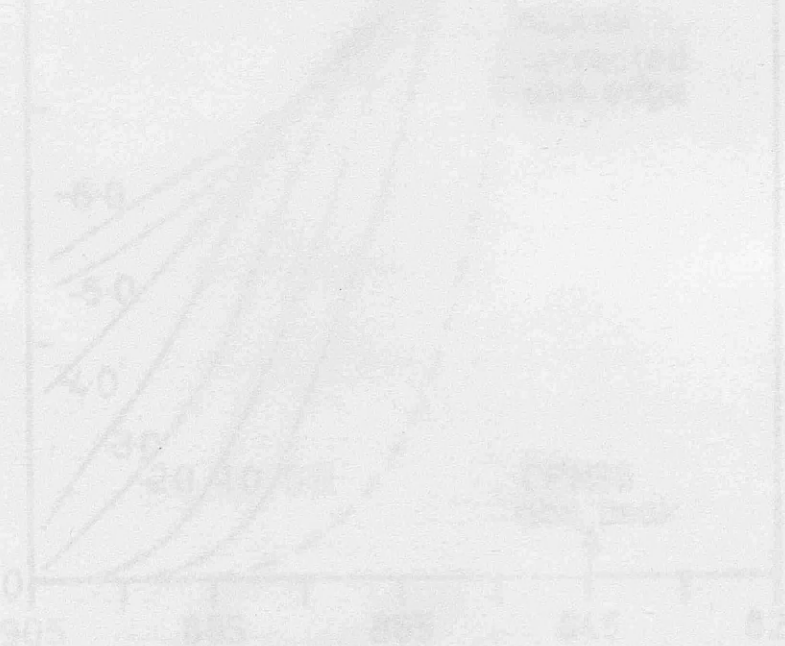


Fig 7-11 A typical set of short, planar waveguide samples mounted for end-fire coupling.

Fig 7-12 Waveguide cross-section as a function of wavelength. The graph shows the waveguide cross-section as a function of wavelength. The x-axis is wavelength (nm) and the y-axis is cross-section (μm). The curves are labeled with values 10, 20, 30, 40, 50, and 60, representing different waveguide lengths or parameters.

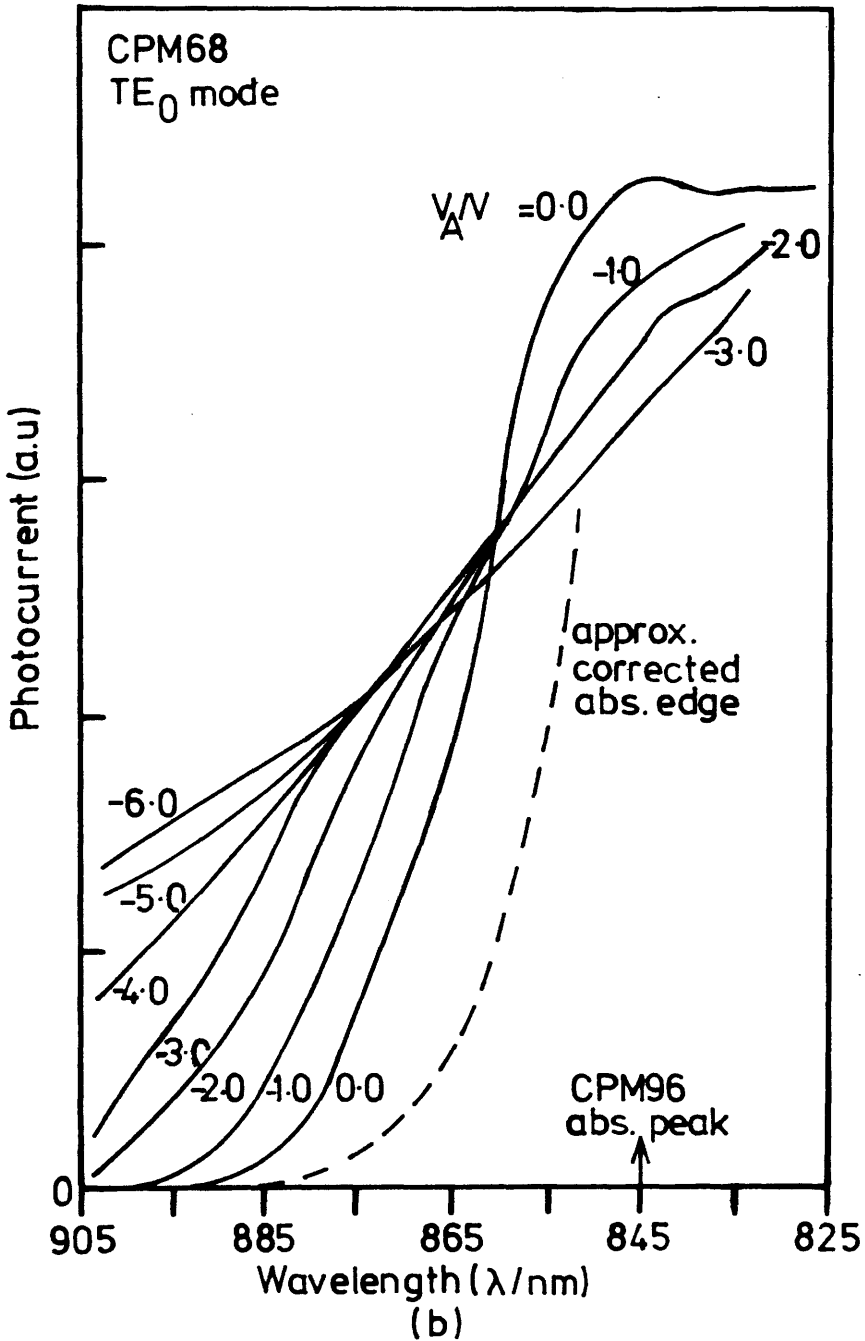
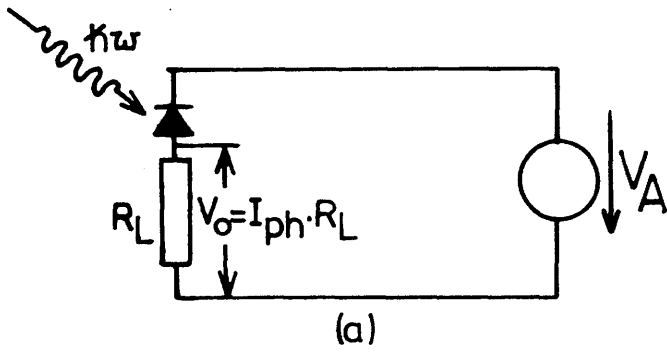


Fig 7-12 MQW-DH CPM68 as a planar waveguide photodetector: (a) the bias circuit used, and (b) the detected photocurrent as a function of applied voltage.

Given the provisos of the preceding paragraph, the $V_A=0$ curve of Fig 7-12 does show a broad peak at $\lambda \approx 845\text{nm}$ at a position close to that of the exciton peak of sample CPM96 (as measured by etalon absorption, see Fig 5-21(b)). The structure of CPM96 is very similar to that of CPM68 and so this peak in the PC spectrum was interpreted as being the excitonic peak of CPM68. As photon energy is reduced the PC for $V_A=0$ drops far slower than would have been expected from the etalon absorption data of CPM96. However, this is because the PC is proportional to the detector transmission, not absorption. If allowances are made for this, the absorption edge will be approximately that sketched in Fig 7-12 as a dashed line (an exact calculation not being possible due to $I_{ph}(\omega)$ not being measurable).

The $V_A=0$ PC curve thus implies that the excitonic peak position of CPM68 is consistent with etalon absorption results on CPM96 but that the absorption edge is less abrupt - consistent with the poorer quality of the PL spectra.

For $V_A < 0$ no quantum Stark shift is observed in the transmission edge measured by the PC. The change in absorption edge is closer to that observed in MQWS when an electric field is applied perpendicular to the wells⁹. The observation of this effect for a perpendicular applied field implies that coulombic impurities present in the MQWS and inhomogeneities in the applied field are very quickly destroying the resonant nature of the MQWS. This causes the excitonic absorption peak to be very quickly destroyed and the 2D density of states edge to be broadened.

7.4.3 Conclusions and Recommendations

The results of waveguide PC spectroscopy have been shown to be difficult to interpret for MQW waveguides with a large product $2\alpha L$. In this region I_{ph} is a complex function of α_{abs} . However, the results for TE propagation demonstrated an absorption edge position consistent with the measured absorption edge of similar structures. For $V_A < 0$ no quantum confined Stark effect was observed due to the poor quality of the MQWS. However, the shift in absorption edge with V_A was rapid and is therefore usable as the basis of an electro-absorption modulator.

The results also confirm that MQW-DH p-i-n diodes have very good light detection properties making them suitable for applications as integrated optical detectors.

PC spectroscopy is the only method of measuring the absorption edge of TE and TM polarised light in a MQWS-DH due to the large absorption coefficient making waveguide transmission experiments up to the exciton peak impossible. However, a vast improvement in the quality of the results would be obtained if a waveguide detector of length say $5\mu\text{m}$ was photolithographically produced. This would allow the detector to be in the regime where $I_{\text{pt}}(\hbar\omega)$ is proportional to $\alpha(\hbar\omega)$ and experimental results could be easily interpreted.

Although not carried out here due to the lack of time it is strongly recommended that in future PC spectroscopy should be used with light transmitted perpendicular to the layers as a very simple method of initially checking the electro-optic quality of MQWS. No complex optical source would be required or complex sample preparation with a simple lamp and monochromator system allowing $I_{\text{pt}}(\hbar\omega, F)$ and hence $\alpha(\hbar\omega, F)$ to be simply and quickly plotted for light polarised parallel with the MQW layers.

7.5 PLANAR WAVEGUIDE RESULTS

The PC spectra presented in the previous section revealed that it would be difficult to draw general conclusions on MQW-DH active waveguide characteristics from the MQW material available since no strong quantum confined Stark effect was evident. However, the absorption edge has been observed to be strongly dependent on the applied electric field. Planar waveguide structures were therefore used to directly investigate electro-absorption in MQW-DH sample CPM68.

The end-fire coupling system was used to couple radiation from the dye-laser into the mounted active waveguides described in section 7.4.2. The dye-laser stabiliser was used to stabilise the output power of the dye-laser over the wavelength range required and over the time interval required for the experiments. The beam was mechanically chopped to allow phase sensitive detection. The electrical circuit shown in Fig 7-12 was used to apply the necessary

bias to the modulators, with all experiments being carried out at DC. The transmitted light was detected using a silicon diode and preamplified before being fed to a lock-in amplifier and displayed on a chart recorder. As in previous examples, effects due to the system were removed by measuring the system transmission with no sample in place.

7.5.1 Absorption Edge Shift

The first experiment undertaken was to measure the change in absorption edge as a function of applied voltage. Reverse bias voltages from 0-4V were applied to the sample with the dye-laser being scanned from $\lambda=903$ to 863nm for each applied voltage. Care was taken to determine accurately the zero level of each measurement to allow the measured transmission to be converted to propagation loss using the expressions derived in chapter six. As in chapter six the propagation loss was only obtained relative to some unknown constant $\alpha(\lambda_0)$. However, by half metallising a planar waveguide sample it was shown that there was no significant difference in the transmission of an active waveguide at $V_A=0$ and a passive waveguide. This allowed the $V_A=0$ results to be equated with the passive waveguide loss measurements of chapter six. $\alpha(V_A, \lambda)$ was thus obtained in absolute loss terms.

The measured absorption edge shift is plotted in Fig 7-13. For $V_A=0$ the shape of the absorption edge is very similar to the passive waveguide result of chapter six. As reverse bias is applied to the diode the absorption edge is seen to shift to lower photon energies. For $V_A < -4V$, measurement of the absorption edge became difficult due to the low level of transmitted power.

Although an absorption edge shift rather than broadening appears to be the dominant effect, this is due to the very low levels of absorption change being measured. Typically waveguide modulators have lengths $L > 200\mu m$. Very small material absorption changes thus produce very large changes in total waveguide loss ($2\alpha L$) and so the absorption edge being measured here is the very tail of the material absorption edge. When only this tail is observed absorption edge broadening can appear as a uniform shift to lower energies, as is observed with the Franz-Keldysh effect in GaAs¹⁵.

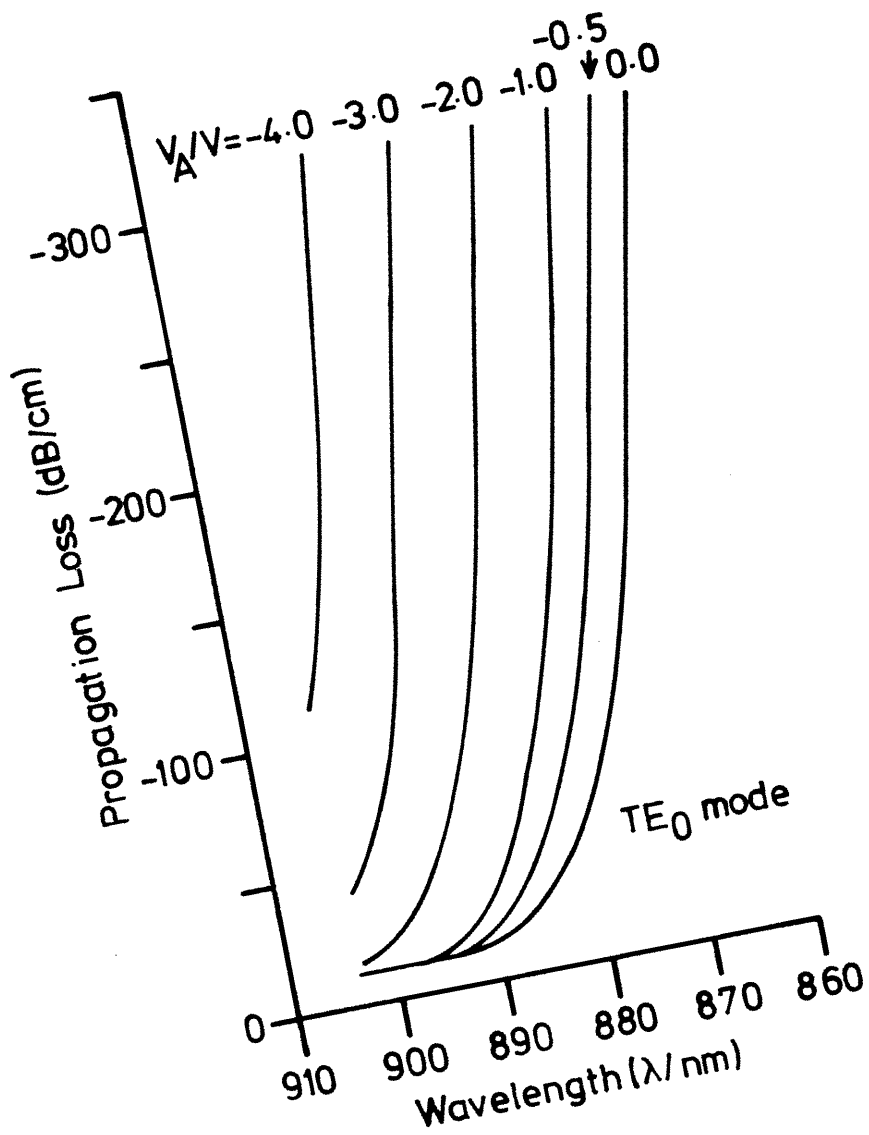


Fig 7-13 The shift in absorption edge with applied voltage in a planar waveguide in CPM68.

The absorption edge shift observed is very large in comparison with the theoretical shifts derived for GaAs and MQWS. Once again this can be explained by the fact that it is the tail of the absorption edge of the MQWS that is being measured. This region is not well described by either the Franz-Keldysh model in GaAs or the Stark effect in MQWS and may be more sensitive to applied field inhomogeneity and coulombic impurities than is taken account of in the quantum confined Stark effect model. This explanation is supported by the fact that the MQW absorption edge measured by Miller et al⁹ is not fitted well by the Gaussian model for $\alpha \approx 4 \times 10^{23} \text{ npr.cm}^{-1}$.

7.5.2 Modulation Depth

Having demonstrated that the absorption edge of sample CPM68 was strongly dependent on applied voltage, several discrete wavelengths were chosen at which to measure the variation of modulation depth with V_A . The results are reproduced in Fig 7-14. For a general wavelength, λ , the propagation loss of the device will increase slowly with V_A until the steep absorption edge begins to pass. Then $\Delta\alpha(V_A)$ will rise quickly and approximately linearly with V_A until an extinction ratio limit is approached at which $\Delta\alpha(V_A)$ tends to saturate. This extinction ratio limit is determined by the amount of background, unguided light detected.

At $\lambda=871.3\text{nm}$, $\alpha(V_A=0)$ is large, and so $\Delta\alpha(V_A)$ quickly increases with V_A until the background level is reached. At $\lambda=880.5\text{nm}$, $\alpha(V_A=0)$ is smaller, and so although $\Delta\alpha(V_A)$ again quickly increases, a larger change in absorption is achieved before the background level is reached. At $\lambda=903.4\text{nm}$, $\alpha(V_A=0)$ is at a minimum. $\Delta\alpha(V_A)$ varies slowly at first until the absorption edge is shifted to 905nm and then $\Delta\alpha(V_A)$ quickly rises until the background level is reached. These measured absorption changes are consistent with the absorption edge shifts reproduced in Fig 7-13.

The maximum extinction ratio achievable was limited by the amount of background light and not any saturation of the electro-absorption effect. The background light in the above experiments was found to partly consist of chopped radiation skimming straight over the device. This light produced an artificially high background level and so a slit was used to filter the near field pattern. Repeating the

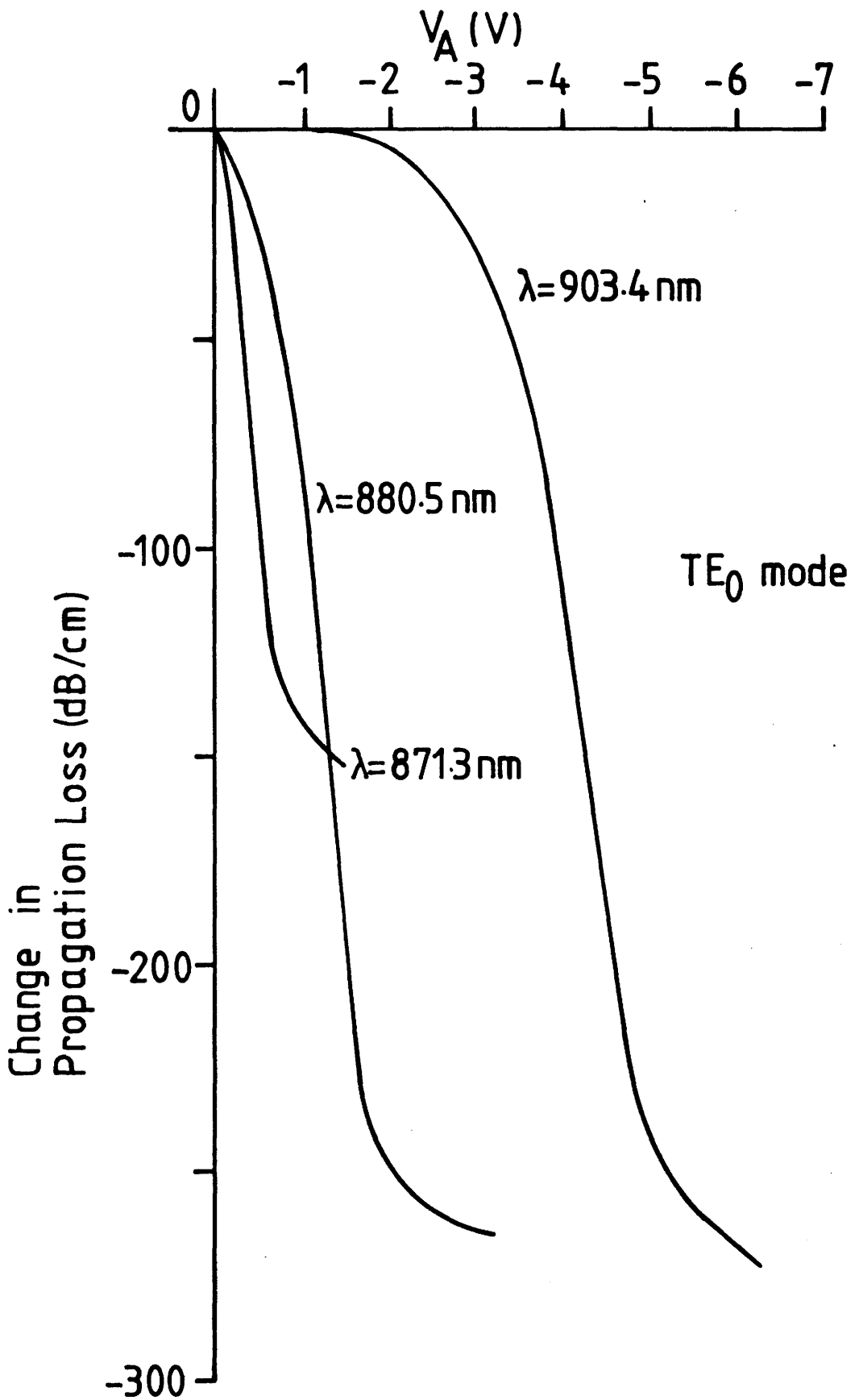


Fig 7-14 The change in propagation loss with applied voltage in a planar waveguide in CPM68.

above experiment at $\lambda=880.5, 888.1$ and 903.4nm resulted in the curves shown in Fig 7-15 with the background level being drastically reduced.

The background level was now determined by unguided light which was observed to propagate through the (Al,Ga)As waveguide cladding layers. Due to the weak confinement of CPM68 and the thinness of the waveguide layer this unguided light is particularly strong. The effects of this unguided light could be reduced in future devices by growing more strongly confined MQW-DH with thicker guide layers, as in the original waveguide design. In addition, the experimental arrangements could be altered so that the active waveguide was modulated at a low frequency rather than the laser beam being chopped. In this way unguided light would not be amplified by the lock-in amplifier and the background level would be further reduced.

Even without these improvements the above experiments have demonstrated that MQWS are capable of very high extinction ratios for extremely low applied voltages. Reinhart¹⁹ carried out experiments on (Al,Ga)As-DH modulators and found an optimum photon energy of 900nm (approximately 60 meV from the absorption edge) gave $\Delta\alpha=10\text{dB}$ for a modulator of length $L\approx 0.5\text{mm}$ and a bias voltage of $V_A=-8\text{V}$. More recently Dymont and Kapron²⁰ have demonstrated $\Delta\alpha=30-35\text{dB}$ for $L\approx 590\mu\text{m}$ but with a switching voltage of $V_A=-24\text{V}$. In comparison MQW-DH CPM68 with $L=480\mu\text{m}$ demonstrates $\Delta\alpha=19-20\text{dB}$ for as little as $V_A=-3$ to -4V . In practice therefore, in situations where power consumption is of importance MQW-DH show a clear advantage over bulk devices.

As indicated in section 7.1, a realistic figure of merit for an absorption modulator is $\Delta\alpha/\alpha$. Using GaAs absorption data from Blakemore¹⁶ Table 7-1 shows that MQW-DH CPM68 has a higher figure of merit than any GaAs or quantum well electro-absorption modulator reported in the literature and for a smaller bias voltage.

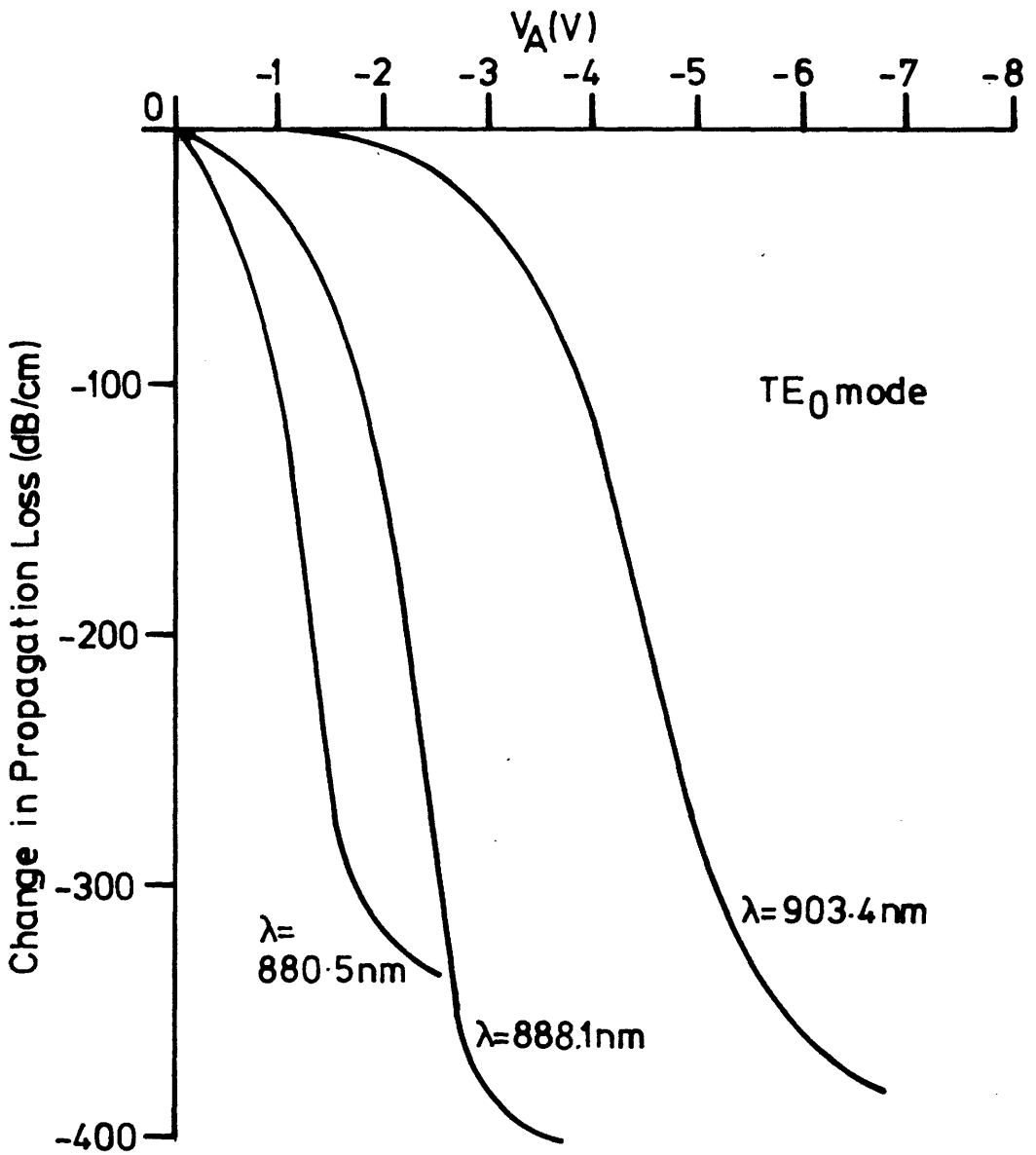


Fig 7-15 The change in propagation loss with applied voltage in a planar waveguide in CPM68.

Table 7-1

	BULK GaAs (20)	BULK Al _{0.3} Ga _{0.7} As (2)	MQW (2)	MQWS-DH (CPM68)
V _a	-24V	?	-20V	-4V
$\Delta\alpha/\alpha$	4.6	4.8	21	35

The figure of merit for MQW-DH CPM68 is limited by the propagation loss of 12dBcm^{-1} far from the band edge. Calculations suggest that a MQW-DH with stronger confinement (similar to the original design) would have a propagation loss far from the band edge as low as the 1.5dBcm^{-1} measured by Glick et al³ in a MQW-DH. This would increase $\Delta\alpha/\alpha$ to approximately 280 with further improvement being possible by increasing the saturation level.

7.6 ACTIVE RIB WAVEGUIDE FABRICATION

Electro-absorption modulators which laterally confine light are required for many applications in integrated optics. Stripe waveguide modulators are advantageous for AC modulation since they can reduce the diode junction area, and thus the device capacitance. This in turn increases the band width of the device. To demonstrate the fabrication of single-mode, stripe electro-absorption modulators in MQW-DH it was decided to fabricate active, strip loaded MQW-DH waveguides in CPM68.

The experiments reported here were planned to be an initial test of the fabrication procedure of MQW-DH stripe modulators. A fire in the fabrication facilities prematurely ended fabrication work and so further optimisation of the presented procedures is recommended.

7.6.1 Fabrication Procedure

The strip loaded waveguides were fabricated by RIE using a metal mask, lift-off technique where the metal mask is used as the top electrode of the device.

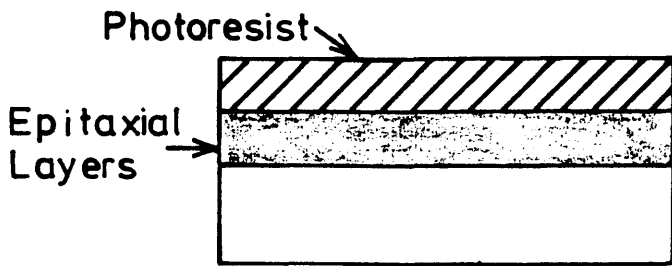
First an Au:Ge ohmic contact was evaporated onto the back of the n^+ substrate and annealed in the usual way. A dark field mask was then used to pattern the surface (see Fig 7-16). Following this an Au:Zn:Ni alloy with an Au capping layer was evaporated onto the top surface. By subsequently immersing the sample in acetone the photoresist was dissolved, carrying away any metal that was coating it. The resulting pattern of metal stripes constituted the mask for RIE.

Fig 7-17(a) reproduces a micrograph of the resulting metal mask which exhibits an edge roughness substantially larger than that present in photoresist masks. The surface of the metal also appears to be rough, due to contamination during this particular evaporation. It is therefore expected that optimisation of the lift-off technique would improve the quality of the metal mask.

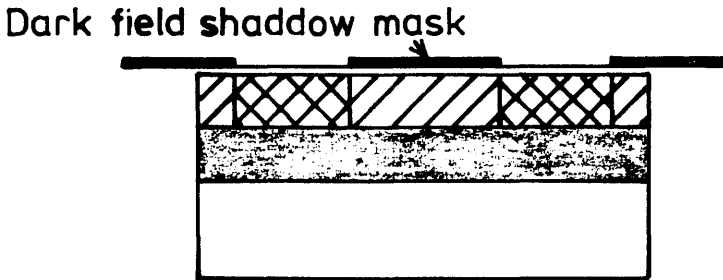
At this stage there was a choice between annealing the mask before or after etching the ribs. The sample was therefore cleaved in two with sample A being annealed in the usual manner before dry etching. Fig 7-17(b) shows sample A after annealing. The annealing process is seen to have further roughened the mask edges and caused bubbling of the metal, but the usual, post-anneal I-V characteristics were observed.

Both samples were then etched using the standard RIE etch conditions outlined in chapter six, resulting in an outer cladding thickness of approximately $0.6\mu\text{m}$. Sample B was then annealed at the usual temperature but using a slower initial increase in temperature at the start of the annealing process. This produced the usual I-V characteristics while ensuring that the metal electrode did not flow down the ridge edges.

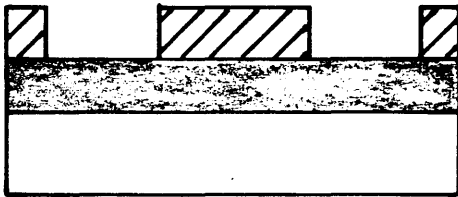
Fig 7-18 shows micrographs of the resulting ridge structures. The bubbling of the metal surface in sample A had caused Zn and Ni to be exposed on the mask surface. These materials were sputtered over the sample during the etch run causing the formation of a large number of cones (Fig 7-18(a)). In contrast, sample B which was annealed after etching exhibited a smooth clean etched surface with no evidence of cone formation (Fig 7-18(b)). However, the ridge walls were still significantly rougher than those produced from photoresist masks.



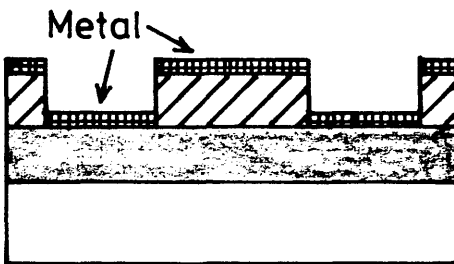
Photoresist spun on to sample.



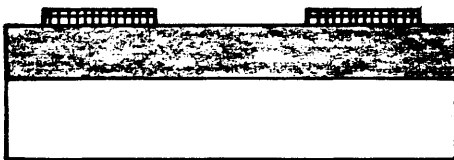
Photoresist exposed to U.V. light through a shadow mask.



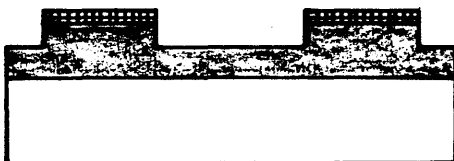
Photoresist developed giving grooves in the resist.



Metal evaporated onto the surface.

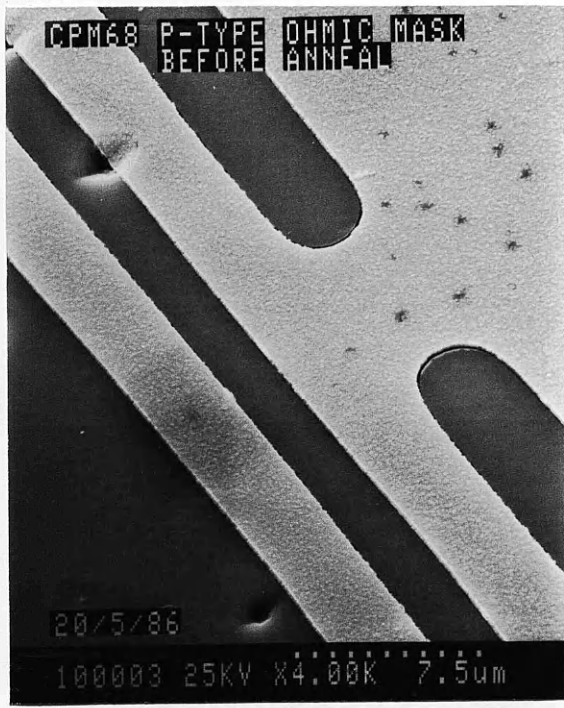


Photoresist dissolved to leave metal stripes.

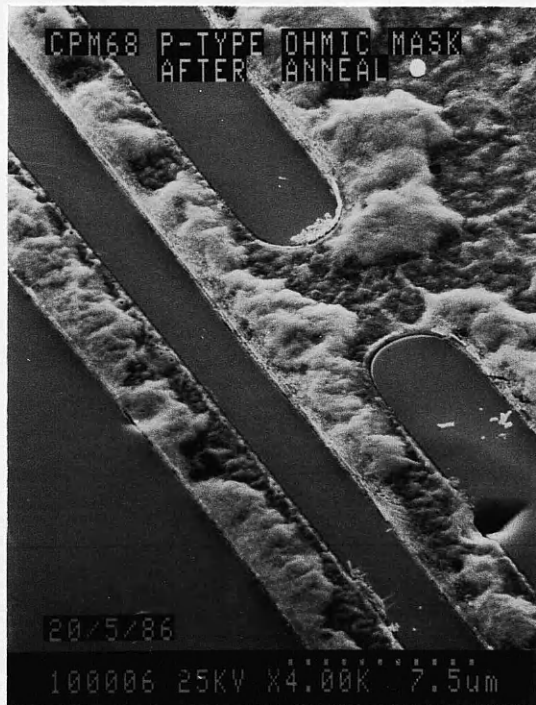


Dry etching using the metal mask leaves ridges with self-aligned contacts.

Fig 7-16 The lift-off technique.

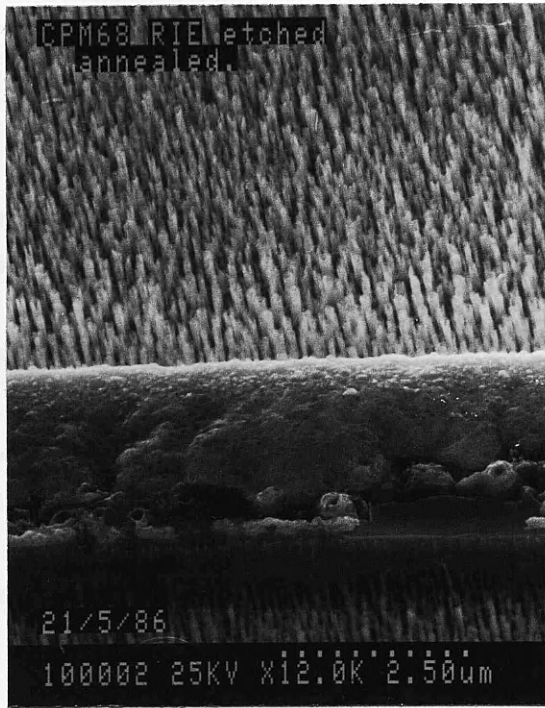


(a)

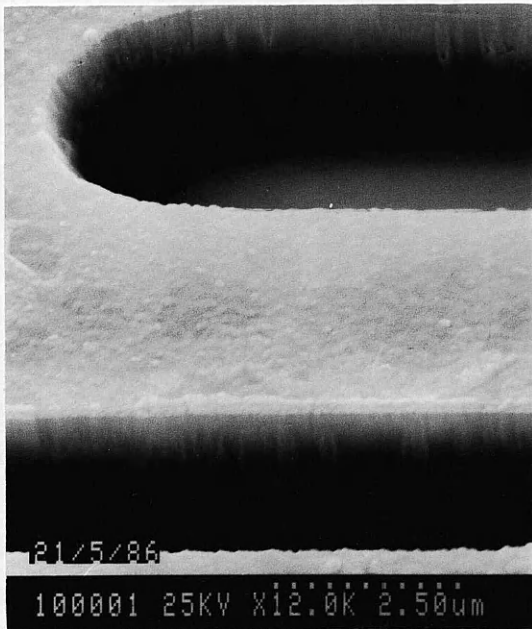


(b)

Fig 7-17 Au:Zn:Ni ohmic etch masks: (a) before annealing, and (b) after annealing.



(a)



(b)

Fig 7-18 Active waveguide structures formed by: (a) annealing the contacts before etching, and (b) annealing after etching.

The preparation technique used for sample B is recommended for the fabrication of active waveguide devices.

7.6.2 Device Results

The etched ridges were of nominal width $3\mu\text{m}$. When measured using a s.e.m. they were found to be $4\mu\text{m}$ wide due to a combination of the original shadow mask gap being too wide and the photoresist being overexposed during lithography. Sample B was cleaved to a length of $560\mu\text{m}$ and the end-fire coupling system was used to couple light into the $4\mu\text{m}$ wide strip loaded structures. The guides were observed to be single-mode from $\lambda=903\text{nm}$ to the absorption edge.

Using an identical procedure to that used for the investigation of planar active waveguides the change in absorption with applied voltage (V_a) for several wavelengths was found to vary as shown in Fig 7-19. The general trend of the results is identical to that of the planar devices but the stripe devices show a reduction in the background light level. Although the maximum change in absorption is thus increased, the overall figure of merit for this device is lower. The device was too short to allow sequential cleaving to determine the propagation loss, but the propagation loss far from the band edge is likely to be at least that of the $3\mu\text{m}$ wide passive waveguides which were measured in the previous chapter to have a propagation loss of 17dBcm^{-1} . This value of propagation loss at zero applied field results in the figure of merit being reduced from that in planar modulators to approximately 27.

At $\lambda=888\text{nm}$ the TM mode was excited in the stripe waveguide and the transmission measured as a function of applied voltage. The resulting curve is shown in Fig 7-19. As expected, the electro-absorption of the MQWS was found to be anisotropic with a larger voltage being required to obtain a given absorption change in the TM mode than the TE mode. This result is consistent with the anisotropy observed in the absorption edge of CPM68. The measured anisotropy in the electro-absorption is the opposite of that observed in GaAs-DH where light polarised parallel with the applied electric field (TM modes) shows stronger electro-absorption than light polarised perpendicular to the applied electric field (TE modes)¹⁹.

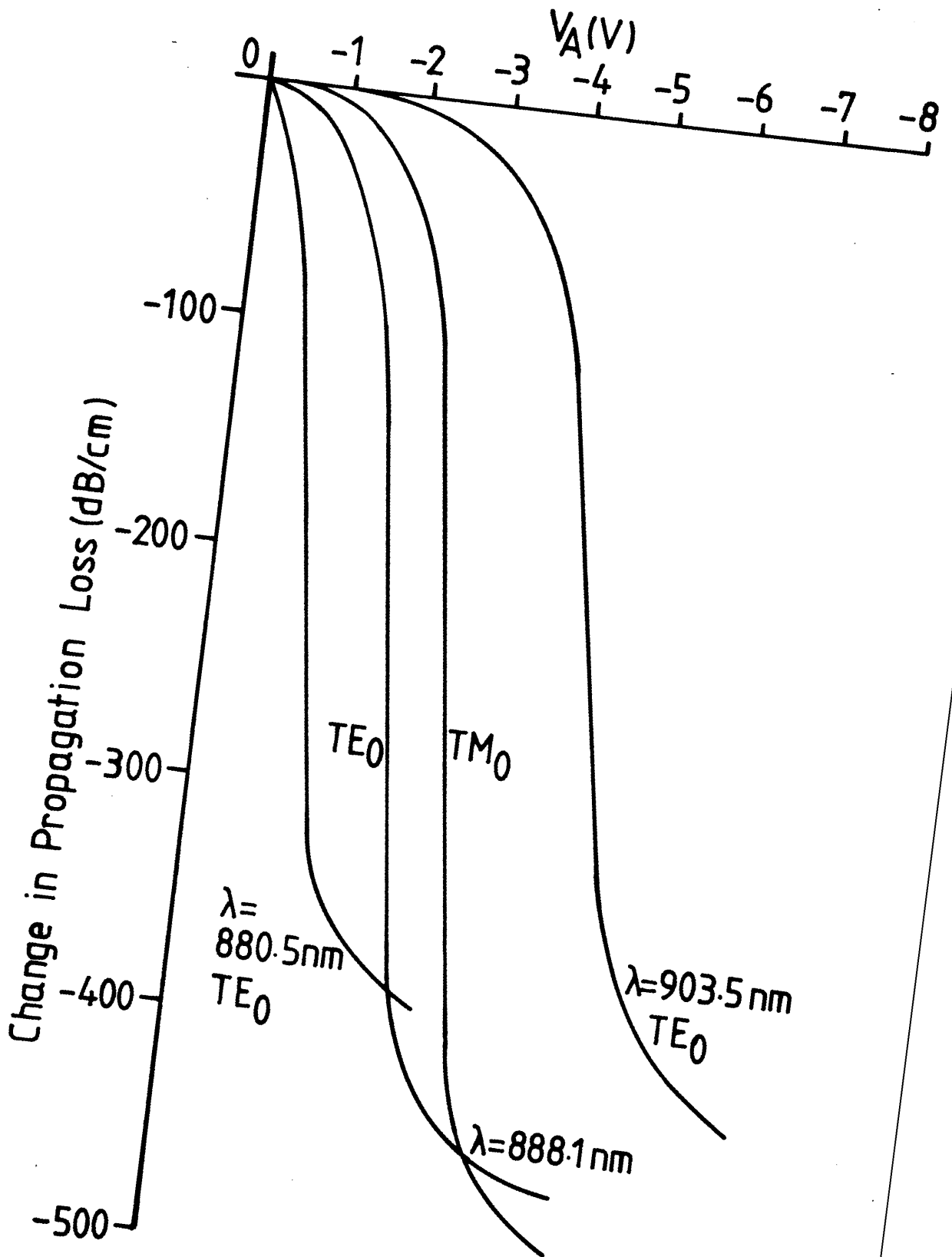


Fig 7-19 The change in propagation loss with applied voltage in a single-mode, strip loaded waveguide in CPM68.

It is not understood why the TM mode should exhibit a lower background intensity than the TE mode, however the observed anisotropy would allow the fabrication of an interesting integrated optical polariser with $\alpha_{TE}/\alpha_{TM} \approx 1$ for $V_A=0$, and $\alpha_{TE}/\alpha_{TM} \approx 4$ at $V_A=-2V$ and $\lambda=888nm$.

7.7 CONCLUSIONS

Theoretically MQWS are predicted to show a stronger electro-absorption effect than bulk GaAs, allowing the design of more efficient electro-absorption modulators with higher figures of merit and lower switching voltages than GaAs devices. Photocurrent spectroscopy has been shown to be a simple way of observing the absorption edge of MQWS-DH, p-i-n diode structures. CPM68 did not exhibit a clear quantum confined Stark effect but the electro-absorption measured in planar MQW-DH waveguides still resulted in a figure of merit higher than any device published in the literature. Electro-absorption modulators were demonstrated in single-mode strip loaded waveguides. Since the observed electro-absorption effect is a purely electronic process, the high frequency limitation on electro-absorption modulation will be determined by device capacitance and series resistance. This combined with the very short device lengths obtainable opens up the possibility of simple but very fast modulators being designed.

The nature of MQWS allows their band edge position to be tailored via well width. This would allow (Al,Ga)As MQW absorption modulators to be tailored via well width to produce optimum modulation for a very wide range of photon energies above the band gap energy of GaAs.

The electro-absorption effect was shown to be anisotropic with the effect for TE modes being larger than that for TM modes, a characteristic that may be useful for the fabrication of integrated optical polarisers.

The success of PC spectroscopy on CPM68 demonstrates the ability of the MQW-DH p-i-n diode structure to act as a photodetector with a high internal quantum efficiency. The one MQW-DH can therefore act as absorption modulator, passive waveguide and photodetector opening up interesting possibilities for MQW integrated optics.

References to Chapter Seven

- 1 J.S.Weiner, D.A.B.Miller, D.S.Chemla, T.C.Damen, C.A.Burrus, T.H.Wood, A.C.Gossard and W.Wiegmann;
"Strong polarization-sensitive electroabsorption in GaAs/AlGaAs quantum well waveguides", Appl. Phys. Lett. **47**, 1148 (1985).
- 2 T.H.Wood;
"Direct measurement of the electric-field-dependent absorption coefficient in GaAs/AlGaAs multiple quantum wells", Appl. Phys. Lett. **48**, 1413 (1986).
- 3 M.Glick, F.K.Reinhart, G.Weimann and W.Schlapp;
"Modification of the electro-optic effect near the band gap in a GaAs/AlGaAs multiquantum well heterostructure", Helvetica Physica Acta **59**, 137 (1986).
- 4 T.H.Wood, C.A.Burrus, D.A.B.Miller, D.S.Chemla, T.C.Damen, A.C.Gossard and W.Wiegmann;
"131 ps Optical Modulation in Semiconductor Multiple Quantum Wells (MQW's)", IEEE J. Q. Electron. **QE-21**, 117 (1985).
- 5 S.Tarucha and H.Okamoto;
"Monolithic integration of a laser diode and an optical waveguide modulator having a GaAs/AlGaAs quantum well double heterostructure", Appl. Phys. Lett. **48**, 1 (1986).
- 6 Y.Arakawa, A.Larsson, J.Paslaski and A.Yariv;
"Active Q switching in a GaAs/AlGaAs multiquantum well laser with an intracavity monolithic loss modulator", Appl. Phys. Lett. **48**, 561 (1986).
- 7 D.S.Chemla, D.A.B.Miller, P.W.Smith, A.C.Gossard and W.Wiegmann;
"Room Temperature Excitonic Nonlinear Absorption and Refraction in GaAs/AlGaAs Multiple Quantum Well Structures", IEEE J. Q. Electron. **QE-20**, 265 (1984).
- 8 D.A.B.Miller, D.S.Chemla, T.C.Damen, A.C.Gossard, W.Wiegmann, T.H.Wood and C.A.Burrus;
"Band-Edge Electroabsorption in Quantum Well Structures: The Quantum-Confined Stark Effect", Phys. Rev. Lett. **53**, 2173 (1984).
- 9 D.A.B.Miller, D.S.Chemla, T.C.Damen, A.C.Gossard, W.Wiegmann, T.H.Wood and C.A.Burrus;
"Electric field dependence of optical absorption near the band gap of quantum-well structures", Phys. Rev. B **32**, 1043 (1985).

- 10 E. E. Anderson;
Modern Physics and Quantum Mechanics (W.B. Saunders Company, London, 1971).
- 11 S. M. Sze;
Physics of Semiconductor Devices, 2nd Edition (John Wiley & Sons, New York, 1981).
- 12 *Properties of Gallium Arsenide*, emis Datareviews series No. 2, Imnspec.
- 13 N. Bottka and L. D. Hucheson;
"Analytical aspects of electroabsorption modulators", *J. Appl. Phys.* **46**, 2645 (1975).
- 14 G. E. Stillman, C. M. Wolfe, C. O. Bozler and J. A. Rossi;
"Electroabsorption in GaAs and its application to waveguide detectors and modulators", *Appl. Phys. Lett.* **28**, 544 (1976).
- 15 J. I. Pankove;
Optical Processes in Semiconductors (Dover Publications Inc., New York, 1971).
- 16 J. S. Blakemore;
"Semiconducting and other major properties of gallium arsenide", *J. Appl. Phys.* **53**, R123 (1982).
- 17 K. Yamanaka, T. Fukunada, K. L. I. Kobayashi and M. Ishii;
"Photocurrent spectroscopy in GaAs/AlGaAs multiple quantum wells under a high electric field perpendicular to the heterointerface", *Appl. Phys. Lett.* **48**, 840 (1986).
- 18 D. A. B. Miller, D. S. Chemla, T. C. Damen, T. H. Wood, C. A. Burrus, A. C. Gossard and W. Wiegmann;
"The Quantum Well Self-Electrooptic Effect Device: Optoelectronic Bistability and Oscillation, and Self-Linearized Modulation", *IEEE J. Q. Electron.* **QE-21**, 1462 (1985).
- 19 F. K. Reinhart;
"Electroabsorption in $\text{Al}_y\text{Ga}_{1-y}\text{As}-\text{Al}_x\text{Ga}_{1-x}\text{As}$ double heterostructures", *Appl. Phys. Lett.* **22**, 372 (1973).
- 20 J. C. Dymant and F. P. Kapron;
"Extinction ratio limitations in GaAlAs electroabsorption light modulators", *J. Appl. Phys.* **47**, 1523 (1976).

CHAPTER EIGHT
THE ELECTRO-OPTIC EFFECT IN MQW-DH

8.1 INTRODUCTION

In comparison to the non-linear properties and electro-absorption properties of MQWS, the electro-optic properties have received little attention in the literature. This is despite the obvious applications of the effect to phase modulators, active directional couplers and Mach-Zehnder modulators. The only published theoretical analysis of the electro-optic (e-o) effect in MQWS¹ was briefly described in chapter two and predicts two orders of magnitude increase in $\Delta n/n$ over that for the corresponding bulk material. This has led to the hope of more efficient integrated optics modulators and switches in MQWS. In practice, Glick et al^{2,3} have found that the linear electro-optic (LEO) coefficient in (Al,Ga)As MQWS shows no such increase at 1.15 μ m or 888nm, but that a strong quadratic electro-optic (QEO) component is introduced at 888nm. However, even this QEO increase may not be unique to MQWS since recent theoretical investigations have predicted a strong QEO effect close to the band gap of bulk zinblend type semiconductors⁴.

There therefore remains a need for a detailed study both experimentally and theoretically of the LEO and QEO effects in MQWS to ascertain whether any increase in the e-o figure of merit ($\Delta n/\alpha$) is achieved by using MQWS. Such a study was beyond the scope of this thesis. However, since CPM68 had exhibited a large electro-absorption (e-a) effect experimentally, it was decided to investigate its e-o effect.

CPM68 is not of an optimum design for the measurement of the e-o coefficient of MQWS. Ideally, the waveguide would be strongly confining so that a large proportion of the optical mode was propagating in the MQWS. In addition, a good p-i-n structure would ensure that all the applied voltage was dropped across the MQWS. In this way only the e-o effect of the MQWS would contribute to the measured phase change.

8.2 EXPERIMENTAL METHOD

MQWS CPM68 had been grown on a $\langle 001 \rangle$ substrate and cleaved along the $\langle 110 \rangle$ and $\langle -110 \rangle$ directions. The electric field was applied perpendicular to the MQW, $\langle 001 \rangle$ layers. The e-o tensor terms involved in the experiment were therefore identical to those in the GaAs experiments of section 4.6. All measurements were carried out at DC with an unclamped crystal so that r_{41}^T would be the measured quantity.

Of the several methods described in section 4.6 for the measurement of r_{41}^T , the phase compensation method was used in the following experiment since it was desired to plot the dependence of phase difference on applied voltage. In addition, this method can compensate for any difference in TE and TM propagation loss within the waveguide device being investigated.

The usual end-fire system with mechanically chopped laser beam and phase sensitive detection was used. First the system was carefully set up and measured to ensure that it did not introduce any phase difference or amplitude difference between horizontally and vertically polarised light. This was done by using a half-wave plate to rotate the horizontally polarised laser emission round to an angle of $+45^\circ$ to the vertical (see Fig 8-1). A Glan-Thompson prism orientated at $+45^\circ$ ensured that light entering the input microscope was linearly polarised. An identical polariser at the output of the output microscope was used to analyse the emerging laser beam which was found to be linearly polarised at $+45^\circ$.

Next a Soleil-Babinet compensator was placed before the analysing prism at 90° to the vertical and adjusted until a zero was observed with the analyser at -45° to the vertical. This defined the compensators absolute zero point. The analyser was then rotated to $+45^\circ$ and the compensator adjusted until a zero was observed. This defined a phase compensation of Π radians. The compensator was thus calibrated.

A planar, active MQW-DH waveguide was fabricated using the methods described in the previous chapter. It was then placed on the translation stage, and the usual electrical circuit used to apply

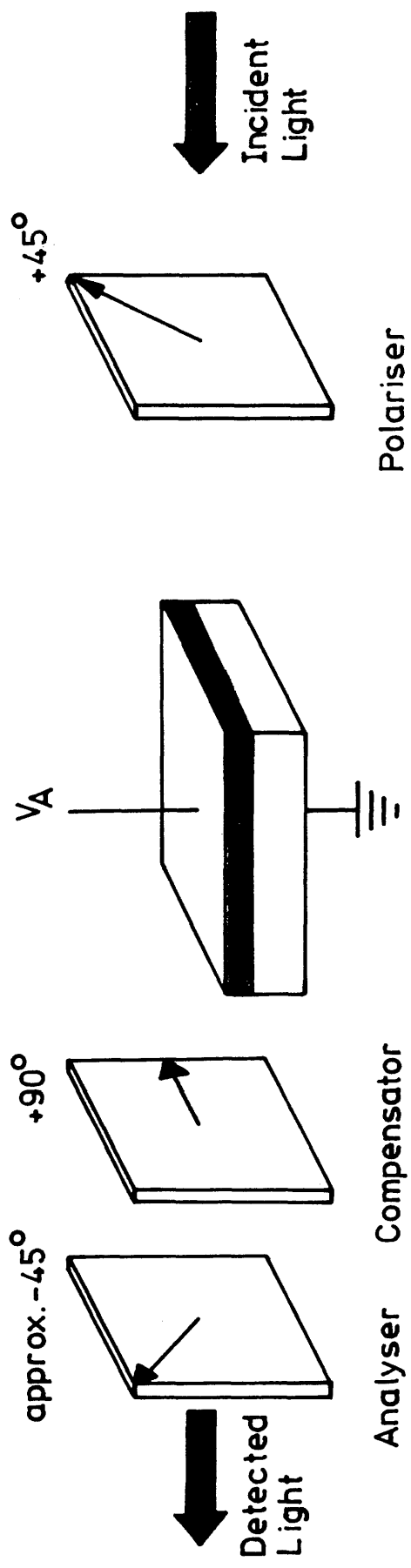


Fig 8-1 The experimental set-up used to measure the electro-optic effect in MQW-DH CPM68.

bias voltage $V_A \leq 0$. The near field pattern was spatially filtered by a slit placed between the output microscope and the compensator. With $V_A=0$ the compensator was adjusted to produce a linearly polarised output. In general, this was not polarised at $+45^\circ$ since the sample introduced a difference in propagation loss between TE and TM modes. The analyser was then rotated through 90° to produce zero output. For each bias applied, the compensator was adjusted to produce zero output from the analyser, the compensator value being the phase difference between TE and TM modes.

This procedure was carried out with the sample orientated for propagation along the $\langle 110 \rangle$ direction. The sample was then rotated through 90° and the experiment repeated for propagation along the $\langle -110 \rangle$ direction.

8.3 RESULTS

The e-o effect of MQWS is of particular interest close to the band edge. The above procedure was therefore attempted at $\lambda=905\text{nm}$ using the dye-laser system. However, as was reported in the previous chapter, CPM68 exhibits a very strong e-a effect close to the band edge, and this was found to swamp any e-o effect when the above experimental procedure was attempted. This e-a is much larger than that observed by Glick et al⁵, and it was thus impossible to repeat their measurements on CPM68.

The e-o effect in CPM68 was therefore investigated at $\lambda=1.15\mu\text{m}$ where no e-a effect was observed. Using the above experimental technique, the compensator was calibrated, one unit being found to represent (200 ± 5) milliradians with phase compensation being measurable to a precision of 0.05 of a unit.

The sample used had an area of $2.25 \times 1.59 \text{mm}^2$. The measured phase difference between TE and TM modes reduced per unit length is shown in Fig 8-2.

8.4 DISCUSSION AND CONCLUSIONS

The phase difference between TE and TM modes was shown in chapter four to follow the relationship:

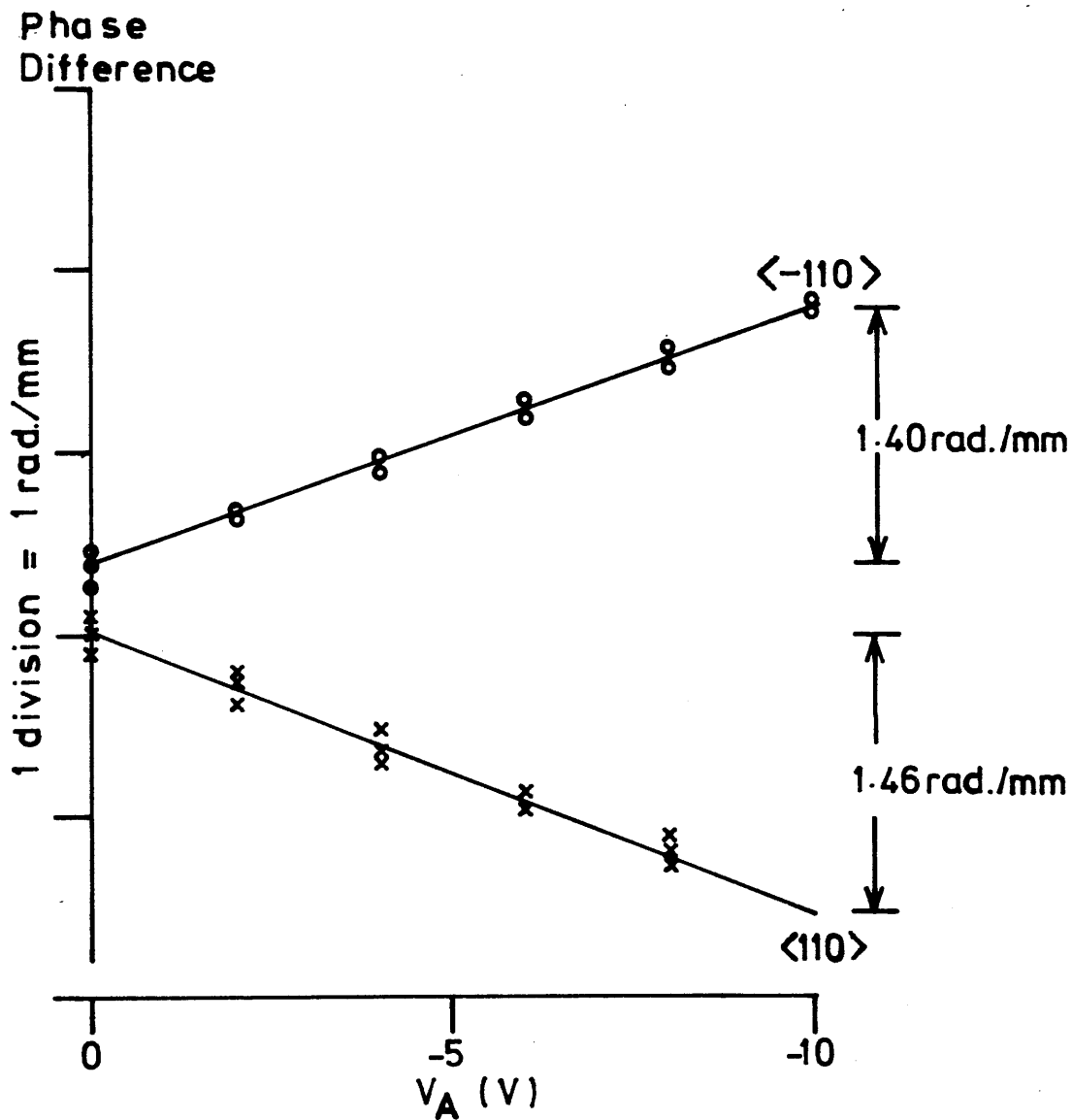


Fig 8-2 The phase difference between TE and TM modes (reduced by length) as a function of applied voltage (V_A).

$$\Gamma = L\Gamma_0 \pm (\pi n^2 L / \lambda) r_{41} (V_t / t) \eta \quad \langle \pm 110 \rangle$$

where L is the active length, n the refractive index of the MQW layer, V_t the total voltage across the junction and t is the guide layer thickness. At a forward bias equal to the built-in junction potential ($V_B=1.04V$ from C-V results) the corresponding built-in birefringence Γ_0 must be independent of the propagation direction. However, it is impossible to achieve $V_A=V_B$ in practice, so the phase difference data $\Gamma(V_A)$ must be extrapolated back to $V_t=0$. However, the experiment only allows the principal values of Γ_0 to be determined. The integer multiples of 2π radians can only be obtained by determining Γ_0 for different diode lengths L , such that the resulting Γ_0 is proportional to L . Since the above experiment was only carried out at two lengths the true Γ_0 value could not be uniquely determined. If Γ_0 were to be accurately and uniquely determined, similar experiments to that described above would have to be carried out at several more diode lengths⁵.

Fig 8-2 shows that the change in phase difference with V_A measured in CPM68 is very similar to that measured by Glick et al² who obtained a change in phase difference of approximately 1.44 rad/mm for a change of V_A from 0 to -10V at $\lambda=1.15\mu m$. In the present results the change is 1.46 rad/mm for $\langle 110 \rangle$ propagation and 1.40 rad/mm for $\langle -110 \rangle$ propagation. Although this dependence on propagation direction is comparable with the accuracy with which Γ could be measured, it may still be significant since Glick et al² noted a similar dependence of smaller magnitude in their experiments. They inferred that this directional dependence arose from higher order effects.

A definitive calculation of the LEO and QEO coefficients of CPM68 at $1.15\mu m$ proved impossible. Although the changes in Γ with V_A in CPM68 are similar to those measured by Glick et al, sample CPM68 is structurally very different in form from their sample which was highly confining with a good p-i-n diode structure. Consequently, although one could expect the overlap coefficient η to be close to 1 for Glick's MQW-DH³, η for CPM68 will be very low.

The overlap integral was calculated for the TE₀ mode in CPM68 using the rms refractive index model and a built-in voltage of $V_B=1.04V$. This resulted in a "f coefficient"⁶ ($f=\eta/t$) of $0.11\mu m^{-1}$ and

$\eta = 2.90 \times 10^{-2}$ at $V_a = -10V$. With such a reduced value of η , the resulting e-o coefficient is $n^3 r_{41}^T = -4.3 \times 10^{-10} \text{ m/V}$, $r_{41}^T = -1.1 \times 10^{-11} \text{ m/V}$ compared with the value of $r_{41}^T = -1.50 \times 10^{-12} \text{ m/V}$ for GaAs at $\lambda = 1.15 \mu\text{m}$ and $r_{41}^T = -1.47 \times 10^{-12} \text{ m/V}$ for Glick's MQWS².

It is very difficult to satisfactorily explain such a large discrepancy between the present results and those of Glick et al. The uncertainties in MQW refractive index and applied field profile in the present analysis are not large enough to account for a factor of 10 error in η . Nor could the experimentally observed phase change be explained by thermal or Fabry-Perot effects. It is therefore suggested that this very large electro-optic effect results from the corresponding very large electro-absorption effect in CPM68 reported in the previous chapter. Further work is required before a definitive value of r_{41}^T for CPM68 can be obtained.

In conclusion then, an experimental system for the investigation of the LEO and QEO effects in MQWS has been developed from the work of Glick et al^{2,3,5}. However, results from initial experiments on CPM68 show a remarkably high LEO effect at $\lambda = 1.15 \mu\text{m}$ with electro-absorption masking any electro-optic effect close to the band gap. Once again CPM68 proved fundamentally unsuited for the investigation of MQW effects due to the waveguide being weak and the diode being p-n rather than p-i-n in nature. In consequence, it is recommended that the above experimental procedure be carried out again using a MQWS-DH closer to the original design and at an increased number of diode lengths so as to accurately determine Γ_0 , and the LEO and QEO coefficients.

In general, MQWS have been shown by Glick et al^{2,3,5} and the work reported above to be capable of enhancing the electro-optic effect in (Al,Ga)As waveguides. In addition, the high built-in birefringence observed by Glick et al shows that the waveguide performance as a static phase plate will also be enhanced. Closer to the absorption edge, the QEO effect is observed by Glick to become stronger, with the choice of light propagation direction becoming relevant for optimum device design. However, there is some theoretical indication that a detailed investigation of GaAs close to the band edge may result in a similar enhancement of the QEO effect (but with a

coefficient with the opposite sign) so a comprehensive comparison between MQWS and bulk materials is not yet possible.

References to Chapter Eight

- 1 H. Yamamoto, M. Asada and Y. Suematsu;
"Electric-field-induced refractive index variation in quantum-well structure", Electron. Lett. **21**, 579 (1985).
- 2 M. Glick and F. K. Reinhart;
"Optical waveguide properties of multiquantum wells", Proc. 3rd Euro. Conf. Integrated Opt. 99 (1985).
- 3 M. Glick, F. K. Reinhart, G. Weimann and W. Schlapp;
"Quadratic electro-optic light modulation in a GaAs/AlGaAs multiquantum well heterostructure near the excitonic gap", Appl. Phys. Lett. **48**, 989 (1986).
- 4 S. Adachi and K. Oe;
"Quadratic electro-optic (Kerr) effects in zincblende-type semiconductors: Key properties of InGaAsP relevant to device design", J. Appl. Phys. **56**, 1499 (1984).
- 5 M. Glick, F. K. Reinhart, G. Weimann and W. Schlapp;
"Modification of the electro-optic effect near the band gap in a GaAs/AlGaAs multiquantum well heterostructure", Helvetica Physica Acta **59**, 137 (1986).
- 6 M. J. Adams, S. Ritchie and M. J. Robertson;
"Optimum overlap of electric and optical fields in semiconductor waveguide devices", Appl. Phys. Lett. **48**, 820 (1986).

CHAPTER NINE
CONCLUSIONS, RECOMMENDATIONS AND SUGGESTIONS
FOR FUTURE WORK

The general conclusions derivable from the work reported in this thesis are limited due to the fact that only one MQW-DH was actually found to be usable as an active waveguide device. However, from the experimental work carried out on the samples available, from the theoretical studies undertaken, and from the information gleaned from relevant publications, observations can be made on the design, growth and performance of MQW waveguide devices. Most of these observations have already been made as they naturally arose throughout the thesis, but they are summarised here together with recommendations and suggestions for further work.

In general, the original design of the MQW-DH waveguide appears to be satisfactory, with a single planar mode being observed to be sustained in structures very similar to the design. Additionally, the working assumption that the refractive index of the MQWS for TE modes can be taken as the weighted rms average of the bulk indices of the constituent layers (the rms model) is seen to predict satisfactorily the modal characteristics of strip loaded MQW-DH waveguides and the coupling length of directional couplers. However, a more detailed analysis of the propagation characteristics of planar and stripe MQW-DH waveguides will require some method (such as grating coupling) of measuring the modal propagation constant in the waveguide.

It was found that a major amount of time and effort went into trying to obtain good quality MQW-DH that met the design requirements. This process was initially hindered by a lack of any effective communication channels with the personnel outwith the department carrying out the semiconductor growth. Growth of MQW-DH structures is of central importance to this project and it is hoped that future work will be carried out in much closer contact with the personnel growing the semiconductor material. It has been shown by photoluminescence that MQWS grown by MOVPE can have well width fluctuations as low as that in the MBE structures available. MOVPE material is thus satisfactory for use in passive or all-optical MQW waveguide devices. However, the fabrication of electro-absorption and

electro-optic devices in MQWS requires the application of very uniform fields, consistent with the MQW guide layer being doped at a level lower than that regularly achievable by MOVPE. It is thus recommended that MBE material be used to maximise the quantum effects in electronically active MQW waveguides.

Several techniques have been investigated that use equipment readily available within the department to test the quality of the MQWS obtained from various sources. These tests have been found to be essential to check the structure of the actual layers grown since they can vary widely from that predicted from growth conditions. In particular, PL, C-V, I-V and s.e.m. examinations have all been shown to be useful. For reasons of morphology it has recently become standard practice for structures grown by MOVPE to include an (Al,Ga)As grade layer with an Al content that rises to 60%. This can be used as an etch stop layer to remove the GaAs substrate and allow etalon transmission experiments to be done. As these experiments involve some time consuming process steps with the measurements being carried out outwith the department, it is recommended that photocurrent spectroscopy be developed as a very simple method of investigating the absorption edge of MQWS. In particular, this simple technique would allow the absorption edge of both TE and TM modes in a waveguide to be measured as a function of applied voltage.

Analysis of planar MQW-DH has shown that, as predicted, they exhibit an anisotropic absorption edge. The propagation loss of the fundamental mode far from the absorption edge was measured to be relatively high (12dBcm^{-1}) due to the low confinement of the fundamental mode in the planar structure available. A structure closer to that designed will show far less propagation loss and MQW-DH are predicted to be potentially as low-loss as bulk GaAs-DH.

A semi-empirical model of the quantum confined Stark effect in MQWS has shown that MQWS have distinct advantages over bulk GaAs as electro-absorption modulators, with a figure of merit ($\Delta\alpha/\alpha$) some 5-6 times larger and optimum modulating fields some 30% lower. MQWS electro-absorption modulators will thus be useful as either individual components or as monolithic external modulators for MQW lasers.

Experimentally no strong quantum confined Stark effect was observed, but even so the maximum figure of merit measured in the fabricated electro-absorption modulators was larger than that reported for other MQW or bulk GaAs devices. However, further improvements could be made. Firstly, the growth of higher quality MQWS will enhance the quantum confined Stark effect. In addition, the measured absorption change ($\Delta\alpha$) was limited by the amount of unguided background light detected; light that propagates through the (Al,Ga)As cladding layers. This background light can be reduced by using the original waveguide design which more strongly confines the guided mode. The amount of detected background light would be further reduced by modulating the device rather than the laser beam for phase sensitive detection. The unguided light would then be discriminated against during amplification. This measurement system more closely resembles the operating regime of modulators in practical integrated optical systems. The figure of merit ($\Delta\alpha/\alpha$) measured was also limited by the minimum propagation loss of 12dBcm^{-1} . Again, increasing the confinement of the waveguide, and thus reducing this minimum loss, will further increase the figure of merit obtainable.

The MQW-DH p-i-n diode electro-absorption modulator has been shown to exhibit a strong anisotropy with the electro-absorption effect being weaker for TM modes. It is thus possible to design a waveguide polariser that would be transparent for both TE and TM modes for zero volts bias but discriminate against TE radiation when reverse biased. This has potential use in integrated optical circuits. Further investigation is recommended.

The electro-absorption modulator was also demonstrated to be a good waveguide photodetector. In theory the wavelength dependence of the detector sensitivity should be tunable via the detector bias voltage using the strong, quantum confined Stark effect. Again this is potentially a very useful integrated optical device and it is recommended that this property of MQW-DH be further investigated.

A strong electro-optic effect was observed in the experimental devices but further work is required before this can be convincingly attributed to an enhanced electro-optic effect. The results of other

workers does, however, suggest the presence of a strong quadratic electro-optic effect in MQWS close to the absorption edge.

It is recommended that investigation take place into the application in integrated optics of such devices as the MQW waveguide self electro-optic effect device (SEED) which can be used as a hybrid optically bistable element, an optical-level shifter and a self-linearised optical modulator since they use the property of MQWS to simultaneously act as modulator and detector.

The work presented has demonstrated the feasibility of using standard semiconductor fabrication techniques to fabricate a full range of modulators, detectors and passive waveguide components in MQW waveguides. Many of the devices are potentially more efficient than the corresponding bulk waveguide devices or are unique to MQWS. All the devices are compatible with semiconductor diode laser wavelengths and have operating voltages compatible with low power semiconductor electronics. When one recalls that MQW laser diodes exhibit much lower passive waveguide loss and threshold current density than bulk diode lasers, it becomes evident that MQW-DH waveguides show great promise of being the ideal medium for the monolithic integration of integrated optical circuits.

FUTURE WORK

It is suggested that future work should initially concentrate on repeating the electro-absorption and electro-optic experiments reported here with a MQW-DH closer to that designed. A project is now proceeding within the department into the production of gratings in semiconductors and it is suggested that this technology be used to grating couple light to a MQW-DH and thus allow a detailed analysis of the propagation constant of MQW-DH close to the absorption edge.

Following this fundamental work several short and long term projects are recommended:

- (1) The fabrication of an efficient MQW-DH directional coupler switch or Mach-Zehnder modulator utilising any enhanced electro-optic effects observed.
- (2) An investigation of the properties of MQW diodes as voltage tunable detectors.
- (3) The study of voltage switchable MQW waveguide polarisers.
- (4) The study of waveguide SEEDS.
- (5) An investigation of the monolithic integration of a MQW laser and external waveguide modulator using the diode laser technology being developed in another project within the department.

APPENDIX A
DEFINITION OF COMPLEX PROPAGATION CONSTANT

Throughout this thesis the loss of a material or the propagation loss of a waveguide has been quoted in either nepers per unit length (npr cm⁻¹) or decibels per unit length (dBcm⁻¹).

If the dimensionless complex dielectric constant of a material is defined as $\underline{\epsilon} = \epsilon_1 - i\epsilon_2$, then the complex refractive index can be expressed as¹:

$$\underline{n} = (\underline{\epsilon})^{1/2} = n - ik$$

where

$$n = (2^{-1/2})[(\epsilon_1^2 + \epsilon_2^2)^{1/2} + \epsilon_1]^{1/2}$$

$$k = (2^{-1/2})[(\epsilon_1^2 + \epsilon_2^2)^{1/2} - \epsilon_1]^{1/2}$$

A electromagnetic wave propagating in the +z direction will thus have a sinusoidally varying amplitude of the form²:

$$\underline{E} = E_0 \exp(i\omega(t - \underline{n}z/c))$$

where c is the speed of light in a vacuum. \underline{E} can therefore be rewritten as:

$$\underline{E} = E_0 \exp i(\omega t - \underline{\beta}z)$$

where $\underline{\beta}$ is the complex propagation constant defined as:

$$\underline{\beta} = \omega \underline{n}/c = k\underline{n} = \beta - i\alpha$$

where $k=2\pi/\lambda$.

α is the propagation loss defined in terms of α and is measured in units of nepers per unit length³ (npr cm⁻¹). Alternatively, the propagation loss can be quoted in terms of power loss (α') where $\alpha' = 2\alpha$, and α' is measured in units of cm⁻¹ or dBcm⁻¹. Throughout this thesis dBcm⁻¹ will be used exclusively.

The relationship between the various units is:

$$2\alpha \text{ (npr cm}^{-1}\text{)} = \alpha' \text{ (cm}^{-1}\text{)}$$

$$\alpha' \text{ (dBcm}^{-1}\text{)} = 10\log_{10}(e) \cdot \alpha' \text{ (cm}^{-1}\text{)}$$

where e is the base of natural logarithms.

References to Appendix A

- 1 J.S.Blakemore;
"Semiconducting and other major properties of gallium arsenide", J. Appl. Phys. 53, R123 (1982).
- 2 B.I.Bleaney and B.Bleaney;
Electricity and Magnetism (Oxford University Press, Oxford, 1978).
- 3 *Fields and Waves in Communication Electronics* (J.Wiley & Sons, London, 1976).

APPENDIX B
SUMMARY OF MQW SAMPLE DATA

Throughout this appendix g=data from growth conditions, s=s.e.m. data, p=polaron data, PL=PL data, CV=CV data.

NJ117

Grown by SERC Central Facility for III-V Semiconductors.

No intentional doping.

29 periods of MQW grown.

n⁺ substrate.

	<u>Composition</u>	<u>Thickness/μm</u>	<u>Doping/cm^{-3}</u>
Cap	X=0 (g)	0.3 (s)	$n \approx 10^{15}$ (g)
Cladding	X=0.3 (g)	1.0 (s)	$p \approx 10^{16}$ (p)
MQW	X=0 / X=0.25 (g)	0.58 (s)	ave. $p \approx 10^{16}$ (p)
Cladding	X=0.3 (g)	3.1 (s)	$p \approx 10^{16}$ (p)
buffer	X=0 (g)	0.5 (s)	$n \approx 10^{15}$ (g)

S.e.m. data from growers.

VG215

Grown by MR J. Frost, MBE (Glasgow).

Growth rates: GaAs $2\mu\text{m hr}^{-1}$

AlGaAs $2.25\mu\text{m hr}^{-1}$

As₄/Ga flux : 10

n-type dopant - silicon.

n⁺ substrate.

growth temperature 690°C

25 wells, 25 barriers.

	<u>Composition</u>	<u>Thickness/μm</u>	<u>Doping/cm^{-3}</u>
Cap	X=0 (g)	0.29 (g)	$n = 1.4 \times 10^{16}$ (g)
Cladding	X=0.25 (PL)	0.959 (g)	$n \leq 1.0 \times 10^{16}$ (g)
MQW	X=0 / X=0.33 (g)	0.555 (s&g)	$n \leq 1.1 \times 10^{16}$ (g)
Grade	X=0.25-0.33 (g)	0.544 (s&g)	$n \leq 1.0 \times 10^{16}$ (g)
Cladding	X=0.25 (PL)	2.445 (g)	$n \leq 1.0 \times 10^{16}$ (g)

S.e.m. data implies 111Å wells and barriers assuming equal width or 104Å wells, 115Å barriers by growth rate difference.

Layer thicknesses are from a combination of RHEED oscillation calibrated growth conditions and early s.e.m. micrographs which did not resolve the wells. Later s.e.m. data which resolved the wells gave a well thickness $\approx (96 \pm 4) \text{Å}$.

VG200

Grown by Mr J. Frost, MBE (Glasgow).

Growth rates and conditions as with VG215.

n^+ substrate.

25 wells, 25 barriers.

	<u>Composition</u>	<u>Thickness/μm</u>	<u>Doping/cm^{-3}</u>
Cap	X=0 (g)	0.29 (g)	$n=2 \times 10^{16}$ (g)
Cladding	X=0.24 (PL)	0.959 (g)	$n \leq 1.5 \times 10^{16}$ (g)
MQW	X=0 / X=0.33 (g)	0.483 (g)	$n \leq 2 \times 10^{16}$ (g)
Grade	X=0.24-0.33 (g)	0.544 (g)	$n \leq 1.5 \times 10^{16}$ (g)
Cladding	X=0.24 (PL)	2.45 (g)	$n \leq 1.5 \times 10^{16}$ (g)

Well and barrier widths = $(97 \pm 4) \text{Å}$ implied assuming equal width.

Layer thicknesses from RHEED calibrated growth conditions.

VG285

Grown by Mr J. Frost, MBE (Glasgow).

Layer thicknesses from RHEED calibrated growth conditions.

	<u>Composition</u>	<u>Thickness/μm</u>	<u>Doping/cm^{-3}</u>
Cap	X=0 (g)	0.1 (g)	$p \approx 2.2 \times 10^{18}$ (g)
Cladding	X=0.27 (PL)	1.5 (g)	$p \approx 1.2 \times 10^{18}$ (g)
MQW	X=0.30 (g)	0.5 (g)	$n \approx 1.4 \times 10^{16}$ (g)
Grade	X=0.27-0.30 (g)	0.1 (g)	$n \approx 1.3 \times 10^{16}$ (g)
Cladding	X=0.27 (PL)	3.0 (g)	$n \approx 1.7 \times 10^{16}$ (g)
Etch stop	X=0.60 (g)	1.0 (g)	$n \approx 1.6 \times 10^{17}$ (g)

CPM66

Grown by SERC Central Facility for III-V Semiconductors by MOVPE.

Grown undoped i.e. GaAs $n \approx 10^{15} \text{cm}^{-3}$.

AlGaAs $p \approx 3 \times 10^{16} \text{cm}^{-3}$ from growth parameters.

n^+ substrate

	<u>Composition</u>	<u>Thickness/μm</u>
Cap	X=0 (g)	0.01 (g)
Cladding	X=0.21 (PL)	2.05 (s)
MQW	X=0 / X=0.3 (g)	0.43 (s)
Cladding	X=0.20 (PL)	2.05 (s)

S.e.m. results imply well and barrier width = $(105 \pm 2) \text{\AA}$.

CPM68

Grown by SERC Central Facility for III-V Semiconductors by MOVPE.

Grown to be p-i-n diode.

n^+ substrate

	<u>Composition</u>	<u>Thickness/μm</u>	<u>Doping/cm^{-3}</u>	<u>Doping/cm^{-3}</u>
Cap	X=0 (g)	0.05 (g)	$p \geq 5 \times 10^{17}$ (g)	
Cladding	X=0.18 (PL)	2.06 (s)	$p \approx 5 \times 10^{17}$ (g)	
MQW	X=0 / X=0.3 (g)	0.263 (s)	$n \approx 1 \times 10^{16}$ (g)	2×10^{16} (CV)
Cladding	X=0.18 (PL)	2.00 (s)	$n \approx 6 \times 10^{16}$ (g)	4×10^{16} (CV)
Buffer	X=0 (g)	0.1 (g)	$n=?$	

S.e.m. results imply well and barrier width = $(114 \pm 4) \text{\AA}$.

CPM96

Grown by SERC Central Facility for III-V Semiconductors by MOVPE.

Grown to be a p-i-n diode.

n^+ substrate.

	<u>Composition</u>	<u>Thickness/μm</u>	<u>Doping/cm^{-3}</u>
Cap	X=0 (g)	0.05 (g)	$p=5 \times 10^{17}$ (g)
Cladding	X=0.16 (g)	2.04 (s)	$p=5 \times 10^{17}$ (g)
MQW	X=0 / X=0.3 (g)	0.40 (s)	$n=1 \times 10^{16}$ (g)
Cladding	X=0.17 (g)	1.53 (s)	$n \geq 5 \times 10^{17}$ (g)
Grade	X=0.05-0.6 (g)	1.00 (s)	?
Buffer	X=0 (g)	?	10^{16} (g)

S.e.m. data implies well and barrier widths = $(97 \pm 3) \text{\AA}$.

NTT203

Grown by MBE at NTT, Japan.

Grown undoped on n^+ substrate.

	<u>Composition</u>	<u>Thickness/μm</u>
Cap	X=0 (g)	0.016 (g)
Cladding	X=0.33 (PL)	1.6 (g)
MQW	X=0 / X=0.33 (PL)	0.41 (s)
Cladding	X=0.33 (PL)	3.4 (g)
Buffer	X=0 (g)	0.05 (g)

S.e.m. data implies well and barrier widths = $(100 \pm 2) \text{\AA}$.

